Low resistance metal semiconductor contacts

Low power nano-electronics and sensing

by

Srinivas Ganti

A thesis submitted in fulfilment for the degree of

Doctor of Philosophy in the School of Electrical and Electronic Engineering

January, 2018

Abstract

Metal semiconductor (MS) contacts are essential in nearly every electronic device. High electrical contact resistance degrades device performance, especially at smaller device geometries. The contact resistance normally scales inversely with the cross-sectional area of the MS contact, and this results in poor electrical conduction in small geometries. Additionally, experiments confirm that surface effects dominate over bulk properties, especially at nanoscale geometries. These conditions impose several restrictions in implementing various device technologies. The electronic properties of metal-semiconductor contacts in some important semiconductors such as Si, Ge, GaAs, among others are found to be largely insensitive to the metal workfunction and semiconductor doping level, due to a phenomenon called Fermi level pinning (FLP). FLP can severely degrade device performance, and creates several fabrication challenges. Many semiconductors lose their applicability in mainstream electronics due to restrictions imposed by this effect. FLP effects are practically observed in many semiconductors doped below 10^{19} cm^{-3} and are most pronounced in lightly doped and (~intrinsic) pure crystals.

This thesis explores material engineering methods to improve contact to semiconductors, without resorting to heavy doping. Large area metal contacts (length/ diameter (d)~ 50-300 µm) are fabricated on Si and Ge. Three key approaches are investigated: **(1)** Modifying interface dipoles and blocking Metal Induced Gap States (MIGS) using ~ nm thick charged oxide interlayers, implementing planar metal interlayer semiconductor (MIS) contacts (Chapter 4). **(2)** Exploiting geometric field enhancement in nanostructured hybrid contacts (Chapter 5) and **(3)** Exploiting voltage controlled non-equilibrium electron heating in island metal films.

The contacts produced by these methods **(2)** and **(3)** are the first experimental demonstrations to show that limitations imposed by FLP can be overcome by modifying the contact material geometry alone, without using heavy doping. Applying mV range bias to these metallizations causes hot carrier emission from these contact's nanostructured surfaces.

Hot carriers are non-equilibrium, energetic carriers that easily overcome the FLP effect in the semiconductor. High conductivity is observed due to the hot carrier effect over a broad range of temperatures –from 4.2 K, tested up to 500 K- despite using low doping in the semiconductor ($N_D \sim 6.4 \times 10^{14}$ cm^{-3}). Novel transport processes are revealed by hot carrier tunnelling and emission mechanisms, which improve conductivity in semiconductors, and will potentially be applicable to other low dimensional materials as well.

The results in Chapter 5 show an interesting demonstration of hot carrier edge scaling current injection used to achieve Ohmic contact to low doped n-Ge. This contact scheme presents a

promising alternative to improving conductivity extrinsically, without using heavy doping, and in a scalable manner. Chapter 6 also contains a proof of concept demonstration. It is shown that closely spaced networks of metal nano-islands of critical dimensions are susceptible to non-equilibrium electron heating, when they receive power in the form of voltage controlled tunnel current. This leads to elevated electron temperatures (~10^3 K) relative to a cold lattice (at ambient temperature). Hot carriers easily overcome small (few eV) electrostatic barriers e.g. Schottky barrier. Consequently, Ohmic conduction is observed at room temperature, and near ballistic hot carrier conduction is observed at 4.2 K through the entire low doped wafer (thickness 0.5 mm, $N_D \sim 6.4 \times 10^{14}$ cm^{-3}).

The wide scope of these findings may find promising applications in nanoelectronic engineering and applied science. There is considerable incentive to continue the research, and obtain a wider range of materials capable of similar effects, described further in the thesis outlook (Chapter 7). Advancing this research further will translate to applications in high speed switching, sensing, optoelectronics and energy harvesting. It is anticipated that these technologies will be applicable to many semiconductors and can be adapted into heterostructures, using advanced fabrication methods.

I dedicate this thesis to my teachers

Acknowledgements

Five years have passed since I first began my studies at Newcastle University. As I now prepare to complete my formal education, I am compelled to reflect on these past years. I believe I will remain indebted to Prof. O'Neill for the rest of my career, for his role in steering my path in science and engineering. In my MSc. (2012) I received lectures from him on Semiconductor device physics (EEE8018/3020). The taught concepts, and more importantly, the method of reasoning I took from his lectures shall remain with me, as part of my scientific method for the rest of my days as a researcher. I would like to thank Prof. O'Neill for instilling these values in all his students, and for believing that I would be a suitable candidate to train for a PhD. I was the only MSc student in my year to receive cleanroom training, shadowing his former student Dr. Nikhil Ponon and PlasmaLab 400 (sputter tool) superuser in the cleanroom. In many ways Nikhil has been my earliest lab mentor and I worked with him in various projects during my Ph.D. and published three papers with him as a collaborator. Thanks to Prof. O'Neill, I now have a close friend and ally. This applies equally to Dr. Peter King and Dr. Erhan Arac. These gentlemen were my main project partners under Prof. O'Neill's A.L.I.E.N. project (Grant ref: EP/J010944/1) which I worked on during 2013-2015. I have received every opportunity to pursue several experimental methods during my four years of research at Newcastle University, not all of which are included in this thesis. Experimental research always carries risk. Amidst a graveyard of failed experiments, discarded drafts, and ideas, I have shared a few small victories with my partners in research. Throughout this time, Prof. O'Neill has been my toughest and most important critic. I have obtained invaluable insight through our countless discussions, which have unquestionably helped me mature as a scientist. I am grateful for his patience, guidance and support over these years and am proud to have been his student.

A greater part of the hours I spent in my research have been in the cleanrooms at Newcastle University. During this period, I had the privilege to study cleanroom practices and codes under Dr. Konstantin Vasilevskiy, our cleanroom manager, and most experienced device fabrication expert at Newcastle University. I am indebted to him for teaching me over the years, sharing his knowledge and experience in fabrication and wafer processing. I wish to thank him for his unwavering support, for his contribution in maintaining a positive learning environment and for ensuring smooth operation of the cleanrooms. I am honoured to bear his trust as an independent cleanroom operator, and in my capacity as a superuser for sputter and XRD tools, including training new tool operators.

In my research on metal semiconductor contacts, I worked closely with Dr. King and Dr. Arac in the cleanroom and electrical characterization labs. In this project, we discovered several peculiar conduction phenomena, over uncounted experimental trials. Sadly, Dr. Arac had to leave Newcastle University at the

end of my second year, followed by Dr. King soon after. Their absence was felt, as the experimental work was almost completely self-driven beyond these stages. Before leaving, they shared a diverse set of research etiquettes, data analysis methods and useful techniques (ALD, XRD) with me and for that, I am most thankful. I would like to thank Peter especially, for continuing to informally supervise me remotely from Helsinki University, under no obligation, after starting his position there as senior ALD researcher. His friendship and support, especially in my third and fourth year has been invaluable towards my research and my personal development as a professional. Together, we took initiative and independently (without additional financial aid) managed to establish new research connections at Cambridge and Royal Holloway University of London (R.H.U.L).

I am indebted to Dr. John H. Quilter (R.H.U.L) for his vital contributions in confirming hot carrier transport in liquid helium I-V measurements. We demonstrated a useful proof of concept only because of this collaboration.

Likewise, I wish to thank Dr. Peter Petrov at Imperial College, London for liquid nitrogen I-V measurements on hybrid contacts (Chapter 5). Special thanks to Dr. Sean Collins (Cambridge), who did STEM-EELS measurements on hybrid contact specimens (STEM-EELS data have not been included in this thesis). I am especially grateful to Sean for sharing his knowledge and expertise on plasmon characterization over several private communications. These works (RHUL, Imperial, Cambridge) were done pro-bono, purely on good faith and in the pursuit of science, for which I hold these men in high esteem.

Behind every successful materials science project, there is at least one very huge microscopist. Our gentle giant is Dr. Karl Dawson. I cannot begin to thank Karl for his exhaustive HR-SEM, HR-TEM, STEM, EFTEM, EBSD surveys of my samples. These experiments helped solidify our understanding of novel crystallization phenomena in materials, shown in Chapters 5 and 6, and complement the electrical behaviour of the specimens. I also wish to thank Dr. Budhika Mendis (Durham University) for performing TEM and EFTEM measurements in our earlier MIS contact work on silicon (Chapter 4).

I would like to thank our partners at NEXUS, Newcastle University for their support in using their XPS facilities. Special thanks to Prof. Peter Cumpson for allowing the work. Thanks to him, I made connections with experienced surface scientists, Dr. Anders Barlow and Dr. Billy Murdoch who helped me study my samples using He ion microscopy (not included in this thesis) and electron emission spectroscopy.

I wish to thank Dr. Jonathan Goss for helpful discussions over the years. Though I am a physicist at heart, my formal training has been in engineering. Our conversations have helped me close gaps in my understanding of solid state physics, which eventually translated into a successful project. I would also

take this opportunity to thank Dr. Alton Horsfall, who is also on my Ph.D panel. Dr. Horsfall was kind enough to introduce me to Rhoderick's book on metal semiconductor contacts in my first-year progression review. This book is a fundamental text in the field, containing reports of seminal works, which helped me understand various transport processes in semiconductors.

I wish to acknowledge and thank Miss. Sinziana Popescu and Dr. Sami Ramadan for inviting me to take part in her research. Together, we managed to contribute towards a new electroless contact technique for Graphene, which was eventually accepted by a high impact journal. Special thanks to Dr. Louise Bailey and Dr. Gary Proudfoot (Oxford Instruments,UK) and Dr. Fernando Rinaldi (Bruker, Germany) for training in sputter process development and in operating the Bruker D8 ADVANCE. I also thank Dr. Lina Persechini (Nature Communications) for encouragement and sharing her expertise on publishing practices in top tier journals.

My departmental colleagues have made me feel at home these past years. Research is rarely ever a solo effort and my work is no exception. I have had the opportunity to connect and work with every research associate in the department. I would like to thank Dr. Kelvin Kwa, Dr. Enrique E. Cousin, Dr. Amit Tiwari, Dr. Neal Wood for their helpful discussions at Merz court, and for our intense stand offs on the squash court. Sincere thanks to Dr. H.K. Chan and Dr. Kelvin Kwa for maintaining the characterization laboratories. A warm thank you to Mrs. Rachael Savidis for helping me on many occasions in the cleanroom. She is dearly missed in the department.

I am grateful to Miss Kabita Adhikari, head of teaching undergraduate labs and Dr. Alex Yakovlev for giving me the opportunity to partake in our school's tradition of teaching. It has been a pleasure to guide undergraduates and MSc's in their lab and coursework.

Many thanks to Allan Wheatley and Gary Potts for support on the mechanical workshop floor and in maintaining the cleanroom. Thanks to Mrs. Gill Webber, Deborah Alexander and Natalie Henderson at the school office for help on several occasions.

I also wish to thank Dr. Glynn Atkinson for allowing me the opportunity to lead an organization committee for the Annual research conference in the capacity of vice chairman and treasurer. These experiences have been most enjoyable and have given me invaluable leadership and management skills, for which I am grateful.

Salutations to my fellow Ph.D researchers from various disciplines. My closest friends- Jonny Naylor, Ashwin Miriyala and Fedor Shmarov have shared considerable insight into their work with me. I am fortunate to have met such fine companions in my journey, and would like to acknowledge our open

conversations, throughout our days as young researchers. Their companionship and support have had monumental impact on my life in Newcastle.

Last, but certainly not least, I would like to thank my parents for this life. Their support allowed me to pursue higher education, for which I am forever in their debt. I have watched them make incredible sacrifices, so I could stand where I am today. There is no price in the world that can repay their struggle. They are my eternal teachers, and I am forever their son. I owe everything to them.

With my best,

Srinivas Ganti

Contents

Chapter 6- Island metal films – hot carrier emitters

Chapter 7- Outlook and future work

Journals, conferences and peer review

Journals

1) "Voltage Controlled Hot Carrier Injection Enables Ohmic Contacts Using Au Island Metal Films on Ge", ***Srinivas Ganti****, Peter J. King, Erhan Arac****,*** *Karl Dawson****,*** *Mikko J. Heikkilä****,*** *John H. Quilter****,*** *Billy Murdoch, Peter Cumpson, and Anthony O'Neill.*

ACS Applied Materials & Interfaces 2017 9 (33), 27357-27364, DOI: 10.1021/acsami.7b06595

I fabricated all the specimens used in this work, developed the process, did electrical & material characterization, data analysis & wrote the final manuscript (including artwork) with Prof. O'Neill. I handled the entire review process independently.

2) "Electroless Nickel Deposition: An Alternative for Graphene Contacting", *Sinziana M. Popescu, Anders J. Barlow, Sami Ramadan,* ***Srinivas Ganti****, Biswajit Ghosh, and John Hedley*

ACS Applied Materials & Interfaces 2016 8 (45), 31359-31367, DOI: 10.1021/acsami.6b08290

I was requested to help during the journal review process for this work. I did XRD on electroless Ni to observe predominant (111) crystallization upon annealing. I performed the metal etching/ Raman mapping experiment, batch processing of Raman data (Fig.9) & helped prepare responses to the referees based on my experimental findings.

3) "Effect of deposition conditions & post deposition anneal on reactively sputtered titanium nitride thin films", *Nikhil K. Ponon , Daniel J.R. Appleby, Erhan Arac, P.J. King,* ***Srinivas Ganti****, Kelvin S.K. Kwa, Anthony O'Neill.*

Thin Solid Films, Volume 578, 2015, Pages 31-37, ISSN 0040-6090.

I helped Nikhil optimize the TiN sputtering recipe by performing 4-point sheet resistance measurements on thin film TiN samples. During my MSc. project I helped Nikhil optimize chamber pressure parameters for his TiN recipe.

4) "Improving metal/semiconductor conductivity using AlOx interlayers on n-type and p-type Si", *P. J. King, E. Arac,* ***S. Ganti****, K. S. K. Kwa, N. Ponon, and A. G. O'Neill*

Appl. Phys. Lett. 105, 052101, 2014, DOI:10.1063/1.4892003

I fabricated MS contacts, MIS contacts, and performed electrical characterization with Dr. Arac & helped Dr. King prepare the manuscript.

5) "Ferroelectric properties in thin film barium titanate grown using pulsed laser deposition", *Daniel J. R. Appleby, Nikhil K. Ponon, Kelvin S. K. Kwa,* ***Srinivas Ganti****, Ullrich Hannemann, Peter K. Petrov, Neil M. Alford, and Anthony O'Neill*

Journal of Applied Physics 116, 124105, 2014, DOI: 10.1063/1.4895050

I helped Nikhil during the review process for this paper, by performing additional C-V-T measurements of MIM capacitors, as requested by reviewers. I obtained a series of data points for Fig.2 in the revised manuscript. The electrical characterization lead on the project (Dr. Dan Appleby) was away from University at the time.

Conferences

1) "Reduced metal contact resistance to silicon using Al based interlayers", ***S. Ganti****, E. Arac, P. J. King, A. J. Barlow, P. J. Cumpson and A. G. O'Neill*

at the 45th Semiconductor Interface Specialists Conference (SISC 2014), San Diego, CA, USA.

I presented a poster highlighting the effect of evaporating thin Al interlayers to Ni contacts on Si. Annealing these contacts also produces conductivity enhancements on both n- and p-Si, like our ALD Al_2O_3 MIS work.

2) "Fermi Level De-pinning In Metal-Semiconductor Contacts Via Nanometre-scale ALD Dielectric Films", *Peter J. King, Erhan Arac,* ***Srinivas Ganti****, Sami Ramadan, Kelvin S. K. Kwa, Anders J. Barlow, Peter J. Cumpson, John Robertson and Anthony G. O'Neill*

at the 12th International Baltic ALD conference (BALD 2014), Helsinki, Finland.

I fabricated samples, did electrical characterization with Dr. Arac. Dr. King did the ALD process and attended the conference.

3) Interface engineering with ALD on Germanium", *Peter J. King,* ***Srinivas Ganti****, Erhan Arac and Anthony G. O'Neill.*

at the 13th International Baltic ALD conference (BALD 2015), Tartu, Estonia.

I fabricated and processed samples, did electrical measurements and characterization. Peter did the ALD process. Erhan did early experiments on Ge MIS contacts before leaving Newcastle University.

Peer review

"Low-energy electron excitation effect on formation of graphene nanocrystallites during carbon film growth process", *Wencong Chen Xi Zhang, and Dongfeng Diao*.
Appl. Phys. Lett. 111, 114105 (2017), DOI: 10.1063/1.4990117

I was recently invited to peer review a work on graphene nano-crystallite carbon films (GNEC), which only required one iteration for revision. These authors demonstrated an interesting sputtering technique to form 2D graphitic island films on Si. Electron cyclotron resonance in the sputtering plasma was used to direct energetic electrons (~ 80 eV) towards the deposited carbon film, along with substrate bias as part of the growth process. Non-equilibrium electron-matter interactions result in the generation of "hot products" at the carbon film surface, forming GNEC i.e. $sp^3 \rightarrow sp^2$ transformation. I recommended publication in APL after the authors clarified and addressed all the issues I raised during review. The final manuscript was improved accordingly, and later accepted by the editor.

Abbreviations

AFM – Atomic Force Microscopy
ALD – Atomic layer deposition
BCC– Body Centre Cubic
BHF– Buffered Hydrofluoric acid (also known as BOE)
BOE – Buffered Oxide Etch
CCD – Charge Coupled Device
CMF – Continuous Metal Film
CMOS– Complementary Metal Oxide Semiconductor
CNL – Charge neutral level
COD – Crystallography Open Database
CTLM – Circular Transfer Length method
C-V – Capacitance-Voltage
DC– Direct Current
DFT–Density Functional Throry
DI – Deionized
DIGS – Disorder Induced Gap States
DMF – Dimethylformamide
EBSD – Electron Backscatter diffraction
EDX – Energy dispersive X-ray spectroscopy
EELS – Electron Energy Loss Spectroscopy
EFTEM – Energy Filtered Transmission electron microscopy
EUV – Extreme Ultraviolet
FCC – Face Centre Cubic
FE – Field Emission
FEG – Field Emission Gun
FET – Field Effect Transistor
FLP – Fermi Level Pinning
GND – Ground/Earth
HAABF– High Angle Annular Bright Field
HAADF– High Angle Annular Dark Field
HCP– Hexagonal closed packing
HLI – High Level Injection
HR – High Resolution
IFIGS – Interface induced gap states
IMF– Island Metal Film
IPA – isopropyl alcohol
ITU – International Telecommunications Union
I-V– Current-Voltage
LCC– Leadless Chip Carrier

LED– Light Emitting Diode
MIGS – Metal Induced Gap States
MIS – Metal interlayer semiconductor
MOS – Metal Oxide semiconductor
MS – Metal Semiconductor
NDC – Negative Differential Conductance
NDR – Negative Differential Resistance
NMP – N-Methyl-2 pyrrolidone
PPE– Personnel Protection Equipment
RTA – Rapid Thermal Annealing
SBH – Schottky Barrier Height
SCS – Semiconductor Characterization System
SEM – Scanning Electron Microscopy
SET – Single Electron Transistor
SMU – Source Measure Unit
STEM– Scanning Transmission Electron Microscopy
STM – Scanning Tunnelling Microscopy
TE – Thermionic Emission
TED – Thermionic Emission Diffusion
TEM – Transmission electron microscopy
TFE – Thermionic Field Emission
TMA – trimethylaluminium
UHV– Ultra High Vacuum
XPS – X-Ray Photoelectron Spectroscopy
XRD – X-Ray Diffraction

"There are more things in heaven and earth, than are dreamt of in our philosophy."

-William Shakespeare

Chapter 1:

Introduction

1. Motivation

Electronic technology is vital in sustaining global infrastructures and forms the backbone of modern physical sciences and healthcare. A long history of advances in solid state physics and engineering have created a global semiconductor industry, worth hundreds of billions of dollars. According to the International Telecommunications Union (ITU), about one in three people has access to a mobile phone[1]. Electronic technology is constantly improving and renewing its presence in the world, with older technologies gradually becoming obsolete in every passing technological generation. Conventionally, computing power scales with number density of devices on chip. This has historically served as a guide to the relentless miniaturization of transistor design. In 1965 Gordon Moore (Intel) predicted that the number of transistors per square inch on integrated circuits will continue to double every 1-2 years, based on trends he had observed since its invention[2]. The prediction became a competitive driver for design innovation in the pursuit of ultra-small scaling. 'CMOS design' and 'CMOS technology' have developed since then using formally separate methodologies to fulfil "Moore's law". State of the art electronics used in smartphones (late 2017) are now approaching the 10 nm node (transistor gate length).

The scaling problem is becoming more and more challenging due to physical material limitations, and the cost of miniaturization. Device scaling is unlikely to continue by planar scaling alone. At these ultra-small dimensions, device performance can be severely compromised. Novel designs and new materials are the needed to continue progress. Alternative technologies are emerging from the bedrock of transistor technology. *There's plenty of room at the bottom,* Richard Feynman's paradigm shifting talks[3][4] set the scene for the nanoelectronics revolution.

Progress is always met with challenges. It is necessary to address the issues encountered in nanoscale electronics to fully realize the extent of possibilities that nanotechnology can offer. Metal contacts are essential in nearly every electronic device, to control its operation externally.

High contact resistance is a severe impairment to proper device operation. Contact resistance usually increases at smaller device geometries. Surface contributions dominate a device's

electronic behaviour, which may result in loss of control and functionality, and even complete device failure in critical cases. The motivation of this thesis is to investigate alternative experimental methods to improve electrical contact resistance to semiconductors.

Real crystal surfaces of semiconductors form defects in the crystal structure, and interface states that govern electronic properties at the interface. These interface states are believed to originate from dangling bonds, adsorbed chemical species, energy band perturbations and contamination, among others. Non-ideal interfaces result in unexpected electronic behaviour and generally, poor device performance. Metal-semiconductor contacts are traditionally improved extrinsically, by doping the semiconductor. However, implant doping techniques[5] could become problematic at small geometries. New techniques are being used to achieve doping feats beyond the solid solubility limit, as is demonstrated in gas immersion laser doping of Ge[6]. However, laser optics set a limit on the feature size that can be selectively doped by annealing. Additionally, there is a restrictive doping uncertainty problem at nanoscale geometries, which can cause reliability issues.

The technology to write and pattern nanostructures using sophisticated lithography methods exists; however, fabrication capacity alone cannot guarantee proper operation, as it is often the nature of the material interface which governs electronic properties.

This thesis explores material engineering options to achieve low contact resistance, without resorting to heavy doping. Three main approaches are explored namely; interface engineering (Chapter 4), geometric field enhancement (Chapter 5), and distributed nanostructures (Chapter 6). These methods aim to improve contact externally, by modifying the metallization scheme.

Silicon is the most widely used material in the semiconductor industry due to well-established protocols of silicon technology and the abundance of the material in the earth's natural resources. However, other elemental semiconductors can offer better intrinsic performance. For example, germanium has superior intrinsic electronic properties, compared to silicon. Ge offers high carrier mobility (especially for holes), superior performance at cryogenic temperatures, high carrier density due to its smaller band gap and low on-state resistance. Despite these benefits, it is yet to succeed silicon as the commercial standard. Germanium surfaces exhibit a strong case of FLP, which severely limits its usability. FLP is a surface phenomenon observed in many crystalline semiconductors. FLP typically restricts the relative energy band alignment at the contact interface to a fixed energetic configuration, making electronic properties largely insensitive towards the metal workfunction (ϕ_M) and doping level (N_D) in the semiconductor. In many cases this results in high resistance in metal-semiconductor contacts. This effect causes

a departure from the ideal Schottky-Mott relationship, where the Schottky barrier height (ϕ_B) at the interface is equal to the difference in the vacuum levels of the metal and semiconductor. Instead, the Schottky barrier height remains fixed due to FLP. The electronic properties of junctions become largely insensitive to the choice of materials, and standard wafer processing techniques and the implementation of scalable logic structures (and other technology) becomes extremely challenging. Most semiconductors - Ge, Si, diamond, InAs, GaAs, InP, and many more exhibit varying degrees of FLP. FLP and electronic properties of metal-semiconductor interfaces have been studied for nearly a hundred years now. A complete theory is yet to be accepted because the origin of FLP is still widely debated. Indeed, there could be multiple causations for the same effect being observed electrically. The Schottky barrier formed at the metal-semiconductor interface is a key parameter in characterizing the contact's electrical properties.

The following section will briefly overview some important models proposed in the literature about Schottky barrier formation at metal-semiconductor interfaces that will help in understanding the observed equilibrium arrangement of energy bands in metal semiconductor junctions. A short summary of gap state models and bond polarization models is given for convenience. A later section describes prior art in contact engineering, to compare potential options to pursue in experimental research. The thesis outline is provided at the end of this chapter.

1.1. Overview of Schottky Barrier Formation

The Schottky-Mott theory predicts that the barrier height at the interface should vary with adjustments between the vacuum levels of the materials (e.g. metal and semiconductor). The ideal Schottky barrier height is given by eqs. (1.1-1.2). Fig. 1 schematically shows the ideal Schottky barrier formation for materials brought into contact, using energy band diagrams.

The electron barrier height ϕ_{Bn}^{0} is given by eq. (1.1)

$$\phi_{\mathrm{Bn}}^{0} = \phi_{\mathrm{M}} - \chi_{\mathrm{S}} \tag{1.1}$$

The barrier height for holes (ϕ_{Bp}^{0}) is given by eq. (1.2),

$$\phi_{\mathrm{Bp}}^{0} = \chi_{\mathrm{S}} - \phi_{\mathrm{M}} + E_{\mathrm{g}} \tag{1.2}$$

χ_{S} and E_{g} are the electron affinity and band gap of the semiconductor respectively.

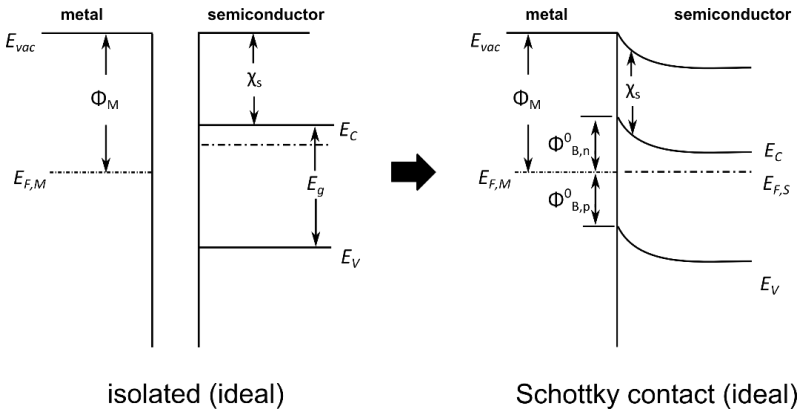

Figure 1.1: Ideal Schottky interface for materials brought into contact. The barrier height ($\phi^0_{B,n}$) is equal to the workfunction difference. Vacuum level is adjusted to maintain equilibrium.

This model discounts any charge interactions that may occur between metal and semiconductor surfaces and usually does not reconcile with experimental observations. The Schottky barrier that forms at a metal-semiconductor junction is experimentally observed to be almost insensitive to the metal workfunction (ϕ_M) in many semiconductors. Bardeen[7] was the first to postulate the presence of interface states lying within the semiconductor band gap, that effectively *pin* the Fermi level at the interface. His model required an interfacial oxide layer that adjusts for the error between experimental and theoretical Schottky barrier height, by dropping remaining potential across the interfacial oxide layer. This interfacial layer is a salient feature in the model and is required for the theory to work. Of course, in modern electronics, intimate contacts are used, which do not contain this interfacial oxide layer and thus, Bardeen's model is incomplete. However, FLP is still observed even using state of the art techniques. Alternative models have been proposed to understand experimental observations of the FLP phenomenon. FLP is usually interpreted in terms of either gap state models, or bond polarization theory, briefly discussed next.

1.1.1. Gap state models

Theoretical models have been proposed as improvements to the ideal Schottky-Mott model. These incorporate the effects of charged *gap states* that may form within the semiconductor's band gap to explain the trends of FLP observed in experimental data. Gap states come in various forms: Metal-induced gap states (MIGS)[8], surface states[7], defect related states[9], disorder-induced gap states (DIGS)[10] and "interface induced" gap states (IFIGS)[11]. Alternatively, chemisorption-induced interface defects have been suggested as a model to explain FLP,

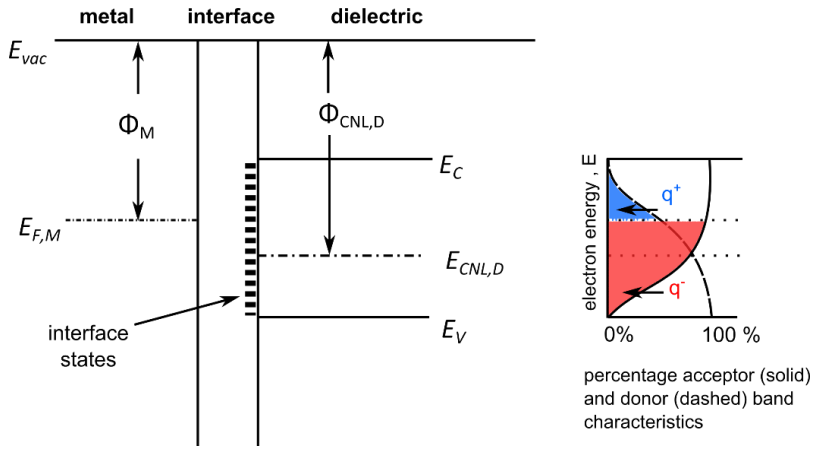

Figure 1.2: Simplified gap states model of a metal-dielectric (or semiconductor) contact. Left- The energy band diagram is shown for the case of no interaction i.e. constant vacuum level for infinite separation between materials. **Right-** Upon contact, charge is exchanged to equalise the Fermi levels leading to an occupation distribution for electronic states in the band gap. The MIGS model for e.g. suggests that the occupation of the interface states is dependent on electron wavefunction spill out close to the metal surface. These electron wave vectors decay evanescently into the semiconductor to form states as shown schematically on the right.

reasonably supporting the experimental data for specific semiconductor surfaces such as (110) GaAs, and a few others in the III-V family[12]. Despite their varied basis, these models are in essence, similar to one another insofar as they assume some distribution of interface/ gap states, shown schematically in Fig.1.2-left, with a density of gap states (D_{gs}) and a charge neutral level (CNL *or* ϕ_0). The net charge density on the semiconductor surface is determined by occupation of gap states, which depends on the Fermi level position, relative to ϕ_0, and the degeneracy of the states involved. The metal supplies an equal image/ screening charge density, and together they create the interface dipole. Potential is dropped across the interface, fixing the Fermi level position and hence, the Schottky barrier height.

These models arrive at expressions for the Schottky barrier height which are of the form:

$$\phi_{\mathrm{Bn}}^{0} = \gamma_{\mathrm{gs}}(\phi_{\mathrm{M}} - \chi_{\mathrm{S}}) + (1 - \gamma_{\mathrm{gs}})\phi_0 \qquad (1.3)$$

with the gap states parameter, $\gamma_{\mathrm{gs}} = \left(1 + \frac{q^2 \delta_{\mathrm{it}} D_{\mathrm{gs}}}{\varepsilon_{\mathrm{it}}}\right)^{-1}$

γ_{gs} is also known as the pinning factor (S) in several works in the literature. Here it assumed that charged metal and semiconductor surfaces are separated by an interfacial region of thickness δ_{it} (~0.5 nm) and dielectric constant $\varepsilon_{\mathrm{it}}$. These assumptions become questionable when one considers intimate contacts, diffused junctions, abrupt junctions or clean surfaces

cleaved in vacuum, which also demonstrate FLP[13].

It can be ascertained that gap states exist and that they contribute to the FLP effect, but these models are neither complete nor standalone, as the origin of the gap states is uncertain. Each model uses a distribution of states to fit experimental data, notwithstanding cases where these models are shown to be inadequate to explain the observed electrical characteristics of the junction. For instance, gap state models can describe the severity of FLP in terms of gap states parameter / screening factor (γ_{gs}), which is proportional to the density of gap states as per eq. (1.3). However, they are unable to justify the sensitive structural dependences of the Schottky barrier height at epitaxial metal-semiconductor interfaces[14]. Non-epitaxial, polycrystalline metal-semiconductor contacts also demonstrate Schottky barrier height inhomogeneity, indicating a structural dependence[15]. Nearly perfect ideality factors and observed voltage dependence of the barrier height also cannot be explained satisfactorily by gap state models[16].

The gap states models include interface dipole formation, resulting from gap state occupancy (sketched in Fig.1.2-right). A rival candidate is the interface bond polarization model (discussed later), which gives a general description of the physical phenomenon of interface dipoles and considers the structural dependences of the Schottky barrier. It arrives at expressions for barrier height with a functional form similar to the one derived from gap state models and independently justifies observed experimental trends in several semiconductors[17].

As per the surface state model, dielectrics and semiconductor surfaces (e.g. Ge and Si) form a distribution of electronic states within the band gap. The energetic arrangement before contact (materials separated) is shown schematically in Fig. 1.2-left. Here a dielectric/ semiconductor is shown with a distribution of interface states in its band gap. The nature of these states becomes more acceptor like towards the conduction band and more donor like towards the valence band (Fig. 1.2- right). The crossover point is the charge neutral level (CNL). The Fermi level is experimentally found to be pinned close to the CNL. The CNL is experimentally deduced to lie ~0.1 eV above the valence band in Ge, and ~0.6 eV above the valence band (i.e. mid-gap) in Si. The Fermi level must be constant throughout the material for there to be charge neutrality at equilibrium. Hence, band bending results in the formation of almost fixed energy barriers.

FLP in Ge is especially interesting because it occurs so close to the valence band. Early experiments indicated that the Ge surface is degenerately p-type, regardless of bulk conductivity; implying n-type Ge surfaces are inverted and p-type Ge surfaces are accumulated. The pinning position of the Fermi level has been confirmed independently by contact

potential[18] and photoelectric measurements[19]. These observations are in reasonable agreement with the theory of surface states, originating from perturbed conduction and valence band states[20]. Unoccupied valence band states above the Fermi level create a 2D hole gas, which leads to metallic surface conductivity in n-type Ge[21]. Applying small (~ 100 mV) negative bias nearly always results in carrier inversion near the surface in n-type Ge. Metallic surface conductivity is also observed on clean Si surfaces and is often attributed to half-filled electronic states at the surface[22].

In n type materials, the Fermi level at the surface is usually found to lie above the CNL. This can be rationalised by treating surface state charging as a response to the ionized donors in the bulk or vice versa. The outcome of this arrangement is that the surface develops a net negative charge at equilibrium, due to occupied acceptor states below the Fermi level. The surface electric field permeates into the semiconductor and a space charge region is formed below the surface, containing fixed ionized dopant impurities (donors) that effectively screen the field. Potential is dropped in this electron depleted (space charge) region. The potential variation in the depletion region, in addition to the surface dipole causes upward band bending at the interface.

In p-type materials, ionized acceptors (fixed negative ions) cannot contribute to the screening of negative surface charge. The Fermi level is pinned close to the CNL at equilibrium. This picture of FLP in Ge is widely accepted as the working model in the literature[23]. A recent study challenges this view. *In vacuo* sheet conductance measurements have shown that clean n-type (001) Ge surfaces tend to be nearly inverted at equilibrium. Metallic conductivity was observed on both bare and hydrogen passivated surfaces, indicating that the structure and passivation of surface states does not alter the electronic properties[21]. These findings are not explained by gap state models. It is implied that either FLP in Ge does not arise exclusively from occupied gap states or atomic hydrogen is somehow unable to passivate these states effectively. Nonetheless, the surface state model is frequently invoked in the literature to explain the fixed band bending in pinned semiconductors.

1.1.2. Bond polarization and interface dipoles

The bond polarization model assumes that chemical bonds are formed between the semiconductor and metal once thermodynamic equilibrium is established. Charge transfer occurs at the interface to equate the chemical potentials of the metal and semiconductor. The bonds are polarized due to the charge transfer dipole, called Schottky dipole (Δ_{Sch}) that adjusts

the potential drop across the interface to form the Schottky barrier according to eq. (1.4).

$$\phi_{\mathrm{Bn}}^{0} = (\phi_{\mathrm{M}} - \chi_{\mathrm{S}}) - q\Delta_{\mathrm{Sch}} \quad (1.4)$$

Upon expansion of terms and rearrangement, the theory arrives at a familiar looking expression for Schottky barrier height given by eq. (1.5),

$$\phi_{\mathrm{Bn}}^{0} = \gamma_{\mathrm{B}}(\phi_{\mathrm{M}} - \chi_{\mathrm{S}}) + (1 - \gamma_{\mathrm{B}})\frac{E_{\mathrm{g}}}{2} \quad (1.5)$$

where the bond polarization parameter, $\gamma_{\mathrm{B}} = 1 - \frac{e^2 \delta_{\mathrm{MS}} N_{\mathrm{B}}}{\varepsilon_{\mathrm{it}}(E_{\mathrm{g}} + \kappa)}$;

Here, the extent of *pinning* is governed by the density of chemical bonds ($\mathrm{N_B}$) formed at the interface, like the gap state models, where D_{gs} is a parameter. Eq. (1.5) has a form similar to eq. (1.3). The bond polarization parameter γ_{B} is analogous to the *screening factor* of gap state models. The interfacial region thickness δ_{it} is replaced by δ_{MS}, which is the distance between the metal and semiconductor atoms at the surface. The dielectric constant of the interface ($\varepsilon_{\mathrm{it}}$) is treated as an average, using the inverse of reciprocal sums of the semiconductor (ε_{∞}) and metal (∞) dielectric constants to yield $\varepsilon_{\mathrm{it}} \sim 2\varepsilon_{\infty}$. A small term κ is included, which is the sum of interaction energies between the nearest neighbours at the atomic interface i.e. between metal-metal, metal-semiconductor and semiconductor-semiconductor atoms.

The validity of this model has been claimed by graphing experimentally obtained pinning factors (S_{ϕ}) for various semiconductors, ranked by their bandgap (E_{g}), in a functional plot of eq. (1.5) i.e. $\left(\varepsilon_{\infty}\left[1 - S_{\phi}\right]\right)^{-1}$ vs. E_{g}

Generally, a good linear fit is obtained. If one compares the γ_B term in eq. (1.5) to the experimentally determined pinning factor for Ge ($S_{\phi} \sim 0$), plugging in the numbers gives a Schottky barrier height ~ $\frac{E_{\mathrm{g}}}{2}$, which is inconsistent with experimental observations. The experimental value of the barrier height is nearly equal to the band gap (E_{g}), as the Fermi level is pinned near the valence band[23].

In contrast, the functional plots for gap state models show considerable scatter in the data, especially for Ge and Si[24]. On the other hand, the fit for GaAs is quite good which is probably why this approach is so popular in the III-V community.

Semiconductor wafers used in fabrication are usually cut from a purified crystalline ingot grown using crystal seeding techniques such as the Czochraslski process. Naturally, the cut results in atomically rough surfaces even after chemical mechanical polishing. Atomic terraces are

formed on the surface, readily observed in high resolution AFM and STM imaging[25]. In the case of GaAs, segregation of As atoms is observed at these terraces, which create local electric dipoles[26]. This sort of polarization by segregation is not directly relevant in elemental semiconductors, although defects in surface reconstruction may contribute to the interface dipole. The tensile and compressive forces experienced by surface atoms in an unrelaxed crystal are not balanced the way they are for atoms deep within the bulk.

The break in lattice periodicity at the surface leads to energy minimization by surface reconstruction. The most common scheme seen on (100)Si and (100)Ge single crystals is the *missing row* or c(4x2) reconstruction, which forms dimers at the surface[27]. Surface charging has been theoretically investigated using first principles by simulating un-doped layers of Ge and Si with dimer surfaces[28][29]. The (001)Ge surface develops a net negative charge due to Ge vacancies, while the balancing positive space charge is provided by self-interstitials. The effect of the resulting positive space charge was shown to extend into the substrate for up to 15 atomic layers (~ 8.4 nm) due to repulsive interactions, apparently independent of the thickness of the simulated structure. These calculations support experimental observations of significant band bending at intrinsic Ge surfaces[30].

An exact description of the FLP phenomenon is yet to be formulated. However, it is certain that the gap state models or bond polarization models alone are unable to account for all the experimental trends observed for semiconductor interfaces.

1.2. Prior Art - Contact Engineering Strategies:

According to the models described previously, an interfacial dipole is responsible for FLP. This serves as motivation to manipulate this dipole experimentally to alleviate the FLP effect. Fermi level "un-pinning" or "de-pinning" techniques (e.g. sections ***1.2.1.*** and ***1.2.2*** below) have been demonstrated in different ways, by several research groups. The key contact engineering methodologies for Ge/ Si are described below, citing only a few examples to represent the basic approaches taken by researchers.

1.2.1 MIS Contacts

An ultra-thin interlayer (< 3 nm), usually a high-κ dielectric material is inserted between the metal and semiconductor to form a metal-interlayer-semiconductor (MIS) structure. A high-κ dielectric with small conduction band offset to the semiconductor is preferred. A polar interface is created between the interlayer and the semiconductor, serving as a "counter dipole" to the

charged semiconductor surface dipole. This adjusts the metal workfunction closer to the semiconductor's conduction band. If the conduction band offset between the interlayer and semiconductor is small, one can achieve low resistance Ohmic contact on n-type materials[31]. Accordingly, the contact to p-type material becomes rectifying due to the shift in FLP position in the bandgap. If the conduction band offset between the dielectric and semiconductor is large, tunnelling resistance dominates, resulting in a poor contact[32]. The contact properties are insensitive to the metal workfunction, even after forming the Ohmic MIS junction by using an appropriate interlayer[33]. The FLP condition is not really alleviated, rather the situation is simply reversed to produce a variant of FLP. The lowest specific contact resistivity reached by this approach on heavy doped Ge is only ~10^{-5} ohm.cm^2 [34][35] and ~10^{-8} ohm.cm^2 on heavy doped Si[36].

1.2.2 Direct Metallization using TiN (on Ge)

TiN thin films are directly deposited onto Ge by sputtering, followed by annealing. Under the right process conditions, a polar, ternary compound Ti-Ge-N layer is formed at the interface. This creates an interface dipole to offset the FLP position towards the Ge conduction band, enabling an Ohmic contact to n-type Ge, but forms rectifying contact to p-type Ge[37][37]. The advantage of this method is that unlike the MIS approach, one need not worry about tunnel resistance of the interlayer or conduction band offsets which could potentially limit design choices. However, like the MIS approach, this too results in a variant of FLP in producing a rectifying contact on p-type Ge and Ohmic contact on n-type Ge.

1.2.3 Embedded Metal Nanoparticles

Ultra-small metal nanoparticles (0.2-2 nm) are deposited onto the semiconductor by sputtering, then coated with (dielectric, optional) metal cap layers, to form embedded metal nanoparticle matrices within the contact. Electric field hot spots are formed at the nanoparticle triple interfaces i.e. $metal_{nano}$/$metal_{cap}$/semiconductor substrate, which enhances thermionic field emission across the junction, thereby lowering contact resistance. So far, only this approach has been shown to enhance conductivity on n-type Ge without degrading performance on p-type Ge[38]. Although, to date, the lowest contact resistivity attained by this method is only 0.02 ohm.cm^2, despite using heavy doping (N_D ~1×10^{20} cm^{-3}).

The "un-pinning" approaches (***1.2.1***) and (***1.2.2.***) described above result in asymmetric conduction on n- and p type semiconductors. Separate metallization schemes are then required to achieve Ohmic contact to both n- and p-type regions in a device, increasing complexity and cost. Furthermore, the improvements in specific contact resistivity achieved using the MIS approach is not very effective at high doping levels[39].

For a metal-semiconductor junction in equilibrium, the sum of the electron and hole barrier heights is usually conserved to equal the band gap value of the semiconductor. This is only a guide, not a rule, as exceptions become apparent when the FLP position is considerably different in n- and p-type materials; for example in (110)GaAs[40]. However, for both n- and p-type Ge the Fermi level is pinned close to the valence band (or conduction band in the case of "un-pinning"), so this relationship holds true due to strong FLP. These considerations seem to indicate that contact engineering solutions for Ge would always result in asymmetric conduction properties for its n- and p-type contact junctions. The same can be said about other strongly pinned semiconductors like InAs[41].

On the other hand, the embedded nanoparticle approach (***1.2.3***) though reasonably successful, requires a specialised tilted target sputtering setup to control the nanoparticle size and is not suitable for large scale coatings due to the nature of magnetron sputtering. The embedded metal nanoparticles seem to be more effective when used on heavy doped substrates, and only provide *quasi ohmic* I-V characteristics on low doped substrates i.e. the reverse current is smaller in magnitude compared to the the forward current for equal/ opposite applied voltages ($\pm V_A$).

1.3. Thesis outline

This thesis will focus on the electronic properties of novel metallization schemes which allow charge carriers to overcome the Schottky barrier and pinning effect observed at the contact interface. The technical chapters in this work are reports of original experimental findings. Novel hot carrier tunnelling and emission mechanisms (Chapters 5 and 6) have been identified in new contact materials, without changing the default pinning arrangement. Hot carriers provide large tunnelling currents in both forward and reverse bias (Chapter 6) without heavy doping. Moreover, the same metallization layer is shown to improve conductivity in both n- and p-type materials. This research is still at a very early stage, and could be advanced further using state of the art fabrication techniques. However, the general conclusions drawn from this work are anticipated to have considerable impact e.g. for applications in sensing, energy harvesting, optoelectronics, as well as switching applications. Two new contact elements are

proposed at the end of the thesis in Chapter 7, which may potentially be scaled down and extended to other semiconductors, low dimensional materials.

Chapter 2 covers background of conduction mechanisms and electrostatic treatments classically encountered in metal-semiconductor junctions, plasma physics and a short review on the basics of Quantum tunnelling. Advanced readers may skip these sections. These are provided for quick reference only, and are not intended to be comprehensive guides.

Chapter 3 briefly summarizes experimental methods and procedures used in this thesis. Complete fabrication protocol of samples is provided. Characterization techniques are only described for convenience. Advanced readers can skip these sections and proceed to results.

Chapter 4 documents results on MIS contacts to low doped n- and p-Si using thermally grown ultra-thin Al_2O_3 interlayers, covering results from our previous publication[42] and including further work using moderately doped Si, to show the limitations of the MIS approach. Pilot studies of MS contacts to Ge are included in this chapter, studying strong FLP condition on low doped n- and p- Ge

Chapter 5 (to be published, manuscript under preparation) reports a new material for contact to pinned semiconductors (like Ge) using thermally self-assembled *hybrid* contacts, which exhibit Ohmic edge scaling (one dimensional) I-V characteristics at normal temperatures (near room temperature) and reverse hot electron tunnelling breakdown over a wide range of temperatures, down to 4.2 K, despite using low doped n^- Ge ($N_D \sim 6.4 \times 10^{14}$ cm^{-3}).

Chapter 6 explores a distributed nanostructures approach, demonstrated using highly orientated Au island metal films (IMFs) on Ge. IMF contacts provide hot carrier emission current at mere mV applied bias over a wide range of temperatures, down to 4.2 K. Voltage controlled hot electron and hot hole currents are observed on n-Ge. One may read an abridged version of this chapter in our recent publication[43].

Chapter 7 concludes the thesis with a brief outlook on the new device elements discovered in this Ph.D. thesis (Chapters 5,6) and their applicability to a wide range of materials. Experiments are proposed towards future work, using advanced state of the art techniques.

‘‘The pure and simple truth is rarely pure, and never simple.’’

-Oscar Wilde

Chapter 2:
Background

Abstract

This chapter covers some background theory about electronic phenomena, relevant to the thesis. The aim of this chapter is to arrive at a basic understanding about electronic properties of materials, carrier transport phenomena in different materials and mediums. An attempt is made to review a wide range of topics like plasma physics, semiconductor physics, carrier transport in metal-semiconductor (MS) contacts and metal-interlayer-semiconductor (MIS) contacts and quantum tunnelling. Some important derivations and results have been adapted from text book refs.[44],[45] and online open courseware available from I.I.T. (India), M.I.T, Purdue University, Colorado University (USA). A broad review of these sources has been organized here in abridged form, for the convenience of the reader. Theoretical and practical considerations taken from these works will help in interpreting results shown in later chapters of this thesis.

2.1 The Big picture

Solids, liquids and gases make up only ~ 1% of matter in the entire known universe. The remaining 99% is in a state of plasma i.e. a high energy state of matter, composed of energetic charged particles, as well as neutral species (atoms). Plasmas are usually observed at very high temperature (~ 10^4 K). Plasmas qualify as a state of matter because they obey principles of charge quasi-neutrality, and exhibit a Debye length. Plasmas are mainly characterized by two important macroscopic quantities - the background particle concentration (n_0) and the temperature (T). Plasmas are interpreted as interpenetrating fluids, obeying (Newton's second law) the equation of motion, and the equation of continuity. These classical treatments are followed similarly while studying electronic phenomena in semiconductors. Electrons in a metal are also treated as a gas in many variants of the so called, "jellium model" throughout literature. In nature, plasmas only occur when the concentration of ionized species exceeds the concentration of neutral species considerably. These conditions are met for example in Earth's atmosphere (ionosphere), stars and other astronomical bodies. In the laboratory, a plasma can

be contained by electromagnetic fields or by the surface energy barriers formed at semiconductor interfaces. The electron, hole (e^-, h^+) concentration in a semiconductor crystal could be interpreted as a two component (e^-, h^+) weak plasma, superimposed onto fixed ionized cores of the crystal lattice. This is a general view considering that (1) charge quasi neutrality is also obeyed in semiconductor crystals, and (2) the degree of ionization in a semiconductor is a function of temperature, as is the case for plasmas.

A key difference is that the charge carrier pairs in a semiconductor are confined by the lattice and therefore, exhibit wave-like phenomena, due to which they can only exist in certain allowed energy states in the energy band structure of the semiconductor. The periodicity of the lattice affects the electron/ hole wavefunctions in the crystal, causing interference effects that create band-gaps/ forbidden energies within the electronic energy continuum of the material. These phenomena have diverse applications, and are heavily exploited in modern electronics for a variety of purposes. It is useful to gain an understanding about charge carrier transport in semiconductors, to interpret novel carrier transport phenomena in emerging, prototype technologies.

The following sections will summarize basic aspects of plasma physics, plasmonic response of materials, semiconductor physics and carrier transport phenomena. These topics are of interest to this thesis as they help interpret new experimental findings shown in later results chapters 4, 5, 6.

2.2 Theoretical and practical considerations

2.2.1. Energy bands, carrier distribution and temperature dependencies in semiconductors.

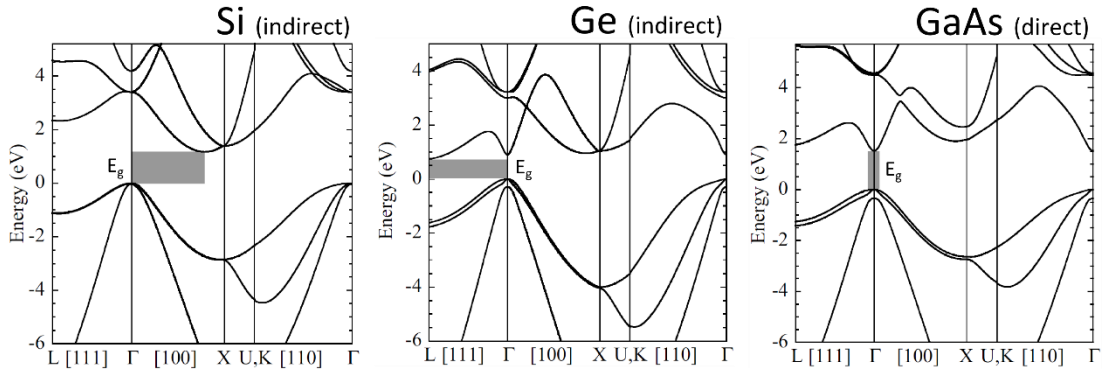

Figure 2.1: E-k diagrams of bulk Si, Ge and GaAs over the whole Brillouin zone (adapted from ref. [46]). Lowest energy gaps relative to the zone centre have been marked using gray boxes. Si and Ge are indirect gap materials while GaAs is a direct gap material.

The expressions, equations and concepts described in this section are adapted from text book ref.[45] (Chapter 1) and important topics are recapped here, for convenience.

Pure crystals of semiconductors have periodic lattice structures. Hence, electrons in the solid experience periodic potential, $V(\boldsymbol{r})$ from the solid-state ionic cores of the lattice. The energy-momentum (E-**k**) relationship of electrons in solids is developed by including the periodic interaction potential experienced by electrons in the lattice, and solving the time independent Schrödinger's eq. (2.1) (see section ***2.5.1*** for more about the general Schrödinger's wave equation).

$$\left[-\frac{\hbar^2}{2m}\nabla^2 + V(\boldsymbol{r})\right]\varphi_{\boldsymbol{k}}(\boldsymbol{r}) = E_{\boldsymbol{k}}\,\varphi_{\boldsymbol{k}}(\boldsymbol{r}) \tag{2.1}$$

In the one electron approximation, the Bloch theorem arrives at an important result - The solution to Schrodinger's equation for a periodic crystal are wavefunctions $\varphi_{\boldsymbol{k}}(\boldsymbol{r})$ that are periodic in the direct lattice expressed in eq. (2.2),

$$\varphi_{\mathbf{k}}(\mathbf{r}) = e^{i\mathbf{k}.\mathbf{r}}\,U_n(\mathbf{k},\mathbf{r}) \;:\text{ Bloch function} \tag{2.2}$$

Here, $U_n(\boldsymbol{k}, \boldsymbol{r})$ is a periodic interaction potential, n is the band index. The Bloch theorem also shows that the energy ($E_{\boldsymbol{k}}$) is periodic in the reciprocal lattice. Consequently, it is possible and convenient to represent all the energy states of the system within the primitive cell of the reciprocal lattice. The Weigner Seitz cell of the reciprocal lattice, i.e. the first Brillouin zone, is used to represent the energy states of the electrons (and holes) in **k** space (reciprocal space). By plotting all the allowed energy states for a given material, one obtains the complete electronic band structure of the material.

Conditions of diffraction are met for certain wave-vectors in a periodic structure. This is readily confirmed in X-ray diffraction experiments. The electron wavefunctions in the lattice also undergo diffraction in the periodic crystal. Destructive interference of the electron wavefunction results in some forbidden energy states within the 'allowed energy states' distribution. This creates "band gaps" in the E-**k** diagrams and Pauli's exclusion principle is obeyed by electrons and holes. E-**k** diagrams are commonly referred to as the energy band-structure of the material. The energy band structure of Si, Ge and GaAs for the complete first Brillouin zone are shown in Fig. 2.1 (adapted from ref. [46]). Electron energy is conventionally treated positive upwards and hole energy is treated positive downwards (negative for electrons). The shaded gray area represents the smallest band gap (E_g) for each semiconductor shown.

Si and Ge are indirect band gap semiconductors because the smallest energy gap does not occur directly above the valence band maximum. On the other hand, GaAs is a direct band gap material with the lowest energy gap occurring along the zone centre. The "forbidden" energy gap/ band gap (E_g) separates the conduction band (above) and valence band (below). The room temperature values of E_g for Si, Ge and GaAs are 1.12 eV, 0.66 eV and 1.42 eV respectively. Several sub-bands constitute the conduction and valence band. The curvature of the E-**k** diagram is proportional to the effective mass (m^*) of electrons and holes. A sharp band corresponds to a smaller effective carrier mass, and a shallow band corresponds with larger effective carrier mass.

Un-doped semiconductors have a relatively small intrinsic carrier concentration (typical $n_i \sim 10^{10}$-10^{13}cm^{-3}) compared to the free electron density in metals (10^{22} cm^{-3}). We are mainly interested in the smallest energy gap ($E_g = E_C - E_V$) as electronic transitions in a semiconductor are most relevant within this energy interval. Charge carriers are thermally excited from the valence band to the conduction band at non-zero temperatures. In Si, Ge and GaAs (among other materials) the band gap has a negative temperature coefficient $\left(\frac{d\,E_g}{dT} < 0\right)$ and follows an empirical relationship with temperature given by eq. (2.3).

$$E_g(T) = E_g(0) - \frac{\alpha T^2}{(\beta + T)} \tag{2.3}$$

Here, α and β are constants for a given material. At a given temperature, the electron density in the conduction band (n) of an intrinsic i.e. un-doped semiconductor is given by the density of available states $N(E)$, and the occupation probability $F(E)$, integrated over a range of energies, starting from the conduction band minimum (E_C) to the top of the conduction band (taken as ∞).

$$n = \int_{E_C}^{\infty} N(E).F(E)\,dE \tag{2.4}$$

At low temperatures and low carrier densities, the density of available states $N(E)$ varies quadratically with energy, for energies close to the conduction band minimum.

$$N(E) = M_c \frac{\sqrt{2}}{\pi^2} \frac{(E - E_C)^2}{\hbar^3} (m_{de})^{3/2} \tag{2.5}$$

Here, M_c is the number of equivalent minima in the conduction band (6 in Si, 4 in Ge and 1 in GaAs). The density-of-states effective mass for electrons (m_{de}) is treated as a geometric mean of effective masses along the principal axes of constant energy surfaces for the different semiconductors. The occupation probability *F(E)* is given by the Fermi-Dirac distribution function eq. (2.6),

$$F(E) = \frac{1}{1 + exp\left(\frac{E - E_F}{kT}\right)} \tag{2.6}$$

Here k is the Boltzmann constant and E_F is the Fermi level. The Fermi energy is defined as the energy at 0 K, below which all allowed energy states are occupied, and allowed states above E_F are all empty (carrier - energy distribution is a step function). The probability of occupation at the Fermi level is $1/2$.

In a bulk semiconductor, the Fermi level may lie in the band gap, or within the conduction/ valence band (degenerate), depending on temperature and doping level (ionized carrier density). In a metal, the Fermi level generally lies within a band (half-filled/ degenerate). In non-degenerate semiconductors, E_F lies several kT below the conduction band minimum E_C and eq. (2.4) is evaluated to give:

$$n = N_C \, exp\left(-\frac{E_C - E_F}{kT}\right)$$

where

$$N_C = 2\left(\frac{2\pi m_{de} kT}{h^2}\right)^{\frac{3}{2}} \tag{2.7}$$

Similarly, for holes one obtains:

$$p = N_V \, exp\left(-\frac{E_F - E_V}{kT}\right)$$

where

$$N_V = 2\left(\frac{2\pi m_{dh} kT}{h^2}\right)^{\frac{3}{2}} \tag{2.8}$$

In a neutral, intrinsic semiconductor, the electron concentration is equal to the hole concentration, and is known as the intrinsic carrier concentration (n_i). Equating and rearranging eq. (2.7) and eq. (2.8) shows that for intrinsic semiconductors, the intrinsic energy (E_i) is equal to the Fermi level, written as eq. (2.9). which lies close to the mid gap energy. The *ln* term on the R.H.S. involving N_C and N_V becomes small at ordinary temperatures and can be neglected, giving the intrinsic energy $E_i \approx \left[\frac{E_C + E_V}{2}\right]$.

$$E_F = E_i = \left[\frac{E_C + E_V}{2}\right] + \frac{kT}{2} ln\left(\frac{N_V}{N_C}\right)$$

giving

$$n_i = \sqrt{N_C N_V} \, exp\left(-\frac{E_g}{2kT}\right) \tag{2.9}$$

This relationship is valid in the bulk semiconductor, but the situation at the surface may differ considerably, since FLP governs the equilibrium condition. However, the idea of charge neutrality in the material is a prerequisite for equilibrium and the effect of doping is included using the law of mass action eq. (2.10),

$$n_i = \sqrt{np} \tag{2.10}$$

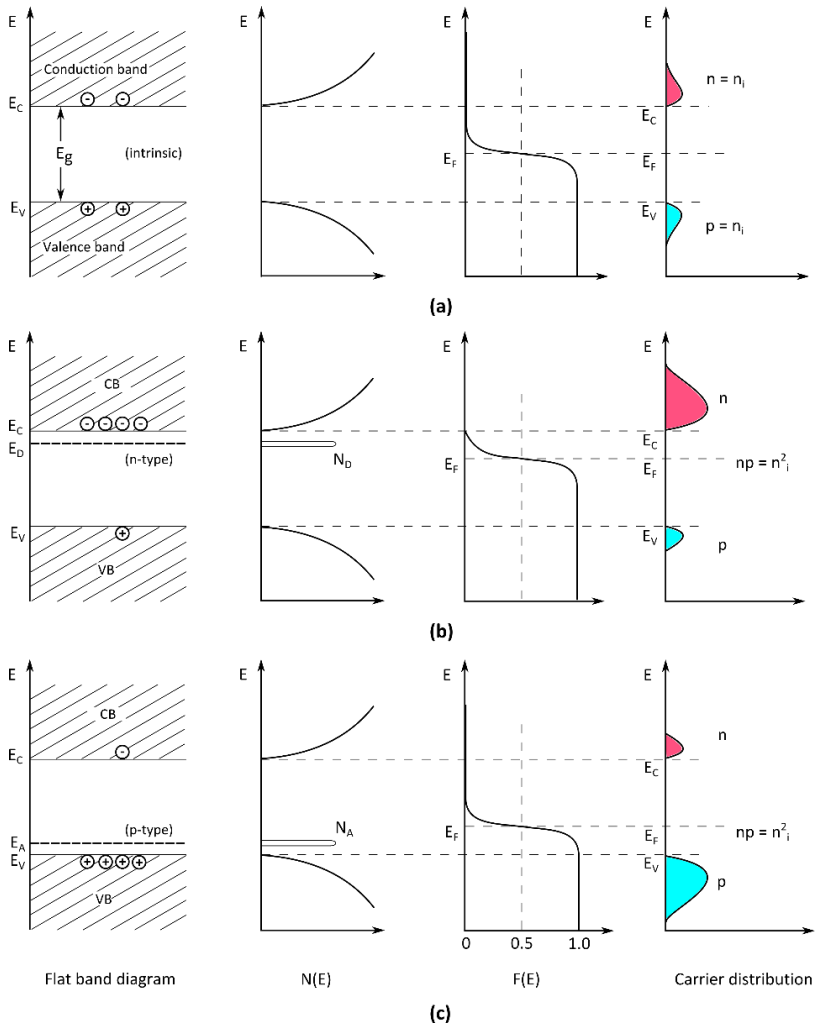

Figure 2.2: Schematic flat band diagram, density of states, Fermi-Dirac distribution and carrier distributions for (a) intrinsic (b) n-type and (c) p-type semiconductors. The law of mass action is obeyed in each case.

Electrons or holes form the majority carriers depending on doping species' density. If the dopants have a sufficiently small ionization energy, their presence in the semiconductor lattice leads to increased occupation of the corresponding majority carrier band in the semiconductor. At any given temperature, the bulk conductivity of the semiconductor is mainly determined by the number of carriers available in the majority carrier band, and their respective mobilities. Eqs. (2.7), (2.8) and (2.10) can be rearranged to evaluate the separation of the Fermi level from the majority bands, based on the assumption that the doping density is sufficiently higher than n_i and dopants are completely ionized. Similarly, the Fermi level separation to the intrinsic level can be obtained by using eq. (2.9) written for n-type doping as,

$$E_F - E_i = \frac{kT}{2} ln\left(\frac{N_D}{n_i}\right)$$

with donor concentration N_D. One obtains a similar expression for acceptors for p-type doping. The effect of doping on majority carrier concentration in the semiconductor can be visualized schematically in Fig. 2.2. Flat band representations of the energy band structure are used, following standard conventions. These diagrams capture the essence of the electronic balance within the semiconductor. From eq. (2.6), the Fermi distribution depends on the temperature, as do the intrinsic electron and hole concentrations in the semiconductor eqs. (2.7), (2.8). At high temperatures, the thermally generated carrier population exceeds the doping concentration and the electronic behaviour is dominated by the intrinsic carrier population, until the material eventually melts or is chemically/ structurally transformed and stops behaving like a semiconductor. The effect of increasing the impurity concentration on the Fermi level separation to the majority carrier band can equivalently be examined from the Fermi level separation from the intrinsic energy. Beyond a certain impurity concentration, the Fermi level will overlap the majority carrier band extrema i.e. the Fermi level – intrinsic energy separation will be equal to $\frac{E_g}{2}$. The semiconductor is said to be degenerately doped under such conditions. For n-type doping, the impurity concentrations for the onset of degenerate doping in Si, Ge and GaAs can be evaluated to be 1.21×10^{18} cm^{-3}, 4.31×10^{17} cm^{-3} and 7.66×10^{16} cm^{-3} respectively at room temperature.

In this thesis, the semiconductor substrates used (Si, Ge) mostly have doping concentrations below these values and so are either described as moderately doped (n-) e.g. $N_D \sim 1 \times 10^{17}$ cm^{-3} or lowly doped (n^-) e.g. $N_D \sim 6.4 \times 10^{14}$ cm^{-3} and are otherwise referred to as highly doped (n^+) e.g. $N_D \sim 1 \times 10^{19}$ cm^{-3}.

2.2.2. Carrier transport phenomena at metal-semiconductor junctions

Metal-semiconductor (MS) Schottky barrier junctions are known as majority carrier devices and are used in high speed switching. Five main current transport processes are illustrated in Fig. 2.3, using the energy band diagram for a (positive voltage, *V*) forward biased, metal/ semiconductor (n-type) contact. These are: (1) Emission over the barrier, (2) Tunnelling, (3) Recombination, (4) Diffusion of electrons and (5) Diffusion of holes. For high mobility semiconductors like Si and GaAs of low-moderate doping ($N_D < 10^{17}$ cm^{-3}), emission over the barrier i.e. thermionic emission is the dominant mechanism while for low mobility semiconductors, diffusion plays the dominant role. The thermionic emission-diffusion (TED) theory is a generalized synthesis of these two theories. In heavy doped semiconductors, tunnelling (field emission) becomes the dominant mechanism, and this mechanism is

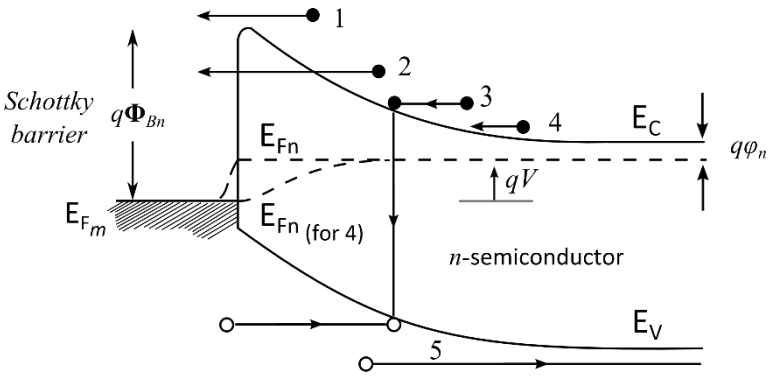

Figure 2.3: Five basic current transport processes for Schottky barrier junctions under forward bias. (1) Thermionic emission (2) Tunnelling, (3) Recombination (4) Diffusion of electrons (5) Diffusion of holes. Figure re-produced from text book ref. [45]- Chapter 3.

responsible for the best ohmic contacts produced in the literature. A Schottky diode performs like an abrupt, one sided p-n junction, but unlike a p-n junction the charge storage time of a Schottky diode is extremely small, and it operates as a majority carrier device.

2.2.2.1. Thermionic Emission (TE) Theory

Thermionic emission theory assumes the Schottky barrier height, $\Phi_{\mathrm{Bn}} \gg kT$. Further, it assumes that thermal equilibrium is established at the plane between the metal and semiconductor that determines emission (close to interface). Net current flow does not affect thermal equilibrium, so we superimpose the two current densities, from metal to semiconductor ($\vec{J}_{\mathrm{MS}}$) and semiconductor to metal ($\vec{J}_{\mathrm{SM}}$). Under these presumptions, when thermionic emission is the dominant mechanism, the electron Fermi level (E_{Fn}) is flat across the entire depletion region and bulk (Fig. 2.3). Now the shape of the barrier is irrelevant, and only the barrier height determines the current fluxes. J_{SM} is the density of electrons (n) headed towards the barrier, with sufficient kinetic energy for emission, illustrated by process 1 in Fig. 2.3. If the average velocity in the x-direction is $\vec{\boldsymbol{v}}_x$ then the conventional current density is given by eq. (2.11)

$$\vec{J}_{\mathrm{SM}} = \int_{E_{\mathrm{Fn}}+q\Phi_{\mathrm{Bn}}}^{\infty} q\vec{\boldsymbol{v}}_{\mathrm{x}}\, dn \tag{2.11}$$

The lower limit ($E_{\mathrm{Fn}} + q\Phi_{\mathrm{Bn}}$) is the minimum energy required for thermionic emission from semiconductor into metal. Differentiating eq. (2.4), the electron density *dn* in an incremental

energy interval is:

$$dn = N(E)F(E)dE$$

$$\approx \frac{4\pi(2m^*)^{3/2}}{h^3}\sqrt{E - E_C}\exp\left(-\frac{E - E_C + \varphi_n}{kT}\right)dE \tag{2.12}$$

The energy terms in eq. (2.12) can be rewritten in terms of carrier velocity over energy intervals in the conduction band, under the assumption that all the energy of electrons in the conduction band is kinetic energy i.e.

$$E - E_C = \frac{1}{2}m^*\boldsymbol{v}^2$$

Substituting for $E - E_C$ in eq. (2.12) gives eq. (2.13),

$$dn \approx 2\left(\frac{m^*}{h^3}\right)^3 \exp\left(-\frac{q\varphi_n}{kT}\right)\exp\left(-\frac{m^*\boldsymbol{v}^2}{2kT}\right)(4\pi\boldsymbol{v}^2 d\boldsymbol{v}) \tag{2.13}$$

For the simple case where electron transport is parallel to the x-axis, eq. (2.11) is solved as per eq. (2.14),

$$\vec{J}_{SM} = \left(\frac{4\pi q m^* k^2}{h^3}\right)T^2 \exp\left(-\frac{q\varphi_n}{kT}\right)\exp\left(-\frac{m^*\boldsymbol{v_{0x}}^2}{2kT}\right)(-\hat{\boldsymbol{x}}) \tag{2.14}$$

The velocity, $\boldsymbol{v_{0x}}$ is the minimum velocity in the x-direction to overcome the Schottky barrier. At equilibrium ($V = 0$) there is a built-in potential energy ($q\psi_{bi}$), which is the energy difference between bulk conduction band minimum (E_C) and surface conduction band minimum (at the interface, with band bending). This band bending changes when a voltage (V) is applied and the Fermi level is shifted by qV.

Hence,

$$\frac{1}{2}m^*\boldsymbol{v_{0x}}^2 = q(\psi_{bi} - V)$$

Substituting in eq. (2.14) we obtain eq. (2.15) for the equilibrium condition $\psi_{bi} = \Phi_{Bn}$,

$$|\boldsymbol{J}_{SM}| = \left(\frac{4\pi q m^* k^2}{h^3}\right)T^2 \exp\left(-\frac{q\Phi_{Bn}}{kT}\right)\exp\left(-\frac{qV}{kT}\right)$$

$$= A^{*}T^{2} \exp\left(-\frac{q\Phi_{\mathrm{Bn}}}{kT}\right) \exp\left(-\frac{qV}{kT}\right)$$

(2.15)

with

$$A^{*} = \left(\frac{4\pi q m^{*} k^{2}}{h^{3}}\right)$$

A^{*} is the effective Richardson constant for thermionic emission[47]. When m^{*} is taken as the free electron mass (m_0), the Richardson constant is a universal constant (A_0 = 120 A/cm^{-2}K^{-2}) Here, the effects of optical phonon scattering, and quantum mechanical reflection are neglected. The Schottky barrier is lowered in the presence of electric field (Schottky effect). This barrier lowering effect ($\Delta\Phi_B$) can be included in eq. (2.15) as a function of voltage, but is not central to developing a basic picture of thermionic emission. For electrons in the metal crossing the interface into the semiconductor, the barrier height does not change with applied voltage bias. Hence, the current density $\vec{J}_{MS}$ should be constant even under bias, and must be equal to the equilibrium current density flowing from the semiconductor into the metal $\vec{J}_{SM}$ at equilibrium (V = 0). Hence, the reverse current density $\vec{J}_{MS}$ is written as eq. (2.16),

$$\vec{\boldsymbol{J}}_{\mathrm{MS}} = A^{*}T^{2} \exp\left(-\frac{q\Phi_{\mathrm{Bn}}}{kT}\right)\hat{\boldsymbol{x}}$$

(2.16)

2.2.2.2. Diffusion Theory

Diffusion theory is derived using the following assumptions: (1) the Schottky barrier height, $q\Phi_{\mathrm{Bn}} \gg kT$, (2) electron collisions in the depletion region are included and (3) Carrier concentration at the interface (x = 0) and edge of the depletion region (x = 0) are unaffected by the current flow. In other words, the equation of continuity is assumed to hold true. In the steady state, the current density is independent of position (x) and is written as a sum of drift and diffusion current densities, given by eq. (2.17),

$$\vec{\boldsymbol{J}}_{\mathrm{x}} = \vec{\boldsymbol{J}}_{\mathrm{n}} = \mathrm{q}\left(n\mu_{\mathrm{n}}\vec{\boldsymbol{E}} + D_{\mathrm{n}}\frac{dn}{dx}\hat{\boldsymbol{x}}\right)$$

(2.17)

Similarly, the current density equation for holes is given by eq. (2.18),

$$\vec{\boldsymbol{J}}_{p} = \mathrm{q}\left(p\mu_{\mathrm{p}}\vec{\boldsymbol{E}} - D_{\mathrm{p}}\frac{dp}{dx}\hat{\boldsymbol{x}}\right)$$

(2.18)

Here, $\mu_{\mathrm{n}}$and μ_{p} are the electron and hole mobilities in the semiconductor. D_{n} and D_{p} are the diffusion coefficients of the semiconductor for electrons and holes. These two parameters are related by the Einstein relation eq. (2.19),

$$\mu = \mathrm{q}\frac{D}{kT} \tag{2.19}$$

The electric field $\vec{\mathbf{E}}$ is defined as the gradient of potential eq. (2.20),

$$\vec{\boldsymbol{E}} = -\vec{\nabla}\Phi \tag{2.20}$$

And so, with eqs. (2.19) and (2.20), eq. (2.17) is reduced to eq. (2.21),

$$|\boldsymbol{J}_{\mathrm{n}}| = D_{\mathrm{n}}\left(\frac{n}{kT}\frac{\boldsymbol{dE}_{\mathbf{C}}}{\boldsymbol{dx}} + \frac{dn}{dx}\right) \tag{2.21}$$

The depletion region width (W_{D}) is expressed in terms of the built-in potential, under the depletion approximation given by eq. (2.22),

$$W_{\mathrm{D}} = \sqrt{\frac{2\varepsilon_{\mathrm{s}}\psi_{\mathrm{bi}}}{qN_{\mathrm{D}}}} \tag{2.22}$$

For p-type semiconductors, N_{D} is replaced with N_{A}. Using Poisson's equation assuming uniform doping density (and complete ionization), the electric field variation in the *x* direction is expressed as eq. (2.23),

$$\boldsymbol{E}(x) = -qN_{\mathrm{D}}(W_{\mathrm{D}} - x)\hat{\boldsymbol{x}} \tag{2.23}$$

Hence, the potential variation in the *x* direction is obtained by integrating eq. (2.23) using appropriate boundary conditions for an abrupt junction in eq. (2.24).

$$\psi_{\mathrm{i}}(x) = |\boldsymbol{E}_{\mathrm{max}}|\left(x - \frac{x^2}{2W_{\mathrm{D}}}\right)$$

with

$$\boldsymbol{E}_{\mathrm{max}} = \frac{qN_{\mathrm{D}}W_{\mathrm{D}}}{\varepsilon_{\mathrm{s}}} \tag{2.24}$$

Eq. (2.21) is solved analytically using an integrating factor $exp\left[\frac{\mathrm{E_C}(x)}{kT}\right]$ and boundary conditions: $E_{\mathrm{C}}(0) = q\Phi_{\mathrm{Bn}}$; $E_{\mathrm{C}}(W_{\mathrm{D}}) = q(\varphi_{\mathrm{n}} + V)$. Since the electron density is known in terms of the Fermi level to conduction band separation eq. (2.7), the values of $n(0)$ and $n(W_{\mathrm{D}})$ are obtained easily in terms of Φ_{Bn} and φ_{n} respectively. The final expression for current density is written in terms of voltage bias and built in potential in eq. (2.25). Image force was ignored in the derivation and so this expression is approximate.

$$\boldsymbol{J}_{\mathrm{n}} \approx \frac{q^2 D_{\mathrm{n}} N_{\mathrm{C}}}{kT}\sqrt{\frac{2qN_{\mathrm{D}}(\psi_{\mathrm{bi}} - V)}{\varepsilon_{\mathrm{s}}}}\exp\left(-\frac{q\Phi_{\mathrm{Bn}}}{kT}\right)\left[\exp\left(\frac{qV}{kT}\right) - 1\right]\hat{\boldsymbol{x}}$$

$$\approx q\mu_{\mathrm{n}}\boldsymbol{E_{max}}\exp\left(-\frac{q\Phi_{\mathrm{Bn}}}{kT}\right)\left[\exp\left(-\frac{qV}{kT}\right) - 1\right] = \boldsymbol{J}_{\mathrm{D}}\left[\exp\left(\frac{qV}{\eta kT}\right) - 1\right]\hat{\boldsymbol{x}} \tag{2.25}$$

Eq. (2.25) has a very similar form to the result obtained by thermionic emission theory eq. (2.15). Here, η is an ideality factor, normally = 1 for low injection condition (small applied voltages). However, the saturation current density in diffusion theory (J_{D}) is sensitive to the applied bias and less sensitive to temperature, unlike $\boldsymbol{J}_{\mathrm{MS}}$ obtained in thermionic emission theory eq. (2.16), which is more sensitive to temperature. It is generally assumed that the minority carrier density in the semiconductor is small. However, under sufficiently large forward bias, the minority carrier density can exceed the doping density, especially in low doped semiconductors (N ~ 10^{13}-10^{14} cm^{-3}). Hence, there is an increase in majority carrier density, to balance the excess minority carriers and maintain charge neutrality. Net charge build-up creates an electric field and current flows and restores equilibrium, causing non-ideal behaviour ($\eta = 2$). This condition is called High level injection (HLI).

2.2.2.3. Thermionic Emission-Diffusion (TED) theory

This theory includes the image force lowering effect into the previous derivations **(**sec. ***2.2.1***) and (sec. ***2.2.2***) and considers quasi Fermi level (E_{Fn}) variation across the depletion region, when voltage bias is applied. The energy band diagram in forward bias is shown schematically in Fig. 2.4 for an n-type semiconductor/ metal contact. Throughout the region between potential maximum (at $x = x_{\mathrm{m}}$) to the edge of the depletion region ($x = W_{\mathrm{D}}$), there will be a drift current $\boldsymbol{J}$ eq. (2.26),

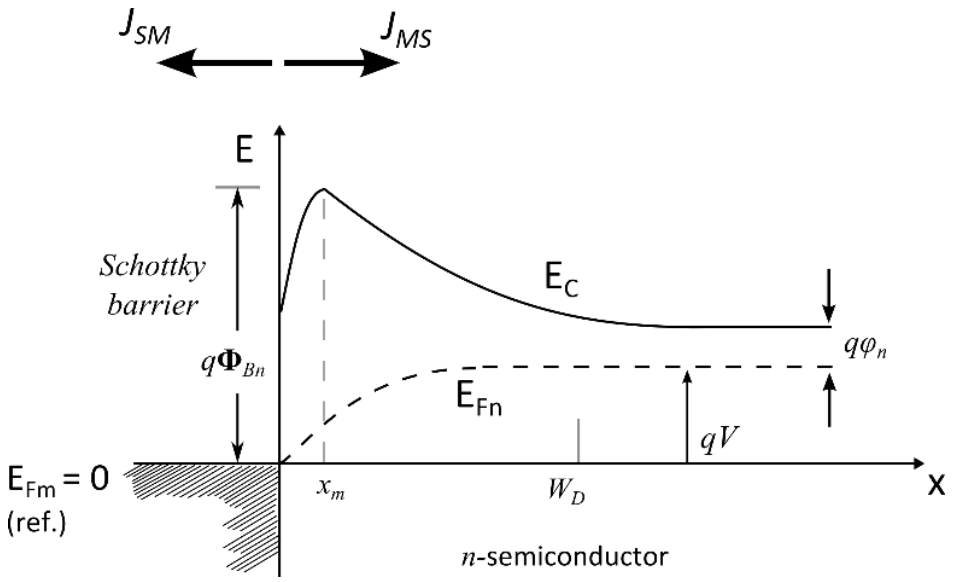

Figure 2.4: Energy band diagram of a forward biased (+*V*) metal/ semiconductor (n-type) contact, incorporating the Schottky effect. The electron quasi fermi level (E_{Fn}) is drawn to show the potential variation near the interface. Energies are measured from the Fermi level ($E_{Fm} = 0$). Figure re-produced from text book ref. [45]- Chapter 3.

$$\boldsymbol{J} = qn\mu_{\mathrm{n}} \frac{dE_{\mathrm{Fn}}}{dx}\, \hat{\boldsymbol{x}} \tag{2.26}$$

The entire depletion region is believed to be isothermal i.e. electron and lattice temperatures (T_e and T_0) are assumed to be equal, even when current flows through the material. The potential barrier profile is modified by image forces experienced by electrons approaching the metal surface (at the interface). The theory assumes that the region between $x = 0$ to $x = x_m$ behaves like a sink/funnel for the incoming electrons into the metal. An average/ effective recombination velocity ($\boldsymbol{v_R}$) is introduced to describe the current density eq. (2.27),

$$\boldsymbol{J} = q(n_{\mathrm{m}} - n_0)\boldsymbol{v_R} \tag{2.27}$$

Where n_{m} is the electron density at the potential maximum ($x = x_{\mathrm{m}}$) when current flows, and n_0 is a quasi-equilibrium/ background electron density at ($x = x_{\mathrm{m}}$), without the barrier lowering effect i.e. $E_{Fn}(x_{\mathrm{m}}) = E_{Fm}$, obtained using eq. (2.7) to give eq. (2.28),

$$\mathrm{n}_0 = \mathrm{N_C} \exp\left(-\frac{q\Phi_{\mathrm{Bn}}}{kT}\right) \tag{2.28}$$

Eq. (2.28) is the first boundary condition. Another boundary condition is obtained by using the Fermi level as the reference energy (E_{Fm}= 0), giving E_{Fn} (W_D)= qV, shown schematically in Fig. 2.4.

Substituting eq. (2.7) in eq. (2.26) and integrating over potential maximum (at $x = x_m$), to the edge of the depletion region ($x = W_D$), $E_{Fn}(x_m)$ is obtained in eq. (2.29),

$$\exp\left(\frac{E_{\mathrm{Fn}}(x_{\mathrm{m}})}{kT}\right) = \frac{\boldsymbol{v}_D \exp\left(\frac{qV}{kT}\right) + \boldsymbol{v}_{\mathrm{R}}}{\boldsymbol{v}_{\mathrm{D}} + \boldsymbol{v}_{\mathrm{R}}} \tag{2.29}$$

Where $\boldsymbol{v}_{\mathrm{D}}$ is an effective diffusion velocity, eq. (2.30) associated with the transport of electrons from the edge of the depletion region to the potential maximum. The diffusion velocity will vary with temperature as the mobility of carriers is a temperature dependent quantity.

$$\boldsymbol{v}_{\mathrm{D}} = D_{\mathrm{n}} \exp \frac{\left(\frac{q\Phi_{\mathrm{Bn}}}{kT}\right)}{\int_{x_{\mathrm{m}}}^{W_{\mathrm{D}}} \exp\left[\frac{E_{\mathrm{C}}}{kT}\right] dx} \tag{2.30}$$

The final expression of thermionic emission diffusion current density ($\boldsymbol{J}_{\mathrm{TED}}$) is obtained written in eq. (2.31), obtained by substituting eqs. (2.26), (2.29), (2.30) into eq. (2.27),

$$\boldsymbol{J}_{\mathrm{TED}} = \frac{aN_{\mathrm{C}}\boldsymbol{v}_{\mathbf{R}}}{1 + \left(\frac{\boldsymbol{v}_{\mathbf{R}}}{\boldsymbol{v}_{\mathbf{D}}}\right)} \exp\left(-\frac{q\Phi_{\mathrm{Bn}}}{kT}\right)\left[\exp\left(\frac{qV}{kT}\right) - 1\right]\hat{\boldsymbol{x}} \tag{2.31}$$

The relative values of $\mathbf{v_R}$ and $\boldsymbol{v_D}$ in eq. (2.31) determine the contribution of thermionic emission and diffusion. The diffusion velocity can be approximated as $\boldsymbol{v_D} \approx \mu_{\mathrm{n}}\boldsymbol{E_m}$ and the thermal velocity $\boldsymbol{v_R} = \frac{A^*T^2}{qN_{\mathrm{C}}} \sim 10^6$ cm/s in Si and ~ 10^7 cm/s in GaAs at room temperature.

It is noted that if $\boldsymbol{v_D} \gg \boldsymbol{v_R}$, then the dominant mechanism is thermionic emission, while diffusion will dominate for $\boldsymbol{v_D} \ll \boldsymbol{v_R}$ i.e. the rate limiting, slower process always determines the dominant mechanism. The semiconductor behaves like a thermionic emitter for the condition $\mu_{\mathrm{n}}\boldsymbol{E_m}(x_{\mathrm{m}}) > \boldsymbol{v_R}$. Quantum-mechanical reflection was neglected in this treatment. When this is included, the effective Richardson constant is modified to include emission and scattering probabilities, and they appear in the reduced effective Richardson constant (A^{**}) in place of A^*, but the form remains identical to eq. (2.31). For n-type Si, for low fields (~10^4 -10^5

V/cm) A^{**} = 110 $Acm^{-2}K^{-2}$ and for p-type Si, A^{**} = 32 $Acm^{-2}K^{-2}$ over a wide range of temperatures.

The variation of the quasi Fermi level over distance is actually very small in moderately doped semiconductors (only ~ meV), and becomes even smaller with heavier doping. The Fermi level essentially remains flat throughout the depletion region, confirming the dominant mechanism for Si and GaAs Schottky diodes is thermionic emission of majority carriers, rather than diffusion.

2.2.2.4. Tunnelling in Metal - Semiconductor Contacts

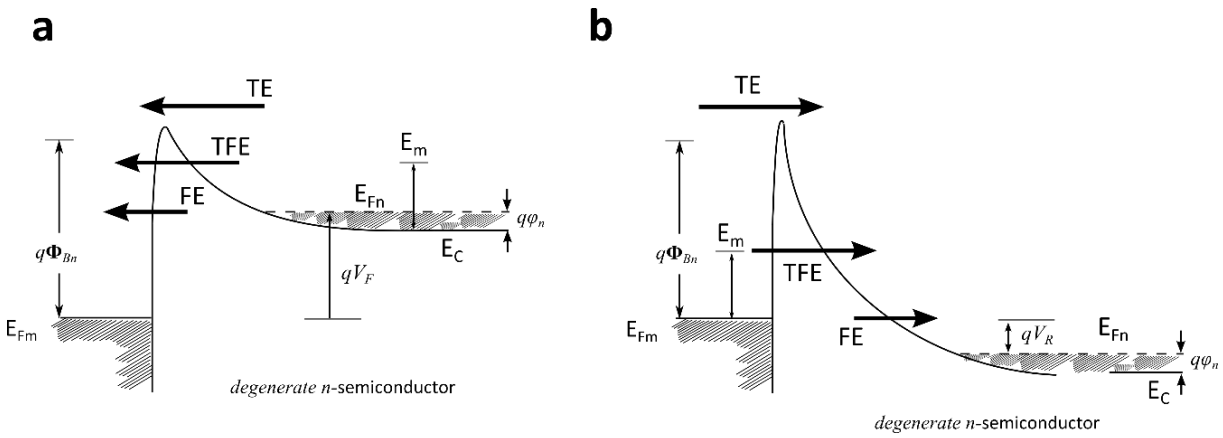

Figure 2.5: Energy band diagrams of a degenerately doped ($q\varphi_n < 0$) semiconductor (n-type)/ metal contact, showing three main transport processes: TE, TFE and FE under **a.** Forward bias (V_F) and **b.** Reverse bias (V_R). Figure re-produced from text book ref. [45]- Chapter 3.

Thermionic emission is a temperature sensitive transport process. At lower temperatures, its contribution becomes negligible and tunnelling dominates the total current. Appreciable tunnelling current in metal semiconductor junctions is usually only observed using degenerately doped semiconductors. Eq. (2.22) shows an approximate relationship between the doping density, and width of the depletion region. When heavy doping is used (e.g. $N_D > 10^{17} – 10^{20}$ cm^{-3}, or higher) the barrier width can become considerably smaller, and a certain fraction of energetic electrons are transmitted across the interface by tunnelling. The current density equation for tunnelling takes the general form given by eq. (2.32),

$$\boldsymbol{J} = J_0 \left[\exp\left(\frac{qV}{\eta kT}\right) - 1\right]\hat{\boldsymbol{x}}$$

(2.32)

J_0 is the saturation current density (extrapolated to 0 V). Here, η is called the "ideality factor", which is related to the slope. For low doped semiconductors at room temperature, $\eta \approx 1$. For higher doping and/or lower temperatures, both η and J_0 increase. Quantum mechanical transmission of electrons through a barrier, at the Fermi energy is called Field emission (FE). Thermally excited carriers (away from the Fermi level) experience a thinner barrier. The associated tunnelling process is called Thermionic Field emission (TFE). Band bending in the semiconductor is approximately parabolic, and the effective width of the barrier width reduces for energies above the Fermi level, resulting in a thinner barrier. In TFE, the most probable tunnelling current flux arrives at the interface at an energy maximum (E_m) above the Fermi level, given approximately by eq. (2.33),

$$E_m = \frac{q(\Phi_{Bn} - \varphi_n - V_F)}{\cosh^2\left(E_{00}/kT\right)}$$

(2.33)

At finite temperatures, the Fermi distribution and density of states describe the electron occupation density eq. (2.4). Three processes: TE, TFE and FE are illustrated for a degenerately doped semiconductor/metal contact, using energy band diagrams representing cases for forward bias, V_F (Fig. 2.5-a) and reverse bias, V_R (Fig. 2.5-b).

Generally, for planar metal-semiconductor contacts, the criterion that governs the dominant transport process is identified by comparing the thermal energy (kT) to a tunnelling parameter, E_{00}, defined in terms of doping density, N in eq. (2.34),

$$E_{00} = \frac{q\hbar}{2}\sqrt{\frac{N}{m^*\varepsilon_s}}$$

(2.34)

The general selection criteria used to identify the dominant mechanism are given below:

- If $kT \ll E_{00}$ i.e. at high doping level, FE is the main mechanism.
- If $kT \approx E_{00}$ i.e. moderate doping level, TFE is the main mechanism, which is a combination of FE and TE.
- If $kT \gg E_{00}$ i.e. low doping level, TE is the main mechanism.

2.2.3. MIS tunnel diode

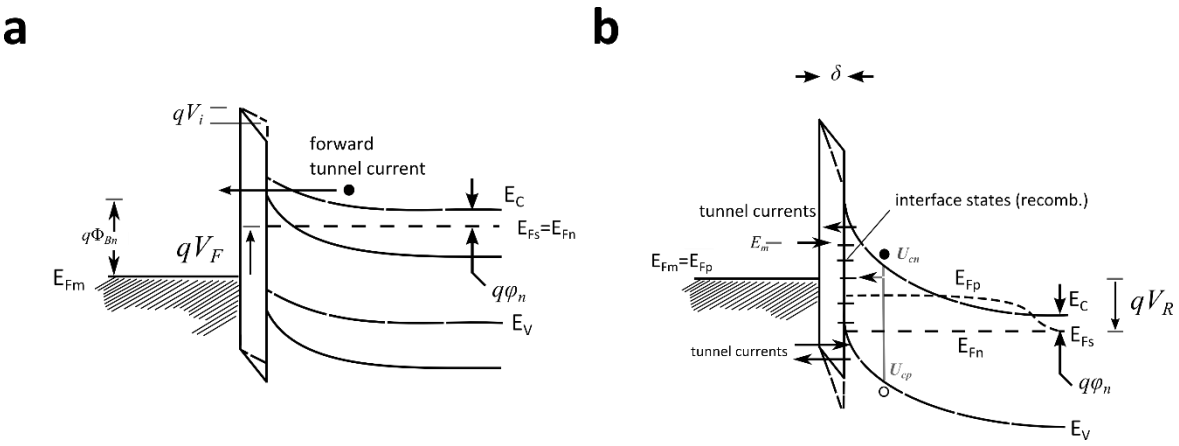

Figure 2.6: Energy band diagrams for MIS contact using a non-degenerately doped ($q\varphi_n > 0$) semiconductor (n-type) for **a.** forward bias and **b.** reverse bias. In forward bias (**a.**), the solid energy bands on the semiconductor side are drawn for equilibrium (0 V) where no net current flows. The dashed bands are drawn for when a forward voltage (V_F) is applied to the contact. In **b.** the band diagram is drawn only for when a reverse bias (V_R) is applied. Quasi Fermi levels for electrons (E_{Fn}) and holes (E_{Fp}) are indicated across the depletion region. In reverse bias, the quasi Fermi levels are split and the holes are in equilibrium with the metal ($E_{Fm} = E_{Fp}$). An enhanced minority carrier injection J_p occurs as the barrier for holes is small. Electron, hole recombination currents U_{cn} and U_{cp} are intermediate transport processes due to interface states with energies within the band gap. Energy band diagrams adapted from refs.[48] and [49].

The previous section dealt with analyses of transport phenomena in conventional metal/semiconductor contacts. The semiconductor was assumed to be in quasi-equilibrium i.e. the electron and hole quasi Fermi levels were aligned when voltage bias was applied. This condition is disrupted by the introduction of a thin interfacial layer between the contact. The MIS (metal/insulator/semiconductor) tunnel diode exhibits lower current density, a smaller effective barrier height, and higher ideality factor (η). The current density is written as eq. (2.35),

$$\boldsymbol{J} = A^{*}T^{2}\exp\left(-\sqrt{\zeta}\delta\right)\exp\left(-\frac{q\Phi_{\mathrm{Bn}}}{kT}\right)\left[\exp\left(\frac{qV}{\eta kT}\right)-1\right]\hat{\boldsymbol{x}} \tag{2.35}$$

Eq. (2.35) is a synthesis of eqs. (2.15) and (2.32), including the potential drop and material parameters of the thin interlayer.

The effective barrier height of the MIS contact, ζ (in eV) is lower than the corresponding MS contact barrier height Φ_{Bn} without the interlayer, because potential is dropped across the thin interlayer region (δ ~ 1-3 nm). While the effective barrier height becomes smaller, charge carriers also experience added tunnel resistance from the interlayer. Hence, the interlayer

thickness appears as a sensitive parameter that governs the current density. The first exponential term in eq. (2.35), $\exp\left(-\sqrt{\zeta}\delta\right)$ is the added tunnelling probability, and is a modification to the effective Richardson constant.

Introducing an interfacial oxide layer (intentionally or unintentionally) leads to the formation of charge traps at either interface - metal/insulator, or insulator/semiconductor, with densities D_{itm} and D_{its} respectively. Generally, for interlayer thickness $\delta < 3$ nm, the interface traps are in equilibrium with the metal, whereas for thicker oxides the traps are in equilibrium with the semiconductor. Introducing the oxide tunnel barrier reduces the overall thermionic emission current density, but because the quasi fermi levels of electrons and holes in the semiconductor are separated, minority carriers are unaffected, and their injection is enhanced by a diffusion like process. This phenomenon is exploited in light emitting diodes (LEDs), and in solar cell technology, by improving the open circuit voltage, which is always smaller than the band gap ($V_{OC} < E_g$). By reducing the effective barrier height, the quasi Fermi level of minority carriers is "depinned" in contrast to the conventional case (MS contact), where FLP usually governs the effective Schottky barrier height. When suitably high doping level is used, the reduction in the thermionic component is irrelevant, as tunnelling becomes the dominant transport process through the tunnel barrier.

For light (n-type) doping in the semiconductor, when the interlayer is sufficiently thick, the variation of the electron qausi-Fermi level (E_{Fn}) is the main driver of forward tunnel current (Fig. 2.6-a) [48]. The variation of E_{Fn} mainly occurs in the interfacial region, because E_{Fn} remains relatively constant throughout the depletion region, such that $E_{Fn} = E_{Fs}$. In reverse bias, if the interlayer is sufficiently thin, holes near the surface readily tunnel through the interlayer, into the metal. This process causes the hole quasi Fermi level, E_{Fp} to maintain equilibrium with the metal i.e. $E_{Fp} = E_{Fm}$ (Fig. 2.6-b) rather than the bulk semiconductor $E_{Fp} \neq E_{Fs}$ [49]. Applying reverse bias therefore, causes the electron/ hole quasi Fermi levels to split. Minority carriers (holes) must diffuse towards the interface and preserve continuity with the tunnel current, and maintain equilibrium at the semiconductor surface. This equilibrium is lost when reverse bias is increased, causing the tunnel barrier to become effectively thinner for incoming carriers as the potential drop across the interlayer increases. Minority carriers from the semiconductor exhibit tunnel breakdown, leading to enhanced reverse current. Hot electrons in the metal may also participate in TFE reverse tunnelling at E_m. The interface states allow excess electron/hole recombination currents, U_{cn} and U_{cp} respectively, which causes non-idealities and "Ohmic" I-V characteristics, instead of double exponent I-V characteristics, expected in the absence of interface states (ideal MIS tunnel diode).

2.2.4. Description of a plasma – macroscopic parameters

Plasma is often called the fourth state of matter as it is usually thought of as the final state, obtained by heating a solid into liquid, then a gas and finally the temperature is sufficiently high to cause considerable ionization of the gas, creating a plasma. Such a description may not be completely accurate, but is quite useful in understanding general particle dynamics. Most plasmas found in nature are very hot, e.g. gas giants and other massive astronomical bodies. The energy needed to ionize hydrogen is 13.6 eV and would require a tremendous amount of heat to cause ionization. The conditions to sustain a hydrogen plasma naturally require huge masses of hydrogen to create the necessary gravitational pressure, to reach the high temperatures required for ionization. Other methods of generating a plasma are photo-ionization, as is the case in our atmosphere, or DC/ RF discharge.

2.2.4.1. Debye Length and Charge Screening

Plasmas observe quasi charge neutrality i.e. the average free electron concentration (n_e) is considered approximately equal to the ion concentration (Z_i. n_{ion}). Consider a singly ionized (Z_i = 1) nascent plasma with a background particle concentration (n_0). One assumes a Boltzmann distribution for the electron and ion populations in the plasma, given by eq. (2.36),

$$n_e = n_0 \ exp\left(\frac{q\Phi}{kT_e}\right)$$

$$n_{ion} = n_0 \ exp\left(\frac{-q\Phi}{kT_{ion}}\right) \tag{2.36}$$

Where T_e and T_{ion} are the average electron and ion temperature respectively. If a test charge Q is placed somewhere in the plasma, then the electric field $\vec{E}$ due to this charge is given by gradient of electric potential (Φ):

$$\vec{E} = -\vec{\nabla}\Phi \tag{2.37}$$

The potential energy, P.E = ± qΦ for ions and electrons respectively and $-q$ is the elementary charge of an electron. In a hot plasma, the electron and ion temperature are assumed to be equal. Using Poisson's equation, the electric field is expressed in terms of net charge density (ρ) in eq. (2.38),

$$\varepsilon_0 \vec{\nabla}.\vec{E} = \rho = q(n_{ion} - n_e) \tag{2.38}$$

The variation of potential in space due to the test charge is assumed to be radially symmetric (no directional preference). Substituting eq. (2.37) into eq. (2.38) and working with the assumption that the temperature is sufficiently high $\left(\frac{\mathrm{q}\Phi}{kT} \ll 1\right)$, using Maclaurin series for exponents on eq. (2.36) gives,

$$\varepsilon_0 \nabla^2 \Phi = (q n_{\mathrm{ion}} - q n_{\mathrm{e}})$$

where, $\mathrm{n_e} = \mathrm{n_0}\ \left(1 + \frac{\mathrm{q}\Phi}{kT_{\mathrm{e}}}\right)$ and $\mathrm{n_{ion}} = \mathrm{n_0}\ \left(1 - \frac{\mathrm{q}\Phi}{kT_{\mathrm{ion}}}\right)$.

Upon substitution, we obtain eq. (2.39),

$$\nabla^2 \Phi = \left(\frac{2q^2 n_0}{\varepsilon_0 T}\right) \Phi \tag{2.39}$$

i.e.

$$\frac{1}{r^2}\frac{\partial}{\partial r}\, r^2\, \frac{\partial \Phi}{\partial r} = \left(\frac{2q^2 n_0}{\varepsilon_0 T}\right) \Phi$$

The coefficient on the right-hand side of eq. (2.39) has the dimensions L^{-2}. It is therefore convenient to define a parameter (λ_D) called Debye length given by eq. (2.40).

$$\lambda_D = \sqrt{\left(\frac{\varepsilon_0 T}{2q^2 n_0}\right)} \tag{2.40}$$

and eq. (2.39) could be re-written as eq. (2.41),

$$\frac{1}{r^2}\frac{\partial}{\partial r}\, r^2\, \frac{\partial \Phi}{\partial r} = \frac{\Phi}{{\lambda_D}^2} \tag{2.41}$$

The solution to eq. (2.41) could be presumed to have a form $F(r)$, like the potential variation caused by a charge in free space, having the general form:

$$\frac{d^2 F}{dr^2} = \frac{1}{r}\, F(r) \tag{2.42}$$

with $\Phi = \frac{1}{r}\, F(r)$

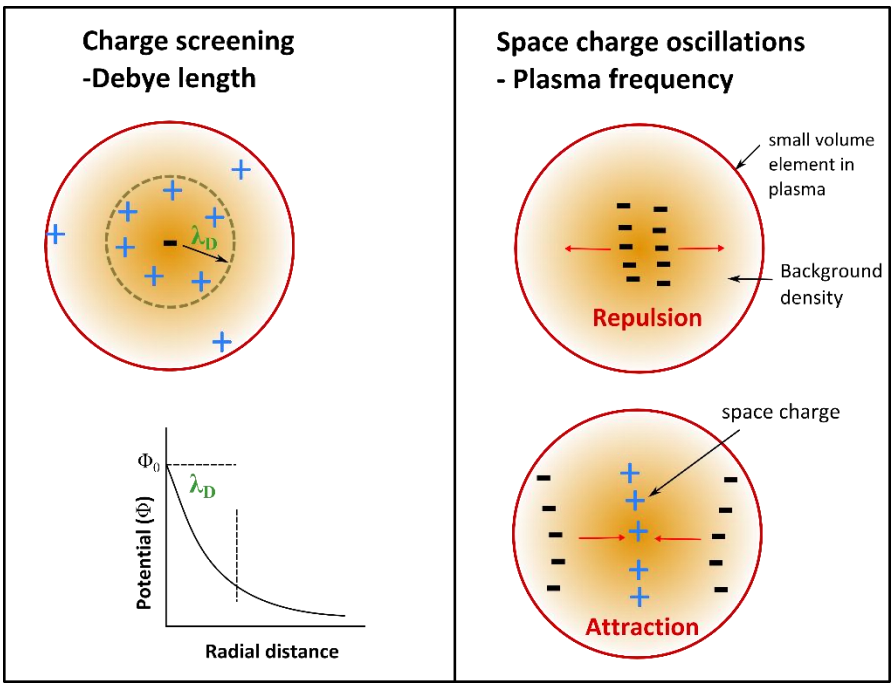

Figure 2.7: Debye length (screening length) and plasma oscillations visualized using illustrations.

The solution for potential variation in space becomes a decaying exponential, assuming potential decreases away from the test charge Q (the positive exponential solution is ignored). Hence, $F(r)$ has the form:

$$F(r) = C_1 \exp\left(-\frac{r}{\lambda_D}\right)$$

C_1 can be deduced by postulating that the screening property of the test charge will vanish at its location in space. Hence, close to the test charge, the potential varies as though it were a charge in free space, but decays exponentially over a distance, of the order of a Debye length. The Debye sheath formation is illustrated in Fig. 2.7 (left panel), along with its plot of potential vs. radial distance, away from the test charge. If the dimensions of the plasma are greater than the Debye length then individual charge interactions can be ignored, or rather the collective behaviour of millions of charges becomes more important, under given experimental conditions. The final solution is obtained as eq. (2.43),

$$\Phi = \frac{Q}{4\pi\varepsilon_0 r} \exp\left(-\frac{r}{\lambda_D}\right) \tag{2.43}$$

2.2.4.2. Plasma Oscillations and Response to Fields

The collective interaction of particles results in a swarm like behaviour with an oscillatory character. Consider the simple case of equal electron and ion charge densities ($n_e = n_{ion} = n_0$) in a two-component plasma. Where there is instantaneous accumulation of electrons in space, the excess charge build-up produces an electric field that pushes them out further than they came in, resulting in a deficiency of electrons i.e. forming positive space charge (image). The electrons are then pulled back by this image charge, repeating the process, illustrated in Fig. 2.7 (right panel). This results in harmonic time oscillations in the background density (n_0), known as plasma oscillations. The plasma oscillation occurs at the plasma frequency (ω_P). A plasma can be resonantly excited by incident waves with frequencies comparable to ω_P.

The plasma frequency (ω_P) is obtained by using Poisson's equation and solving the equation of motion. An accumulation of charge results in a small variation in electron density (n_1), which has an oscillatory nature in time. This is the net space charge – the instantaneous difference between the electron and background density. Hence, the electron density is written as a perturbation in the background density eq. (2.44).

$$n_e = n_0 + n_1 \tag{2.44}$$

Applying Poisson's equation on the space charge region, we obtain eq. (2.45),

$$\varepsilon_0 \nabla^2 \Phi = q(n_e - n_0) \quad \text{i.e.} \quad \nabla^2 \Phi = \frac{q n_1}{\varepsilon_0} \tag{2.45}$$

In the presence of an electric field, particle dynamics are described by the equation of motion. The electric force is equal to the rate of change of momentum eq. (2.46),

$$-q\vec{E} = m\frac{d\vec{v}}{dt} \approx m\frac{\partial \vec{v}}{\partial t} \tag{2.46}$$

If we assume the total time derivative to be equal to the partial time derivative, then we have one equation that describes the velocity of the electron fluid in terms of potential. The potential is known in terms of the density perturbation eq. (2.45). Another equation is obtained by using the equation of continuity eq. (2.47),

$$\frac{\partial n_e}{\partial t} + \nabla.(n_e \vec{v}) = 0 \tag{2.47}$$

Substituting eq. (2.44) in eq. (2.47), assuming n_1 is small, and n_0 doesn't change, we get eq. (2.48),

$$\frac{\partial n_1}{\partial t} + \nabla.(n_0 \vec{\boldsymbol{v}}) = 0$$

(2.48)

Differentiating eq. (2.48) we get eq. (2.49),

$$\frac{\partial^2 n_1}{\partial t^2} + n_0 \nabla.\frac{\partial \vec{\boldsymbol{v}}}{\partial t} = 0$$

(2.49)

Substitute eqs. (2.45), (2.46) into eq. (2.48) to obtain eq. (2.50),

$$\frac{\partial^2 n_1}{\partial t^2} + \left(\frac{q^2 n_0}{m\varepsilon_0}\right) n_1 = 0$$

(2.50)

The solution to eq. (2.50) has the form:

$$n_1 = n_{10} \exp(-i\omega_P t)$$

The coefficient of the second term on the left-hand side of eq. (2.50) has the dimensions of s^{-2}. Hence, we define plasma frequency (ω_P) as,

$$\omega_P = \sqrt{\frac{q^2 n_0}{m\varepsilon_0}}$$

(2.51)

Eq. (2.51) implies plasmas with high charge density will exhibit space charge oscillations at a higher frequency than those with low charge density. It is concluded that plasmas support space charge oscillations in time. The effect of temperature has been ignored in this derivation. When this is included, these plasma oscillations are called 'plasma waves'. They move, they carry energy, like electromagnetic (EM) waves. Plasma waves are mostly responsible for accelerating electrons to very high energies up to GeV in thermo-nuclear reactors and some particle accelerators. Incident waves interact resonantly at the plasma frequency – leading to various phenomena such as heating the plasma or scattering, among others.

The plasma frequency(ω_P), electron density (n_e), and electron temperature (T_e), are key properties that describe a plasma. Plasmas are characterized by their macroscopic properties such as: DC conductivity (σ_{DC}), Thermal conductivity (χ_{th}) and refractive index (η). These quantities are given below without proof (see ref.[44] for detailed proofs).

The DC conductivity of the plasma is given by eq. (2.52).

$$\sigma_{\mathrm{DC}} = \frac{q^2 n_e}{m\upsilon} \tag{2.52}$$

The collision frequency (υ) varies with the electron temperature ($\upsilon \sim T_{\mathrm{e}}^{-3/2}$). Thermal conductivity of the plasma is given by eq. (2.53). It also depends on the electron density, the collision frequency, and includes the thermal velocity (v_{th}).

$$\chi_{\mathrm{th}} = \frac{3}{4}\frac{{v_{\mathrm{th}}}^2 n_{\mathrm{e}}}{\upsilon} \tag{2.53}$$

In a strongly ionized plasma (no neutrals) the collision frequency decreases with increasing temperature and the electrical and thermal conductivities of a plasma can attain values comparable to metals, or even higher. In very hot plasmas for e.g. in stars, they can be extremely large.

For an incident plane wave with phase velocity (v_{ph}), the refractive index (η) of the plasma is given by eq. (2.54).

$$\eta = \frac{c}{v_{\mathrm{ph}}} = \left[1 - \frac{{\omega_{\mathrm{P}}}^2}{\omega^2}\right]^{1/2} \tag{2.54}$$

Eq. (2.54) indicates that plasmas are a dispersive media i.e. refractive index depends on the incident wave frequency. Furthermore, $\eta < 1$, i.e. $v_{\mathrm{ph}} > c$, which is a peculiar behaviour. A wave with $\omega < \omega_{\mathrm{P}}$ does not penetrate a plasma, because refractive index becomes imaginary. Very similar behaviour is also observed in metals (see **Sec. 2.5**). Semiconductors have mobile electrons and holes, as well as fixed lattice ions. These materials qualify as solid-state plasmas and the concepts of plasma frequency, effective temperature, scattering, Debye screening etc. are inherent in their various theoretical formulations, used to study particle dynamics and system evolution. For semiconductors, the relative permittivity enters the equations, but their general forms remain. Similar expressions hold for metals like Au or Ag- Their plasma frequency is in the ultra- violet region and the Debye length is ~ Å dimensions, causing them to behave like charge mirrors, practically impervious to electric field upon excitation far below the plasma frequency. However, for excitation above the plasma frequency they become transparent.

2.2.4.3. Plasma Dynamics

Species	Density	Mass	Charge	Drift velocity	Temperature
Electrons	n_e	m_e	q	$\vec{v}$	T_e
Ions	n_{ion}	m_{ion}	$Z_i q$	$\vec{v}_{ion}$	T_{ion}
Neutrals (atoms)	n_n	$m_n \approx m_{ion}$	0	0	T_n

Charge number (Z_i) = 1 for singly ionized atoms.

Table 2.1: Important macroscopic parameters used to describe a three component plasma.

Two important concepts – the equation of motion, and the equation of continuity, form the foundation of the theoretical analysis of plasmas. We are interested in understanding the response of plasmas to internal and external fields, such as a DC electric field or external magnetic field. The most important macroscopic parameters of a plasma are summarized in Table 2.1. which are used to obtain an equation that governs the drift velocity and the density evolution of these particles in the presence of an external electromagnetic fields.

In the first approximation, some assumptions are made about the plasma, (1) the electrons are the lightest particles in the plasma and we are mainly interested in understanding electron dynamics. (2) the ions and neutrals are assumed to be stationary. The effect of ion motion is also ignored. The plasma is a collisional swarm-like entity, and momentum is considerably randomized in nature. Collisions are assumed to be elastic, with an average change in momentum, per collision $\approx m\vec{v}$. With collision frequency (υ), the momentum lost per second = $m\vec{v}\upsilon$. This is the collisional drag force ($\vec{F}_{col}$) experienced by electrons. The ion velocity, $\vec{v}_{ion}$ is sometimes included for completeness eq. (2.55), but can be ignored. At a given temperature, the electron velocity is usually higher than the ion velocity, at least by a factor $\sqrt{m_{ion}/m_e}$.

$$\vec{F}_{col} = m_e \upsilon (\vec{v} - \vec{v}_{ion}) \tag{2.55}$$

In the presence of an electric and magnetic field, the electromagnetic forces on the electron are given by eq. (2.56) and eq. (2.57) respectively.

$$\vec{\boldsymbol{F}}_{\mathrm{E}} \;=\; -q\vec{\boldsymbol{E}} \tag{2.56}$$

$$\vec{\boldsymbol{F}}_{\mathrm{M}} \;=\; -q\left(\vec{\boldsymbol{v}} \times \vec{\boldsymbol{B}}\right) \tag{2.57}$$

The two main components of the plasma, ions and electrons are treated like a Maxwellian gas in the absence of external fields. In the presence of external fields, the drift velocity can become non-uniform. Non-uniform particle densities may arise, which create partial pressure due to electron accumulation. Consider a volume element of unit area cross section, of width Δx, where the electron pressure changes in the $\hat{\boldsymbol{x}}$ direction from P_{e}, to $P_{\mathrm{e}} + \Delta P_{\mathrm{e}}$. Then the net pressure on the volume element is ΔP_e, producing a net force on the volume element = $-\Delta P_{\mathrm{e}}.\hat{\boldsymbol{x}}$. The net force per electron due to partial pressure is given by eq. (2.58).

$$\vec{\boldsymbol{F}}_{\mathrm{PP}} \;=\; \frac{-\Delta P_{\mathrm{e}}}{n_{\mathrm{e}}\Delta x}\,\hat{\boldsymbol{x}} = \;-\frac{1}{n_{\mathrm{e}}}\,\frac{\partial(n_{\mathrm{e}}T_{\mathrm{e}})}{\partial x}\hat{\boldsymbol{x}} \tag{2.58}$$

$\vec{\boldsymbol{F}}_{\mathrm{PP}}$ can be generalized in three dimensions using the del operator, instead of the partial derivative used in eq. (2.58). Summing the forces in eqs. (2.55) to (2.58) and ignoring ion motion in eq. (2.55), the complete equation of motion is written as eq. (2.59)

$$\vec{\boldsymbol{F}}_{\mathrm{net}} \;=\; m_{\mathrm{e}}\frac{d\vec{\boldsymbol{v}}}{dt} = \;-q\vec{\boldsymbol{E}} - m_{\mathrm{e}}\vec{\boldsymbol{v}}v - q\left(\vec{\boldsymbol{v}} \times \vec{\boldsymbol{B}}\right) - \frac{1}{n_{\mathrm{e}}}\nabla(n_{\mathrm{e}}T_{\mathrm{e}}) \tag{2.59}$$

The velocity terms (on RHS) in eq. (2.59) will vary with location, so velocity field $\vec{\boldsymbol{v}}(\vec{\boldsymbol{r}}, t)$ is considered instead, and time average velocity needs to be calculated. In this case the total and partial derivatives are not equal.

$$\frac{d\vec{\boldsymbol{v}}}{dt} \neq \frac{\partial\vec{\boldsymbol{v}}}{\partial t}$$

Using Taylor expansion, the relationship between total and partial derivatives is written as:

$$\frac{d\vec{\boldsymbol{v}}}{dt} = \frac{\partial\vec{\boldsymbol{v}}}{\partial t} + \vec{\boldsymbol{v}}.\nabla\,\vec{\boldsymbol{v}} \tag{2.60}$$

The second term in the RHS of eq. (2.60), $\vec{\boldsymbol{v}}.\nabla\,\vec{\boldsymbol{v}}$ is called the convective derivative. It is attributed to many non-linear phenomena in plasmas, such as harmonic generation, parametric instabilities and electron heating. Now the expanded equation of motion is written as eq. (2.61),

$$m_{\mathrm{e}}\left[\frac{\partial \vec{\boldsymbol{v}}}{\partial t}+\ \vec{\boldsymbol{v}}.\nabla\,\vec{\boldsymbol{v}}\right]=\ -q\vec{\boldsymbol{E}}-m_{\mathrm{e}}\vec{\boldsymbol{v}}\upsilon-q\left(\vec{\boldsymbol{v}}\ \times\vec{\boldsymbol{B}}\right)-\ \frac{1}{n_{\mathrm{e}}}\nabla(n_{\mathrm{e}}T_{\mathrm{e}})$$

(2.61)

In weak fields, the non-linear terms are ignored to obtain the linearized equation of motion. The equation of continuity is applied to the electron density by considering a flux ($n_e\vec{\boldsymbol{v}}$). Steady state is described by eq. (2.62),

$$\frac{dn_{\mathrm{e}}}{dt}+\nabla(n_{\mathrm{e}}\vec{\boldsymbol{v}})=0 \tag{2.62}$$

Since moving charges produce electric and magnetic fields, the equation of motion eq. (2.61) and equation of continuity eq. (2.62) are combined with Maxwell's equations of electro-dynamics, to obtain complete solutions. In gaseous plasmas, polarization and magnetization / dipole moments are usually ignored.

Consider a simple case of uniform electric field applied to a plasma (or equally, to a semiconductor). To obtain drift velocity, we make further simplifying assumptions. We presume the density and temperature in the plasma is uniform. Hence, the pressure gradient is ignored. Magnetic field is absent. The external source produces uniform electric field, $\vec{\boldsymbol{E}}=\overrightarrow{\boldsymbol{E_0}}$ (independent of position). Hence, the response, $\vec{\boldsymbol{v}}$ is also independent of position. Therefore, the convective derivative term becomes zero, and the equation of motion is reduced to eq. (2.63),

$$m_{\mathrm{e}}\left(\frac{\partial \vec{\boldsymbol{v}}}{\partial t}\right)=\ -q\overrightarrow{\boldsymbol{E_0}}-m_{\mathrm{e}}\vec{\boldsymbol{v}}\upsilon$$

(2.63)

In the steady state, the collisional force balances the electric force and velocity becomes constant. The steady state drift velocity, $\vec{\boldsymbol{v}}$ is given by eq. (2.64),

$$\vec{\boldsymbol{v}}=\ -\frac{q\overrightarrow{\boldsymbol{E_0}}}{m_e\upsilon}$$

(2.64)

The current density ($\vec{\boldsymbol{J}}$) is defined as the charge flowing per unit area, per unit time eq. (2.65).

$$\vec{\boldsymbol{J}}=\ -qn_{\mathrm{e}}\vec{\boldsymbol{v}} \tag{2.65}$$

Substituting, eq. (2.64) into eq. (2.65), the current density is written as eq. (2.66) in terms of the electrical conductivity σ,

$$\vec{\boldsymbol{J}} = \left(\frac{q^2 n_{\mathrm{e}}}{m_{\mathrm{e}} \upsilon}\right)\vec{\boldsymbol{E}} = \sigma\vec{\boldsymbol{E}}$$

(2.66)

2.2.4.4. Plasma Field and Non-Equilibrium Phenomena

The coefficient on the RHS of eq. (2.66) is called the DC conductivity (σ). It is important to note that the DC conductivity of electrons in a plasma can be much higher than a metal. Consider typical values in a hot plasma (n_{e}= 10^{20} m^{-3} and $\upsilon = 10^3$ s^{-1}) and a metal (n_e= 10^{28} m^{-3} and $\upsilon = 10^{12}$ s^{-1}). Furthermore, the conductivity of metals gets worse at higher temperatures due to electron phonon interactions ($\upsilon_{\mathrm{e-ph}} \sim T^{\frac{1}{2}}$), while the conductivity of a plasma increases with temperature ($\upsilon \sim T^{-\frac{3}{2}}$). The conductivity of a semiconductor also increases at higher temperature, although this is mainly because the intrinsic carrier concentration increases exponentially with temperature, eq. (2.9). When an electric field is applied, the work done by the electric force, per second is,

$$= -e\vec{\boldsymbol{E}}.\vec{\boldsymbol{v}} = \frac{q^2}{m_{\mathrm{e}}\upsilon}\boldsymbol{E_0}^2$$

Hence, electrons receive energy from the field. If the mean fraction of excess energy lost per collision is δ, then the average kinetic energy of electrons ($\frac{3}{2}\ T_{\mathrm{e}}$) is obtained in eq. (2.67) by taking time average,

$$\frac{\partial}{\partial t}\left(\frac{3}{2}\ T_{\mathrm{e}}\right) = -e\vec{\boldsymbol{E}}.\vec{\boldsymbol{v}} - \frac{3}{2}\ \delta\ (T_{\mathrm{e}} - \ T_0)\upsilon$$

(2.67)

Here, T_0 is the temperature of the ion or heavy scatterer. If $T_{\mathrm{e}} > T_0$ then a fraction (δ) of energy is dissipated during collisions. If $T_{\mathrm{e}} \approx T_0$ then the energy lost in collisions is neglected. The second term in the RHS of eq. (2.67) is called the loss rate. The values of δ are usually ~ 10^{-3} in bulk semiconductors, and $\approx {m_{\mathrm{e}}}/{m_{\mathrm{ion}}}$ **(~** 10^{-4}**)** for the case of elastic collisions in a fully ionized plasma. In the case of semiconductors and weak plasmas, the collision frequency increases with temperature approximately as eq. (2.68),

$$\upsilon = \upsilon_0 \left(\frac{T_{\mathrm{e}}}{T_0}\right)^{\frac{1}{2}}$$

(2.68)

Substituting eq. (2.68) in eq. (2.67) and solving for the steady state gives eq. (2.69),

$$\left(\frac{T_e}{T_0}-1\right)\frac{T_e}{T_0}=\left[\frac{2}{3}\frac{q^2}{m_e v_0 \delta T_0}\right]\boldsymbol{E_0}^2=\frac{\boldsymbol{E_0}^2}{\boldsymbol{E_P}^2} \tag{2.69}$$

The RHS coefficient in eq. (2.69) has the dimensions of m^2V^{-2}, and its inverse square root is called the plasma field ($\boldsymbol{E_P}$). The plasma field is a very important quantity, as it is the threshold field required to heat electrons above the equilibrium temperature T_0. This threshold is not very large in high mobility semiconductors. An important distinction between electron transport in semiconductors and plasmas, is the phenomenon of negative differential conductance (NDC). Unlike semiconductors, there is no variation of electron mass in a plasma for particle speeds < *c* (speed of light). Whereas, in a semiconductor, the electron/ hole effective mass usually increases for higher energies in the conduction/ valence band. An example of this phenomenon is found in n-GaAs, known as Gunn oscillations, after J.B. Gunn[45]. Applied electric field strength greater than the plasma field ($\boldsymbol{E_0} > \boldsymbol{E_P}$) causes promotion of carriers to higher energy bands (**Γ→L,** see Fig. 2.1), where the effective mass (m^*) increases and conductivity decreases as per eq. (2.66). This leads to drifting charge domains that propagate in the crystal. When a domain arrives at the edge of the crystal/contact, the current receives a boost and returns to equilibrium value after a recovery period. The period of current oscillations can be engineered by modifying the length of the substrate. This is the cheapest method to produce microwave signals (Gunn diode).

In a hot plasma, the collisions are between electrons and ions (fully ionized plasma). The total velocity, $\boldsymbol{v}_{\text{total}} = \boldsymbol{v_{th}} + \boldsymbol{v_d}$ (thermal and drift velocity) is used in the derived expressions, most importantly appearing in the collision frequency (υ_{e-ion}), which varies with the carrier velocity as $\upsilon_{e-ion} \sim \boldsymbol{v}_{\text{total}}{}^{-3}$. However, the collisional forces do not increase indefinitely with increasing velocities. The collisional drag force reaches a peak value when $\boldsymbol{v_d} \sim \boldsymbol{v_{th}}$ and decreases with further increase in the electric field strength. Hence, unlike in solids/ semiconductors, the particles in a hot plasma can be accelerated in a non-equilibrium manner beyond this stage. The electric field required to cause the collision frequency to peak at its maximum (before decreasing upon further increasing electric field strength) is called the Dreicer field ($\boldsymbol{E_D}$)[50][51]. A steady state cannot be achieved for $|\vec{\boldsymbol{E}}| > \boldsymbol{E_D}$ and runaway effects are observed.

2.2.5. Dielectric response of semiconductors and metals

Sec. 2.2.4. provided a basic description of gaseous plasmas and their response to external electromagnetic (EM) fields, Debye sheath formation, plasma oscillations, non-linear responses of a plasma, and runaway effects. Similar phenomena and responses are also produced in semiconductors, described by the Lorentz model and in metals, described by the Drude Lorentz model. The Lorentz model is described first, to inspect the dielectric response of a dielectric medium e.g. semiconductor. The condition for resonance is described as it is a topic of interest to this thesis.

In the absence of external EM field the electron cloud around the nucleus of atoms in a dielectric material are assumed to have zero dipole moment. In the presence of electric field, the electron cloud around the nucleus is displaced/stretched, and the material is said to be polarized in response to the applied field. The nucleus exerts a restoring force on the displaced electrons. For small DC electric fields (sufficiently below ionization), the external electric force will be balanced exactly by the internal restoring force exerted by the nucleus. Once the applied field is removed, the electron cloud will perform a harmonic oscillation about the atom's nucleus. For a similar experiment using DC magnetic field, the oscillation would occur in the direction the spin axis for the electrons orbiting the nucleus. There are dissipative forces at work which damp these oscillations and restore equilibrium/steady state. In general, any harmonic oscillation can be studied using the analogy of a *mass on a spring* and studying its impulse response. For the first case of applied electric field $\vec{\boldsymbol{E}}$, polarization $\vec{\boldsymbol{P}}$ is induced between the nucleus and displaced electron cloud. Using Maxwell's first law, we can write the displacement $\vec{\boldsymbol{D}}$ and simplify to eq. (2.70) as,

$$\vec{\boldsymbol{D}} = \varepsilon_0 \vec{\boldsymbol{E}} + \vec{\boldsymbol{P}}$$

$$= \varepsilon_0 \vec{\boldsymbol{E}} + \varepsilon_0 \chi \vec{\boldsymbol{E}},$$

Where $\varepsilon_0 \vec{\boldsymbol{E}}$ is the displacement of charge in free space with the polarization $\vec{\boldsymbol{P}} = \varepsilon_0 \chi \vec{\boldsymbol{E}}$. Here χ is the electric susceptibility giving,

$$\vec{\boldsymbol{D}} = \varepsilon_0 (1 + \chi) \vec{\boldsymbol{E}},$$

which is rewritten in terms of complex relative permittivity $\widetilde{\varepsilon_r} = (1 + \chi)$ as,

$$\vec{\boldsymbol{D}} = \varepsilon_0 \widetilde{\varepsilon_r} \vec{\boldsymbol{E}} \tag{2.70}$$

The electric susceptibility is the impulse response of the dielectric medium to the electric field. Now the equation of motion is written as eq. (2.71) describing the electron cloud using the *mass on a spring* analogy. Here the restoring "spring force" is written explicitly in terms of ω_0 which is the natural frequency, to study the condition of resonance where displacement ($\vec{\boldsymbol{r}}$) of electron density from the nucleus reaches a maximum. A damping constant Γ is used to include the dissipative losses in the oscillation.

$$m\frac{\partial^2\vec{\boldsymbol{r}}}{\partial t^2} + m\Gamma\frac{\partial\vec{\boldsymbol{r}}}{\partial t} + m\omega_0^2\vec{\boldsymbol{r}} = -q\vec{\boldsymbol{E}} \tag{2.71}$$

Resonance occurs when the phase difference between the displacement and driving force is $\frac{\pi}{2}$. Secondary waves are emitted by the individual atoms undergoing resonant excitation which interfere with the driving field, leading to several interesting nonlinear phenomena.

To perform a harmonic analysis, take Fourier transform of eq. (2.71) and simplify to obtain $\vec{\boldsymbol{r}}(\omega)$ in eq. (2.72),

$$\vec{\boldsymbol{r}}(\omega) = -\frac{q}{m}\frac{\vec{\boldsymbol{E}}(\omega)}{\omega_0^2 - \omega^2 - j\omega\Gamma} \tag{2.72}$$

Giving the dipole moment $\vec{\boldsymbol{p}}(\omega) = -q\vec{\boldsymbol{r}}(\omega)$, expanded in eq. (2.73),

$$\vec{\boldsymbol{p}}(\omega) = -\frac{q^2}{m}\frac{\vec{\boldsymbol{E}}(\omega)}{\omega_0^2 - \omega^2 - j\omega\Gamma} \tag{2.73}$$

Eq. (2.73) is rewritten in terms of the Lorentz polarizability $[\alpha(\omega)]$, as $\vec{\boldsymbol{p}}(\omega) = [\alpha(\omega)]\vec{\boldsymbol{E}}(\omega)$. The Lorentz polarizability is a tensor quantity but is written here in its scalar form $\alpha(\omega)$ for simplicity in eq. (2.74).

$$\alpha(\omega) = -\frac{q^2}{m}\frac{1}{\omega_0^2 - \omega^2 - j\omega\Gamma} \tag{2.74}$$

Eq. (2.74) gives the Lorentz polarizability of a single atom. To account for the effect of all the atoms in a lattice, statistical averages are taken over the entire volume of the dielectric. The polarization per unit volume is written in terms of the atomic density *N* in eq. (2.75).

$$\vec{\boldsymbol{P}}(\omega) = N\langle\vec{\boldsymbol{p}}(\omega)\rangle = \varepsilon_0\chi(\omega)\vec{\boldsymbol{E}}(\omega) \tag{2.75}$$

And one obtains an expression for the susceptibility in eq. (2.76) using eqs. (2.73), (2.74) and (2.75).

$$\chi(\omega) = \frac{N\alpha(\omega)}{\varepsilon_0} = \left(\frac{Nq^2}{\varepsilon_0 m}\right)\frac{1}{\omega_0^2 - \omega^2 - j\omega\Gamma} \tag{2.76}$$

Comparing to eq. (2.51) a similar term appears on the R.H.S. of eq. (2.76). This is the plasma frequency (ω_p) and is used to define the complex permittivity $(\tilde{\varepsilon_\mathrm{r}})$ of the dielectric in eq. (2.77).

$$\tilde{\varepsilon_r}(\omega) = \big(1 + \chi(\omega)\big) = 1 + \frac{\omega_\mathrm{p}^2}{\omega_0^2 - \omega^2 - j\omega\Gamma} \tag{2.77}$$

Which can be separated into the real part $\dot{\varepsilon_r}(\omega)$ and imaginary part $\ddot{\varepsilon_r}(\omega)$,

$$\dot{\varepsilon_r}(\omega) = 1 + \omega_\mathrm{p}^2 \frac{\omega_0^2 - \omega^2}{(\omega_0^2 - \omega^2)^2 + \omega^2\Gamma^2} \tag{2.78}$$

$$\ddot{\varepsilon_r}(\omega) = \omega_\mathrm{p}^2 \frac{\omega\Gamma}{(\omega_0^2 - \omega^2)^2 + \omega^2\Gamma^2} \tag{2.79}$$

Eq. (2.78) suggests that for $\omega > \omega_0$, the resonant frequency, $\dot{\varepsilon_r}(\omega) < 1$ and becomes negative at high frequencies. The imaginary term $\ddot{\varepsilon_r}(\omega)$ only exists when there is loss and when there is loss, the real part $\dot{\varepsilon_r}(\omega)$ also contributes to it. Both these quantities are closely related to optical properties of the dielectric such as refractive index, absorption coefficient and reflectance, which have implications towards several physical phenomena.

Maximum absorption occurs at resonance, a property that is exploited in semiconductor solar cells by designing them to operate under resonant conditions and obtain higher photocarrier excitation from the absorbed light. On the other hand applications in communication have devices and carrier mediums designed to operate far from resonance to reduce losses and increase transmittance.

For metals the Lorentz parameters are simplified and are called Drude parameters. In metals with a high density of conduction electrons, the restoring force considered in the *mass on spring* model is negligible. Unlike dielectrics the electron cloud is not localized around the atom's nucleus and $\omega_0 \approx 0$, so the complex dielectric function is reduced to eq. (2.80).

$$\widetilde{\varepsilon_r}(\omega) = 1 - \frac{\omega_\mathrm{p}^2}{\omega^2 + j\omega\Gamma} \tag{2.80}$$

and the plasma frequency is written now in terms of the free electron density (N_e) and effective mass (m_e) in eq. (2.81) with an identical form to eq. (2.51).

$$\omega_\mathrm{p} = \frac{N_\mathrm{e} q^2}{\varepsilon_0 m_\mathrm{e}} \tag{2.81}$$

Here the damping term Γ is written in terms of a mean collision rate τ, which is the mean momentum scattering time for the conduction electrons in the lattice, $\tau = \frac{1}{\Gamma}$, and Eq. (2.80) is rewritten in terms of real and imaginary parts in eq. (2.82).

$$\widetilde{\varepsilon_r}(\omega) = \left(1 - \frac{\omega_\mathrm{p}^2\tau^2}{1 + \omega^2\tau^2}\right) + j\left(\frac{\omega_\mathrm{p}^2\tau^2/\omega}{1 + \omega^2\tau^2}\right) \tag{2.82}$$

In practice, metals are often described in terms of their real valued permittivity and conductivity, which is deduced using Ampere's circuit law eq. (2.83),

$$\nabla \times \vec{\boldsymbol{H}} = j\omega\varepsilon_0\widetilde{\varepsilon_r}\vec{\boldsymbol{E}} = \sigma\vec{\boldsymbol{E}} + j\omega\varepsilon_0\varepsilon_r\vec{\boldsymbol{E}} \tag{2.83}$$

which by rearranging terms on L.H.S. and R.H.S. shows that,

$$\widetilde{\varepsilon_r} = \varepsilon_r - j\frac{\sigma}{\omega\varepsilon_0} \tag{2.84}$$

The conductivity σ is obtained by comparing terms in eq. (2.84) and eq. (2.82), and with the DC conductivity defined as $\sigma_0 = \varepsilon_0\omega_\mathrm{p}^2\tau^2$ identical to eq. (2.52) is written in eq. (2.85) as,

$$\sigma = \frac{\sigma_0}{1 + \omega^2\tau^2} \tag{2.85}$$

The complex refractive index ($\tilde{\eta}$) is defined in eq. (2.86),

$$\tilde{\eta} = \sqrt{\widetilde{\varepsilon_r}} \tag{2.86}$$

Eqs. (2.86) and (2.80) give eq. (2.87), which has an identical form to eq. (2.54).

$$\tilde{\eta} = \left(1 - \frac{\omega_p^2}{\omega^2 + j\omega\Gamma}\right)^{\frac{1}{2}} \tag{2.87}$$

It is observed from eq. (2.87) that for excitation above the plasma frequency the metal becomes transparent as loss vanishes and $\eta \approx 1$. An extreme case is seen for e.g. using X-Rays. For excitation near the plasma frequency, both real and imaginary terms in the permittivity are significant and maximum loss occurs i.e. most of the incident wave is attenuated. The absorbed energy may be dissipated via several processes that depend on the material geometry, material properties, temperature etc. Such phenomena are actively researched in the research field called plasmonics e.g. in plasmon resonance enhanced solar cells. For excitation below the plasma frequency, the permittivity becomes imaginary and metals behave like good conductors. For this reason, metallic structures are generally operated below the plasma frequency. Typical plasma wavelengths for metals lie in the ultraviolet (82 – 137 nm).

2.2.6. A brief review of Quantum tunnelling

This brief review is aimed at developing a basic understanding of transmission across electrostatic barriers. This section will close the chapter by describing Quantum tunnelling more generally, with focus on sharp metal tips and field emission.

2.2.6.1. Historical Perspective

The history of field emission dates to the early 1900's. Electron emission into vacuum was observed from sharp metal tips, placed under high voltage bias, against a metal collector. Electrons in a metal object are confined by the surface barrier, and only small saturation current density i.e. thermionic emission should be observed from the tip, obeying eq. (2.15). The experimental setup is illustrated in Fig. 2.8 along with flat band representations for equilibrium ($V_{bias} = 0$), when the vacuum level is flat across the gap, and for increasing applied bias, where it develops a slope. When bias is applied, the barrier develops a finite width. Classically, above the barrier, electrons obey the equation of motion ($\boldsymbol{F} = m\mathbf{a}$), and transmission through the barrier is forbidden. However, experimentally it was observed that current exhibits a voltage dependence. This implies there must be a process by which electrons are transmitted across barriers. A fundamental breakthrough came in 1923, with the de Broglie hypothesis. This was the first formal postulation of "matter waves", the idea that matter has both particle and wave nature. The electron emission into vacuum was later successfully

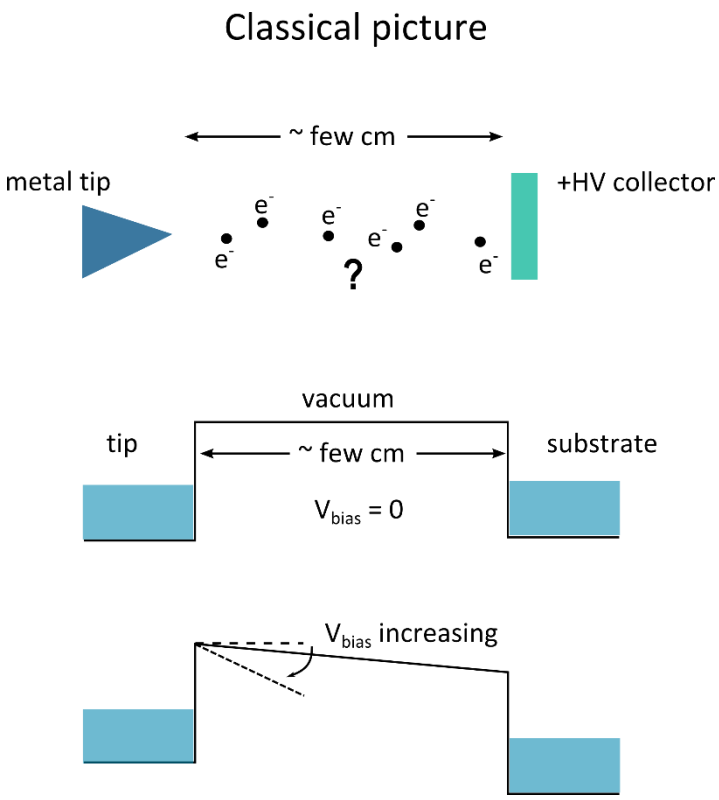

Figure 2.8- The classical picture of field emission from sharp metal tips in a vacuum gap, or into a conductive substrate. The emitter and collector (tip/ substrate) are represented as potential wells occupied up to the Fermi energy (shaded blue). No current flows when V_{bias} = 0 and the vacuum level is flat across the gap. Increasing V_{bias} creates a barrier with finite width. Classical theory cannot explain the field emission phenomena.

explained in terms of quantum interference phenomena in electrons arriving at the potential barrier. A similar duality is observed in light, which can travel like rays or waves depending on the scale of confinement (d). Either particle or wave nature is manifested as illustrated in Fig. 2.9. The de Broglie wavelength, $\lambda_{\text{de Broglie}}$ is given by eq. (2.88), related to the Planck constant h and momentum p.

$$\lambda_{\text{de Broglie}} = \frac{h}{p} \tag{2.88}$$

If electrons are nearly free i.e. $d \gg \lambda_{\text{de Broglie}}$, then particle nature is observed. Whereas, if $d \approx \lambda_{\text{de Broglie}}$, wave nature is observed (e.g. in a crystal lattice). In 1926, Erwin Schrödinger developed the famous axiom – the Schrödinger wave equation, which finally offered a substantial advance towards explaining the emission from sharp metal tips, in a biased vacuum gap. The Schrödinger wave equation describes the wave field and motion of the "matter waves"

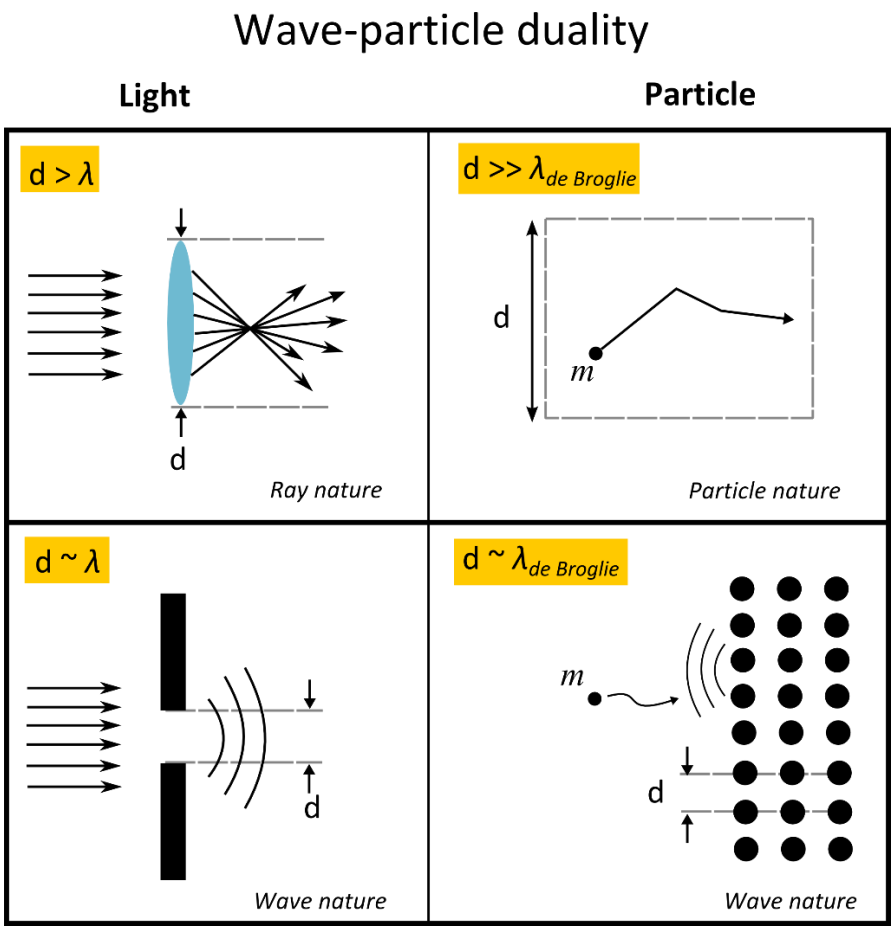

Figure 2.9 – Wave particle duality. Light and particles both exhibit wave particle duality as the confinement *d* scales from macroscopic dimensions, down to lengths comparable to the de Broglie wavelength ($\lambda_{de\ Broglie}$).

proposed by de Broglie, including evolution in time and position. Waves are delocalized in space and can interfere with one another (or with themselves, e.g. in the double slit experiment). This would suggest that that electrons are physically smeared out into space.

However, this view was later corrected by Max Born, who suggested that the wavefunction should be interpreted as a probability amplitude instead. There is an inherent uncertainty embedded in the quantum nature of reality. Hence, only averages/ expectation values can be formulated. Quantum mechanics offers analogues to all the classical quantities such as momentum, position etc. in terms of expectation values i.e. probability amplitudes, integrated over all allowed energies. This allows one to study the system's evolution in time and space. As per the postulates of Quantum mechanics, the probability of finding an electron at a position *r* is given by eq. (2.89), where the wavefunction $\psi(\vec{r})$ is normalized and multiplied by its complex conjugate $\psi^*(\vec{r})$ and integrated over an open interval.

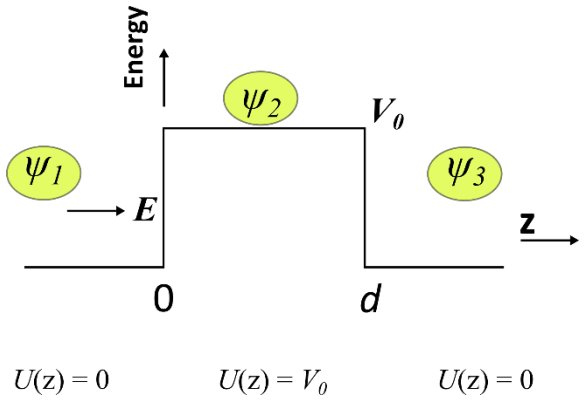

Figure 2.10 – Solutions to Schrödinger's equation are obtained for regions outside, and including a square barrier (z = 0 to z = *d*) of height V_0. The potential *U(z)* is known and only energies $\boldsymbol{E < V_0}$ are considered in the analysis.

$$\text{Probability} = \int_{-\infty}^{\infty} \psi(\vec{\boldsymbol{r}})\psi^*(\vec{\boldsymbol{r}})d^3\vec{\boldsymbol{r}} \tag{2.89}$$

And the expectation value for a measured physical quantity $\boldsymbol{X}$, is its average, given by eq. (2.90),

$$\langle \boldsymbol{X} \rangle = \int_{-\infty}^{\infty} \psi(\vec{\boldsymbol{r}})\ \boldsymbol{X}\ \psi^*(\vec{\boldsymbol{r}})\, d^3\vec{\boldsymbol{r}} \tag{2.90}$$

The Hamiltonian operator $\boldsymbol{H}$ is defined as eq. (2.91),

$$\boldsymbol{H} = -\frac{\hbar^2}{2m}\nabla^2 + U(\vec{\boldsymbol{r}}) \tag{2.91}$$

Where $U(\vec{\boldsymbol{r}})$ is the interaction potential, which describes how a particle of mass *m*, will interact with its environment. The first term is related to the kinetic energy of the particle. Schrödinger wave equation is written as eq. (2.92), which is the compact form of eq. (2.1).

$$\boldsymbol{H}\,\psi = \boldsymbol{E}\,\psi \tag{2.92}$$

Eq. (2.92) needs to be solved for ψ over all allowed energies. Tunnelling occurs in the barrier region, between the classical regimes and particles are freed from a finite barrier (up to ~ 3 nm). Fowler and Nordheim solved the time independent Schrödinger's equation for the emission problem, by finding detailed solutions for the wavefunction ψ, which will not be covered here. Their work showed that the electron wavefunction decays exponentially in the barrier region, but the electron energy remains unchanged! Wave-packets are propagated across the barrier

into vacuum where classical laws are obeyed. Although the actual shape of the potential barrier is not known, we are mainly interested in identifying the functional form of the tunnelling probability, which is presumed have similar characteristics regardless of the details of the barrier shape. The square barrier is chosen to obtain this insight, as eq. (2.92) can be solved analytically for this case. The problem is illustrated in Fig. 2.10, for a square barrier (thickness *d*, height V_0). Solutions for the wavefunction are written for each region on either side of, and including the square barrier. For all energies $\boldsymbol{E} < \boldsymbol{V_0}$, eq. (2.92) is rewritten as eq. (2.93).

$$-\frac{\hbar^2}{2m}\frac{d^2\psi}{dz^2} + U(z)\psi = \boldsymbol{E}\psi \tag{2.93}$$

The solutions to eq. (2.93) have the form:

$$\psi_1 = e^{\boldsymbol{i}kz} + Ae^{-\boldsymbol{i}kz} \tag{2.94}$$

$$\psi_2 = Be^{-\alpha z} + Ce^{\alpha z} \tag{2.95}$$

$$\psi_3 = De^{\boldsymbol{i}kz} \tag{2.96}$$

where,

$$k^2 = \frac{2m\boldsymbol{E}}{\hbar^2} \tag{2.97}$$

$$\alpha^2 = \frac{2m(\boldsymbol{V_0} - \boldsymbol{E})}{\hbar^2} \tag{2.98}$$

Here *A*, *B*, *C*, *D* are constants in eqs. (2.94-2.96). If eq. (2.93) is written in its time dependent form, with its complex conjugate, differentiating eq. (2.89) in time, followed by substitution allows us to define a probability current density $\boldsymbol{J}_{\text{prob}}$ given by eq. (2.99)

$$\boldsymbol{J}_{\text{prob}} = -\frac{i\hbar}{2m}\left[\psi^*\frac{d\psi}{dz} - \psi\frac{d\psi^*}{dz}\right]\hat{\boldsymbol{z}} \tag{2.99}$$

With the solutions for wavefunctions at hand in eqs. (2.94-2.98), the transmitted current density ($\boldsymbol{J}_{\text{trans}}$) and incident current density ($\boldsymbol{J}_{\text{inc}}$) can be written in terms of transmission probability *T* in eq. (2.100),

$$\boldsymbol{J}_{\text{trans}} = -\frac{i\hbar}{2m}\left[{\psi_3}^* \frac{d\psi_3}{dz} - \psi_3 \frac{d{\psi_3}^*}{dz}\right]\hat{\boldsymbol{z}} = T\frac{\hbar \boldsymbol{k}}{m} \tag{2.100}$$

$$\boldsymbol{J}_{\text{inc}} = -\frac{i\hbar}{2m}\left[{\psi_1}^* \frac{d\psi_1}{dz} - \psi_1 \frac{d{\psi_1}^*}{dz}\right]\hat{\boldsymbol{z}} = \frac{\hbar \boldsymbol{k}}{m} \tag{2.101}$$

And the transmission probability T for $\boldsymbol{E} < \boldsymbol{V_0}$ is:

$$T = \left|\frac{\boldsymbol{J}_{\text{trans}}}{\boldsymbol{J}_{\text{inc}}}\right| = \frac{1}{1 + \frac{(k^2+\alpha^2)^2}{4k^2\alpha^2}\sinh^2(\alpha d)} \tag{2.102}$$

For $\alpha \sim 10 - 15\ \text{nm}^{-1}$ and a wide barrier, at low energies, $\alpha d \gg 1$ and eq. (2.102) is approximated as eq. (2.103),

$$T = \frac{16k^2\alpha^2}{(k^2+\alpha^2)^2}\, e^{-2\alpha d} \tag{2.103}$$

Eq. (2.103) shows that the transmission probability decays exponentially as a function of interlayer thickness (d). Hence, the wavefunction in the barrier region will also have the form:

$$\psi(z) = \psi(z=0)e^{-2\alpha d}\,\hat{\boldsymbol{z}} \tag{2.104}$$

Using eq. (2.89), the probability of observing an electron at some distance z inside the barrier becomes a decaying exponential eq. (2.105),

$$|\psi(z)|^2 = |\psi(0)|^2 e^{-2\alpha z} \tag{2.105}$$

The expressions of quantum tunnelling eqs. (2.89-2.105) and the transmission of wave-packets through single/ multiple square barriers can be simulated and visualized, using the free java applet provided by University of Colorado, Boulder, USA[52]. The problem of field emission shown in Fig. 2.8 cannot be reconciled with classical theory. The formalism of Quantum mechanics shows that a finite electron current density escapes the narrow barrier confining them in the metal. Once free, i.e. once transmitted across the barrier, the electrons behave like classical particles once more. The electric field between the emitter and collector accelerates the transmitted electrons, leading to increased current as a function of applied voltage in the

vacuum gap.

2.2.7. Toy Model for Tunnelling

In the previous derivation, the influence of the atomic cores/ periodic potential wells in the lattice was ignored. When this is included, the solutions to the wavefunction become very complicated. However, the result obtained in eq. (2.105) holds generally. Fig. 2.11 shows the toy model of tunnelling. The atomic core potentials are also included here. When a voltage ΔV is applied, only the electrons in occupied states aligned to available (empty) states across the tunnel barrier can participate in the tunnelling process. The current will be proportional to the probability of electrons in the shaded region reaching $z = d$, given by eq. (2.106),

$$I = \sum_{E_F - q\Delta V}^{E_F} |\psi(0)|^2 e^{-2\alpha z} \tag{2.106}$$

It is useful to define the Local Density of States (LDOS) $\rho(z, \boldsymbol{E})$, eq. (2.107), which is a measure of electron density/ eV in an energy interval ε.

$$\rho(z, \boldsymbol{E}) = \frac{1}{\varepsilon} \sum_{E_F - \varepsilon}^{E_F} |\psi(0)|^2 e^{-2\alpha z} \tag{2.107}$$

The LDOS has some interesting features: (1) It is independent of the volume of the metal. (2) For a given z and $\boldsymbol{E}$, it reflects the energy band-structure of the metal and (3) It can be used to obtain an expression for the net tunnel current. The limits in eq. (2.107) are re-written in terms of applied bias ΔV, as shown in eq. (2.108),

$$\rho(z, \boldsymbol{E}) = \frac{1}{q\Delta V} \sum_{E_F - q\Delta V}^{E_F} |\psi(0)|^2 e^{-2\alpha z} \tag{2.108}$$

Arriving at the final current equation eq. (2.109), valid for small applied voltages i.e. $q\Delta V \rightarrow 0$.

$$I = q\Delta V \, \rho(0, E_F) \, e^{-2\alpha d} \tag{2.109}$$

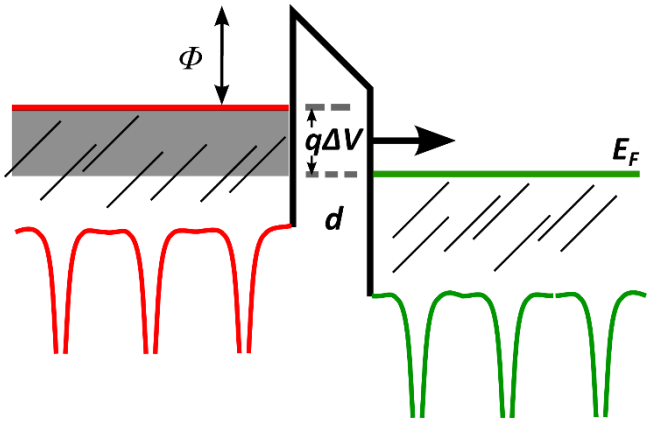

Figure 2.11 – Toy model to derive tunnel current in terms of local density of states (LDOS). The gray shaded area is the energy interval where tunnelling may occur near the Fermi level (E_F). Atomic cores have been included in the schematic on either side of the tunnel barrier, with finite thickness (d)

Eq. (2.109) is a very useful as it allows one to observe the line current density and derive terms which are proportional to the energy band structure of the substrate leading to direct applications in surface science, spectroscopy and microscopy. Observing changes in the tunnel conductance at low temperatures allows one to observe the profile of the density of states by differentiating the experimental I-V data (see Chapter 5).

2.7. Summary

Various electronic phenomena in solid state mediums, their junctions were reviewed along with notes on plasma dynamics and plasmonic response of dielectrics and metals. A basic understanding of carrier transport and response to fields was obtained. A useful toy model of tunnelling was described to study the functional form of tunnelling current. The topics covered in this chapter will aid in interpreting new results, shown in later chapters 4,5 and 6.

"For the things we have to learn before we can do them, we learn by doing them."

-Aristotle

Chapter 3:

Experimental procedures and techniques

Abstract

This thesis deals in experimental research on metal-semiconductor contact technology. Various material combinations are explored using large area metal contacts (d ~50-300 µm) on semiconductors. Commercially available pure Czochralski grown Si,Ge wafers (Pi Kem Ltd.) with low and moderate doping were used as substrates for patterning metal contacts. Chemical cleaning procedures, material deposition and processing techniques used in this work are described here. The complete workflow of metal contact fabrication and processing is described using schematics and photographs. The material structure of specimens described in Chapters 4, 5 and 6 were studied using several electrical and material characterization techniques, and their working principles are summarized here for convenience.

3.1. Sample fabrication

All fabrication work was done in cleanrooms at Newcastle University, after receiving cleanroom induction and training from Dr. Konstantin Vasilevskiy (for wet processing Si, contact photolithography, e-beam evaporation, reactive ion etching, thermal oxidation, vacuum annealing, rapid thermal annealing). Dr. Nikhil Ponon and Dr. Louise Bailey (Oxford instruments, UK) shared valuable expertise on DC magnetron sputtering and process development, which helped improve the fabrication workflow. Dr. Erhan Arac and Dr. Peter King provided useful insight about test structure design, specimen preparation, and training for Atomic layer deposition tools respectively. Detailed fabrication protocols were developed while working with, and independently from these esteemed colleagues. A general methodology is detailed here. Several experimental trials were performed over the course of this Ph.D. thesis, all following the same basic workflow described next.

3.1.1 Wet processing of Si and Ge substrates.

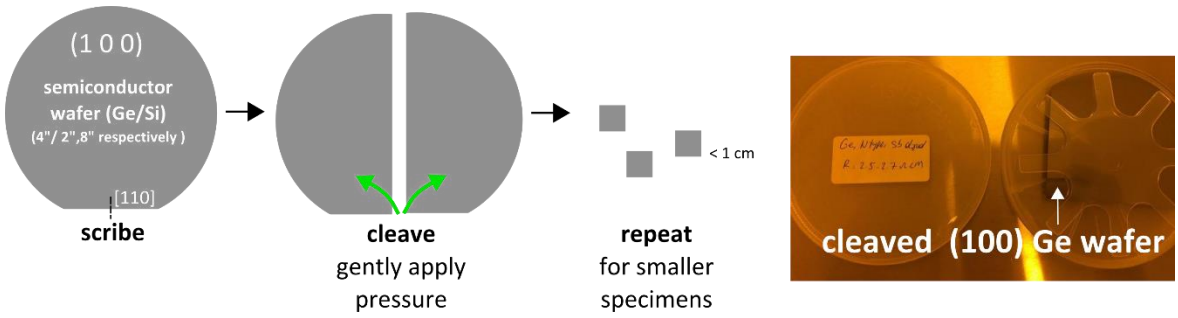

Figure 3.1: Cleaving crystalline (100) wafers - Small substrate specimens are cleaved/ dislocated along crystal fault planes, using a diamond scribe. The wafer is cleaved into small squares or rectangular shapes for further processing.

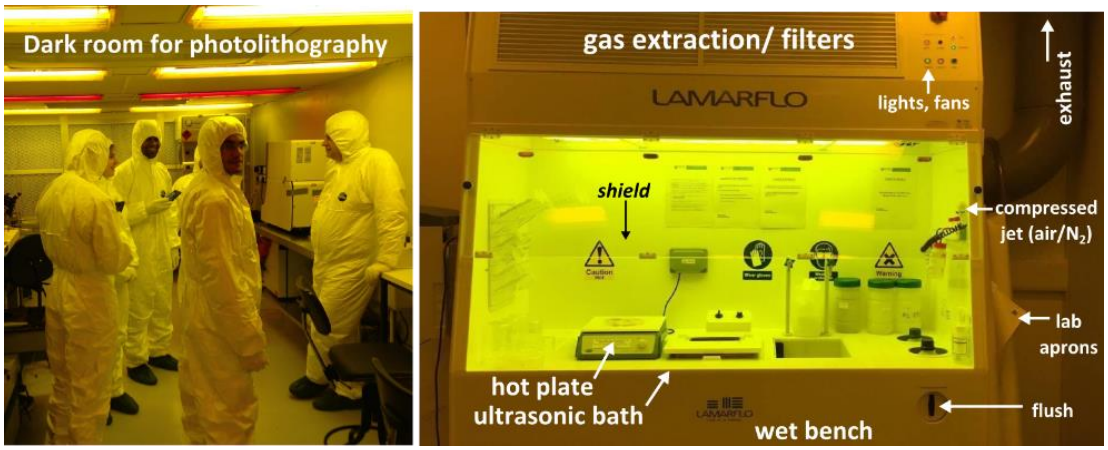

Figure 3.2: (Left) Receiving clean room induction (2013) from Dr. Konstantin Vasilevskiy – all personnel must wear cleanroom overalls and blue plastic overshoes to preserve cleanroom integrity. **(Right)** Wet bench for specimen cleaning, etching etc.

Single crystal Czochralski grown semiconductor wafers (Si, Ge), purchased from Pi Kem Ltd. were cleaved using diamond scribes and tweezers, by gently applying pressure on either side of the substrate illustrated in Fig. 3.1. Small substrate specimens (< 1 cm^2) were cut from the wafer, ready to be cleaned. The underside of these samples can be scribed, to distinguish them throughout later experiments. All contact fabrication procedures were done in a class 10000 cleanroom (cleanroom 4). ALD/ sputter- deposition and cleaning of processed specimens was done in a class 100 cleanroom (cleanroom 1). All chemical cleaning work on samples is done at the wet bench. (Fig. 3.2.-right). See appendix for detailed wet processing steps.

3.1.2 Contact photolithography

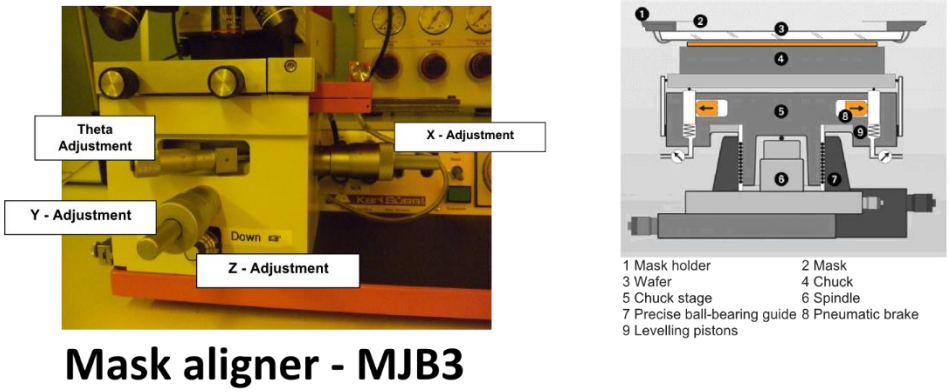

Figure 3.3: Top- Photograph and schematics showing the mask aligner instrument stage, with schematic diagrams. **Middle-** Hard contact mode is used for +ve and −ve lithography (first exposure). Soft contact mode is used for pattern reversal (−ve photolithography only). **Bottom-**The workflow is visualized schematically, showing the formation of pattern windows in the PR, ready for further processing.

Chemically cleaned and dried substrates are spin coated with photoresist (PR) resin prior to selective UV light exposure using specifically designed photolithography masks. The mask is in contact with the PR layer on the sample and it is exposed to UV light. This causes a change in the chemical structure of the PR molecules, causing them to become readily soluble in a developer solvent after exposure (See appendix for stepwise procedure used to prepare samples described in this thesis). This technique is used as an intermediate step in wafer processing to create multiple layers in the material geometry. As this thesis is focused on metal semiconductor junctions, one masking step is sufficient to study planar metallizations electrically. The basic workflow is described using graphics and images shown in Fig. 3.3.

3.1.3 Electron-beam evaporation and contact formation

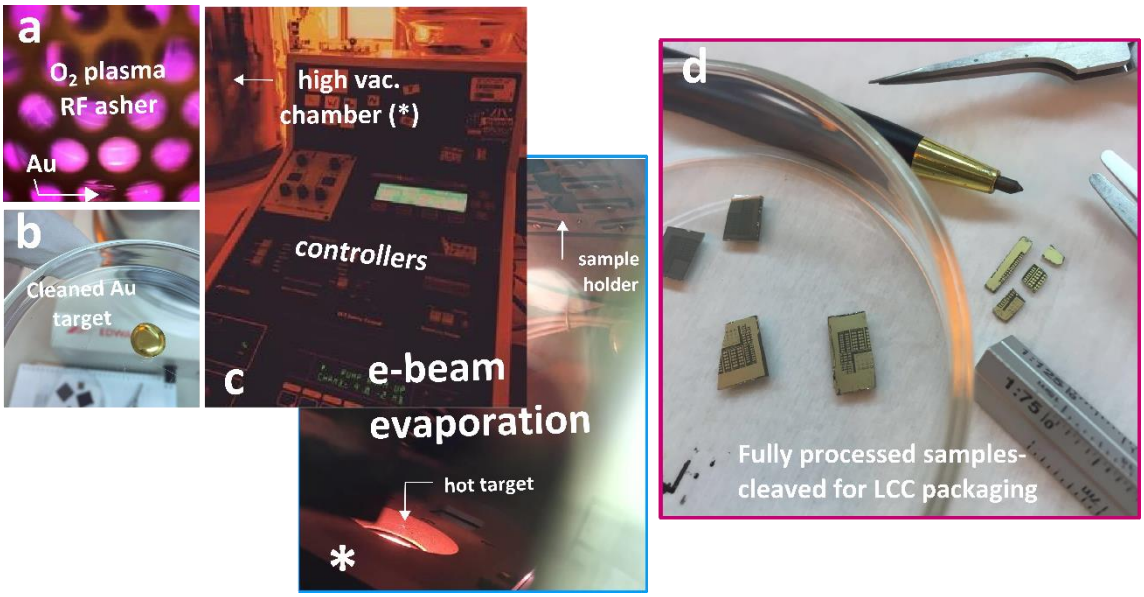

Figure 3.4: a. Au target being cleaned in an RF plasma asher, to remove organic impurities from the metal surface. **b.** Cleaned Au target, 10 mins in asher at max. power. **c.** Photograph of the e-beam evaporator. (*) inset shows Au target being evaporated onto Ge samples inside the high vacuum chamber. **d.** Fully processed rapid annealed Au/Cr/ Ge specimens (Hybrid contacts on Ge, Chapter 5) cleaved using procedure described in Fig. 3.1, ready to be mounted in < 4mm^2 leadless chip carriers (LCC), used for electrical testing at liquid helium temperature (4.2 K) at Royal Holloway University of London.

Metal contacts are formed on patterned samples by electron beam evaporation from metal targets. The Edwards e-beam evaporator is an evacuated bell jar assembly holding the samples. High vacuum conditions are achieved using a diffusion pump, backed by a roughing pump (and liquid nitrogen cold trap). Metal targets are prone to gather soot or other organic contaminants over prolonged use. Targets like Au (noble metals) are cleaned in an RF plasma furnace/ asher. The oxygen plasma burns away volatile hydrocarbon impurities, shown in Fig. 3.4- (a, b). Inside the e-beam chamber, the metal target is placed in a ceramic crucible and heated using an electromagnetically focused electron beam, melting the metal target when the current is sufficiently large, causing evaporation from a molten metal 'lake' scanned (XY) by the focused electron beam to achieve a uniform plume of evaporated material leaving the metal target. The electron-beam current, and chamber pressure conditions determine the deposition rate, which can be adjusted using process knobs on the EB3 controller (Fig. 3.4- c). A line-of-sight physical shutter prevents the evaporated material flux leaving the metal target from reaching the samples. Deposition onto samples begins only when the line of sight shutter is opened. A quartz crystal

microbalance monitors the deposition rate and film thickness for a given set of process parameters, which are observed on the controller's display. Once a steady deposition rate is achieved, the shutter is opened and thin films layers begin to form on the samples mounted onto the holder above (Fig. 3.4-c). Once deposition of required thickness is complete, the shutter is closed. The quartz crystal microbalance is reset and the beam current is gradually reduced (5 mA/ min) to cool the target slowly to prevent thermal shock. The e-beam source, XY scanners are then switched off. The metal target is hot and is allowed to cool (~15min) *in vacuo* before venting the chamber to atmosphere, to remove samples. Once samples are retrieved, the evaporator is pumped back to high vacuum, before switching it to standby mode. Contact patterns are realized by solvent lift-off (see appendix).

3.1.4 Atomic layer deposition (ALD)/ Sputtering cluster tool

Ultra-thin layers of alumina (Al_2O_3) were grown using thermal ALD for the MIS contact work shown in Chapter 4. The alumina layers were deposited in an Oxford Instruments Flex Al reactor, shown in Fig. 3.5, using adduct-grade trimethylaluminium (TMA) and H_2O as precursors. Chemically cleaned samples prepared for the ALD work were placed onto individual steel carrier wafers, then loaded onto the wafer/ cassette holder. The cassette holder is placed in the loadlock and the chamber is closed. The samples are now stored on carrier wafers in the loadlock, which is then pumped down to high vacuum using a mini tubro-molecular pump.

The sputtering chamber, ALD reactor and loadlock chamber are isolated from the transfer chamber by gate valves. The robot arm can transfer wafers between any of these evacuated chambers as required, without breaking vacuum via. gate valves, controlled by software. The carrier wafer holding samples are transferred from the loadlock into the ALD reactor/sputterer and process schedules are sequentially performed on several wafers in a batch run. The Al_2O_3 ALD process is described by the binary reaction[53][54]:

$$2Al(CH_3)_3 + 3H_2O \rightarrow Al_2O_3 + 6CH_4 \quad (3.1)$$

Which can be split in the following two surface half reactions eqs. (3.2-3.3):

$$AlOH^* + Al(CH_3)_3 \rightarrow AlOAl(CH_3)^* + CH_4\,, \quad (3.2)$$

$$AlCH_3^* + H_2O \rightarrow AlOH^* + CH_4 \quad (3.3)$$

The asterisk (*) in eq. (3.2-3.3) denotes surface species.

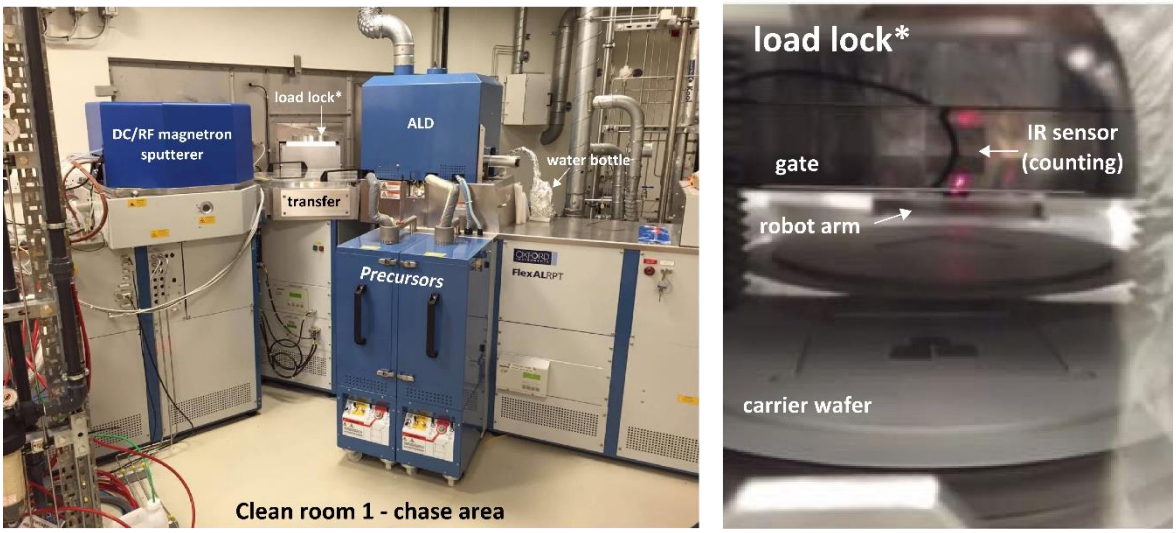

Figure 3.5: Oxford instruments Flex Al reactor/ PlasmaLab 400 integrated cluster tool allows wafer transfer between ALD and DC/ RF sputtering tools without breaking vacuum. A robot arm transports carrier wafers between the load lock and reactor chambers via. transfer chamber, all evacuated to high vacuum or better. Several controllers monitor the state of the cluster tool. An IR sensor counts wafers in the cassette holder, keeping track of processed jobs. The tool can perform scheduled recipes, batch processing on selected wafers in the cassette holder in sequences controlled by the tool user.

First the TMA reacts with hydroxyl (OH^*) species and produces a surface saturated with dimethylaluminium eq. (3.2). In the next half cycle, water reacts with $AlCH_3^*$ species and rehydroxilates the surface eq. (3.3). When excess precursors are used in every ALD half-cycle, the film growth becomes self -limiting, because surfaces become sterically saturated with reacted species and no further reaction is possible. Al_2O_3 film of required (~nm) thicknesses can be obtained with excellent control in terms of reaction cycles eqs. (3.2-3.3). Further process details about ALD Al_2O_3 are provided in Chapter 4.

3.1.5 DC magnetron Sputtering – Al back contact formation

An Oxford instruments PlasmaLab 400 sputter instrument is integrated, as part of the cluster tool shown in Fig. 3.5-(left). A high purity (99.99 %) Al target (Kurt Leskar Ltd.) was installed under the DC magnetron (position 2) and conditioned for target outgassing, removal of oxide layer, ready to be used. Patterned/ processed samples are first cleaned in IPA, UltraPure water and blow dried in compressed N_2, prior to Al back contact formation. Dried samples were placed on the carrier wafers, patterned side facing down. The cassette holder is loaded with required wafers for processing. As with the ALD Flex Al, the loaded cassette holder is placed in the

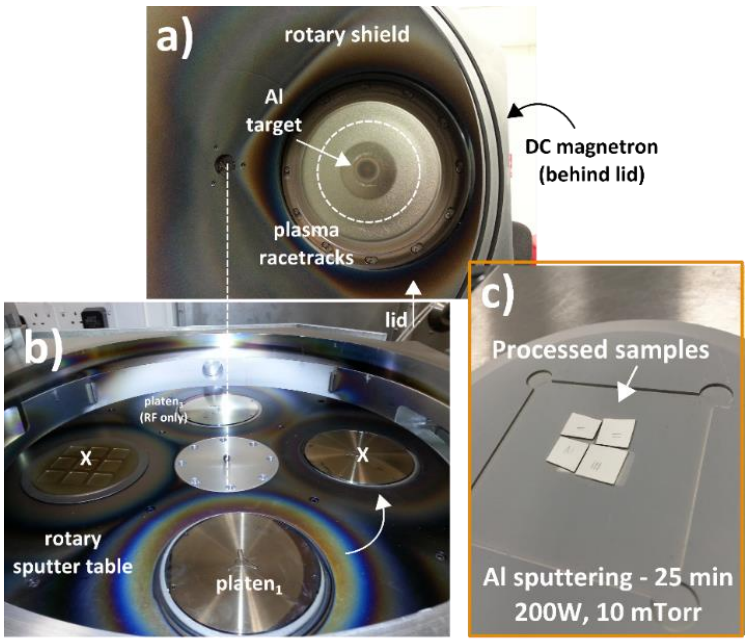

Figure 3.6: PlasmaLab 400 DC/ RF sputtering tool- a) Shield **/** target/ magnetron/ lid assembly- A rotary shield is used to block/open the sputter target's line of sight with the sputter table during conditioning steps. During deposition, the shield is in its open position as shown, but the entire assembly is sealed in UHV conditions. **b)** Temperature controlled rotary sputter table with platens- The robot arm places the carrier wafer (holding samples) onto platen$_1$. The table is rotated under high vacuum, to position platen$_1$ under the desired magnetron/ target. Ar^+ plasma sputters the Al target under DC bias. The Ar^+ plasma is contained by magnetic field under the target, forming race track patterns where maximum sputtering occurs. **c)** Sputter coated large area Al back contacts formed on sample's underside (patterned sides facing down on carrier wafer).

loadlock and the chamber is closed. The samples are stored in the loadlock, which is then pumped down to high vacuum by a mini turbo-molecular pump.

The recipe scheduler (software) commands the robot arm to transfer wafers for processing, one run at a time. Once the carrier wafer is in the deposition chamber, target and substrate platen conditioning steps are performed (target shield – closed, sputter table at set temperature). The Al target is conditioned for ~ 10min to reach the optimal deposition parameters (magnetron power, ion current, relative chamber pressure) in gradual steps – from low power, high pressure (100 W, 20 mTorr, Ar) to medium power, low chamber pressure (200 W, 10 mTorr, Ar). Once the ion current reaches a steady value under 200 W, 10 mTorr, the target shield is opened and deposition begins. The rotary shutter position is like shown in Fig. 3.6-a (target shield-open) for this step.

The sputter table can also be rotated around its axis like the target shield (dashed white line) marked in both Fig. 3.6-a,b. Only platen$_1$ is active when the PlasmaLab 400 is operated using the robot arm to deliver wafers from the loadlock. The sputter table is rotated to position platen$_1$ under the available DC and RF magnetron/ target assemblies to deposit required materials. If the tool is being used manually (without loadlock), then the chamber must be opened (breaking vacuum) to load samples under specific magnetrons. This method seriously reduces the process throughput and can cause target contamination, requiring longer duration in achieving ultra-high vacuum, and in conditioning steps before deposition (target outgassing, dead layer removal etc.)

After target conditioning, Al was sputtered onto the underside of samples to form large area back contacts using the cassette holder/ load lock method. Platen$_1$ holding the carrier wafer (samples) is rotated under the Al target, while maintaining sputter table temperature at ~ 104º C. Al deposition rate for (200 W, 10 mTorr) is 13 nm/ min forming ~ 300 nm Al layer over the entire carrier wafer, sputter coating the entire underside of samples (Fig.3.6-c) with Al metal (sheet resistance ~0.05 ohm-cm). The contact patterns on the face down side of the samples are unaffected by this process step, as DC magnetron sputtering is a line of sight PVD method, and because the test structures are closer to the centre of the samples by design.

3.2 TECTRA vs Rapid thermal annealing – crystallization

If annealing is required for samples, it is performed before the Al back-contact step described previously i.e. after lift-off/ contact formation, drying steps. For annealing in vacuum, a bell jar assembly, like the e-beam (Edwards) is used, called TECTRA is used. This is a custom-built vacuum furnace, available in Newcastle University clean room 4. Its chamber is usually kept under vacuum.

In this machine the stage cools via metal heatsink stands and the set points need to be entered manually between steps. After completing the last annealing step and reaching the lower set point, switch off the heater once temperature reaches < 50° C. Allow the ceramic stage to cool for 15min. Perform the pumping sequence in reverse to retrieve samples. Leave the chamber in high vacuum before switching off the diffusion pump and water (after cool-down ~ 30min).

The temperature of the TECTRA stage is monitored by a thermocouple, and regulated using a proportional controller. Hence, there is considerable temperature ‘clocking’ around the setpoint temperature, especially at lower temperatures < 400° C. Non-uniform heating can be

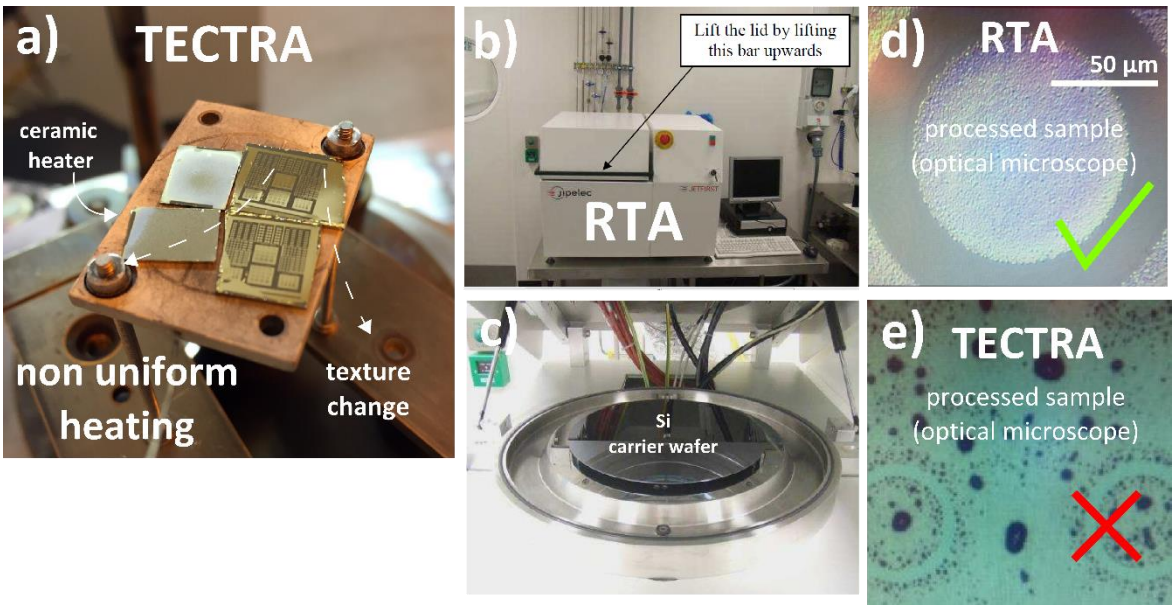

Figure 3.7: TECTRA vs RTA. a) Annealing can be performed on samples in vacuum (TECTRA) on a small ceramic/ resistor heating stage. The ceramic stage is cooled by convection via the metal stands supporting it. A proportional controller adjusts the current flowing through the ceramic heater, receiving feedback from a thermocouple. For low temperatures < 400° C this method of annealing is unreliable due to issues with non-uniform heating. b) Benchtop Rapid Thermal Annealing (RTA) JetFirst 200 unit in our clean room, with lid closed. **c)** Open the lid and place samples on the carrier wafer (never directly at the centre). The lid is closed during operation and the chamber is pumped down using its inbuilt turbomolecular pump. The chamber ambient is controlled by flowing process gases. During annealing, halogen lamps deliver heat the chamber and Si carrier wafer (+ samples). A pyrometer monitors the temperature of the Si wafer (at centre). PID controllers try to maintain setpoint temperatures by adjusting the lamp power (%). **d)** Optical microscope image of Au/Cr patterns on Ge processed at 400° C for 5-10s using RTP shows uniform textures, with patterns preserved after process. **e)** Optical microscope image of Au/Cr patterns on Ge processed using TECTRA/ vacuum annealing at a temperature setpoint of 350° C, for 5min. Agglomeration is visible and contact patterns appear damaged on the surface.

problematic in semiconductor wafer processing. An example of non-uniform heating at low temperature set-point in TECTRA is shown in Fig. 3.7-a. A photograph of Ge samples with Au/Cr contacts is shown after annealing (bell jar removed). Non-uniform textures are seen in metal layers on patterned and un-patterned samples, a result of non-uniform heating form the stage. The patterned samples were later tested electrically and showed non-linear I-V curves, with a reduced effective Schottky barrier height (~ 0.2 eV) (more details in chapter 4). Rapid thermal annealing (RTA) was found to be a superior annealing technique, obtaining uniform textures across patterns that correlate geometrically to the improved electrical behaviour (more in Chapter 5). The benchtop RTA unit in cleanroom 1 is shown in Fig. 3.7-b. In this technique, unlike in TECTRA, the method of heating is not resistive. During process (lid closed), the chamber is first pumped and purged with several litres of ultra-high purity (UHP) N_2 to regulate a steady chamber ambient. Once required chamber conditions are reached, halogen lamps are

powered ON. This heats the carrier gas (available: N_2, forming gas, O_2) and the Si carrier wafer gets hot. The pyrometer is calibrated for 6" or 8" Si wafers using updated PID look-up tables. When the temperature exceeds 330° C, the pyrometer can detect the temperature of the Si carrier wafer. A PID controller regulates the lamp power, allowing fine control over the process temperature. RTA is usually a very fast process, which allows one to perform short duration annealing, on the order of a few seconds. The temperature can be increased several 100° C/sec and carrier gases can cool the sample when halogen lamps are turned off. Fast cooling is extremely important in crystallization processes (more details in chapter 5, 6). Process outcome is considerably improved using RTA over TECTRA, e.g. compare in optical microscope images Fig. 3.7-(c,d).

3.3 X-ray diffraction - Crystallography

Condition for diffraction:

X-rays Diffraction is an indispensable tool for crystallography i.e. the study of crystal structure of materials. The condition of diffraction is discussed in the context of waves interacting with a crystal lattice. Consider an incident wave with wavelength λ, travelling along unit vector $\vec{\boldsymbol{S}}_{\boldsymbol{0}}$ and upon interaction with an atomic core (at O in Fig. 3.8-a.) is scattered along some unit vector $\vec{\boldsymbol{S}}$.

$\vec{\boldsymbol{S}}_{\boldsymbol{0}}$ can originate from outside the sample (e.g. X-Rays, light) or from within the sample (e.g. electron wavefunctions). Consider the situation shown in Fig. 3.8-a. Two sets of parallel, incident and scattered unit vector beams are drawn with reference to the origin of the crystal lattice (O). The second set of vectors interacts at another real lattice point (A). By definition, eq. (3.4) $\overrightarrow{\boldsymbol{OA}}$ is a real lattice vector.

$$\overrightarrow{\boldsymbol{OA}} = p\vec{\boldsymbol{a}}_{\boldsymbol{1}} + q\vec{\boldsymbol{a}}_{\boldsymbol{2}} + r\vec{\boldsymbol{a}}_{\boldsymbol{3}} \quad \textbf{(3.4)}$$

With real lattice basis vectors $\vec{\boldsymbol{a}}_{\boldsymbol{1}}, \vec{\boldsymbol{a}}_{\boldsymbol{2}}, \vec{\boldsymbol{a}}_{\boldsymbol{3}}$

And *p*, *q*, *r* are integers.

In this case the path difference magnitude is equal to ***OE***. This path difference can be expressed in terms of the known lattice vector $\overrightarrow{\boldsymbol{OA}}$ by projecting its components along unit vectors $\vec{\boldsymbol{S}}_{\boldsymbol{0}}$ and $\vec{\boldsymbol{S}}$ given in eq. (3.5),

$$\text{Total path difference} = -\left(\vec{\boldsymbol{S}} - \vec{\boldsymbol{S}}_{\boldsymbol{0}}\right).\overrightarrow{\boldsymbol{OA}} \quad \textbf{(3.5)}$$

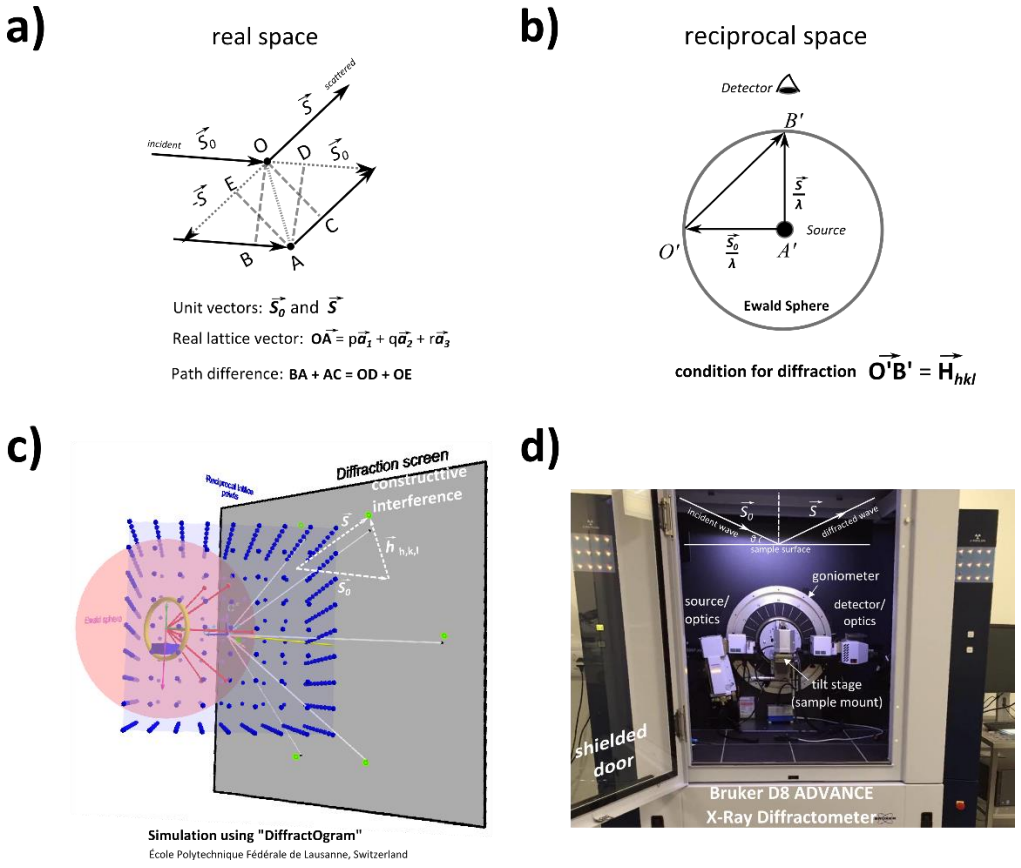

Figure 3.8: X-ray diffraction. a) Path difference in real space **b)** Condition for diffraction – Diffraction occurs when the Ewald sphere surface (radius, 1/λ) intersects with a valid reciprocal lattice point ($\vec{H}_{hkl}$), with respect to origin of reciprocal lattice O'. **c)** Simulated diffraction pattern for source (λ = 4 Å) aligned normal to the (110) simple cubic plane appears on the screen as spots of constructive interference. **d)** Bruker D8 advance X-Ray diffractometer has a fixed in-plane goniometer for the source and detector within their respective 80° sectors relative to the normal (dashed white line). Sample/ Tilt stage is first aligned to the source/ detector plane before taking a measurement.

Diffraction is an interference phenomenon. Constructive interference occurs between the incident wave vector $\vec{S_0}$ and scattered wave vector $\vec{S}$ when their phase difference is an integral multiple of 2π. A path difference of λ corresponds to a phase difference of 2π. Therefore, a path difference of $(\vec{S} - \vec{S_0}).\overrightarrow{OA}$ corresponds to total phase difference given by eq. (3.6),

$$\text{Total phase difference} = -\frac{2\pi}{\lambda}(\vec{S} - \vec{S_0}).\overrightarrow{OA}$$

$$= -2\pi\left(\frac{\vec{S}}{\lambda} - \frac{\vec{S_0}}{\lambda}\right).\overrightarrow{OA} \quad (3.6)$$

The terms in the parenthesis eq. (3.6) have dimensions L^{-1} and therefore must represent some reciprocal lattice vector and so, in terms of the reciprocal lattice basis vectors ($\vec{b}_1, \vec{b}_2, \vec{b}_3$) using some arbitrary constants *h*, *k* and *l* is written as eq. (3.7),

$$\left(\frac{\vec{S}}{\lambda} - \frac{\vec{S}_0}{\lambda}\right) = h\vec{b}_1 + k\vec{b}_2 + l\vec{b}_3 \qquad (3.7)$$

Hence, Total phase difference $= -\frac{2\pi}{\lambda}\left(\vec{S} - \vec{S}_0\right).\overrightarrow{OA}$

$$= -2\pi\left(h\vec{b}_1 + k\vec{b}_2 + l\vec{b}_3\right).\left(p\vec{a}_1 + q\vec{a}_2 + r\vec{a}_3\right)$$

$$= -2\pi(hp + kq + lr) \qquad (3.8)$$

Constructive interference occurs when the total phase difference is an integer multiple of 2π. Because real lattice vectors are defined in terms of integer multiples of the real basis vectors, the RHS of eq. (3.8) can only be an integer if *h,k,l* are also integers. Therefore, eq. (3.7) represents a valid reciprocal lattice point represented by $\vec{H}_{hkl}$. This situation can be visualized graphically in terms of the Ewald sphere (radius = $1/\lambda$) in Fig. 3.8-b. The conditions for diffraction in a crystal are met when the surface of the Ewald sphere intersects with its reciprocal lattice, e.g. simulation shown for simple cubic case, using DiffractOgram[55] in Fig. 3.8-c.

Cu K_α (λ = 1.5418 Å) X-Rays are produced by bombarding a copper plate with high energy electrons. X-rays are focused by a series of lenses and collimated using Göbel mirror optics at the source. Further physical fine-slits can be added to improve resolution, but this causes the signal intensity to decrease. The D8 Advance has a LynxEye detector with 192 channels that are scanned relative to the sample normal, detecting diffraction events (counts per sec. or total counts) from crystal planes for a given source/ incidence angle. In θ/ 2θ XRD measurement, both source and detector are scanned in equal angles i.e. θ and θ relative to the sample normal. More advanced measurements such as ϕ scan (in Chapter 6) require 360º goniometers to rotate the stage, along with tilt adjustment to align the source and detector at precise angles (e.g. rocking curve measurement), but operate under the same principle of wave interference described above. Detailed instructions to operate these tools will not be included here. Additional details about XRD measurements are included in later results chapters 5,6. Crystallography Open Database (COD) and built in Bruker software/ database provide a wide range of resources to lookup expected diffraction peaks and analyse data for a wide range of materials. A vast literature on crystallographic studies is available via Newcastle University's open access to most major science journals.

3.4 SEM/ EDX - investigating textures and nanomaterials

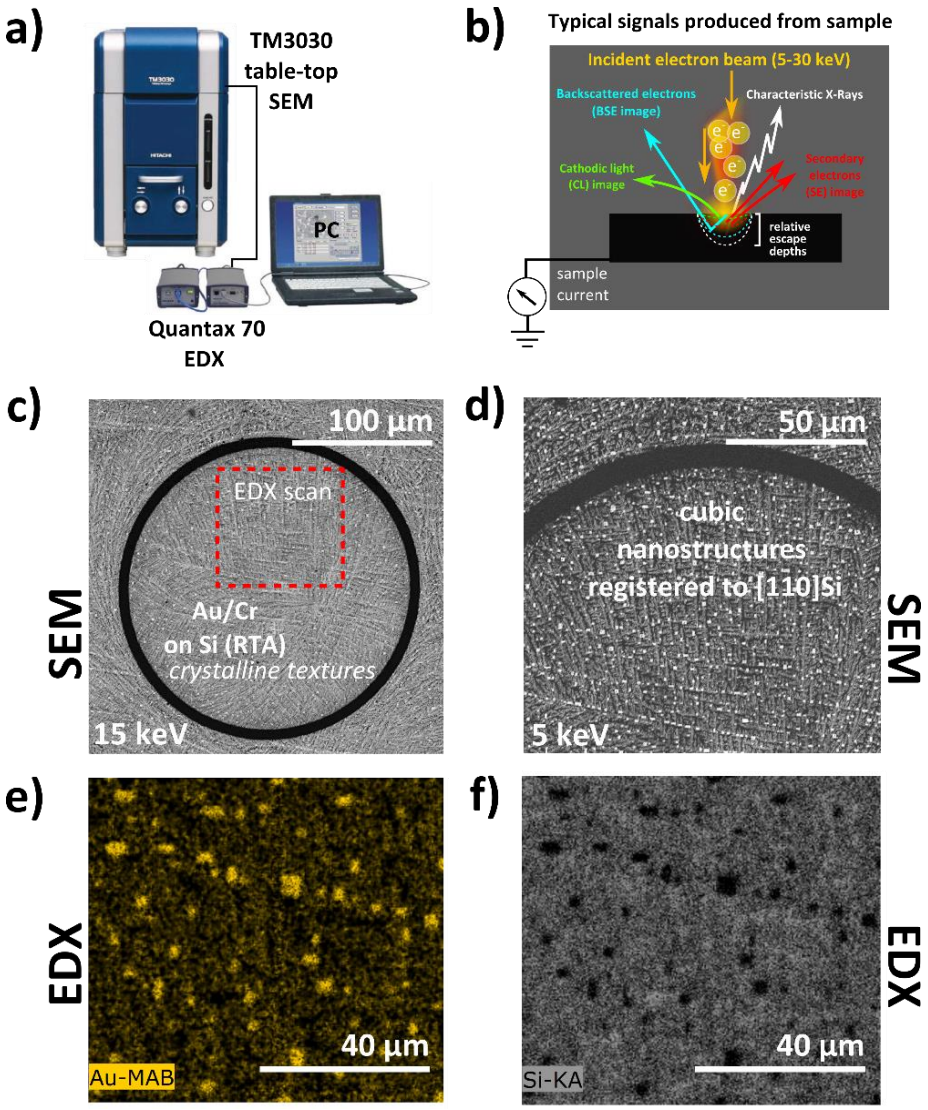

Figure 3.9: Scanning electron microscopy (SEM) and energy dispersive X-Ray (EDX) imaging – a) Overview of the Hitachi TM3030 benchtop SEM, equipped with Bruker Quantax 70 EDX detector and acquisition/ analysis software. **b)** Schematic showing typical signals produced from a sample interacting with intermediate electron beam energies (5-30 keV) used in SEM, along with their relative escape depths, sketched for representation purposes only. In practice, SEM images are mostly obtained using secondary electron emission from near the sample surface with the incident electron beam. Fast electrons interact with a larger sample volume. Some electrons are backscattered with energies comparable to the incident beam, while characteristic X-Rays are produced when core electrons are knocked out of their atoms by the incoming electron beam. Characteristic X-Rays are unique to the elements in the periodic table. Elemental information is characterized using an in-built Si based FET detector that converts the information about X-Rays (energy) to charge/ current signals. TM3030 software reconstructs images during acquisition. **c)** SEM image of Au/Cr Si sample after RTA taken using 15 keV electrons. Orthogonal textures apparent on the metal patterns. **d)** Corresponding image taken using lower incident beam energy, 5 eV. The nanocrystals appear brighter because their edges are sharp and emit more secondary electrons. Red boxed region in **c)** was selected for EDX scan. **e) and f)** EDX signal image filtered for Au (Mα,β) and Si (Kα) X-rays. Cubic Au nanostructures are identified in Au/Cr/Si hybrid films (more in Chapter 5).

Benchtop SEM is an invaluable research tool for studying microstructure and nanoscale features of materials. The Hitachi TM3030 (Fig. 3.9-a) can image conductive and non-conductive materials using its unique low vacuum technology called "Charge up reduction". This tool is available for use at the NEXUS facility, Newcastle University, to authorized personnel. An illustrative guide to its operation will not be provided here, although the reader is directed to a useful website that instructs SEM imaging practices in an interactive virtual SEM[56]. Typical signals produced from a sample under electron beam illumination are

sketched in Fig. 3.9-b. SEM relies on inelastic interactions of intermediate energy (5-30 keV) beam electrons with matter to create images, most frequently using secondary electrons, emitted from the conduction or valence band of the material into vacuum. Secondary electrons have relatively low energy (> 50 eV) compared to the incident electron beam. Fast electrons also knock out inner shell electrons, leading to the emission of characteristic X-Rays, which serve as unique identifiers of the elements in the periodic table.[57] With a sensitive EDX detector acquisition/ analysis setup (like Bruker Quantax 70 or similar), SEM/EDX images filtered by characteristic X-Ray energy are obtained (pixel brightness represents total X-Ray counts). X-Ray counts from a region on the sample are collected by the detector over an extended period (max~240sec) as the electron beam is slowly raster scanned over the sample area. Longer acquisition time usually provides higher total X-Ray counts. Thus, providing best possible elemental contrast. The spatial resolution for elemental analysis is ~ µm in the TM3030.

The TM3030 was mainly used for investigating texture changes and island formations within patterned regions on samples, shown in later chapters 5, 6. Fig. 3.9-c shows an example SEM image obtained from an RTA processed Au/Cr contact pattern (hybrid contact, Chapter 5) on low doped p-Si using 15 keV electron beam illumination. A beautiful texture with orthogonal features is observed in SEM, not visible under optical microscope. The same sample was also imaged using 5 keV illumination, shown in Fig. 3.9-d. The image appears darker because fewer secondary electrons are emitted from the sample for a lower beam energy. However, nanostructures with sharp edges appear brighter, as they emit more secondary electrons due to the so-called edge effect[58]. A region on the sample (red box) shown in Fig. 3.9-c was scanned for EDX. Images are filtered to obtain Au (M α,β) and Si (K α) elemental intensity maps, shown in Fig. 3.9-e and Fig. 3.9-f respectively. A novel crystallization phenomenon has occurred in the Au contact, forming predominantly (110)Au, highly oriented to [110]Si directions, appearing as orthogonal nanostructures on the surface (more in Chapter 5).

3.5 Energy filtered Transmission Electron Microscopy (EFTEM)

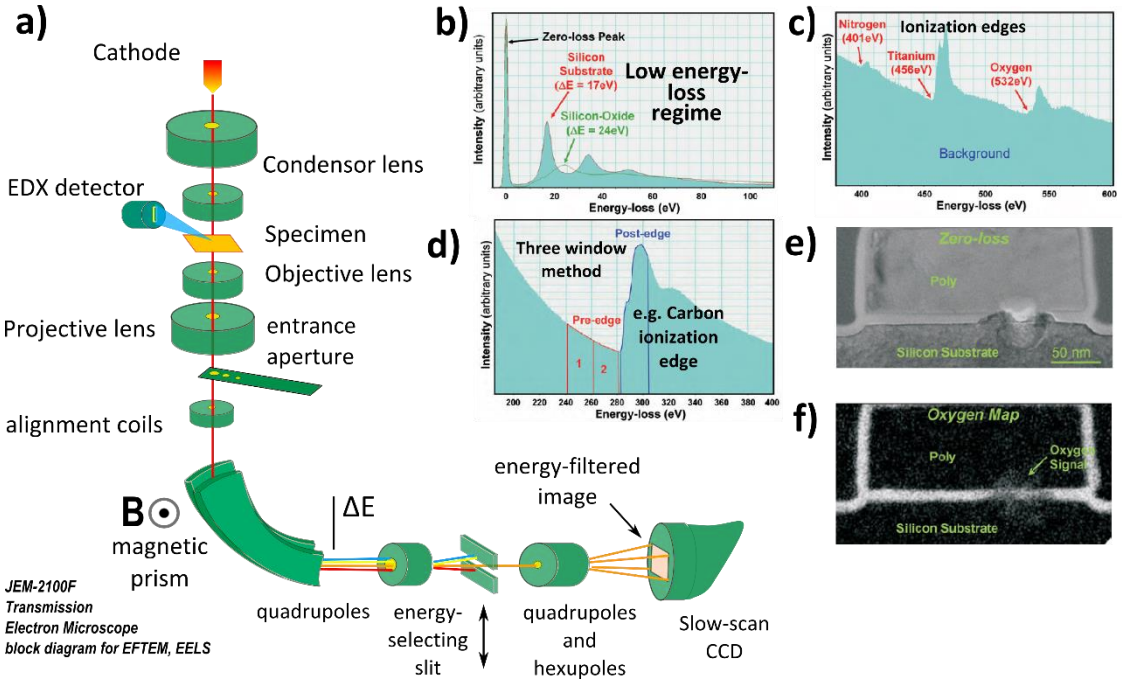

Figure 3.10: Energy filtered Transmission electron microscopy (EFTEM)- a) Block diagram showing the components of a typical transmission electron microscope, equipped post column energy filtering capabilities for EFTEM, EELS. A magnetic prism accepts the post column electron beam and disperses electrons according to energy loss. An energy selecting slit only allows a certain range of energetic electrons to pass. A series of quadrupole and hexupole magnetic lenses restore the image. The final image is recorded on a slow-scan CCD. **b)** The high energy electron beam ~ 300 keV contains many (elastic) electrons that do not lose any energy while passing through the sample (with zero-energy loss) while some lose energy (inelastic) due to valence interactions with the atoms in the sample. Energy filtered images are reconstructed by applying filters to the spectra for each pixel and performing inverse transforms on the data. **c)** Information about core excitations is present within the high energy loss spectrum e.g. Oxygen ionization edge (532 eV). **d)** Three window method - for obtaining energy filtered images, shown e.g. near the Carbon ionization edge, reproduced from ref. [59]. Typically, three images are recorded along with the zero-loss image to subtract the background energy loss signal. **e)** and **f)** are zero loss and Oxygen map images of a device respectively, Energy filtered Oxygen map is obtained using the three window method, reproduced from ref. [59].

Thin specimens (10-200 nm) also emit X-rays, Auger electrons and secondary electrons when illuminated using high energy electrons (60-300 keV), similar to SEM. However, unlike SEM, in this case most of the incident electrons are transmitted through the sample, either elastically - used e.g. in Transmission Electron Microscopy (TEM), Electron Backscatter Diffraction (EBSD), or ineleastically - used e.g. in Electron Energy Loss Spectroscopy (EELS) and Energy Filtered Transmission Electron Microscopy (EFTEM). By introducing a post-column energy selecting slit, images of the sample are reconstructed using magnetic lenses and signal processing to obtain high resolution spatial mapping of elements in EFTEM[60]. The basic

block diagram of the instrument (with specimen being measured) is shown schematically in Fig. 3.10-a. A magnetic prism disperses the post column transmitted electrons according to their energy. An energy selecting slit is used to physically allow only a certain energy range of electron to continue their journey. The image is finally reconstructed using a series of quadrupolar and hexupolar magnetic lenses. A slow scan CCD collects the final image[60]. The JEOL-2100F instrument equipped with Gatan Imaging Filters (GIF-963) can reconstruct raw energy filtered images during acquisition. Data are collected and filtered in post-analysis by expert microscopists. A typical energy loss spectrum consists of the zero-loss peak (elastic electrons), plasmon modes from the specimen, other valence interactions (Fig. 3.10-b), while the core excitations appear at higher energies, with significant ionization edges e.g. carbon, oxygen (Fig. 3.10-c). The ionization edges at higher energies can have significantly lower intensities than the plasmon peaks and so the background needs to be subtracted from the spectrum, to filter images using the ionization energy of elements. In the three-window technique[59], three energy filtered images of the specimen are obtained sequentially- one image post edge (just above ionization energy) and two pre-edge images, taken just before the ionization edge, shown e.g. at carbon edge in Fig. 3.10-d. Using the pre-edge images, the background signal is extrapolated and then subtracted from the zero-loss image e.g. Fig. 3.10-e and Fig. 3.10-f, following similar procedure for oxygen edge, showing its spatial distribution in the specimen (reproduced from ref.[59]).

3.6 Theta probe – X-Ray Photoelectron emission spectroscopy

The theta probe instrument (Fig. 3.10) at NEXUS, Newcastle University is used to detect photoelectron emissions from a sample area, illuminated by a micro-focused X-ray source (spot size 15-400 µm). Combined electron and ion flood sources are used for non-conductive samples to alleviate charging effects, which reduce the photoelectron yield. The multi-element electrostatic radian lens is used for conventional spectroscopy. It provides both energy and angular dispersion on the 2D detector in the output plane, both collected simultaneously; enabling angle resolved XPS without tilting the sample. A fast entry load lock chamber (Fig. 3.10-a) allows easy access to the sample stage, without breaking vacuum in the XPS chamber. A fracture stage decouples from the main stage in the XPS chamber, seen from the viewport (Fig. 3.10-b). Electrical feedthroughs are provided as part of the fracture stage, which comes into physical electrical contact with the terminals on the main stage, when engaged with the leads on the fracture stage, completing the external circuit, when used. Turbomolecular pumps maintain UHV conditions ($< 10^{-7}$, up to 10^{-10} mbar) in the XPS chamber. Once the stage is in

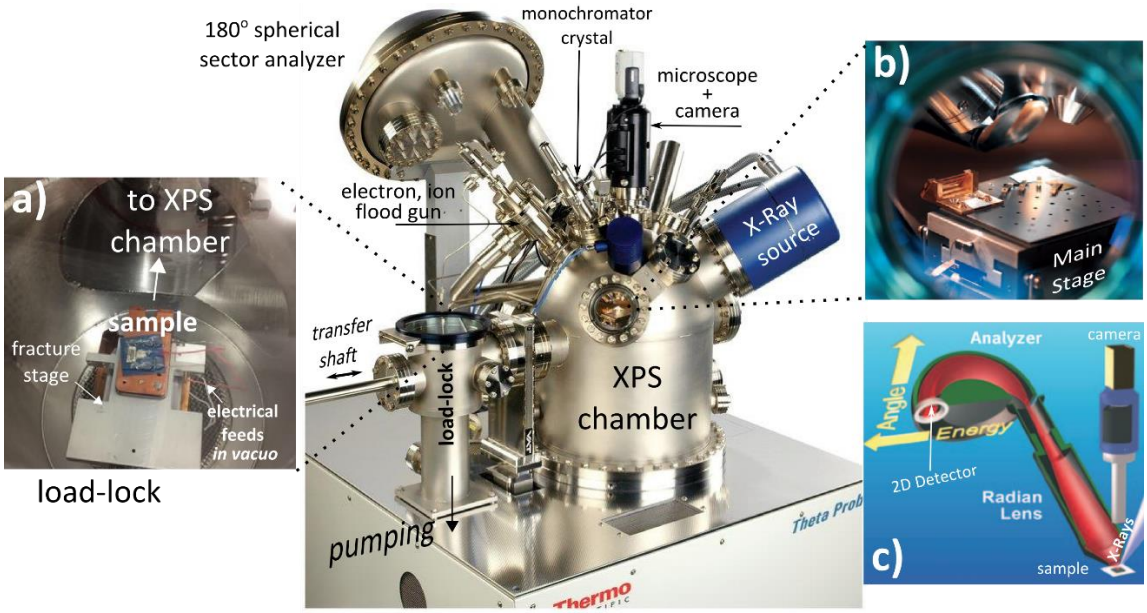

Figure 3.10: Theta probe XPS instrument overview. Theta probe can collect angle resolved X-ray photoelectron (XPS) spectra from samples, covering a 60° angular range in parallel, and without tilting the sample. It can as well be used in the conventional mode (without angle resolved information) for spectroscopy. Typical measurement involves a micro-focused X-Ray beam incident on a sample region, releasing photoelectrons which are detected by the instrument. **a)** UHV preparation chamber/ transfer block for sample loading, isolated from the XPS chamber by a software controlled gate valve. Electrical feedthroughs are provided in the instrument. The stage is conveyed into the main XPS chamber for measurements. **b)** Photograph showing the inside of the XPS chamber, with the bottom half of the fracture stage in view, close to the radian lens aperture. **c)** Schematic overview of XPS acquisition in Theta probe.

place with the sample, the region of interest on the sample is aligned close to the radian lens, along with the zoom microscope/ CCD camera for viewing. The usual Theta probe operation is schematically summarized in Fig. 3.10-c, illustrating its angle resolving capabilities.

Chapter 6 of this thesis contains research dealing with low voltage (~1 V) controlled hot electron emission into vacuum from island metal films (IMFs)[43]. In this work, the Theta probe instrument was used to detect the electron emission spectra from the sample (Fig. 3.10-a). However, both X-Ray source and flood gun were disabled during acquisition because we are only interested in observing voltage controlled electron emission spectra from nanostructures. Spectroscopic mapping studies are reserved for future work.

3.7 Two-terminal I-V measurements

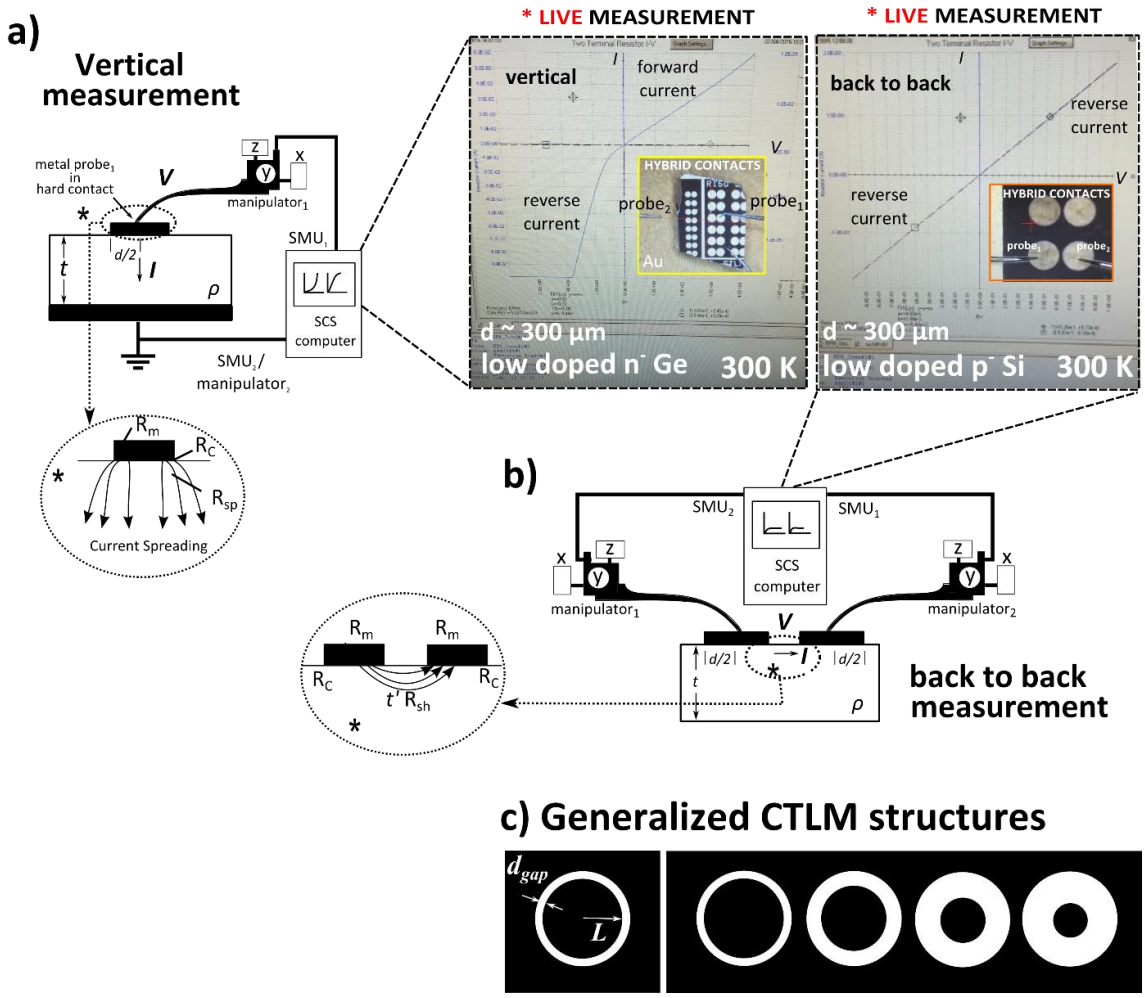

Figure 3.11: Two terminal I-V measurements using a semiconductor characterization system (SCS) computer-a) Vertical measurement- Current flows through the top contact, into the substrate of thickness *t* and resistivity *ρ* and through the large area back contact. Inset shows a live measurement of a hybrid contact to n^- Ge at 300 K (Chapter 5). Bubble inset (dotted circle) shows current paths spreading from the contact. **b) Back to back-**Current flows parallel to the substrate plane in the gap between contacts. Inset shows a live measurement of hybrid contacts on p^- Si (Chapter 5). Bubble inset (dotted circle) shows current paths spreading from the contact over distance comparable with the transfer length. **c)** Generalized scheme of circular transmission line method structures with gaps (d_{gap}) and inner contact radius *L*. In the CTLM structures used in this thesis (Chapter 4), the inner contact radius is fixed and only the gap spacing is varied. The formulae for contact resistivity calculation are therefore simplified.

Engineered metal semiconductor contacts are studied in this thesis using their I-V characteristics. The photomask used to realize the contact structures is mainly designed for two terminal measurements. Two terminal measurement (and by extension, Transmission line methods) provide the simplest test structures to obtain the contact resistance[61]. Two types of measurement configurations are investigated, **a)** Vertical measurement using patterned top

contact and large area bottom contact, shown in Fig. 3.11-a and **b)** Back to back measurement, shown in Fig. 3.11-a with both contacts on the top surface. The insets show photographs taken during measurement of hybrid contacts (Chapter 5) to n^- Ge and p^- Si measurement, shown in Fig. 3.11-a with both contacts on the top surface. The insets show photographs taken during measurement of hybrid contacts (Chapter 5) to n^- Ge and p^- Si samples respectively. A semiconductor characterization system (Keithley 4200 SCS) is used to perform measurements and acquire data. Two Source Measure Units (SMU_1 and SMU_2) measure the current flowing through the sample ($I_{in} = I_{out}$) for an applied voltage, V. Voltage bias sweeps are forced by the source SMU_1 controlled using the KITE software on the SCS computer. Samples were tested for repeatability and hysteresis, using dual voltage sweeps. All I-V measurements described in this thesis, unless otherwise stated were performed using CASCADE compatible Au microprobes (~ 25 µm tip), in hard contact with the sample patterns (Fig. 3.11-b inset), or one probe is shorted to the back contact (Fig. 3.11-a inset).

Following Schroder's book ref.[61], Assuming uniform resistivity (ρ) and thickness (t) in the entire semiconductor, and ignoring probe/ metal resistance R_m and back contact resistance (large area contact), the total resistance (R_T) in the vertical geometry is given by eq. (3.6),

$$R_T = R_C + R_{sp} \quad (3.6)$$

Where, R_C is the top contact's resistance. For planar contacts, one can express R_C in terms of contact resistivity (ρ_c) as eq.(3.7)

$$R_C = \frac{4\rho_c}{\pi d^2} \quad (3.7)$$

R_{sp} is the spreading resistance, directly under the metal contact pattern. For thin film contacts ($t \gg d$) the spreading resistance can be approximated as in eq. (3.8),

$$R_{sp} = C\frac{\rho}{2d} \quad (3.8)$$

C is a correction factor related to ρ, d, and the current distribution in the sample under bias. For widely separated planar contacts on a uniformly doped semi-infinite substrate, C ≈ 1. In this approximation, for vertical geometry, the contact resistance is obtained by subtracting the spreading resistance from the total resistance eq. (3.9).

$$R_C = R_T - C\frac{\rho}{2d} \quad (3.9)$$

This method is prone to large errors, as R_{sp} is not known accurately and cannot be measured independently. Hence, this approach only works when $R_{sp} \ll R_C$, valid for small contact

radius[62]. Alternatively, if small contacts of varying diameters are prepared, the RHS of eq. (3.9) is a linear function of reciprocal contact area, and the slope of this line gives contact resistance[63]. In order to minimize spreading resistance in the lateral geometry, heavy doped epi layers (having sheet resistance R_{sh}) are normally shallow implanted (depth, t) under the contact structures, confining most of the current in this region. This can be avoided for planar contacts by using Circular Transfer Length Method (CTLM) structures, where the current can only flow between the inner and outer contacts. A generalized scheme for CTLM structures having contacts with varying gap lengths (d_{gap}) and/or inner contact radius (L) is shown in Fig. 3.11-c. The total resistance is measured between the inner contact and the outer (large area) contact and for CTLM structures with $L \gg d_{gap}$, R_T is given by eq. (3.10),

$$R_T = \frac{R_{sh}}{2\pi L}\left(d_{gap} + 2L_T\right)C^* \tag{3.10}$$

Here, C^* is a correction factor given by eq. (3.11),

$$C^* = \frac{L}{d_{gap}} ln\left(1 + \frac{d_{gap}}{L}\right) \tag{3.11}$$

and L_T is the transfer length, given by eq. (3.12),

$$L_T = \sqrt{\frac{\rho_c}{R_{sh}}} \tag{3.12}$$

The transfer length can be thought of as the region over which most of the current transfers from the semiconductor to the metal. For practical contacts with diameters up to 400 µm and d_{gap} of 5-50 µm, the correction factor is needed to compensate for the circularity of contacts and to adjust the transfer length to obtain a linear fit to eq. (3.10), when R_T values are plotted against d_{gap}. Without the correction factor, the contact resistance is over-estimated. In the CTLM structures designed on the pattern mask used in Chapter 4, the inner contact radius is fixed and only the gap spacing is changed and so eqs. (3.10 – 3.11) are adjusted accordingly.

"Change is not always progress… A fever of newness had been everywhere confused with the spirit of progress."

-Henry Ford

Chapter 4:

MS and MIS contacts – Schottky to Ohmic

Abstract

This chapter covers pilot experiments on metal-semiconductor contacts using low doped Si and Ge substrates, to study FLP. The influence of inserting ALD alumina (AlO_x) interlayers (IL) is investigated on Si. Thermal atomic layer deposition was used to form ultra-thin interlayers in metal/IL/semiconductor (MIS) Ohmic contacts on n-type and p-type Si. ALD AlO_x of thickness 1–2 nm was deposited at 120 °C on Si substrates prior to patterning/ metallization, forming Ni/AlO_x/Si contacts. Inserting AlO_x interlayers improved conductivity by two orders of magnitude but the contacts retained rectifying character. Upon annealing at 200 °C, the conductivity increased by another order of magnitude and the contacts became Ohmic. A minimum specific contact resistivity (ρ_c) ~ 10^{-3} Ω-cm^2 was obtained for structures based on lightly doped (10^{15} cm^{-3}) n- and p- Si substrates. Existing models that describe Fermi level de-pinning do not fully explain these findings, but these results are nevertheless consistent with other experimental data in the literature. A few closing remarks about the effectiveness of the MIS methodology and severity of FLP are made at the end of the chapter.

4.1. Introduction

The findings in this research summarize a few key results obtained while working with Dr. Peter King and Dr. Erhan Arac, while investigating metal-semiconductor (MS) and metal/IL/semiconductor (MIS) contacts to low doped Si and Ge. Recently reported simulation and experimental work[39] shows that the effectiveness of the MIS approach towards improving contact resistance is unsatisfactory when using high doped semiconductors. MS contacts using heavy doped Si considerably outperform equivalent MIS Ohmic contacts. The contact resistivity improvement obtained by inserting thin interlayers is ultimately limited by the added interlayer tunnel resistance, despite using heavy doping in the semiconductor. Field emission dominates for $N_D > 10^{20}$ cm^{-3} and traditional MS contacts achieve lower specific contact resistivity than MIS contacts. The MIS approach is better suited to applications using

low doped semiconductors (< 10^{19} cm^{-3}) only. The main drawbacks for strongly pinned semiconductors are more pronounced on relatively low doped semiconductors ($N_D \ll 10^{21}$ cm^{-3}). The heavy doping strategy may overcome some limitations, but as mentioned in Chapter 1, doping presents various obstacles at nanoscale geometries. Further, heavy doping increases impurity scattering of carriers and degrades carrier mobility in devices.

The effect of inserting thin interlayers in contacts to low doped semiconductors is not fully understood. There is a vast literature on MIS contacts using interface dipole engineering, as well as suppression of metal induced gap states (MIGS). The choice of interlayer material is usually a high-κ material with a small band offset to the semiconductor. At a certain interlayer thickness, the new Schottky barrier height is small either for electrons or holes, resulting in improved conductivity on either n- or p- semiconductors exclusively. A large band offset (interlayer/ semiconductor) is expected to degrade conductivity, as the height of the tunnel barrier is a parameter for carrier transport across the interface. A thick interlayer will dramatically lower contact performance due to increased tunnelling resistance. As tunnelling probability reduces, the overall conductivity of the contact reduces. From a simple electrostatics point of view, a charged interlayer will modify the surface dipole on the semiconductor surface, modifying the band bending at the interface.

The room temperature band gaps of Si and Ge are 1.12 eV and 0.67 eV respectively with the Fermi level pinned close to the Charge Neutral Level (CNL). In Si, the CNL is experimentally found to be near the mid-gap energy (~ 0.6 eV above the valence band) whereas in Ge, it is found close to the valence band (~ 0.1 eV). The Schottky barrier height (Φ_B) is extracted from diode I-V characteristics, and by analysing its temperature (T) dependencies.

From thermionic emission theory (section ***2.2.1***), reverse current density (J) saturates against voltage, taking the general form:

$$J = A^* T^2 \, e^{\left(\frac{-q.\Phi_B}{kT}\right)} \tag{4.1}$$

where $A^* = \lambda_R A_0$

The pre-factor A^* is the corrected Richardson constant which includes a material specific parameter λ_R to adjust the universal constant A_0= 1.20173 × 10^6 A $m^{-2}K^{-2}$. By observing the temperature dependencies of reverse current at a given voltage, the 0 K Schottky barrier height is extrapolated. This relationship generally holds for metal contacts to low doped semiconductors with a large Schottky barrier height. For higher doping levels (> 10^{19} cm^{-3}),

thermionic field emission, and field emission become the dominant mechanism (section ***2.2.4***) and eq. (4.1) needs to be modified to include the Schottky effect and tunnelling. In the presence of large electric fields, the Schottky effect/ image force lowering must be included to account for voltage dependence in the pure thermionic emission component. Tunnelling mechanisms are weakly dependent on temperature and dominant tunnelling makes it difficult to distinguish changes in the Schottky barrier height from I-V characteristics. The focus of this work is on low doped semiconductors to avoid this complication and eq. (4.1) is used for MS contacts to evaluate the effective Schottky barrier height at a given temperature, since the value of A^* is known over a range of temperatures[64].

The influence of thermal ALD AlO_x interlayer (IL) thickness on conductivity is studied on Ni/IL/Si structures fabricated on RCA cleaned, last HF treated Si. Ohmic behaviour is observed on low doped n- and p- Si (10^{15} cm^{-3}) using a nominal AlO_x thickness ~ 1.5-2 nm. The specific contact resistivity (ρ_c) using these MIS contacts on low doped n- and p-Si was found to be quite high ~ 10^{-2}-10^{-3} ohm.cm^2 but is improved by two orders or magnitude when high doping (~10^{19} cm^{-3}) is used, providing average $\rho_c \sim 1 \times 10^{-5}$ ohm.cm^2 and lowest $\rho_c \sim 8.9 \times 10^{-6}$ ohm.cm^2. These values are larger in comparison to other published studies using MIS methodology e.g. ref. [65] and those required by the ITRS for sub-10 nm devices (better than 10^{-9} ohm.cm^2). However, the results in this chapter do shed light on some shortcomings of the MIS method, while demonstrating a planar contact method to achieve concurrent Ohmic contact on both n- and p-Si using the same fabrication process.

It may be possible to fabricate graded heterojunctions, multi-laminate interlayers, doped interlayers, among other strategies used by researchers to alleviate some challenges in the short term. But ultimately these techniques rely on heavy doping in one form or another and therefore, all suffer from the interlayer thickness providing the last bottleneck towards achieving ultra-low specific contact resistivity.

4.2. General methodology used in fabrication

Commercially available (PiKem Ltd.) pure Czochralski crystalline/ c-Si (single/double side polished) and Ge (single side polished) wafers of select low doping levels were used in this work. The wafers were diced into ~ 1 cm^2 specimens prior to wet processing. Detailed chemical cleaning protocols for Si and Ge are described in the appendix. For the ALD work, RCA cleaned Si specimens were dipped in BHF and blow dried using compressed N_2 just prior to loading in

the ALD reactor. The specimens (including controls) received identical preheat treatments in all experiments. Ultrathin AlO_x layers were grown by thermal ALD using an Oxford Instruments Flex Al reactor, with adduct-grade trimethylaluminium (TMA) and H_2O as precursors. ALD layers were deposited over a range of thicknesses at a deposition temperature of 120 °C, with pulse/purge times of 0.2/1.5 s and 0.2/6 s for TMA and H_2O, respectively. The precursors were supplied to the chamber by vapour draw. Following photolithography and patterning, metal contacts were deposited by e-beam evaporation to form contacts using solvent lift-off in warm N.M.P. (at 60° C). Well defined contacts were observed using an optical microscope. The specimens were annealed post metallization at 200° C, 5 min. in high vacuum (~ 9×10^{-7} mbar).

For both control and IL contact studies, planar thin film metal contacts form pairs of diodes separated by a small gap 10 – 20 µm apart, and are measured as illustrated schematically in Fig. 4.1-a for the control case (without IL). Prior to metallization for control specimens, the patterned specimens were dipped in BHF 7:1 (HF: NH_4F = 12.5: 87.5%) for 10 s and rinsed in DI water for 2min. This treatment results in micro-rough surfaces with predominantly dihydride terminations (H-Si-H)[66]. The contact pairs are identical patterns (radius 100-150 µm).

4.3. Results

4.3.1. Control: Schottky barrier height and FLP in Si

Two terminal I-V measurements are used to study the reverse current for this contact geometry, shown in Fig. 4.1-a. Only the reverse current i.e. current flowing from the metal side into the semiconductor is observed in this measurement as one contact in the pair becomes reverse biased (−) and exhibits a high resistance state in either polarity of the voltage sweep (+ / −) performed in the measurement. The contact pair (1-2) is probed by a source measure unit (SMU) and I-V characteristics are recorded for the contact pair.

At equilibrium, there is no current and the energy band diagram is as shown in Fig. 4.1-b. for low doped n-Si (N_D ~10^{15} cm^{-3}). Schottky barriers are formed at the metal-semiconductor interfaces. A depletion region (W) extends into the semiconductor and the Fermi level (E_F) is constant across the entire geometry. For simplicity, if the electron barrier heights for the contact pair ($\Phi_{B1,n}$ and $\Phi_{B2,n}$) and the depletion widths (W_1 and W_2) are assumed equal then ideal diodes obeying thermionic emission should produce saturating I-V characteristics, appearing

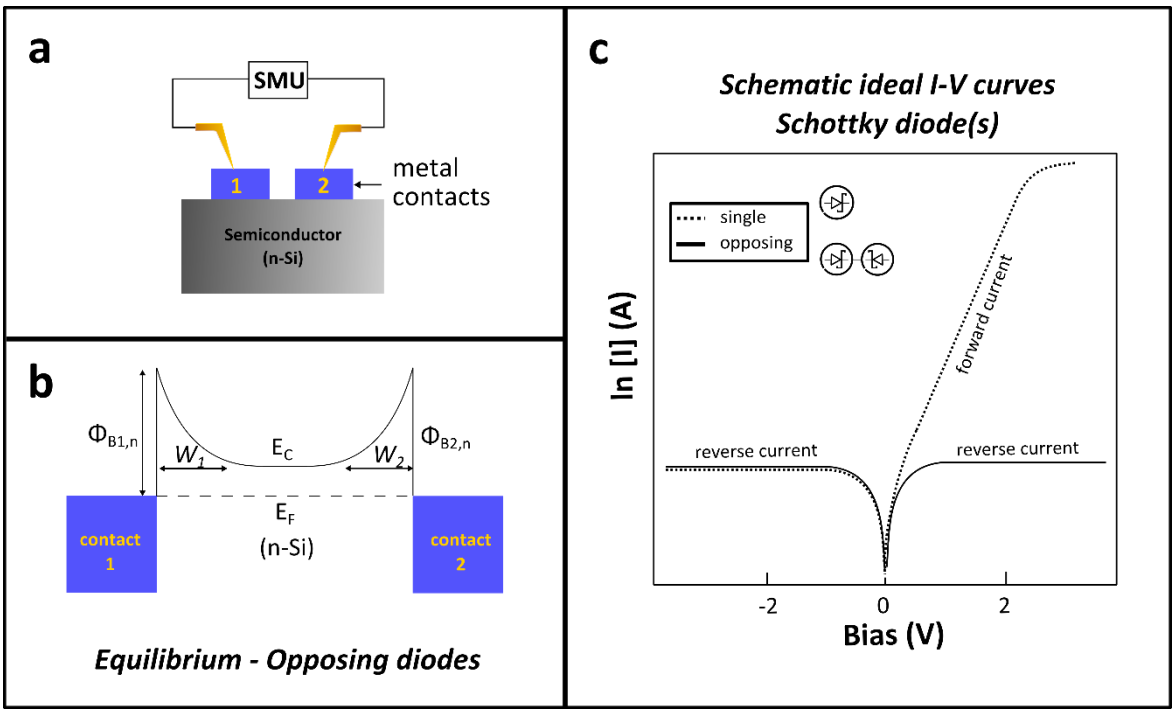

Figure 4.1: a. Schematic cross section of the MS contact geometry used in this work, showing the measurement configuration. Metal probes are used to apply biasing voltage between the metal contacts and the semiconductor (e.g. n-Si). **b.** Energy band diagram for opposing diodes or back to back diodes at equilibrium. **c.** Schematic I-V curves comparing opposing diodes (solid line – only reverse I-V characteristics) and single diodes (dotted line - complete I-V characteristics). Only the reverse current is measured in either voltage polarity (-/+) for the opposing diodes case.

symmetric in either voltage regime (+/−), shown schematically by the solid line in Fig. 4.1-c. Complete diode I-V characteristics are shown for comparison (dotted line). The Schottky lowering/ image force lowering was not considered here. Following Chiquito *et al*'s formulation for back to back diode I-V characteristics[67] real reverse I-V curves can be described approximately by the formula given by eq. (4.2),

$$J = A^{*}T^{2}e^{\left(\frac{-q\Phi_B}{kT}\right)}\left(\frac{\sinh\left(\frac{qV}{2kT}\right)}{\cosh\left(\frac{qV}{2nkT}\right)}\right) \tag{4.2}$$

The ideality factor (n) can account for some non-ideal behaviour in reverse I-V characteristics, which are generally attributed to Schottky lowering, increased tunnelling or recombination at the interface. Curve fitting is used to extract diode parameters and compare with expected values. This method allows quick evaluation of diode parameters, without using high temperature testing, and provides additional confidence in values obtained by other analytical

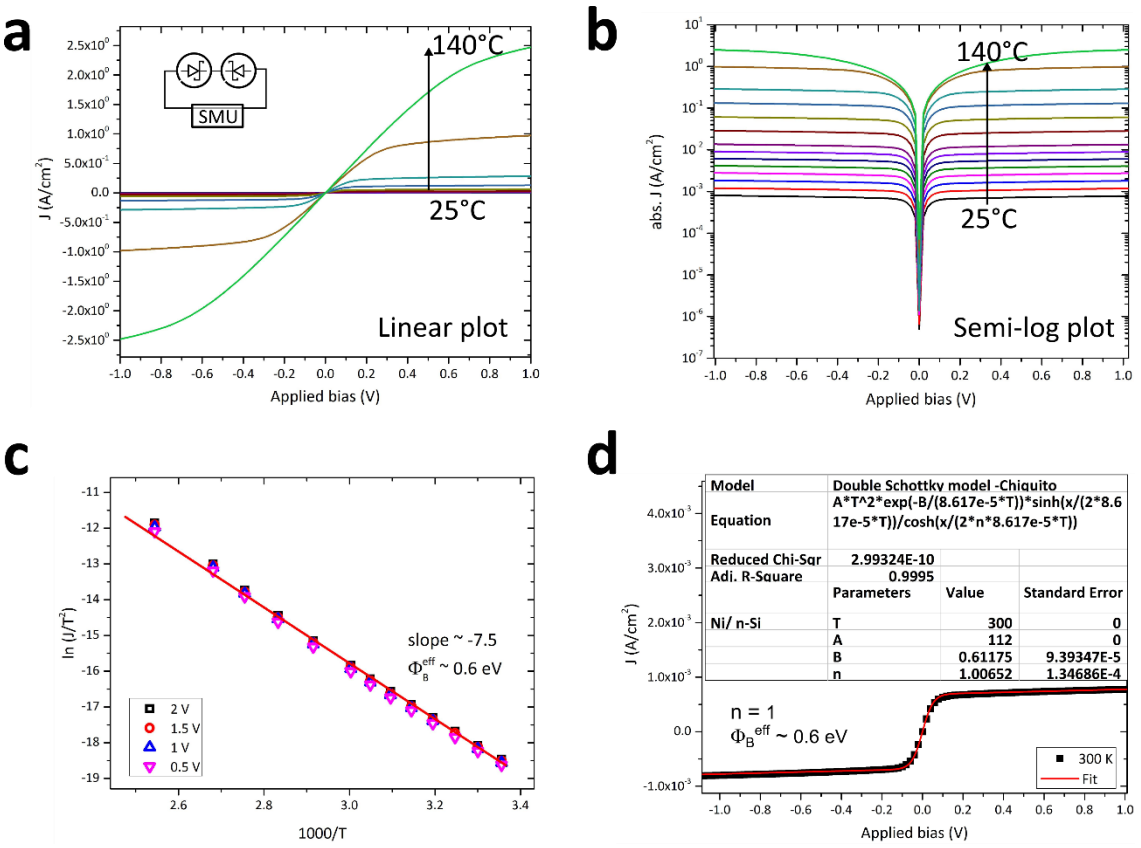

Figure 4.2: a. Back to back diode linear I-V characteristics of Ni/n-Si (N_D~ 10^{15} cm^{-3}) after annealing at 200° C in vacuum, for 5 mins. Measurements were taken at various temperatures (25-140 ° C) to observe temperature dependencies. At lower temperatures, nearly saturating and symmetric I-V characteristics are observed, indicating equal Schottky barrier heights for the contact pair behaving like nearly ideal diodes. **b.** Same data shown on a semi-log plot to compare changes in magnitude of reverse current as temperature varies. **c.** Effective 0 K Schottky barrier height extracted using high temperature I-V data at different applied bias on a functional plot obtained from eqn. 4.1. Nearly saturating, symmetric I-V curves at lower temperatures result in nearly fixed slope over a small voltage range, giving a constant Schottky barrier height ~ 0.6 eV. **d**. Function fitting using eqn. 4.2 on room temperature I-V data assuming known values of *A** for Si provides similar value of effective Schottky barrier height ~ 0.6 eV. Results are representative data reproduced over three sample batches (Ni/Si).

methods. It was found that eqn. 4.2 fits well to the data, and the extracted diode parameters are comparable to those obtained using other graphical and analytical methods (e.g. Werner method[68], Cheung method[69], Richardson method[70]). For example, we studied control Ni and Al metal contacts on Si and concluded that Ni is a superior contact metal in terms of thermal stability and electronic properties.

Al tends to anodize during evaporation and forms aluminium oxide during deposition if the evaporation rate is kept low. Forming non-uniform aluminium oxides at the contact interface can cause Schottky barrier height inhomogeneity, and this can be quite large across several tested contacts (± 0.3 eV). Instead, for Al contacts the metal deposition rate needs to be kept

high (~1 nm/s) to obtain a mirror like finish, as opposed to the matted gray appearance of partially oxidised thin films. The shiny Al contacts produce somewhat less variable Schottky contacts but are degraded upon annealing in the presence of oxygen. Pitted white formations were observed on the Al contacts under optical microscope. Their I-V curves were asymmetric/ un-saturating, and in many trials, were found to be worse than the as-deposited contacts. On the other hand, Ni metal contacts were found to be far more reliable and produced smaller variability in I-V characteristics across multiple contacts tested before and after annealing, while exhibiting nearly ideal diode behaviour.

Ni is routinely used in self-aligned silicide process in VLSI technology, as silicidation by Ni consumes less Si (the substrate material) than alternative metallizations for silicidation like Co and Ti, while providing better sheet resistance[71]. Ni mono-silicide phase begins to form at relatively low annealing temperatures < 400º C[72]. Very high annealing temperatures > 600º C, are avoided because it results in a high resistivity $NiSi_2$ phase.

Although the sheet resistance of low temperature silicides is very low, the contact resistance depends mainly on the Schottky barrier height- which seems to be more

sensitive to interface properties, rather than granularity/ domains within the planar metal contact. FLP determines the Schottky barrier height and this was verified using Ni contacts on Si, shown for example in Fig. 4.2. Because the contacts have a relatively large planar geometry, current scales by the contact's area and so data are reported in terms of current density (J). The I-V characteristics of back to back Ni contacts on low doped n-Si (N_D ~10^{15} cm^{-3}) are shown for increasing temperatures (25-140º C) in Fig. 4.2-a and Fig. 4.2-b on linear and semi-log scales respectively. Using eqn. (4.1) and rearranging the terms, the functional plot: ln (J/T^2) vs (1000/T), known as the Richardson plot, is used to extract the 0 K barrier height at various applied bias, as shown in Fig. 4.2-c. The effective Schottky barrier height (Φ_B^{eff}) is ~ 0.6 eV and is nearly constant over a small range of applied bias, due to nearly saturating I-V curves. A similar value was obtained using the fitting function, eqn. (4.2) using the room temperature I-V data and assuming the known value for corrected Richardson constant (A^*) of n-Si[64], 112 $A.cm^{-2}.K^{-2}$. The fitted parameters give Φ_B^{eff}~ 0.6 eV and $n \approx 1$. Both methods (Fig. 4.2- c, d) show that the Fermi level at (100)Si surface is located near its mid-gap energy. The FLP condition is believed to originate from surface defects but interestingly, the contacts follow nearly ideal thermionic behaviour as per their reverse saturation I-V characteristics. Similar curve fitting for annealed Ni/p-Si contacts (using A^* = 32 $A.cm^{-2}.K^{-2}$ [64]), along with high temperature analysis showed Ni/p-Si interface has Φ_B^{eff}~ 0.5 eV, confirming the roughly mid-gap CNL/pinning position in the Si bandgap[73].

Inferences:

In the absence of FLP and interface charges (ideal Schottky contact)- Ni, with its high work function (~ 5.2 eV) is expected to form Ohmic contact to p-Si[73] but this is not found to be the case experimentally. Large Schottky barrier heights ~ $E_g/2$ eV were observed using Ni contacts on both n- and p-Si. The annealing temperature used here is lower than required for onset of silicide formation. This allows comparison in the properties of the Ni/Si interface as opposed to the Ni-silicide/Si interface, to understand the effect brought about by the insertion of ALD interlayers, and to study the effect of annealing on the final contact interface, shown next.

4.3.2. Thermal AlO_x ALD interlayers enable Ohmic contact to n- and p-Si

The ALD AlO_x recipe used in this work was developed by Dr. Peter King, in collaboration with the Centre for Process Innovation (CPI) at Newcastle University. Spectroscopic ellipsometry and AFM topography measurements on oxide step etched Si were used to calibrate the growth rate of the ultra-thin interlayers, to number of reaction cycles (0.05 nm/cycle) using the thermal ALD process. The range of cycles/thicknesses that were studied for MIS contacts is annotated in Fig. 4.3-a. An ALD AlO_x deposition of at least 10 cycles is necessary to form a continuous layer, below which an island growth mechanism is seen.[74] For this study, AlOx interlayers were grown using 20, 30, and 40 ALD cycles, corresponding to nominal film thicknesses of 1, 1.5, and 2 nm. Our experiments operate just over the minimum cycle limit for a continuous layer. ALD and control samples were patterned using contact photolithography and lift-off, followed by post deposition annealing (see Chapter 3 and appendix for detailed methods). Microscopy work was commissioned to Durham University and was performed by Dr. Budhika Mendis. Fig. 4.3-b shows a high resolution transmission electron microscope (HRTEM) image of an annealed Ni/ (30 cycles) AlO_x /Si specimen in cross section. The measured thickness agrees as per the schematic shown in Fig. 4.3-a. Polycrystalline Ni domains emerge from multiple nucleation centres at the rough AlO_x interface. Energy filtered transmission electron microscopy was used to map the distribution of oxygen in the specimen. Bright pixels of the image shown in Fig. 4.3-c are from the K edge/ inner shell ionization energy level in elemental oxygen. Aside from the AlO_x interlayer, a considerable O signal is seen in the metal despite Ni having a high stability against oxidation under low temperature annealing conditions used. This suggests that the O signal is either noise or could possibly be due to mobile interstitial oxygen

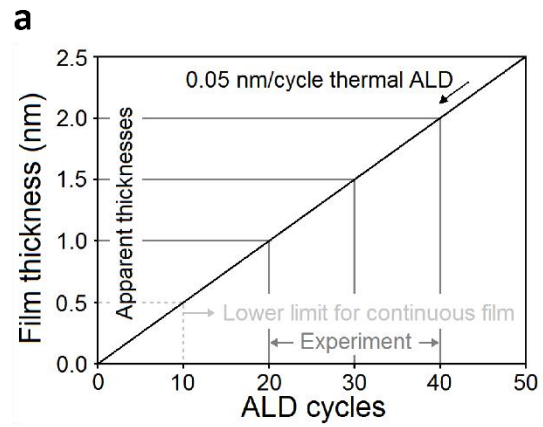

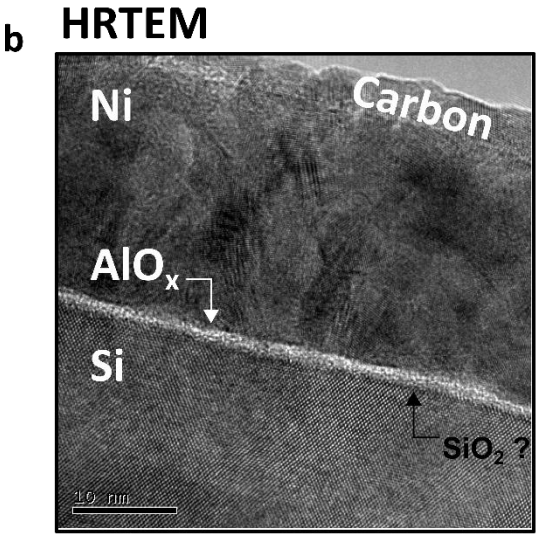

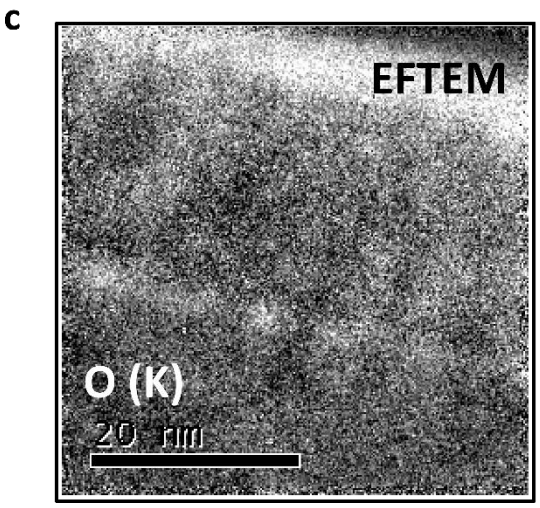

Figure 4.3: a. Schematic showing thermal ALD AlO_x deposition rate, extrapolated from ellipsometry on thicker layers. The range of ALD cycles used in the experiments, and the apparent resulting film thicknesses are sketched, based on data collected in AFM step etch surveys and ellipsometry studies done during ALD process development. **b.** High resolution transmission electron microscope (HRTEM) of the specimen in cross section, showing the contact interface Ni/ AlO_x/ Si after annealing at 200° C in high vacuum, for 5min. **c.** Energy filtered transmission electron microscope (EFTEM) image of a section of the contact, showing the Oxygen (K) edge filtered data, reconstructed to form an image. Bright pixels representing Oxygen are observed at the expected location of the ALD AlO_x interlayer as well as in regions within Ni layer, against the background noise.

between Ni grain boundaries and crystal defects. The ALD layers conformally coat the microroughened Si surface post RCA and last HF cleaning prior to metallization. Ni grain growth during annealing occurs via defect sites to minimize surface energy, leading to intersecting grain boundaries, creating additional defects in the metal. Annealing accelerates diffusion of oxygen from interfaces, which could explain the EFTEM result in Fig.4.3-c showing streak like patterns of O signal in the metal.

The electronic properties of these MIS contacts were studied using room temperature I-V measurements. Control specimens (n-, p-Si) prepared alongside the n- and p-Si specimens undergoing ALD, received identical pre-heat treatments (but 0 cycles) in the ALD reactor. ALD AlO_x interllayers (IL) – 20, 30, 40 cycles were used before the contact patterning step. The prepared controls and IL specimens were patterned using negative mask exposure

photolithography to form Ni planar contacts (70 nm thick). Representative I-V characteristics of n-Si and p-Si specimens are shown in Fig.4.4-(a, b) and Fig.4.4-(c, d) respectively on linear and semi-log scales. Compared to the control Ni/Si contacts (linear data rescaled in inset), inserting 20, 30 cycles of AlO_x improves conductivity by nearly two orders of magnitude, as seen in Fig.4.4-b and Fig.4.4-d. but the I-V characteristics retain rectifying characteristics.

Their apparent/ effective Schottky barrier heights (Φ_B^{eff}) are plotted together in Fig.4.4-e against ALD thickness in cycles. It appears that Φ_B^{eff} reduces for both n- and p-Si attaining minima at 30 cycles AlO_x (1.5 nm). The trend appears to saturate for higher thicknesses before conductivity eventually becomes worse for thicker AlO_x (> 5nm, not shown). (Lines drawn as guide to the eye and are not actual data.) The sum of Φ_B^{eff} for n- and p- Si is approximately the band gap of Si only for the controls (0 cycles) and not for the IL specimens. This result appears to violate the outcome expected from the MIS methodology where either n- or p-contact is supposed to develop a large Φ_B^{eff} in order that the improved contact (n- or p-) attains a lower Φ_B^{eff}, together summing to the semiconductor band gap energy.

AlO_x is a unique oxide because it creates a negatively charged interface with Si/ SiO_2 while other transition metal oxides and passivating materials such as SiN_x form positively charged interfaces respectively[75]. The negative charges are believed to originate from tetrahedrally co-ordinated Al atoms in Al_2O_3 that directly bond with the O atoms in the native/ interfacial SiO_2[76]. The net negative charge density at the Al_2O_3 or ALD AlO_x has been estimated by C-V techniques by observing shifts in the flat-band voltage and is of the order of 10^{12}-10^{13} cm^{-2} [75][76], comparable to the density of surface states on cleaned (100)Si. The enhanced electric field arising from the negative charges effectively passivates the surface and lowers the

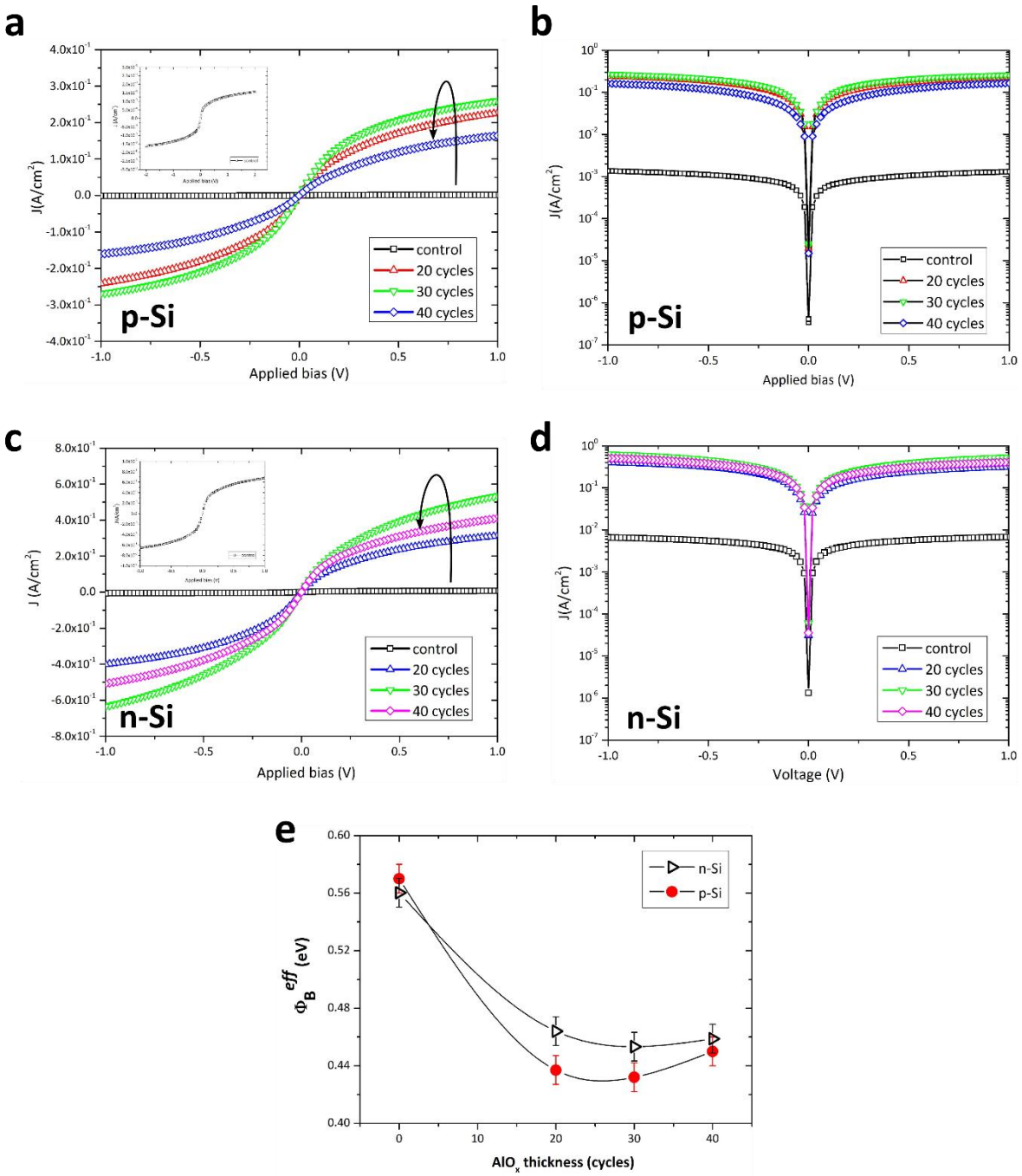

Figure 4.4: ALD AlO_x modulates conductivity on both n- and p-Si**. a. and b.** show representative I-V data, reported as current density on linear and semi-log scales respectively, for p-Si specimens. The total current increases with ALD cycles up to 30 cycles and then begins to slowly degrade with increasing ALD cycles. **c. and d.** show representative linear and semi-log I-V data reported as current density for n-Si specimens. Interestingly, conductivity also increases on n-Si, while maintaining the same optimal thickness of 30 cycles. **e.** The apparent/ effective Schottky barrier height extracted by fitting eqn. 4.2 for the complete sample series, including control specimens (0 cycles) plotted against ALD AlO_x thickness in cycles. The lines connecting the data are guides to the eye and are only drawn to show the nearly saturating trend of effective Schottky barrier height for intermediate ALD films thicknesses. Error bars represent the deviation in the extracted Schottky barrier heights for 5 contacts per sample (control and IL samples).

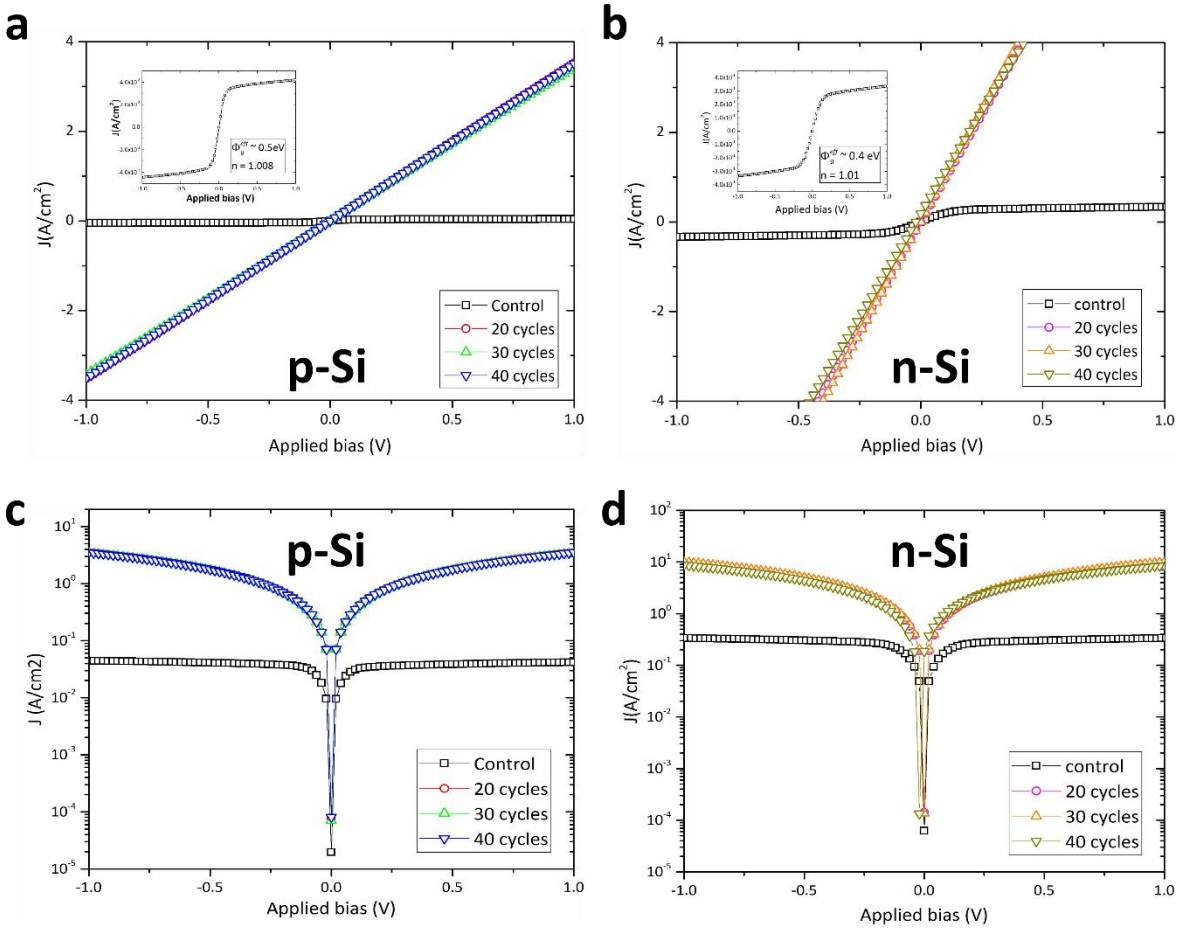

Figure 4.5: Annealing results in Ohmic contacts to both n- and p-Si**. a. and b.** show representative I-V data reported as current density on linear scale, to show Ohmic characteristics on p- and n- Si respectively. The total resistance is almost independent of the interlayer thickness used (1-2 nm). **c. and d.** show the same data on a semi-log scale to compare the magnitude of reverse current. The contacts to n-Si exhibit lower resistance than identically fabricated p-Si specimens. The overall conductivity of the MIS contacts increases by another order of magnitude, compared to the as-deposited contacts shown in Fig. 4.4-(b,d).

recombination velocity of carriers at the interface. Hence, Al_2O_3 is treated as a choice material in solar cell technology where long-lived photoexcited carriers and their separation at the contact interface is of importance. Field induced passivation is observed on both n- and p-Si and the resulting interface dipole causes accumulation on p-Si and inversion on n-Si.[77] Strong electric field at the interface requires charge build-up, but this effect will gradually reduce as the interlayer gets thicker. The same is true for Al_2O_3 grown over thin SiO_2 (~1.5 nm)/ Si because the negative charges are moved further away from the Si interface. The changes observed in the apparent Schottky barrier height can be qualitatively correlated to the build-up of negative charges, which ultimately must be limited by the available surface Oxygen sites at the native SiO_2/Si interface.

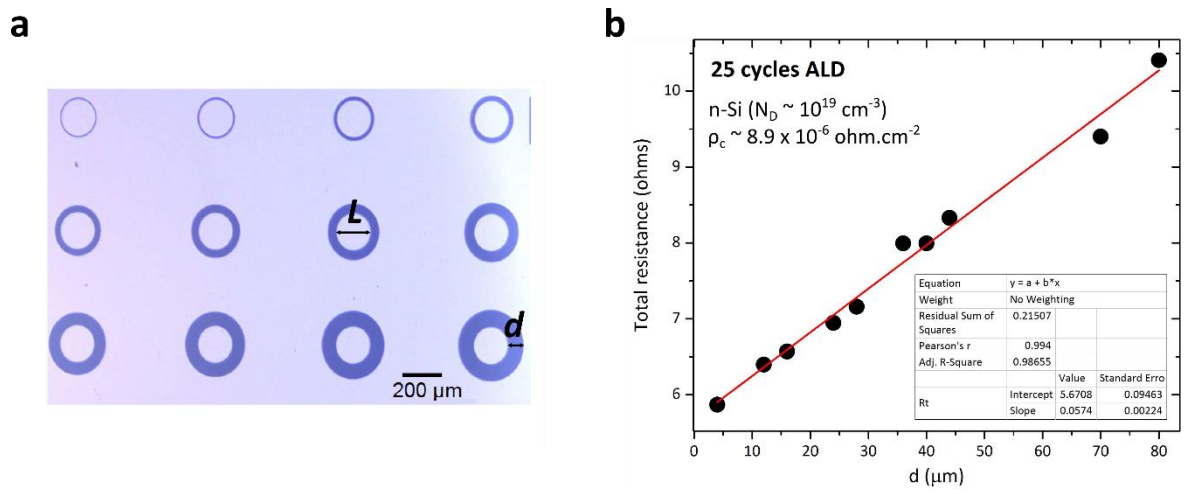

Figure 4.6: a. Optical microscope image of CTLM structures patterned on top of the ALD AlO_x layers with inner contact radius (L/2) ~ 100 µm. **b.** Total resistance of the annealed MIS Ohmic contacts to heavy doped n-Si (N_D ~10^{19} cm^{-3}) using 25 cycles of ALD AlO_x plotted against contact gap separation of the CTLM structures. These data have been corrected using correction factor C= (L/2*d*)*{ln(1+[2*d*/L]}). The y intercept = $2R_c$ gives the specific contact resistivity ρ_c ~ 8.9 × 10^{-6} ohm.cm^2

The specimens were annealed in high vacuum (~10^{-6} mbar) at 200º C for 5 min. Both sets of substrates produced similar results i.e. resistor like/ Ohmic I-V characteristics obtained on n- and p-Si, shown on a linear scale in Fig.4.5- (a, b) respectively. Their corresponding semi-log plots are shown in Fig.4.5- (c, d).

The Schottky barrier height of the control specimens remains close to the Si mid-gap energy (CNL) and rectifying characteristics are observed. Conductivity of the MIS specimens improved by another order of magnitude and the contacts became Ohmic after annealing. Circular transfer length method (CTLM) structures shown in Fig. 4.6-a were used to obtain the specific contact resistivity[42] ρ_c ~ 1.7 × 10^{-2} ohm.cm^2 on p-Si and ~5 × 10^{-3} ohm.cm^2 on

n-Si. The ALD Al_2O_3 (or AlO_x) interlayer has a large band offset to Si conduction/ valence bands which adds tunnelling resistance.

Heavy doped substrates can be used to improve performance. But as explained in ref. [39] the benefit of the MIS approach is lost with increased doping and this strategy becomes unfavourable compared to traditional silicided MS contacts using the same doping level. The experiments were repeated on heavy doped n-Si (N_D ~10^{19} cm^{-3}), which produced lowest specific contact resistivity (ρ_c) of only 8.9 × 10^{-6} ohm.cm^2 as shown for example in Fig. 4.6-b. These results could be improved by using heavy implant doped epi-layers to reduce current spreading under the contact.

AlO_x IL contacts were also fabricated using low doped n- and p-Ge substrates but these contacts did not become Ohmic and further MIS investigations were suspended. FLP in Ge is far more severe than in Si and inserting AlO_x interlayers with mismatched band offset to Ge did not provide the required effect.

Inferences:

Negatively charged ultra-thin AlO_x layers (< 2 nm) modulate the apparent Schottky barrier height when inserted between Ni contacts to n- and p-Si. This leads to increased reverse current but cannot be attributed to Fermi level de-pinning alone. Occupied acceptor states near the mid-gap energy are repelled by fixed negative charge density (10^{12}-10^{13} cm^{-2}) at the Al_2O_3/ SiO_2 interface, causing inversion (attracting holes) at the n-Si surface when sufficient reverse bias is applied. The resulting sharp band bending at the interface allows excess tunnelling currents to flow across thin interlayers (< 5 nm). The same field enhancement accumulates the p-Si surface, lowers the effective Schottky barrier. The Ni/Al_2O_3 workfunction has been previously reported to be 4.5 eV.[78] and the conduction/ valence band offsets of Al_2O_3 on Si have been measured by several works to be 2.5 eV and 3.2 eV respectively, as summarized in ref.[79]. Annealing causes oxygen to diffuse towards the Al_2O_3 side of the Al_2O_3/SiO_2 interface and increases the negative fixed charges[74]. This effect is most likely responsible for the observed increases in conductivity of annealed MIS specimens. Since the Al_2O_3 has valence band offset greater than its conduction band offset on Si, the height of the tunnel barrier at equilibrium favours electron transport close to the metal Fermi level. This could explain why the MIS contacts to low doped n-Si in Fig.4.5- b exhibit lower resistance than the contacts to p-Si in Fig.4.5- a.

4.4. The cost of de-pinning methods and severe FLP in Ge

By choosing AlO_x over positively charged interlayers (e.g. SiN_x) it is possible to achieve Ohmic contact to both n- and p-Si, owing to the enhanced electric field arising from its negatively charged interface to Si. This has an advantage over other strategies that de-pin the Fermi level towards the conduction band or valence band exclusively. However, the specific contact resistivity attained by this method is quite poor compared to the state of the art using MIS methodologies, adapted specifically to de-pin the Fermi level towards either majority carrier band. The lowest reported specific contact resistivity using ALD grown Al_2O_3, La_2O_3 interlayers on heavily doped Si is of the order of 10^{-8} ohm.cm^2.[73] whereas state of the art

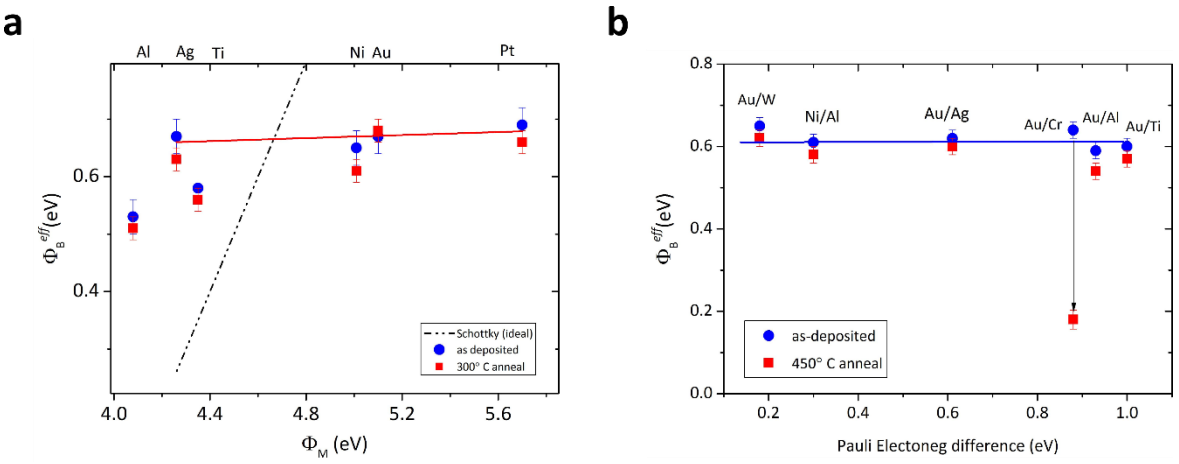

Figure 4.7: Severe FLP in Ge**. a.** Various metals and their effective Schottky barrier heights on low doped n-Ge for as deposited and annealed specimens. Error bars indicate variation in Φ_B^{eff} taken over 10 contacts on each metal. **B**. Various metal bilayer combinations (100/3 nm) used as contacts to Ge. Their Φ_B^{eff} are plotted against the Pauli electronegativity difference between the metal layers. The extracted values are compared for as-deposited specimens, and after annealing in high vacuum, for 5min. Only the Au/Cr combination shows a pronounced shift in the effective Schottky barrier height. The corresponding p-contacts for all the metal combinations used were Ohmic (Φ_B^{eff} ~ 0). Error bars show deviation in the extracted barrier height of 10 contacts for each metal/combination in 2 samples each.

metal-semiconductor (heavy doped) contacts have reached a record $\rho_c \sim 2 \times 10^{-9}$ ohm.cm^2 [80]. These techniques use doping levels in the semiconductor of the order of 10^{21} cm^{-3} or higher to achieve these results. When moderate doping is used, Fermi level de-pinning results in contacts to only either n-, or p-semiconductor becoming Ohmic, because the Fermi level position in the band gap at equilibrium is shifted towards one of the majority carrier bands (conduction / valence). Therefore, the new effective Schottky barrier heights for electrons and holes are approximately conserved to the band gap energy. This is the cost of Fermi level depinning techniques and special contact recipes need to be developed to cater to n- and p-regions in a device where a good Ohmic contact is required.

The situation is worse for Ge because native GeO_x dissolves readily in D.I. water, an essential process fluid. The lack of a stable surface oxide further degrades significant improvements that could come from annealing ALD AlO_x interlayer contacts. Hence, one is left to choose from special oxides that will have a suitable conduction or valence band offset to the semiconductor. While each of these materials may find suitable applications in various industrial sectors, the increased complexity in fabrication and the added cost to performance outweigh the benefits of adopting the MIS method for contact technology used in state of the art microelectronics. The FLP effect is known to be quite severe in Ge and this was confirmed by fabricating and testing

contacts using a range of different metals and metal bi-layer combinations, by examining the apparent Schottky barrier height formed on low doped (100)Ge ($N_D \sim 6.4 \times 10^{14}$ cm^{-3} and $N_A \sim 5.6 \times 10^{14}$ cm^{-3}) shown in Fig. 4.7-a. For metal contacts on n-Ge, $\Phi_B^{eff}$is on average ~ 0.6 eV i.e. the Fermi level is pinned close to CNL near the Ge valence band ($E_g \sim 0.67$ eV at room temperature). The corresponding contacts to p-Ge were all Ohmic ($\Phi_B^{eff} \sim 0$). Ge exhibits strong FLP, with the Schottky barrier height being fixed at the CNL, nearly insensitive to the metal's workfunction (Φ_M).

Locally enhanced electric field, arising from workfunction difference between high workfunction metal nanostructured interlayers and low workfunction capping metals have previously been shown to improve conductivity on low doped n- and p-Ge to form quasi Ohmic contacts[38]. Following our MIS work we explored potential metal bilayer combinations with a large electronegativity differences that could potentially improve contact to both n- and p-Ge. The contact to p-Ge is already Ohmic and we do not want to disturb this arrangement. Tunnelling contributions arising from enhanced surface electric fields could meet this requirement. Metal bi-layer film contacts (100/3 nm) were sequenced according to increasing Pauli electronegativity difference to test for shifts in the apparent Schottky barrier height. These data are plotted in Fig. 4.7-b for as-deposited specimens and after annealing in high vacuum at 350º C, 5min. The trend of severe FLP is present for all the as-deposited specimens, with $\Phi_B^{eff} \sim$ 0.6 eV. But interestingly, Au/Cr contacts showed a reduced $\Phi_B^{eff} \sim$ 0.2 eV after annealing and showed $10^3\times$ higher reverse current than the as-deposited contact, producing non-linear reverse I-V characteristics and quasi-Ohmic behaviour. The corresponding as-deposited and annealed contacts to p-Ge remained Ohmic and showed identical I-V characteristics.

XPS surveys were performed on the vacuum annealed Au/Cr n-Ge specimen by Dr. Anders Barlow, then at NEXUS, Newcastle University which revealed a considerable Ge signal at the surface of the annealed contacts. This might suggest alloying/ intermixing between Au and Ge, akin to the recipe for Ohmic contact to n-GaAs[81].

Inferences:

The MIS strategy using ALD AlO_x is unfavourable for Si and Ge state of the art microelectronic devices. Planar metal contacts on low doped Ge have the Fermi level pinned close to the Ge valence band, resulting in Ohmic p-contacts and Schottky n-contacts. The FLP effect is quite severe in Ge, in that no single metal could produce a significant change in the apparent Schottky

barrier height on low doped substrates. Metal bi-layer contacts were investigated. Most combinations also preserved strong FLP characteristics. However, thin Au/Cr shows a significant shift of ~0.4 eV in Φ_B^{eff}. The corresponding contact to p-Ge remained Ohmic, which indicates that the improvement in conductivity cannot be attributed to Fermi level de-pinning.

4.5. Conclusions

The ALD AlO_x or other MIS methods provide significant improvement to contact resistance only on low doped semiconductors while traditional MS contacts outperform MIS contacts when heavy doping is used. FLP is more severe in Ge than in Si. Several attempts were made to try and optimize different metal bilayer contacts by modifying the annealing and fabrication routine to achieve low contact resistance. However, the annealing method (in vacuum) proved to be quite unreliable in terms of repeatability. Optical microscope studies occasionally showed the formation of pits/ blots in the contact, which was probably caused as a reaction to the increased temperature in the heat treatment. Using a lower annealing temperature (< 300° C) did not produce any appreciable enhancement in conductivity. The Au/Cr bilayer combination needs to be studied carefully to understand the mechanism by which conductivity is increased, leading to the apparent 0.4 eV reduction in Schottky barrier height. The corresponding contact to p-Ge remained Ohmic, indicating that once again, the improvement in conductivity is due to some form of enhanced tunnelling effect, rather than Fermi level shifting within the band-gap.

“The practical success of the idea, regardless of its inherent advantages, depends on the attitude of people. If it suits the time, it is accepted.”

-Nikola Tesla

Chapter 5:

Ohmic Hybrid contacts - 1D injection in semiconductors

Abstract

This chapter explores a new type of contact geometry that exploits hot carriers generated in semiconductor nano-crystalline regions, embedded in the contact metal – A hybrid structure between thin metal films and semiconductor nanocrystals is observed. Semiconductor nanocrystals are embedded in a high workfunction contact metal film with a low workfunction adhesion/interface metal layer. The semiconductor nanocrystals have abrupt heteroepitaxial interfaces with both metals, which forms geometric triple points. This results in grid like features in the contact. Hot electron tunnelling current is observed with one-dimensional character over entire patterned areas. The phenomenon is demonstrated here for n- and p- Ge with Au metal contact and Cr adhesion layer, but will have applicability to other material systems.

5.1. Introduction

Realizing Ohmic contact on semiconductors with strong FLP using a planar metallization is quite challenging. FLP is less severe in Si than in Ge but a planar Al metallization forms Ohmic contact to lightly doped p-Si and Schottky/ rectifying contacts to n-Si[82]. The conventional approach for improving contact resistance is to use higher doping in the semiconductor. Heavy doped spacer layers (e.g. delta doping) are often introduced below the contact layer to enhance tunnelling and mitigate the effect of the Schottky barrier as seen on low doped substrates. This doped spacer layer strategy has been adapted by several research groups to improve contact performance. Particularly for GaAs, Ohmic contact recipes for low doped n-GaAs have been discovered[83][84]. However, Ohmic contact to p- GaAs is quite difficult to obtain and also usually requires heavy doping to improve contact[85]. In Ge, the situation is more complicated. Moderate doping does not guarantee good Ohmic contact.

Alloyed contacts to semiconductors suffer from a problem known as ‘spiking’, which as the name suggests involves the formation of metal protrusions into deeper layers of the semiconductor below. This phenomenon can degrade the properties of junctions buried below

the contact[86]. Annealing duration and temperature become critical parameters in ensuring that a stable contact is formed. Reliability of contacts in devices operating at higher temperatures or large power densities could be compromised, as spiking may still occur during operation due to thermal and/or electromigration[87]. Diffusion barrier layers can be introduced to mitigate spiking effects[88], however only at the expense of increased contact resistance due to its inclusion in the contact stack. Annealing duration for such processes typically are of the order of hours. Diffusion mechanisms dominate the outcome of the process in terms of material structure and integrity.

From the contact engineering strategies for Ge covered in Chapter 1 (section ***1.2***), direct sputtering of TiN onto Ge, followed by annealing results in unpinning i.e. Ohmic contact is formed on n-Ge and is accompanied with Schottky contact on p-Ge for the same metallization. Refractory metal nitrides have a good thermal stability so this material may be suitable for high temperature applications. TEM work on these contacts have shown a nominally flat interface, without spiking[89]. The FLP problem is now reversed, with high contact resistance on p-Ge. Au is not commonly used in foundries because it is known to degrade carrier lifetime in Si. Furthermore, Au has previously been identified as an amphoteric dopant in Si[90]. Au alloys with other metals (and semiconductors e.g. Au/Ge alloy on GaAs) and is frequently applied in contact technology.

In this chapter, short duration and low temperature rapid thermal annealing (RTA) is explored for processing Au/Cr bilayer films on Ge. Rapid annealing (< 20 s) is used to exploit film de-wetting and eutectic reactions at the contact metal/ semiconductor interface. This short annealing schedule prevents the formation of complex diffused alloys. Liquid interfaces formed during annealing underpin epitaxial growth in the crystallized Au(Cr)/Ge thin film system. A thermally self-assembled hybrid structure was discovered during process development, which provides Ohmic contact on both n- and p-Ge. This material provides remarkable improvements in conductivity, even using low doped Ge ($N_D \sim 6.4 \times 10^{14}$ cm^{-3}). Hybrid structures described here are block-like Ge nanocrystals embedded in crystalline Au/Cr films. The results described next are anticipated to have wider applicability to many materials, as the hybrid geometry and scale are responsible for the observed electronic effects. The following section outlines the material properties of the Au/Ge and Au/Cr/Ge material systems upon annealing. TEM microscopy surveys provide insight into material formation. HRTEM (data shown in Figs. 5.5 – 5.7) and HRSEM (data in Figs. 5.3, Fig. 5.8 and Fig. 5.9) experiments were done by Dr. Karl Dawson at Liverpool University.

5.2. Results I- Material characterization

5.2.1. Annealing Au thin films on Ge results in cluster formation and heteroepitaxy

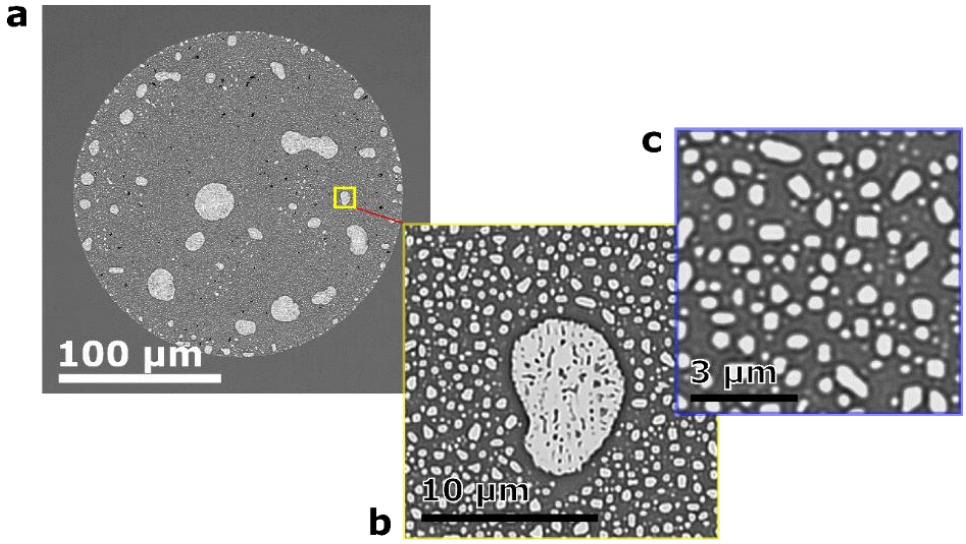

Figure 5.1: SEM collage of Au (100 nm)/ Ge. annealed in vacuum at 400° C, for 5min. Plan view of a circular patterned area with scale bars for **a.** 100 µm **b.** 10 µm and **c.** 3 µm showing higher magnification of clusters formed by thermal re-assembly. Isolated Au clusters and platelets are observed on Ge.

Deposition of thin metal layers by evaporation is not as well controlled as deposition by sputtering. The substrate temperature, surface energy, deposition rate, target yield, chamber ambient, and pressure all influence the morphology of the deposited films.

Since at room temperature Au has a higher surface energy (1.33 J/m^2) than Ge (1 J/m^2)[91], initial stages of growth (first few monolayers) pertain to island formations at nucleation sites on the substrate. Islands eventually coalesce into a continuous film, as more material arrives onto the substrate[92]. As-deposited metal films are typically polycrystalline i.e. they have no preferred crystal orientation.

Thin Au films were deposited onto chemically cleaned, patterned Ge using e-beam evaporation in high vacuum conditions (1.5×10^{-6} mbar). The film thickness and deposition rate were monitored using a quartz crystal balance. A nominal deposition rate (0.1 nm/s) was used to form 100 nm films. Contacts were fabricated using contact photolithography, as described in Chapter 3. The specimens were later annealed above the Au/Ge eutectic temperature ($T_{Au/Ge}$

~360° C) at 400° C for 5min in high vacuum (1.5×10^{-6} mbar). The annealing schedule is ended abruptly (heater off), following which the annealing stage is cooled via its metal heat sinks for 10min before evacuating the chamber. Scanning electron microscopy (SEM) revealed cluster formation, which is typical in annealed Au films on dielectric substrates[93]. Fig. 5.1-(a, b) shows the extent of aggregation in various regions of a circular patterned contact (radius = 100 µm). The bright regions are isolated, self- assembled Au islands on the Ge substrate (with dark background), confirmed in Energy-dispersive X-Ray (EDX) spectroscopy. Higher magnification images reveal cube and cuboid shaped clusters, amidst a distribution of polyhedron structures in Fig. 5.1-c. Clusters are formed because Au has a higher surface energy compared to Ge, which leads to the formation of ball-like structures of Au, surrounded by Ge rich layers post eutectic mixing[94]. Surface energy is minimized by exposing the crystal facet which has the lowest surface energy. Usually this is the {111} plane in f.c.c. metals, as it has the highest number of bonds in plane (close packed). This crystallization is prevalent in most f.c.c. metals upon annealing. However, in the Au/Ge system, a heteroepitaxial matching is observed, which induces an alternative preferred Au orientation i.e. (110)Au. Annealing at temperatures above $T_{Au/Ge}$ has recently been shown to result in mixed Au $_{f.c.c.}$ and Au $_{h.c.p.}$ island structures on Ge[95]. The proportion of f.c.c. to h.c.p. stacking depends on the cooling rate. More f.c.c. phases are prevalent for a faster cooling rate, while the h.c.p. structure is exotic and requires special conditions and slow cooling to form. The clusters seen in Fig. 5.1 appear consistent with the fast cooling case. Au and Ge form a liquid interface, then rearrange according to the orientation relationship {110}//(100). This arrangement leads the edges of the Au clusters to align with the [110] directions of Ge. Significant surface energy mismatch forces cluster formation with high curvature of de-wetting, surrounded by Ge rich crimp layers (the darker halos apparent around Au clusters in Fig. 5.1-c).

The separation between for observable islands is on average 150 nm (±50 nm). Two probe I-V measurements taken on the patterned areas revealed rectifying behaviour on n- Ge and Ohmic contact to p-Ge, consistent with FLP in Ge. These findings suggest that any diffusion or alloying of Au into the Ge substrate or vice versa, which might have occurred during annealing does not alter conduction properties significantly. The characteristics of FLP are preserved in the limit of such large Au clusters on Ge, unlike annealed Au/ n- Si contacts, which become Ohmic after annealing at 400° C[96]. The larger island formed in Fig. 5.1-b is like a Au platelet formed on the Ge substrate. Some emergent Ge features are apparent within this island.

Inferences:

Annealing 100 nm Au on Ge above $T_{Au/Ge}$ forms a discontinuous film. Au clusters are dynamically constructed from the eutectic liquid interface with the Ge substrate, and are surrounded by pure Ge crimp layers. Thin film de-wetting prevents the formation of extended planar Au geometries, aside from regions where self-organization permits coalescence. Characteristics of FLP were seen retained on n- and p-Ge.

5.2.2. Cr adhesion template for heteroepitaxial Au crystallization over extended areas

Adhesion layers like Cr or Ti are commonly incorporated into Au contacts in several applications.[97] The thickness of these layers can vary depending on the application, and is typically 2-5 nm on SiO_2. In this case, Cr is preferred over Ti as the adhesive material because Cr is known to form an epitaxial alloy with Au[98]. Additionally, the (110)Au and (100)Ge lattice planes are mismatched by < 2%. A tight match between Au, Cr and Ge lattice planes can arise, as shown schematically in Fig 5.2-a. This allows controlled heteroepitaxy between Au and Ge.

Cr has surface energy (~3 J/m^2)[99], higher than both Au and Ge. Due to its high affinity to oxygen it readily forms nucleation centres on the substrate and assists film formation during subsequent stages of Au deposition. In the limit of low Cr coverage (< 1.5 nm), initial Au crystallite size and critical thickness for coalescence is not significantly affected, because the density of Cr nucleation centres is sparse. While for higher density of Cr nucleation centres, the growth of flat Au crystallites forming continuous film-like elements is onset at considerably smaller values (2-4 monolayers Au)[100].

A nominal thickness of 3nm Cr was chosen to study this epitaxial orientation relationship. 100/3 nm thick Au/ Cr contacts were prepared using the standard method described in Chapter 3, except that for the Cr layer, the deposition rate had to be lowered to 0.03 nm/s to try to maximize uniformity of the layer. Prior to deposition, the Cr target was conditioned in high vacuum using a high beam current. The chamber was gettered to reduce oxygen contamination before patterned specimens were exposed to the Cr vapours. Room temperature I-V measurements of as-deposited 100/3 nm Au/Cr contacts to low doped n- (N_D ~6.4 × 10^{14} cm^{-3}) and p-Ge (N_A ~5.6 × 10^{14} cm^{-3}) specimens confirmed that FLP was unaffected. The electron Schottky barrier height (ϕ_{Bn}^0) was estimated ~ 0.6 eV from high temperature I-V measurements. Continuous metal film patterns were observed in SEM. Ideally, the Ge

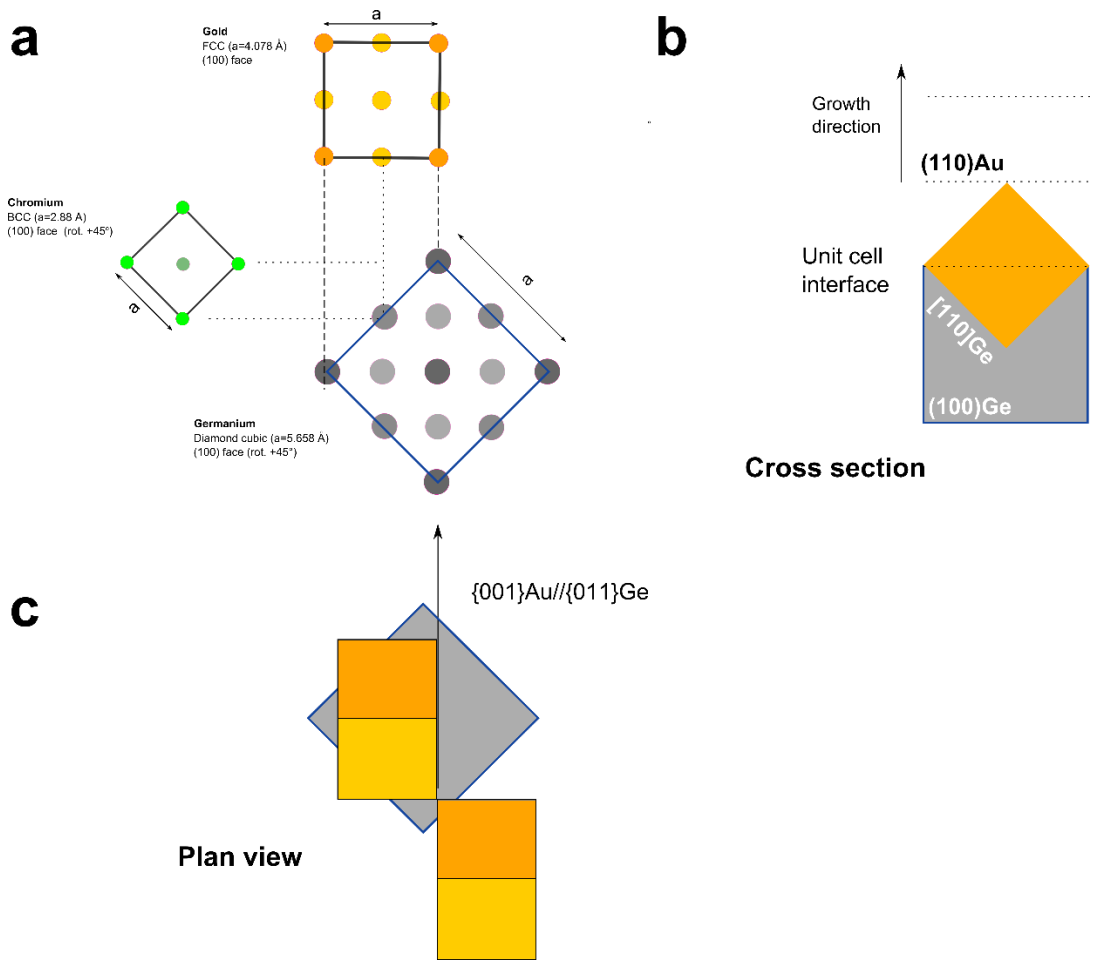

Figure 5.2: **a.** Schematic 2D projection of cubic (100)Au, (100)Cr and (100)Ge cubic faces, showing a possible epitaxial arrangement. **b.** Schematic showing preferred (110) Au growth on Ge, because {110}Au= 0.5*a(Ge)=2.884 Å. **c.** Orientation relationship between Au and Ge is observed because {220}Ge = {100}Au= 4 Å.

substrates should be heated *in-vacuo*, prior to deposition, to out-gas any solvent or water residues. The surface diffusion of Cr on preheated substrates would also be promoted during deposition, improving uniformity of the nucleation sites. Cr is known to enter the Au lattice by substitution at temperatures above 400 K, forming an epitaxial alloy[98]. Thus, an epitaxial (110)Au interface could be seeded during deposition. Unfortunately, our e-beam evaporator is not equipped with a working substrate heater module, so seeding of the epitaxial layers was attempted post deposition, by annealing. The method of annealing was changed to rapid thermal annealing (RTA) to exploit faster convection cooling and aid the crystallization process by using purge gas flows. The specimens were rapid annealed in ultra-pure N_2 and then cooled in N_2 purge flows for 10min, before venting the chamber. When the peak annealing temperature does not exceed $T_{Au/Ge}$ by a large margin (< 420° C), the Au film continuity is semi-preserved and Ge islands emerge in the Au matrix, shown in Fig. 5.3.

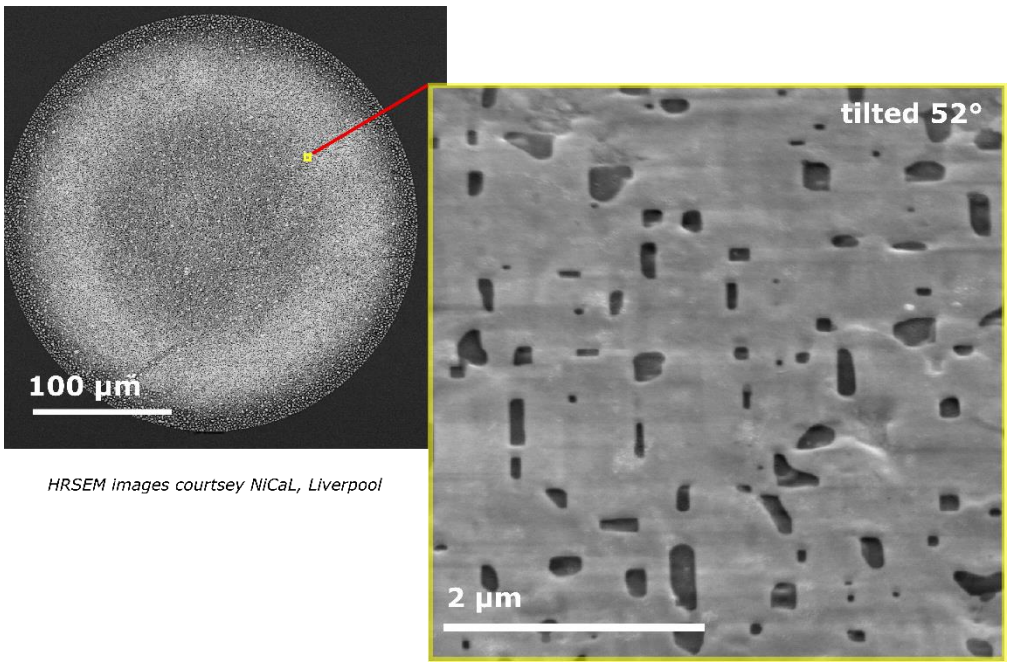

HRSEM images courtsey NiCaL, Liverpool

Figure 5.3: HRSEM of a circular contact (*d* = 300 µm) 100/3 nm Au/Cr on Ge after RTA, revealing the emergence of crystalline Ge nano-islands in an Au matrix. Inset shows orthogonally arranged Ge islands under higher magnification, at a tilted viewing angle.

Observation of orthogonally arranged interfaces between Ge islands in the Au film show that the Au has predominantly crystallized in its (110) orientation and is heteroepitaxially registered to the (100)Ge substrate over a large area. Thus, the Ge islands will be aligned to the [110] directions of the substrate, as per the schema drawn in Fig. 5.2. This can be confirmed by examining the wafer flat direction <110>, from which the specimens were cleaved. This configuration dictates that Ge islands must register as Au{001}//Ge[110] because the Au film grows in the (110) direction. Multiple epitaxial interfaces discussed so far result in the general orientation relationship {110}Au//{001}Ge. This situation in Fig. 5.3. is visually complementary to the case shown in Fig. 5.1 where self-assembled Au islands were observed on the Ge substrate. The key difference here being the clusters in this case are epitaxial semiconductor nanocrystals, and the medium is a crystallized Au/Cr film. The crystal orientation of the annealed Au/Cr film was inspected using X-ray diffraction (XRD) θ-2θ measurement shown in Fig. 5.4. An intense, well defined peak is observed at 2θ = 65°, which confirms (110) oriented Au. Thus, by using a 3 nm Cr adhesion layer and low temperature rapid annealing, an extended heteroepitaxial Au/Cr/Ge hybrid film is observed. Previous demonstrations of heteroepitaxial (110) Au films have been limited to commensurate growth only on (110) oriented substrates[101].

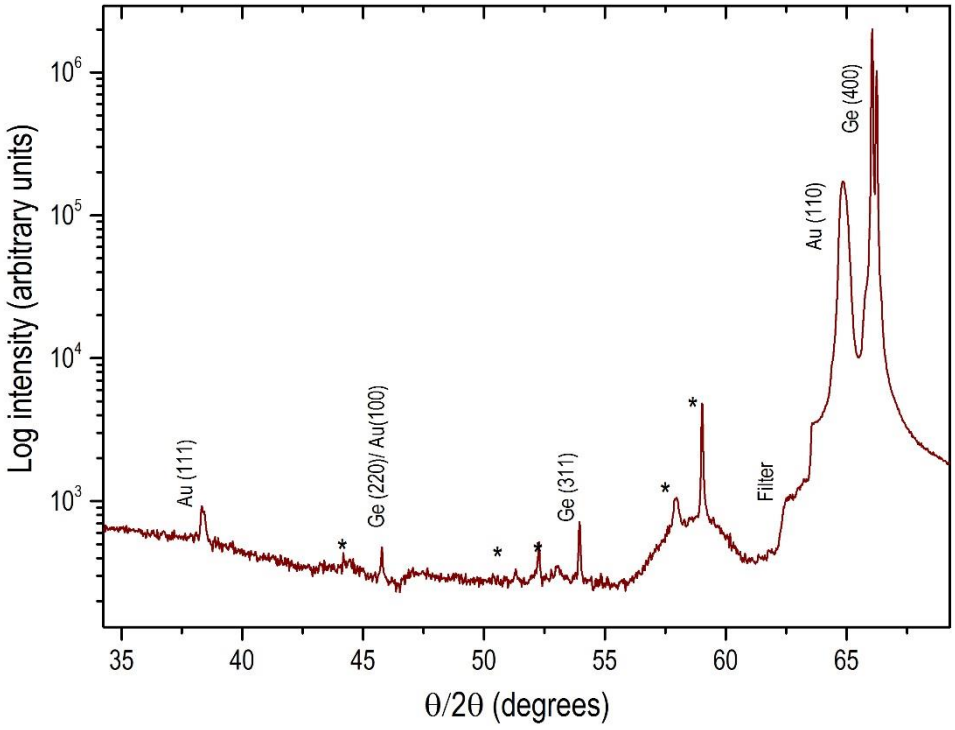

Figure 5.4: XRD θ/2θ measurement of 100/3 nm Au/Cr after rapid thermal annealing. Intense peak at 65° indicates predominantly (110) Au crystallization is observed. Some peaks remain unidentified (marked by*).

These promising results justified cross-sectional studies of the material. HRTEM surveys were commissioned to Liverpool University to gain insight on the hybrid film's formation. Multiple epitaxial interfaces were observed, in excellent agreement with the schema presented in Fig. 5.2. Received TEM data were processed using free Gatan Digital Micrograph software. Fig. 5.5-a shows on the left, a representative lamella/ lift out section taken from the annealed contact, aligned to the plan view HRSEM of the region from which it was excavated. This lamella was inspected using HRTEM, shown on the right.

Three main features are annotated in the lamella as regions of interest (ROI), in Fig. 5.5-b. These are, (1) Regions that showed inward transport of Au into the Ge substrate, (2) Regions where the Au is heteroepitaxial on Ge, but not transported across the Cr interlayer, thus leaving the original interface intact, and (3) Ge island formation in the Au film, indicating outward Ge transport. Fig. 5.5-c shows HRTEM image of ROI 1. A dark, blurred region above the substrate is observed, highlighted using dashed lines. Its position and extent approximately match the description of the original Cr layer. Au appears to have diffused through the Cr and registered with the Ge substrate. The extent of inward Au migration is annotated as a guide, to the mark the second interface. Atomically sharp edges are observed, reminiscent of Au assisted etching of Ge[102][103].

To study crystallinity of Au in the growth direction, Fast Fourier transform (FFT) diffraction patterns of the Au and Ge in HRTEM were obtained (shown as insets), and the observed lattice plane spacing (d-spacing) was measured. Diffraction spots (FFT) from TEM image were chosen in the normal direction of the lattice image. These points were masked and its corresponding image was reconstructed using inverse FFT (IFFT), presented alongside to compare with the HRTEM image. Histograms used to estimate the average lattice spacing from both IFFT images are shown in Fig. 5.5-d. The interplanar spacing correspond to d-spacing of {001}Au (4.08 Å) and {011}Ge (2 Å). The close lattice match promotes the orientation relationship {001}Au //{011}Ge we observe. Satellite diffraction spots and higher frequency patterns were observed in the Au FFT, corresponding to smaller real lattice spacings which suggests there are crystalline impurities in the lattice. These are most likely original Cr substitutions in Au, forming epitaxial Au/Cr alloys or Ge impurities that remained unseparated. Fig. 5.6-a. shows the HRTEM of ROI 2, a continuous region of Au with the original Cr interlayer interface preserved. Lattice plane registry {100}//{110} is maintained, consistent with ROI 1. The HRTEM image FFT and the reconstructed IFFT images are shown alongside the HRTEM image. The Au lattice spacing in the growth direction has been measured (d_{110}= 5.68 Å) from the IFFT histogram shown in Fig. 5.6-b, consistent with Fig. 5.2-b.

The Ge island/ crystallite in ROI 3 forms triple interfaces at the left and right edges in view. It is embedded in the (110)Au film, supported by an intact Cr interlayer, as shown in. Fig. 5.7-a-c. The Ge island edges retain remnants of the separation process in which Ge is selectively segregated out of molten Au[94], shown in Fig. 5.7-b. Crystal twinning is observed along the {111} Ge plane in the middle of the Ge island cross section, shown in Fig. 5.7-c. This feature was observed in every Ge island which was surveyed from the lamella. Therefore, it is unlikely that the Ge islands are formed by upward Ge transport across the Cr layer i.e. from the substrate volume beneath observed sites of island formation. If this were the case, there would be visible voids or disorder in the Ge crystal structure, which is not observed.

Both Ge island and Ge substrate's FFT showed no break in symmetry and produced well defined, bright spot patterns as expected in Ge. It appears that the liquid Ge is precipitated laterally out of the Au and segregated into islands during cooling. Ge islands are observed to be epitaxially registered in the Au matrix, twinning along the {111} plane, which has the highest co-ordination number in the diamond-cubic type lattice. Fig. 5.7-d. shows HRTEM of the right edge of the Ge island/ Au film interface. The FFT pattern is quite noisy on the Au side, probably due to incomplete Ge separation and/or Cr substitutional impurities

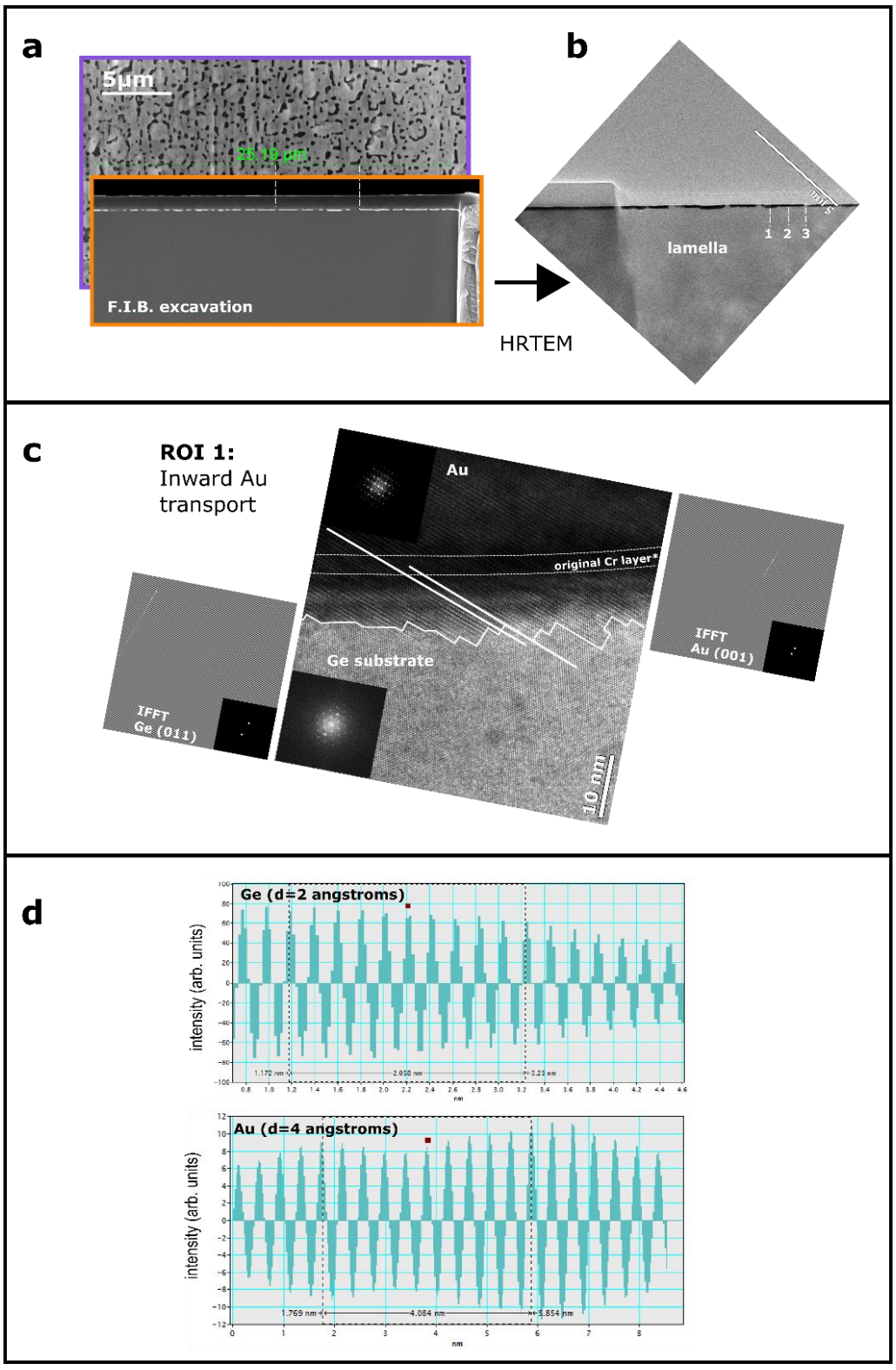

Figure 5.5: TEM survey of 100/3 nm Au/Cr on Ge after RTA. **a.** Plan view of the 100/3 nm Au/Cr annealed film, superimposed by the FIB excavation cross section. **b.** TEM lamella extracted for inspection with annotated (1,2,3) regions of interest (ROI). **c.** HRTEM of ROI 1 showing inward transport of Au, heteroepitaxially registered to Ge. Annotated lines are drawn as a guide to the eye. Reconstructed IFFT images using masked diffraction spots (inset FFT) from the original image are presented alongside. **d.** Average lattice spacing obtained from histograms of the IFFT images are in good agreement with expected Au and Ge parameters.

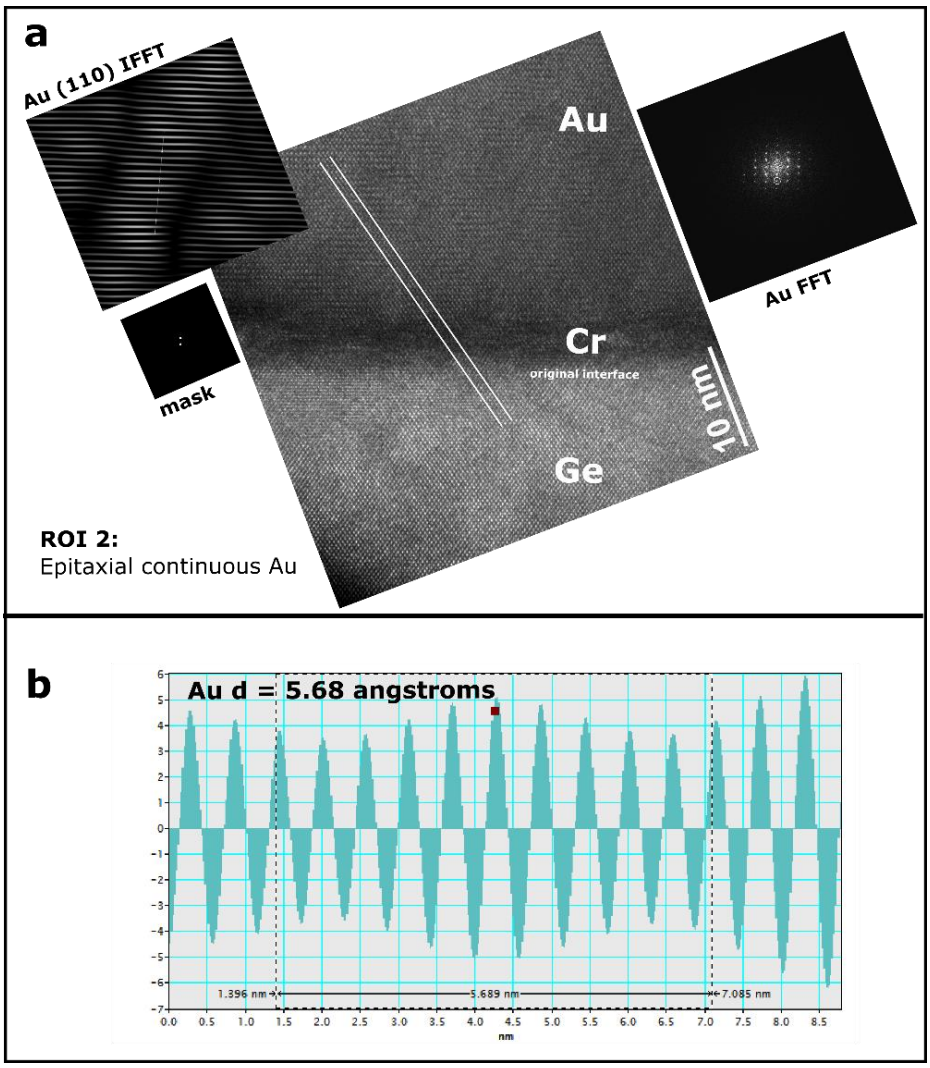

Figure 5.6: a. HRTEM of ROI 2, as annotated in Fig. 5.5-a. **b**. Semi-continuous heteroepitaxial (011)Au is formed over the original interface Cr. The lattice plane registry can be seen across the interface, annotated using white lines. Au diffraction pattern (right), reconstructed masked IFFT image (left) **b.** Histogram obtained from reconstructed Au IFFT image shows the lattice spacing of Au in the growth direction, indicating predominantly (110)Au, following schematics shown in Fig. 5.2.

in the lattice. However, the orientation relationships are preserved, including the triple interfaces. It is noted that the segregated Ge nanocrystal dimensions are comparable to the initial film thickness. For thicker Au films, e.g. 300 nm Au has average crystallite size > 300 nm (shown later in Results II). While the orientation relationships appear to remain consistent from SEM inspections, the nanocrystal size is on average larger, implying Au mass thickness plays a role in the way the eutectic reaction proceeds. Thick Au specimens were not investigated in HRSEM and HRTEM because they do not exhibit special electrical properties, discussed later in further detail. The focus of this work is on the unique properties of thin hybrid films and not the chemistry of eutectic reactions, but a simplified model can be inferred from the microscopy studies shown so far.

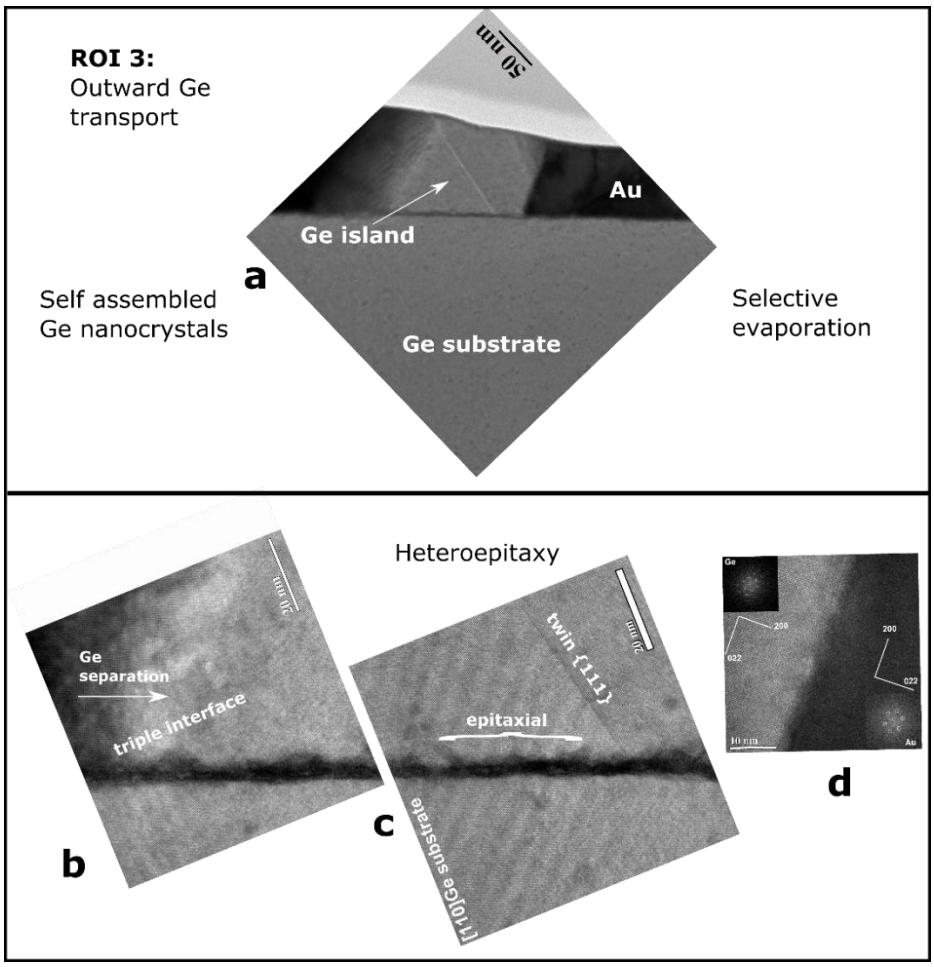

Figure 5.7: **a.** HRTEM of ROI 3 showing a Ge island embedded in the Au film, sharing interfaces with the Cr interlayer and Au film. **b.** Detailed view of the left island edge shows (< nm) sharp triple interface between Au, Cr and Ge. Remnants of the Ge separation process can be seen across the ordered interface. **c.** The Ge island is twinned about the {111} plane. Heteroepitaxial orientation relationship to the substrate is preserved across the interlayer. **d.** The right interface between Ge/Au shows similar crystalline order to its twin on the left. FFT insets are shown for Ge and Au. The Au FFT is quite noisy, possibly due to Ge incorporated in Au, which remained unseparated at the end of short duration annealing schedule.

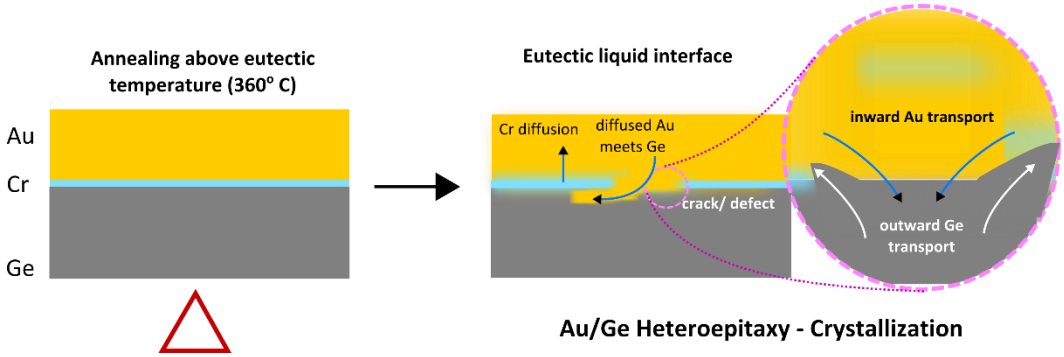

Figure 5.8: Schematic illustrating the likely steps involved in film reorganization

The film reorganization mechanism due to annealing most likely includes the following steps, illustrated schematically in Fig. 5.8:

1. Annealing initiates surface self-diffusion in the thin film (higher at patterned edges, corners). Au diffuses through the thin Cr layer across widespread regions in the film to meet the Ge surface. (Fig.5.5)

2. Ge melts and forms a eutectic interface with Au at ~ $T_{Au/Ge}$ (360° C). The {011}Ge and {001}Au planes form atomic registry. (Fig.5.5)

3. Inward and outward transport of Au and Ge respectively occurs through defects in the Cr layer and at liquid Au/Ge interfaces. Ge is incorporated into hot Au, followed by segregation by selective evaporation process[103]. In this case, Ge islands form within the Au matrix. (Fig.5.7).

4. F.C.C. Au grows in the preferred (110) direction on Ge, in part due to seeding from the Cr layer. The {100} crystallization front propagates through the material, twinning in certain areas. In the cooling phase, the molten hybrid film is crystallized, resulting in the observed film pattern of Ge islands. (Fig.5.6)

If the annealing temperature exceeds $T_{Au/Ge}$ significantly (> 450° C) or, is allowed to continue for too long (~1 min, even at lower temperatures), the film becomes discontinuous due to hole formation. Hole/ void formation in patterned films is primarily driven by surface self-diffusion, which is a highly temperature dependent phenomenon[104]. The dynamics of the eutectic intermixing and nanocrystal separation are complex in nature. If the optimum annealing temperature (360-420 °C) is exceeded, the film breaks apart by surface self-diffusion driven film retraction mechanisms. Fig. 5.9-a shows the plan view of two pairs of circularly patterned 100/3 nm Au/Cr contacts on Ge after rapid annealing. Void formations grow and overlap with neighbouring voids to form even bigger holes in the film, as seen in Fig. 5.9-b. Voids readily form around the peripheral regions of contacts. This is due to high radius of curvature in the thin film at the lithographically patterned edge. Early stages of this process were also seen in Fig. 5.3. Smaller plate like Au formations appear within the holes in Fig. 5.9-c. Ripple patterns can be observed in these islands, preserving 'snapshots' of the edge retraction- precursors to hole formation. In the semi-continuous regions of the film (Fig. 5.9-d) the Ge island formation and heteroepitaxy is retained. When the annealing duration is kept short (5s) but the annealing temperature just reaches 450 °C, film de-wetting dominates, forming a patch network of Au

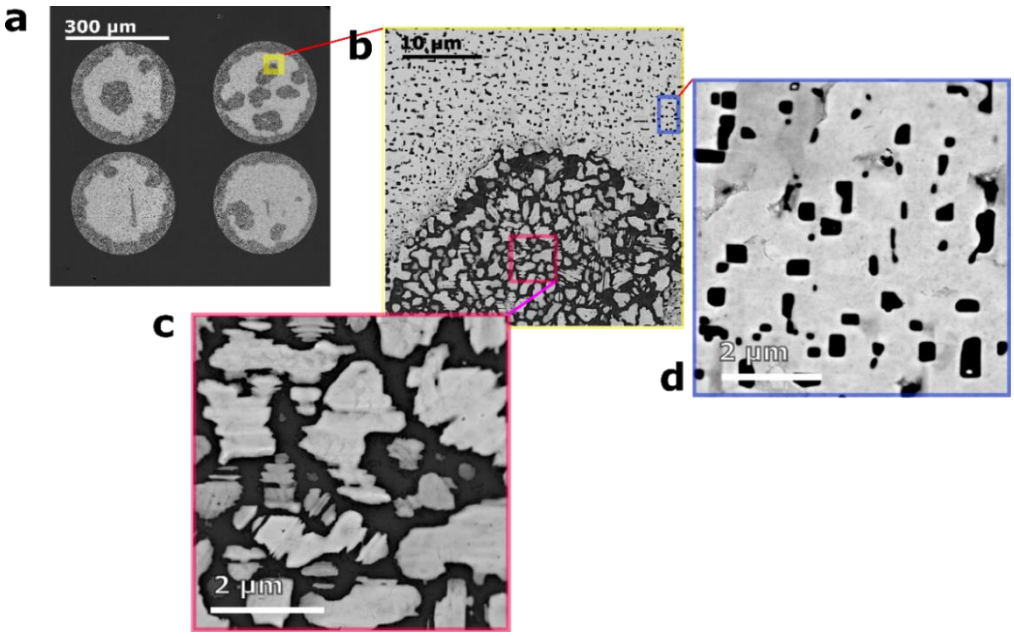

Figure 5.9: SEM collage of 100/3 nm Au/Cr film, annealed above critical temperature results in void formation. Plate island formations appear within holes. Insets show close-up views of the highlighted regions. The orthogonal arrangement of Ge islands in the film is preserved.

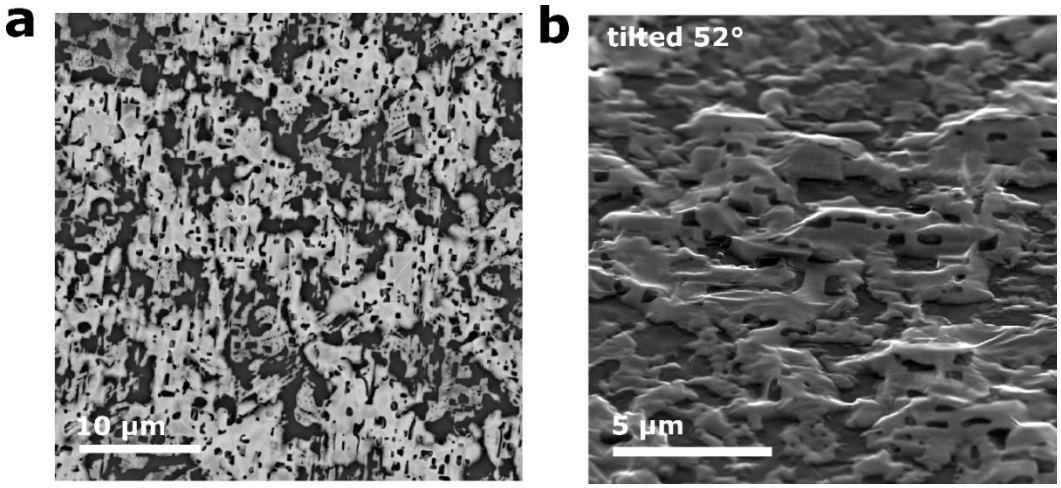

Figure 5.10: HRSEM of flash annealed 100/3 nm Au/Cr. **a.** Plan view showing extent of coverage. **b.** Tilted view showing the features and undulation in the film.

platelets with embedded Ge islands. Fig. 5.10-a shows the plan view of the film in HRSEM. In contrast to Fig. 5.3, the film is no longer planar, as seen from the tilted view in Fig. 5.10-b. The process needs to be carefully regulated to obtain desired outcomes.

The optimal process temperature for obtaining unbroken hybrid films is lies in the vicinity of $T_{Au/Ge}$ and is quite close to the low temperature sensing limit of the pyrometer ~ 340° C on the JETFIRST 200 benchtop RTA system. There is additional uncertainty about the actual temperature of the samples lying on the carrier wafer, at thin film contact interfaces, given that the annealing routines used were already kept short on the order of a few seconds and the process temperature is never steady within this duration.

5.3. Summary I

A simple method of fabricating extended heteroepitaxial (110) Au/Ge hybrid structures on Ge has been discovered by rapid thermal annealing thin Au/Cr thin films above the Au/Ge eutectic temperature for a short duration, on the order of seconds. The process is highly sensitive to the annealing temperature and annealing duration, and needs to be carefully controlled to exploit fully the benefits offered by this unique material system. HRTEM and HRSEM surveys reveal nanoscale features within the hybrid film- composed of epitaxial Ge nanocrystals, surrounded by metals. Crystallite/ island size is correlated to the initial film thickness and annealing duration. This will play a crucial role in the electronic properties offered by the material, discussed next.

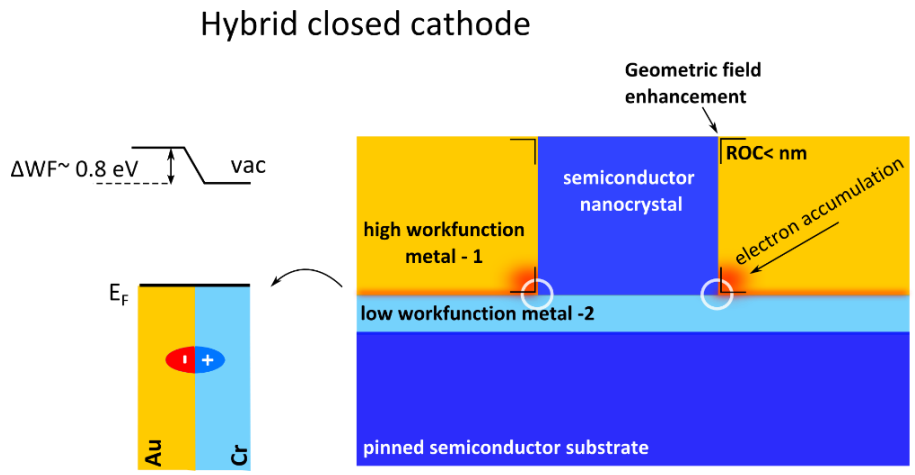

Figure 5.11*:* General schematic of a hybrid film element, forming a closed cathode geometry. Electron accumulation is expected in regions with a sharp radius of curvature (ROC) due to the interface dipole between metals e.g. Au/Cr - workfunction (WF) dipole sketched on the left. These regions form geometric 'triple points' (encircled)

Hybrid contacts constitute a new class of material due to their novel electrical properties. The materials structure of hybrid films on Ge have been described in the previous section. HRTEM revealed the formation of epitaxial Ge nanocrystals embedded in a thin (110)Au/Cr bilayer matrix. These Ge nanocrystals are isolated from the substrate by an intact Cr interlayer and registered to the [110] directions of the Ge substrate. Ge nanocrystals are encapsulated by metals on five sides to form a closed geometry. This physical description is complementary to metal nano-clusters forming on the substrate, resulting from annealing, or during the growth of very thin (<1 nm) metal films[105]. A simplified/ general cross section schematic is shown in Fig. 5.11. Triple interfaces (encircled) are formed between the Ge nanocrystal edges, the Cr interlayer and the surrounding Au film. These regions are electric field hot-spots because of geometric field enhancement effects.

The electric field is locally enhanced around sharp nanostructures, inversely proportional to their geometric radius of curvature (ROC) [106]. The dielectric breakdown field of most commercially important semiconductors is ~ 10^5 V/cm. Field strength in excess of this critical value will allow plasma generation within the contact. Tunnelling through energy barriers is enhanced in the presence of large electric fields and this allows high current densities to pass through the semiconductor interface. Au/Cr interfaces in equilibrium form an interfacial charge

dipole equal to the difference in their workfunction (~ 0.8 eV). Their vacuum levels adjust to equalize the Fermi levels and the higher workfunction side (Au) becomes electron accumulated. The charge screening distance in solids is a function of electron number density of the material and is typically < 1 Å in metals[107]. There is practically no potential drop across this kind of interface (metal/ metal). The electric field cannot penetrate the metals beyond this distance in quasi-static conditions. However, the local field strength in the immediate vicinity of their interfacial dipole is significantly enhanced in the Ge nanocrystals due to charge crowding at geometries approaching atomic sharpness (Fig. 5.7). Applied bias disturbs equilibrium and in the limit of small Ge nanocrystals, dielectric breakdown results in generation of hot carrier pairs within the contact.

In metal/Ge contacts, the Fermi level is found pinned close to the charge neutral level/ CNL (ϕ_0), which lies 0.09 eV above the valence band[108]. For n-type and intrinsic Ge, this causes a large upward band bending near the interface leading to carrier inversion near the surface, to maintain charge neutrality. Electrons in the metal occupying energy states close to the Fermi level are usually reflected by the effective Schottky barrier when low doping is used in the semiconductor. Hence, metal contacts to n- Ge typically exhibit rectifying characteristics.

Geometric field enhancements in the hybrid contact allow concurrent Ohmic contacts to low doped (N_A~$5.6 \times 10^{14}\,cm^{-3}$ and $N_D \sim 6.4 \times 10^{14}\,cm^{-3}$) and moderately doped ($N_D \sim 1\times10^{17} cm^{-3}$) Ge. If the Cr interlayer is metallic, it would screen the enhanced electric field within the Thomas Fermi screening distance (< 1 Å). If it is partially oxidised/ contains atomic impurities etc. the interlayer would add resistance or possibly de-pin the Fermi level. It will be shown later that the FLP condition is unaffected by the rapid annealing process.

Whatever the conductivity enhancement mechanisms may be, they do not alter/ degrade the Ohmic I-V characteristics, normally observed for p-Ge under the FLP condition. The Schottky barrier for holes is small, consistent with the normally observed FLP condition for Ge. Current flows easily because holes overcome the small Schottky barrier at ordinary temperatures. Novel current transport phenomena have been identified using the same contact layers on n-Ge, observed in room temperature and low temperature I-V measurements. The results corroborate the hypothesis of plasma generation in the contact responsible for fascinating carrier transport phenomena operating at the nanoscale. The nature of tunnelling is one dimensional and this is fully embodied in the electrical characteristics of the hybrid material, described next.

5.4.1. Annealing transforms - Ohmic hybrid contacts

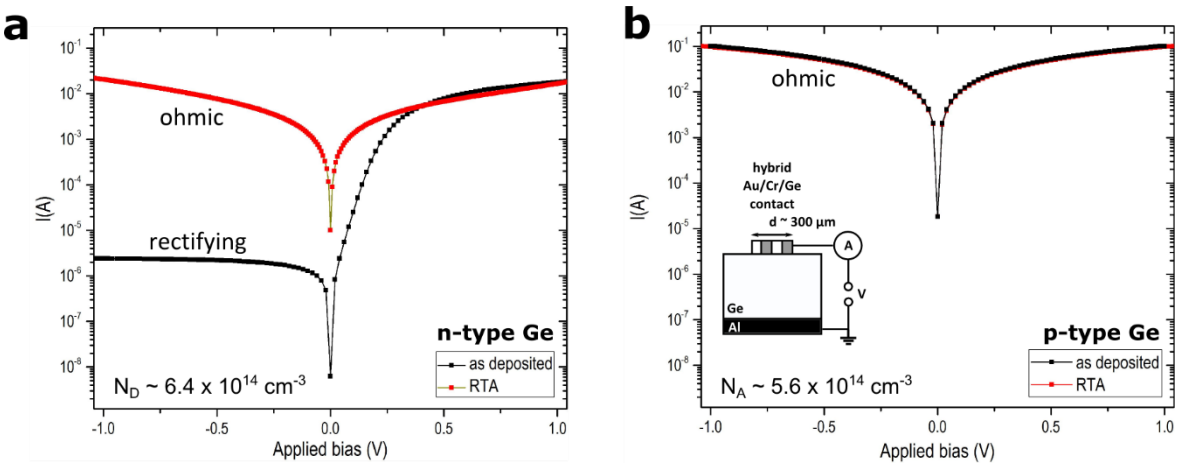

Figure 5.12: Semi-log I-V characteristics of as deposited and RTA Au/Cr (100/ 3 nm) hybrid films (d ~ 300 µm) on **a.** low doped n-type Ge and **b.** low doped p-type Ge. Annealing produces ohmic contacts on both substrates using the same fabrication process.

I-V measurements were obtained using a probing station, in a two-terminal, back contacted arrangement (see Chapter 3, section **3.11**). Here, probe 1 is in direct contact with the top layer of the patterned area and is used to force an applied voltage bias (V_A) sweep relative to the large area (1 cm^2) Al bottom contact (- probe 2 to GND). The probe contact radius is ~ 20 µm. During measurement, the specimens were kept electrically isolated from the stage using a ceramic substrate.

Fig. 5.12-a and Fig. 5.12-b compare the semi-log I-V characteristics of planar Au/Cr thin film contacts and hybrid contacts on low doped n^- Ge (N_D ~ 6.4 ×10^{14} cm^{-3}) and p-Ge (N_A ~ 5.6 ×10^{14} cm^{-3}) respectively. Data are shown for square patterned structures with characteristic length (d) ~ 300 µm. Inset shows a schematic of the measurement configuration used. The as-deposited Au/Cr thin film metallization on n^- Ge produces rectifying contact, as expected from dominant FLP. Annealing transforms the material, producing Ohmic contacts. The as deposited Au/Cr contacts on p-Ge are Ohmic and remain Ohmic even after annealing.

The FLP position is unlikely to have shifted closer to the Ge conduction band, as it does using Fermi level unpinning methods. Materials that successfully unpin the Fermi level produce Ohmic contacts on n- Ge and rectifying contacts on p-Ge [109], or quasi Ohmic characteristics on both- which is not the case here. Concurrent Ohmic contacts are observed reproducibly on the same samples, and repeatably across several experimental trials.

A linear relationship ($I \propto V$) is observed in the low bias regime (< 0.5 V) regardless of bulk conductivity of Ge.

The hybrid film has a distributed geometry. The feature size of Ge nanocrystals formed in the Au film ranges from 50 nm to < 1 µm, and is influenced by the initial Au thickness and annealing parameters. The embedded Ge islands are in contact with metals on all but one side i.e. the interface to air/ vacuum where oxide formation/ surface adsorption is expected. High concentration of dopants in/ around the Ge nanocrystals is unlikely, given that the starting substrate material is low doped ($N_D \sim 6.4 \times 10^{14}$ cm^{-3}) and only the upper layers of the substrate volume near the contact interface are involved in liquid transport of materials. Self-assembled Ge nanocrystals observed here are more likely to be pure/ nearly intrinsic Ge.

FLP is assumed by default at all Ge nanocrystal interfaces. It remains uncertain as to whether the Ge nanocrystals segregated in Au have dopant atoms incorporated within them. If dopant atoms were present, they would be ionized at ordinary temperatures, resulting in a positive space charge region inside the nanocrystal. A positive space charge is plausible regardless of donor concentration, based on the theory of surface reconstruction dipoles, mentioned in Chapter 1 (section ***1.1.2***). The intrinsic/ weakly n-type nature of the Ge nanocrystals under the FLP condition causes carrier inversion below the surface. The inversion layer screens the electric field originating from occupied acceptor surface states[110][21].

At equilibrium, acceptor-type states lying in the band gap, above the Fermi level mostly remain unoccupied. Electrons occupying acceptor type interface states below the Fermi level give rise to negative surface charge[23]. Therefore, a positive image charge is created in the surrounding materials to screen this surface charge, developing p-type character on n-type Ge (like a buried junction). The geometry enhanced Au/Cr interface dipole further modifies the equilibrium charge density distribution in the hybrid film, as sharp points are susceptible to carrier crowding, resulting in enormous local electric field.

The Ohmic I-V data on low doped n-type Ge (n^- Ge) in Fig. 5.12-a are shown on a linear scale in Fig. 5.13-a. alongside its differential conductance (dI/dV) vs. applied voltage ($V_{A)}$ plot in Fig. 5.13-b. These line-shapes viewed together indicate two distinct conductivity regimes (linear and non-linear). At low voltages, a linear high resistance *mode I* is observed. As the bias voltage is increased in either polarity the conductance changes non-lineally indicating the onset of other conduction mechanisms. At high forward bias (V_A > 1.3 V), a dip in dI/dV vs V_A indicates the current is limited by the series resistance of the bulk and high-level injection (HLI) effects at the edge of the depletion region. In contrast, dI/dV continues to increase under large

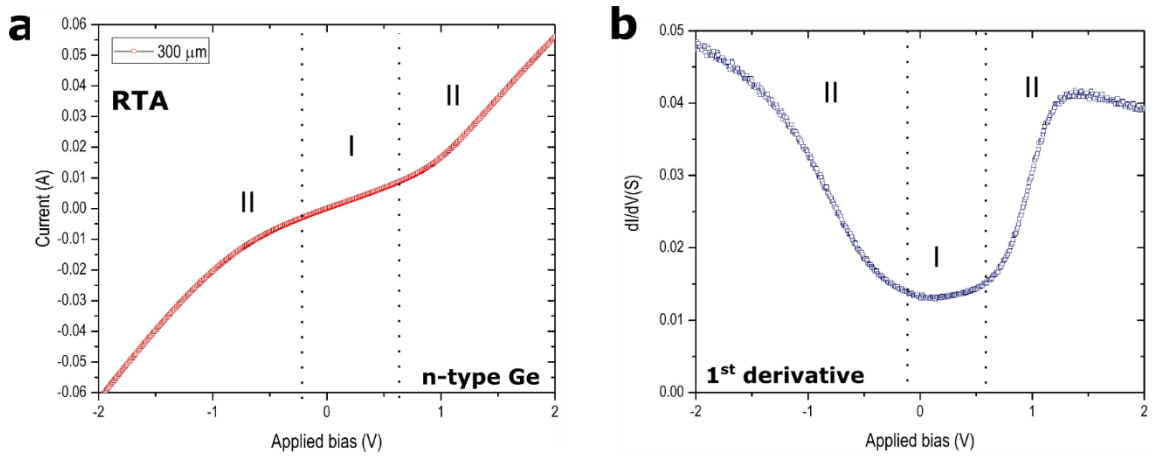

Figure 5.13: **a.** Linear I-V characteristics of the hybrid contact to low doped n-type Ge reveal distinct, voltage dependent conduction regimes, annotated I, II. **b.** First derivative of the I-V data (differential conductance) vs voltage allows examination of the nature of observed conduction modes.

reverse bias (for the measured data points). A turning point is observed in dI/dV at V_A ~ -0.1 V (vertical dotted line), which was also observed across several contacts (different pattern sizes, shapes). This feature suggests that a tunnelling effect dominates in the reverse bias. (See toy model for tunnelling in Chapter 2, section **2.5.2**)

An important parameter that governs the magnitude of tunnelling current is the transmission probability across the barrier, which has a decaying exponential dependence on the width of the energy barrier. In a Schottky contact, potential is almost completely dropped across the interface for low and moderate voltages. In first approximation, the width of the barrier can be treated equal to the depletion region width (W) i.e. from the contact interface up to the quasi neutral bulk. The applied voltage, doping level and built-in potential all affect W. In reverse bias, the width of the Schottky barrier is narrower near the top of the barrier. However, the probability of reverse tunnelling at energies > few kT above the Fermi level is expected to be quite small at T ~ 300 K. Hence, only small contributions from thermionic field emission (TFE) are expected for the doping level used (see section ***2.2.4***). Control specimens - planar metal contacts to moderately doped n-Ge with $N_D \sim 1 \times 10^{17}$ cm^{-3} are also rectifying. The depletion region is narrower (W~ 60 nm at equilibrium, using built in potential ~ 0.2 eV) for this doping level, compared to the low doped case (W~0.74 μm for $N_D \sim 6.4 \times 10^{14}$ cm^{-3}) but is still too large for tunnelling to dominate, and as a result, diode like characteristics are observed. For increasing Au thickness, using the same annealing schedule, it is observed that the average size of Ge islands in the film increases to μm dimensions, as shown in Fig. 5.14 for 300 nm Au. In this limit, the Ohmic conduction on n-type (n- and n^-) Ge is lost and rectification is restored-

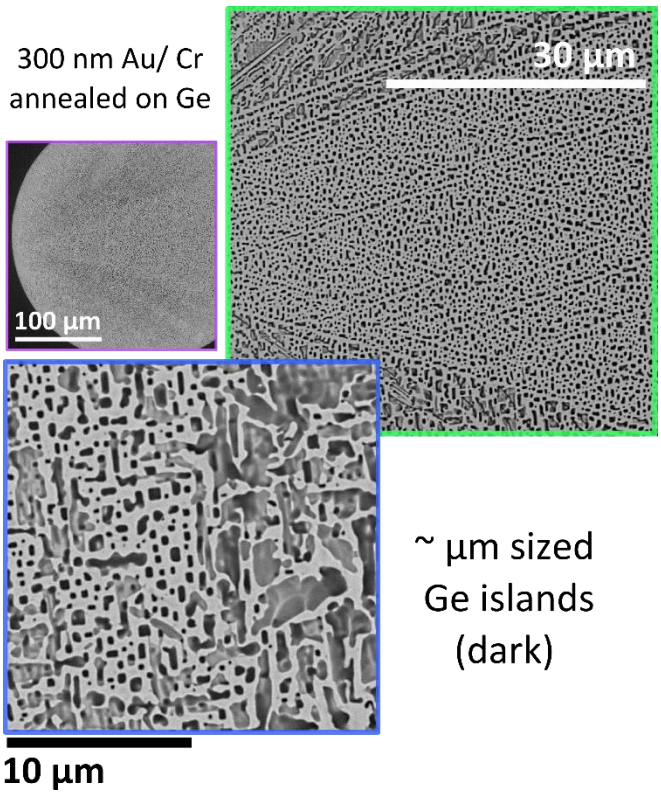

Figure 5.14: SEM collage of 300 nm Au/ Cr (3 nm) annealed on Ge. Ge Island segregation is observed but these are considerably larger compared to the small islands seen for 100 nm Au in Fig.5.3 and Fig. 5.7.

Thicker annealed contacts exhibit the same properties as other typical planar metallization on n-Ge. The corresponding contacts to p-Ge are Ohmic regardless of Au thickness or annealing conditions (like Fig. 5.12-b). The orthorhombic shapes of Ge islands indicate that the Au is still (110) orientated. These findings indicate that the FLP condition is un-changed and the conduction mechanism is critically dependent of feature sizes within the contact. HRSEM and HRTEM investigations were not performed because the electrical properties represent the standard case of FLP in Ge.

The case of thin hybrid contacts ($\leq$ 100 nm Au) is quite interesting, and will be the focus of the remainder of this chapter. A supply of hot carriers is made available from the plasma that ensues from dielectric breakdown in Ge nanocrystals. Ge nanocrystals must remain equipotential with the Au film on four sides at equilibrium and under bias (relative to the substrate). Meanwhile the Au/Cr dipole field will penetrate small (intrinsic) Ge nanocrystals completely. Dielectric breakdown creates pairs of hot carriers with energy $\geq E_g$. The lifetime of carriers in a plasma largely depends on the mean free path and their recombination cross-section. Larger Ge nanocrystals will be unfavourable in this regard, as the supply of hot carriers will be considerably diminished by scattering and recombination processes.

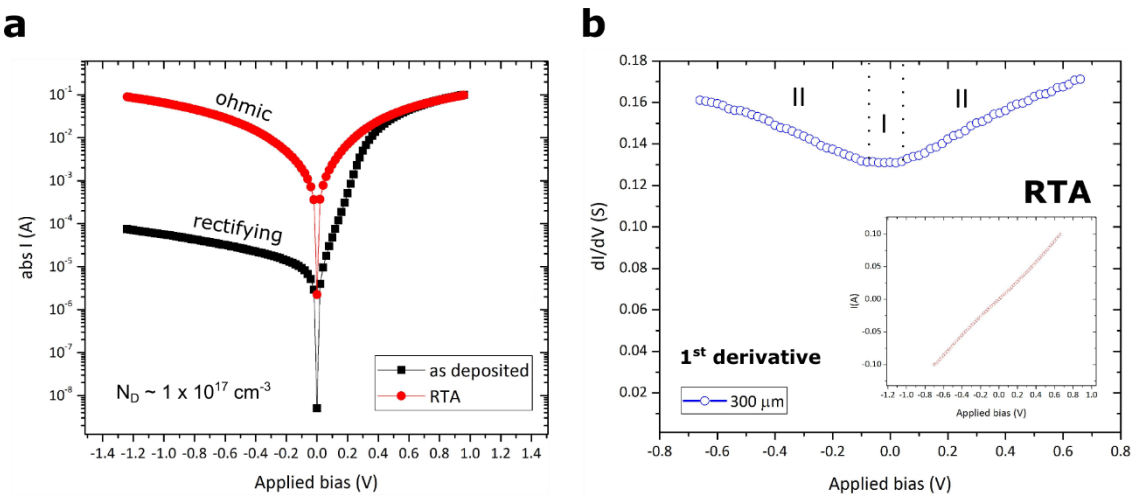

Figure 5.15: **a.** Comparison of semi-log I-V characteristics of as deposited and RTA 100/3 nm Au/Cr contacts (d ~ 300 µm) on moderately doped n-Ge. Ohmic characteristics are obtained upon annealing as expected, with higher absolute current compared to the low doped case shown in Fig. 5.12. **b.** Differential conductance of the I-V data shows the conduction modes I and II are present. Mode II is onset at lower forward bias. Inset shows original I-V data on a linear scale.

Tunnelling contribution to the total current precedes over other mechanisms. TFE contribution is normally found to be small using planar metallization on moderately doped n-Ge ($N_D \sim 1 \times 10^{17}$ cm^{-3}), where the reverse current increases only by an order of magnitude in high reverse bias for most metal combinations. The inverted (p+) surface of n-type Ge behaves like an additional blocking layer for electrons[110][21] in the metal, preventing them from crossing the interface. The applied potential difference is mainly dropped across this p+ layer and the depletion width does not change significantly in reverse bias. And yet, large non-linear current injection is observed using hybrid contacts, even while using low doped n^- Ge. The reverse current increases by four orders of magnitude (for $V_A = -0.5$ V), compared to the control case (Fig. 5.12-a).

Reverse tunnelling current will be enhanced further with increased doping level. Hybrid contacts were fabricated on n-Ge ($N_D = 1 \times 10^{17}$ cm^{-3}) to confirm. The corresponding I-V curves are shown in Fig. 5.15-a on a semi-log plot, comparing as deposited and annealed contacts. Symmetric high conductivity is obtained in either voltage polarity. Reverse current increases by ~ 3 orders of magnitude (for $V_A = -0.5$ V) after annealing. Fig. 5.15-b shows the dI/dV vs. V_A plot. Conduction modes I and II are observed, similar to the low doped case (Fig. 5.13-b). Inset shows the I-V data on a linear scale. Higher doping increases the zero-bias conductance, by an order of magnitude. Interestingly, the turning point at $V_A \sim -0.1$ V is still observed, providing additional confidence in the tunnelling mechanism. The I-V curve shown in the inset appears more symmetric as modes I and II begin to overlap. The influence of minority carriers

in the substrate can be neglected at this doping level and high-level injection is minimized. Consequently, negative differential conductance (dip) is not observed in the forward bias, as it was in the low doped case (Fig. 5.13-b).

Inferences:

The hybrid material forms Ohmic contact to Ge without changing the FLP arrangement. Conductivity is improved with moderate doping. As a result, two major drawbacks of the severe FLP effect in Ge are bypassed, simply by modifying the contact geometry.

5.4.2. Geometric edge current injection

The path of least electrical resistance must lie along the geometric triple points (Fig. 5.11) in the hybrid material, based on the idea that electric field strength will be highest in these regions. Accordingly, the effective current injection cross section of the contact is the total peripheral length of the Ge nanocrystals in the hybrid contact pattern. It is recalled that the Ge nanocrystals maintain strong orientation relationships with the [110] substrate directions, forming orthogonal patterns in Au film (reproduced in Fig. 5.16-a). The total peripheral length of the nanocrystals is proportional to the characteristic length (d) of the contact pattern. This can be confirmed by inspection of the plan view of the material. A simplified schematic is shown in Fig. 5.16-b. Constructing projections from the epitaxially registered Ge nanocrystals onto the contact diameters shows that every length in the material sub-system can approximately be expressed as proportional to d. Therefore, the complete cross-section for injection must also proportional to d. This proportionality holds true even if all the nanocrystals are not all sized equally (cubes, cuboids and their combinations). The orientation relationships (100)Au//[110] Ge are observed across the entire patterned film. This ensures that the Ge nanocrystal edge lengths are always proportional to the pattern dimensions. Hence, if the hypothesis of triple point injection is correct, scaling the I-V data by the contact's perimeter ($\propto d$) should produce a normalization in peripheral current density (J_p) using different sized contacts. Hybrid contacts of varying characteristic lengths (d ~ 50-300 µm) were fabricated on n^- Ge. Their respective I-V characteristics are shown in Fig. 5.16-c. on a linear scale. Dividing the data by perimeter of the patterned regions gives the expected peripheral current scaling behaviour, shown in Fig. 5.16-d. A significant overlap is observed in the measured contact's peripheral current density (J_p) vs V_A plot. Minor discrepancies in the data are expected, since the film surface receives probing/

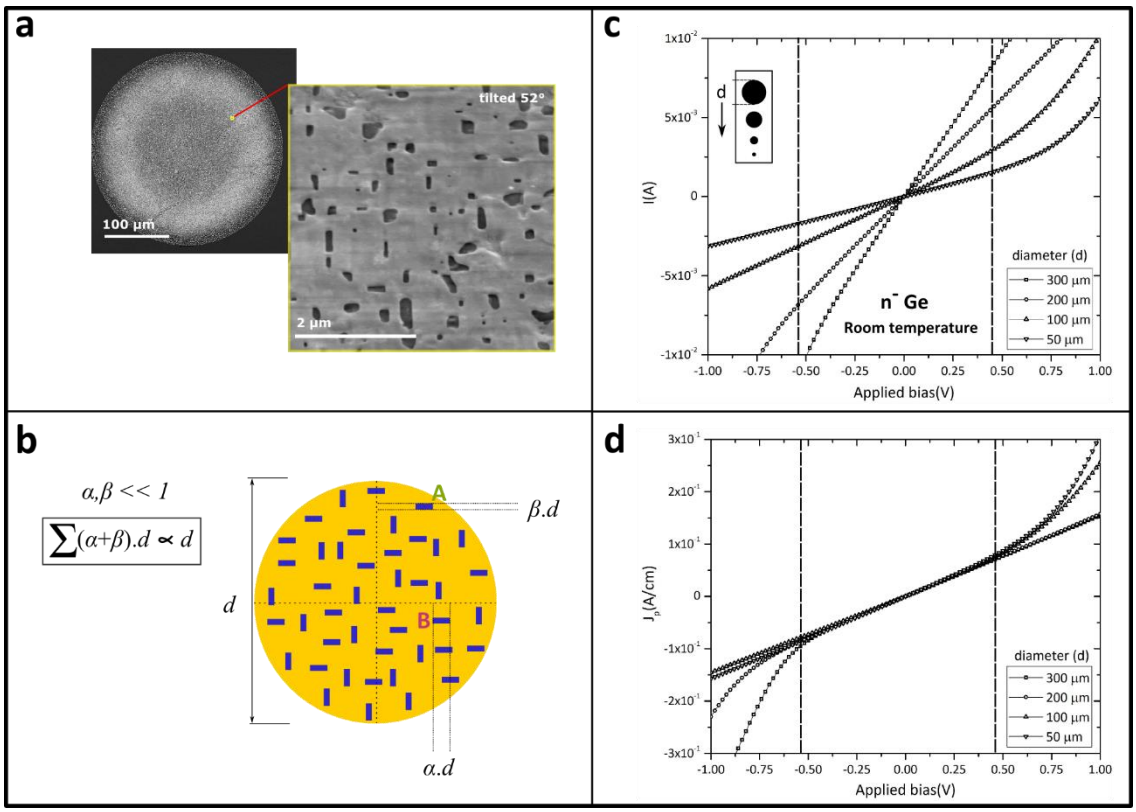

Figure 5.16: a. HRSEM of a circularly patterned, extended hybrid film contact. Inset shows the tilted view of the film surface. Vertical Ge nanocrystals are embedded in the Au film. **b.** Schematic plan view of the hybrid film. Epitaxial nanocrystal edges are projected onto the pattern diameter for two sample locations A and B. The sum of all nanocrystal edges i.e. the triple point cross section, is proportional to the pattern diameter (*d*) used. **c.** I-V characteristics of hybrid contacts to low doped n-type (n^-) Ge for various *d* sizes. **d.** Peripheral current density dominates the total current at low applied bias, as indicated from the overlap in the family of curves.

scrubbing damage from the sharp probes used in the measurement. Care was taken to place the forcing contact at the centre of the contact pad to minimize variability, but this becomes challenging while probing structures with dimensions that are comparable to the probe itself (smallest contact $d \sim 50$ µm, probe diameter 20 - 25 µm). Nevertheless, a satisfactory match is observed in J_p across the whole data series.

On the other hand, dividing by the pattern area ($\propto l^2$) did not produce an overlap in either mode I or II. Normally, current scales according to the metal's patterned area. However, as dimensions reduce, edge effects become significant and devices are often protected using guard-ring structures to prevent fringing fields from causing damage. It is important to note that the field enhancement in the hybrid film is distinct from this fringing effect. Here the electric field enhancement occurs *within* the hybrid contacts and is localized at triple interfaces. Metals otherwise screen electric field completely (below certain optical frequencies)[111]. The data shown in Fig. 5.16 validate the hypothesis of current injection via triple interfaces in the hybrid

contact and it is concluded that the effective cross section of the hybrid structure has one dimensional/ edge character at low voltages.

The sub-nm radius of curvature (ROC) near the nanocrystal provides an enormous geometric field enhancement within the semiconductor nanocrystals. Tunnelling across an energy barrier is favourable in the presence of high electric field but can only occur if there is a density of available/ empty states for carriers to tunnel into. Ge is known to have a distribution of acceptor type interface states close to the CNL[112]. The conductive nature of Ge interface states effectively allows a vertical shunt for current[113]. Electron capture into interface states is a likely intermediate step in the conduction mechanism. The Ge interface states on either side of the Cr interlayer will be electronically coupled because their capture cross-sections are comparable owing to heteroepitaxy (Fig. 5.7-c). Therefore, the measured current must predominantly inject from the Ge nanocrystal surfaces.

The fabrication and annealing steps were also tested on Si. (110)Au crystallization and 1-D scaling were both observed. Highly linear Ohmic I-V characteristics are observed at room temperature on both n- and p-Si for low and moderate doping levels, comparable to the Ge work described in this chapter. However, this was not investigated further because Au is known to degrade carrier lifetime in Si. Moreover, the FLP is not as severe in Si. The focus of this chapter is therefore on Ge, rather than Si. However, the current scaling behaviour and film texture on Si support the idea that high conductivity phenomena observed for annealed specimens arise from geometric features in the contact.

Inferences:

The discovery of hybrid contacts has broad implications. It has been shown here that vertical interfaces to Ge nanocrystals serve as conduction paths into n type Ge, offering the prospect of scaling to small geometries- one could obtain a small device footprint and contact to low dimensional materials. Process optimization for this design may provide intrinsically superior performance at the nanoscale, where surface effects dominate over bulk properties.

5.4.3. Low temperature I-V characterization

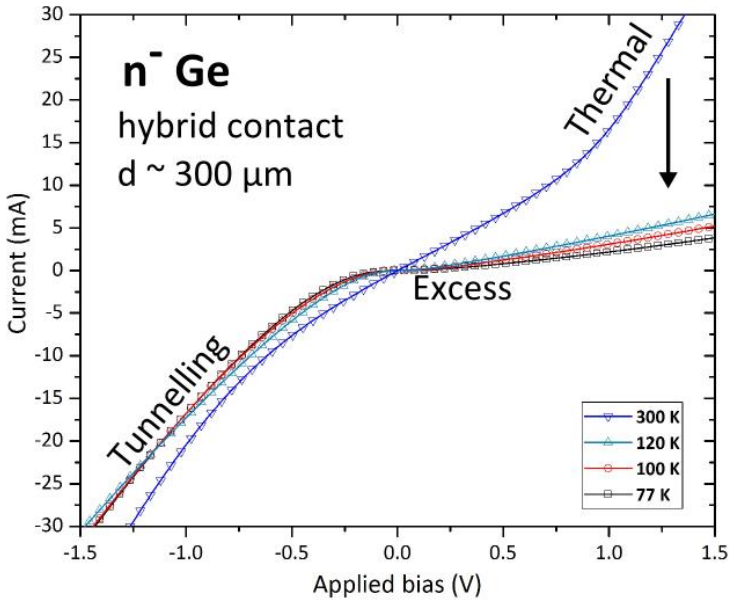

Figure 5.17: Select Low temperature I-V data (77 K-300 K) of a *d* ~ 300 µm hybrid film contact to low doped n-type (n^-) Ge on a linear scale. Dominant conduction mechanisms are annotated.

Temperature is a crucial variable that enters most carrier transport equations. By controlling the ambient temperature during measurement, one can identify temperature dependencies of various mechanisms that contribute to the measured property. For Schottky contacts to non-degenerate semiconductors, the reverse current depends mainly on the temperature and the Schottky barrier height. Delocalized electrons in the metal exchange energy with the lattice and thermal equilibrium is maintained via electron-phonon interactions. As a result, the energy distribution of these carriers is affected by the ambient temperature. Below certain critical temperatures, contributions from thermionic emission and thermionic field emission mechanisms become negligibly small, especially on low doped semiconductors.

Heavily doping the semiconductor narrows the depletion region near the contact interface. Electrons at the metal Fermi level can tunnel into the semiconductor's conduction band through a narrow barrier, provided the Fermi level is aligned with states in the conduction band or via impurity states and traps. This results in Ohmic conduction and is observed when $W < 3$ nm. The doping level required to obtain such junctions is usually of the order 10^{20} cm^{-3} [5][114] as the barrier ($W \sim 2$ nm) is almost transparent to electrons at equilibrium. The abrupt change in the potential from the pinned surface in towards the bulk semiconductor creates a large electric field at the interface of the order of 10^6 V/cm. Tunnelling current demonstrated in these contacts

demonstrate a weaker temperature dependence. For n^- Ge ($N_D \sim 6.4 \times 10^{14}$ cm^{-3}) the surface electric field is expected to be small~ 10^3 V/cm and *W*~ 0.74 µm is too large for direct tunnelling to be possible. However, hot carriers generated in the Ge nanocrystals will have a minimum energy equal to the bandgap of Ge. Hence, reverse biasing the contact will allow hot electrons to easily tunnel across the Cr interlayer and Schottky barriers, into the substrate. Low temperature I-V measurements support this model. The hybrid geometry provides an interesting example of reverse tunnelling using voltage controlled plasmas generated in the contact. Control (annealed Pt/Cr and as deposited Au/Cr) and hybrid contacts (*d* - 200 µm and 300 µm) were fabricated on n^- Ge for low temperature (77 K– 300 K) testing at Imperial College, London. These measurements were performed by Dr. Peter Petrov.

Two terminal I-V characteristics were first confirmed to be reproducible and repeatable on several contacts at room temperature, before cooling the sample down to liquid nitrogen temperature (77 K). Subsequent measurements were taken at higher temperatures in 20 K increments using the cryostat. Select I-V-T data of the hybrid contact are presented in Fig 5.17. The conduction modes I and II that previously appeared symmetric in I-V characteristics taken at room temperature become distinct at lower temperatures. In this temperature range, the reverse current is weakly sensitive to the temperature, whereas in forward current reduces with decreasing temperatures. Thermal current onset is offset to higher V_A at lower temperatures (outside scale, not shown) and its contribution becomes less important at lower voltages. In other words, mode II in forward bias is wiped out and only excess currents corresponding to the edge scaling current in mode I (Fig 5.13-a) are observed at low temperatures, verified by J_p-V data overlap. The temperature dependence of reverse current of the hybrid contact and control contact are compared in Fig 5.18 using an Arrhenius plot, for a nominal reverse voltage (V_A = -0.3 V) over temperature range 200-300 K. Blue and red scales are different for control and hybrid contact data respectively. An exponential trend is observed for the control sample, consistent with Schottky emission while temperature insensitive tunnelling behaviour is observed for the hybrid contact.

The activation energy of recombination processes depends on the band-gap of the semiconductor. Hence, at lower temperatures, recombination is weaker and the forward current reduces. The I-V characteristics of the hybrid contact are qualitatively similar to those of a *backward diode*, also known as *backward Esaki/ reverse* diode[115]. The backward diode is a special case of the (p^+n^+) Tunnel diode, where the *n* side is not degenerately doped (p^+n). Backward diodes normally do not exhibit negative differential resistance (NDR) as observed in Tunnel diodes. I-V characteristics of the Tunnel diode and backward diode are schematically

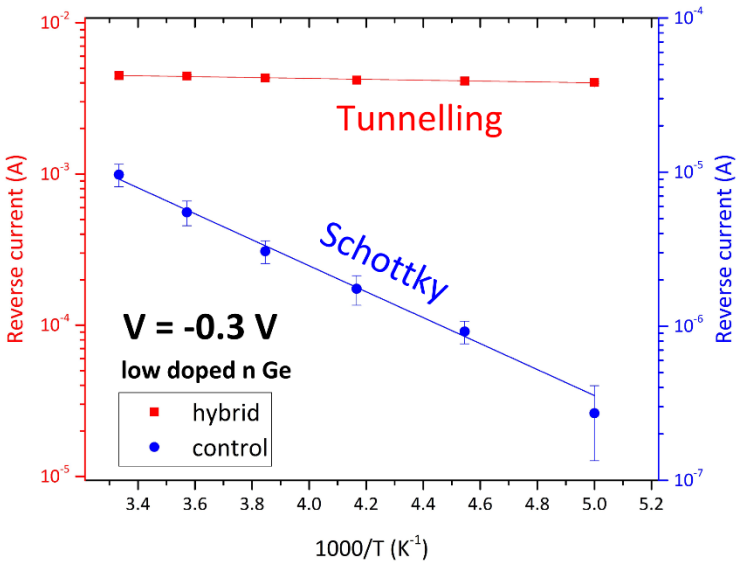

Figure 5.18: Comparing the temperature dependence of reverse current in control and hybrid contacts (d ~ 300 µm) to low doped n type Ge at a nominal reverse bias V= −0.3 V. The hybrid contact allows temperature independent current injection, while the control sample exhibits exponential dependence on temperature. Error bars represent the spread in observed reverse current in 4 contacts.

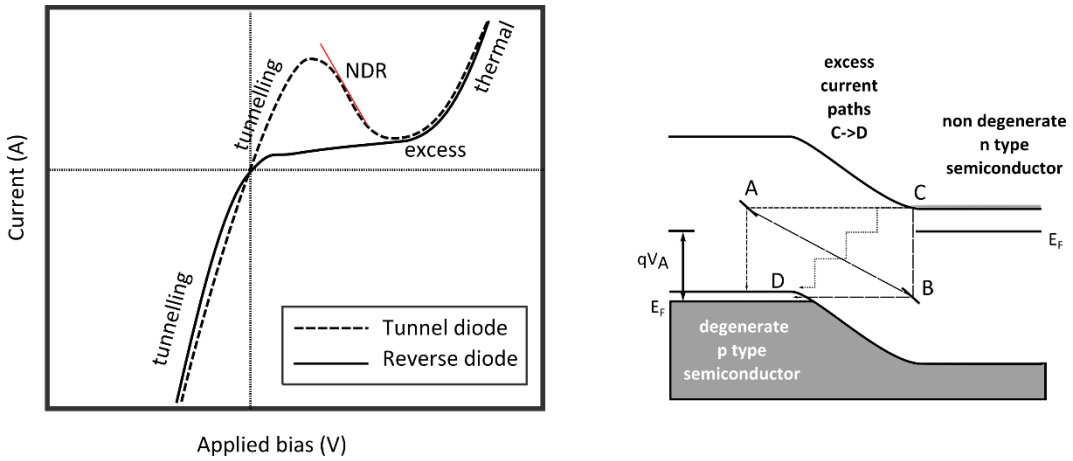

Figure 5.19: Schematic I-V characteristics of Tunnel diode and Reverse diode. Main current contributions due to different mechanisms have been annotated. The tunnel diode shows NDR. The reverse diode normally does not show NDR when the n- side is low doped. Schematic adapted from textbook ref. [45]

compared in Fig. 5.19 (left) (adapted from textbook ref. [45]). Their operation is described by classic conduction regimes: tunnelling, excess current and thermal (diffusion) current. Excess currents are normally attributed to multi-step tunnelling in addition to recombination processes in the semiconductor, either through defect levels in the bulk or via interface states. Several

possible paths (tunnelling transitions) may exist for the forward excess current, from the conduction band of the *n* side (C) to the valence band of the *p* side (D), as illustrated schematically Fig. 5.19 (right) [45]. This can occur through local intermediate levels such as interface states or impurity levels lying within the bandgap (following a path like CBD, or CAD). Alternatively, there could exist a dissipative process CABD where electrons lose energy in making the transition between the local energy levels. Finally, multi-step tunnelling tunnelling transitions from C to D are possible (dashed line in Fig. 5.19 (right)) provided there is a high enough density of intermediate levels. Here too, the electrons lose their energy while making transitions between the intermediate levels.

Since the excess current observed in the case of hybrid contacts has one-dimensional/edge character, it is inferred that the excess current conduction occurs via interface states of the Ge nanocrystals and substrate.

5.4.4. Tunnelling spectra and excess current

Non-linear devices are usually characterized by a figure of merit called curvature coefficient (γ) [45], defined as the ratio of the second ($\dot{G}$) and first (G) derivatives of current with respect to applied voltage:

$$\gamma = \dot{G}/_{G}$$

When G in the denominator is replaced by the zero-bias differential conductance G_0 ($V = 0$), γ describes the *nonlinearity* figure of merit of the device element. The quantity γ is the normalized rate of change of conductance. At small applied bias, most of the voltage drop occurs at the Schottky interface and series resistance effects are negligible. The applied voltage corresponds to Fermi level separation between the substrate and triple points/ metal(s). Since the Fermi level is pinned close to the CNL (~0.09 eV above the valence band) at equilibrium, applying a forward bias sweeps the Fermi level through the vacant acceptor states lying in the band gap. Conductance changes as the Fermi level *crosses* or *uncrosses* allowed electronic energy states.

The low temperature I-V data of patterned hybrid contacts (*d* - 200 µm and 300 µm) are used to obtain the tunnelling spectra by plotting the magnitude of curvature $|\gamma|$ against V_A. The second derivative (d^2I/dV^2) data were divided by the zero-bias differential conductance(G_0).

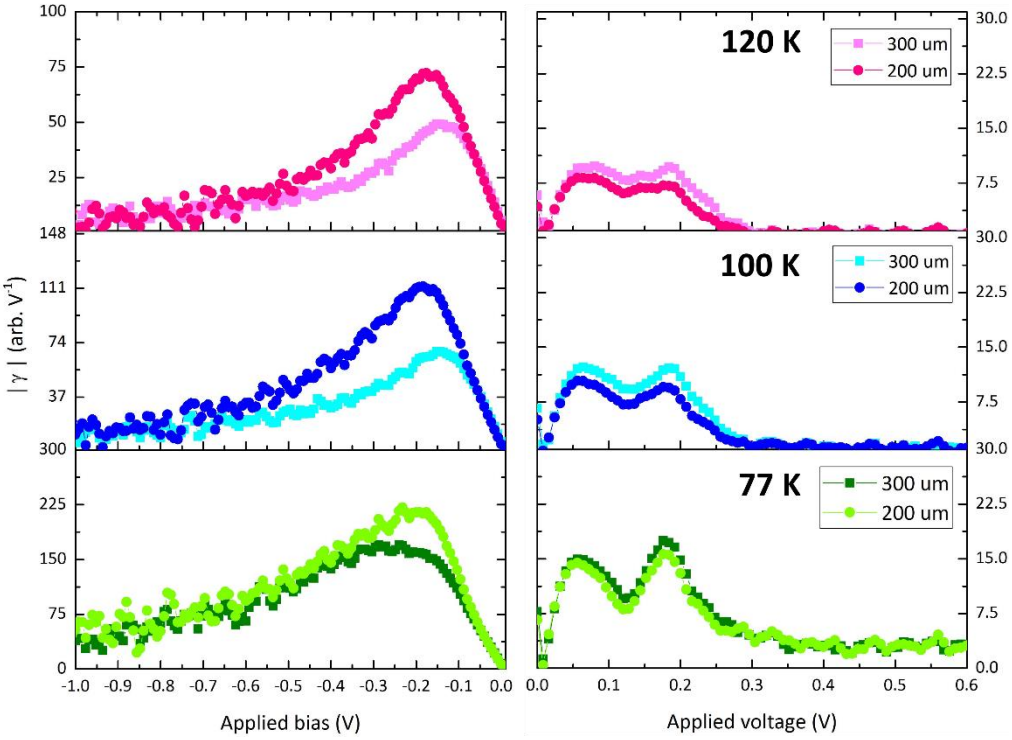

Figure 5.20: Normalized | γ | vs V_A at low temperatures reveal evidence of excess currents via Ge interface states lying within the bandgap.

These data were then normalized by the ratio of contact pattern radius to account for the edge scaling nature of current at small applied bias. Fig. 5.20 shows these processed data. A consistent overlap between the derived values of | γ | is observed in the forward bias and large reverse bias in the breakdown regime, upon normalizing for contact size. The spectral line-shapes are inherent at different temperatures, giving a self-consistent picture of the tunnelling density of states, following eq. (2.109) (See chapter 2). It was previously hypothesized that the turning point in conductance observed at room temperature for $V_A < -0.1$ V marked the onset of hot electron tunnelling. The trends observed in Fig. 5.20 provide additional confidence in this model. While the trends in γ vs V_A are reproducible across a range of temperatures, it is observed that the magnitude of curvature (| γ |) for a given V_A steeply rises as the temperature reduces (comparing vertical scales in the panel). This is expected, because the magnitude of tunnel current is weakly dependent on temperature (Fig. 5.18), whereas the recombination becomes weaker at lower temperatures. Hence, the rate of change in conductance is considerably higher at low temperatures.

These data are further evidence that the Fermi level of the hybrid contact remains pinned near the CNL at equilibrium. In reverse bias, the Fermi level cuts the valence band ($V < -0.1$ V) near the surface, resulting in strong inversion. This will enhance the Cr/ Ge interface dipole where

the voltage drop occurs. Higher reverse bias only increases the incident energy of hot electrons at the interface prior to tunnelling. In forward bias, the Fermi level sweeps through interface state energies in the band gap, initiating recombination processes. The acceptor states in the Ge band gap are conductive[116]. The density of acceptor states in the Ge band gap is expected to be highest near the CNL, decaying at higher energies closer to the conduction band[112][117][23].

This trend is qualitatively observed in the experimental data. The first peak occurs at ~ 0.04 eV, the surface state resonance energy S_{r1}-S_{r2} of (100)Ge, as reported by Popik *et al* using low energy electron spectroscopy[22], accompanied by a shoulder at ~ 0.1 eV, which remains unidentified. The second, most intense maximum is observed at ~ 0.19 eV, similar to surface state energies of clean (2x1) reconstructed (111)Ge surfaces, previously reported using scanning tunnelling spectroscopy by Feenstra *et al* [118] and the S_6 state (0.18 eV) on (100) Ge, reported by Popik *et al* [22]. Although interface state energies may be modified compared to surface states on clean, free surfaces, the $|\gamma|$vs V_A plot proves to be a useful tool for data visualization and examination of transport mechanisms.

Inferences:

The hybrid contact has I-V characteristics qualitatively similar to a backward diode. One dimensional tunnelling and excess currents flow between coupled Ge interface states, separated by the Cr interlayer.

5.4.5. Hot electron transport

The thermal and excess current can be almost eliminated by lowering the sample temperature below the carrier freeze-out temperature of Ge. Control (planar Pt/Cr on Ge) and hybrid contact specimens were fabricated on n^- Ge and cleaved down to ~3x3 mm^2 for mounting onto leadless chip carriers (LCC). Mounted LCCs were sent to Royal Holloway University of London for cryogenic I-V measurements at liquid helium temperatures. These measurements were performed by Dr. John H. Quilter. The contacts were wire bonded to the LCC and connected to the cryostat's electrical feedthrough. I-V characteristics of the contacts were obtained after immersing the samples in liquid helium (4.2 K). The control sample (not shown here, but in Chapter 6) exhibited no discernible I-V characteristics at low voltages (comparable to open circuit current) and its measurements were dominated by system noise, as expected for n^- Ge

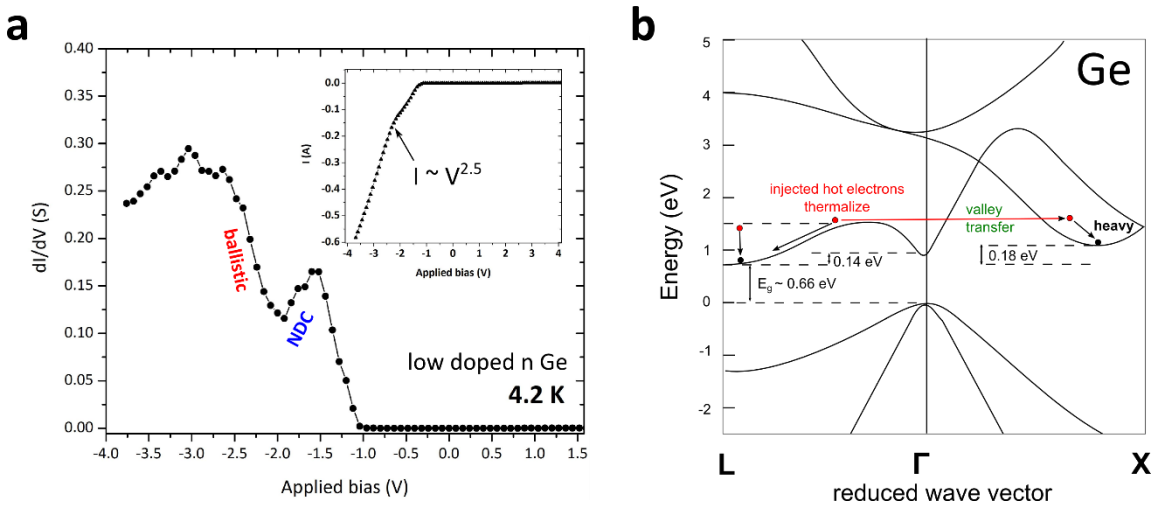

Figure 5.21: a. Differential conductance-voltage data of a hybrid contact at 4.2 K. Inset shows the I-V data on a linear scale. NDC is observed at V_A = −1.5 V, followed by nearly ballistic electron transport. **b.** Schematic Ge band structure adapted from textbook ref. [45], illustrating the inter-valley transfer process from **L- X** states.

below carrier freeze-out. In contrast, I-V characteristics of hybrid contacts to n^- Ge demonstrate very high conductivity in the reverse bias, confirming non-equilibrium carrier transport phenomenon. Negative differential conductance (NDC) is observed in the reverse bias for −2 V < V_A < −1.5 V, as shown in Fig.5.21-a. Inset shows the corresponding I-V data on a linear scale. NDC can be understood by considering an electron valley transfer effect in the Ge conduction band from **L** <111> towards **X** <100> (Fig.5.21-b). The higher conduction band minimum in the Brillouin zone near **X** is only 0.18 eV above the conduction lowest band minimum at **L**. Tunnelling hot electrons are scattered into the higher valley upon thermalization. The conduction band in the relevant Brillouin zone consists of 4

equivalent minima at **L** and 6 equivalent minima lying near the zone edge **Γ→X**.[119]. The conduction band near **X** has a shallower curvature (E-k relationship) than the conduction band at **L**. Consequently, the effective mass of electrons occupying states in the **X** valley is higher and mobility reduces[120]. This phenomenon manifests as NDC in n-Ge. Hot electron transport is demonstrated in low doped n-type (n^-) Ge at 4.2 K. NDC in Ge Schottky diodes has previously been attributed to hot electrons transmitted across the contact interface by TFE[121]. This mechanism vanishes below certain critical temperatures (>> 4.2 K) and cannot be responsible for the results in the study. Furthermore, super-linear current injection is observed for V_A< −2 V. The I-V curve in this region follows a power law ($I \propto V^{2.5}$), which resembles ballistic transport of energetic hot carriers [122] across the entire low doped Ge substrate. Ballistic carrier transport in materials is normally observed in low dimensional materials

wherein carriers undergo minimal scattering in certain directions due to confinement effects and observe Newton's law of motion in special device geometries (e.g. carbon nanotube FETs[123]). Lattice vibrations are significantly reduced at cryogenic temperatures and phonon-carrier scattering is relatively suppressed. This may explain the typical power law I-V characteristics observed in the data using hybrid contacts at 4.2 K (in Fig.5.21-a. inset).

The electrical characterization studies all point towards plasma generation in the contact leading to significant improvements in conductivity due to tunnelling hot electrons. Hot electrons originate from triple points in the contact and scatter into the substrate.

Inferences:

Applying reverse bias to the hybrid contact provides hot electron tunnelling current into the Ge conduction band. Injected carriers thermalize in the lattice by scattering. The energy of tunnelling hot electrons increases with the applied voltage, leading to thermalization into higher energy conduction valleys. Electron- lattice scattering is weaker at 4.2 K and the I-V characteristics suggest ballistic carrier transport across the Ge substrate.

5.5. Discussion

The hybrid material serves as a one-dimensional ambipolar contact despite severe FLP in Ge. Conductivity improves due to non-equilibrium carrier transport phenomena occurring in the contact layer. Although significant improvement is observed in transport characteristics owing to hot electron generation in the contact, this technology is not ideally suited to many existing device geometries e.g. MOSFETs, where hot electron injection into the gate oxide, arising from short channel effects is known to compromise device integrity. Nevertheless, from a phenomenological point of view the findings of this chapter shed light on a means to improve conductivity extrinsically.

Dipoles are formed between materials interfaces when their vacuum levels are unequal i.e. these are workfunction dipoles. As a result, one side of the interface tends to be accumulated with electrons and the other side is deficient (−/+). The dipole screening length depends mainly on the carrier density at the surface of the joined materials. The FLP condition in low and moderately doped Ge creates a Schottky barrier which confines electrons in the metal. It has recently been shown that electron accumulation at nanoscale metal geometries raises the Fermi

level in energy[124]. Charge build-up increases the electron potential energy relative to the continuum of available states beyond the Schottky barrier. As a result, resonant tunnelling current flows to the nearest available states when the barrier is sufficiently thin.

The ~ nm radius of curvature at triple points provides enormous geometric field enhancement. The Au/ Cr dipole (−/+) field is screened by the Ge nanocrystal surfaces at equilibrium. However, when the hybrid contact is biased against the substrate, high energy electrons at accumulated triple points can tunnel into the Ge nanocrystal, in which they will eventually thermalize. The intrinsic Debye length of Ge is 0.68 μm[125]. Ge nanocrystals smaller than this length scale will be unable to completely screen the coulomb potential from the metals surrounding it on 5 sides. As a result, carriers gain energy from the electric field and eventually strike a hot carrier plasma in the Ge nanocrystal. The electro-acoustic resonant frequency of Ge is ~9.3 GHz.[126][127]. It is inferred that the electron speeds in the presence of field enhancement are sufficiently large for the weak plasma to be sustained in the contact, under steady state conditions. Electrons, being lighter than ions and holes, will have higher temperature and speed in the plasma[128]. Hence, they arrive at the nanocrystal's surface first, charging it negatively. Holes and ions screen the excess negative charge in the form of a double layer. This phenomenon is identical to Debye sheath formation. At small applied voltage, the acceptor states lying within the Ge band gap are first occupied by electrons (recombination), followed by resonant tunnelling from the edges. Hence, one-dimensional injection characteristics are observed. Increasing the applied voltage creates even hotter electrons which are directly injected into the Ge conduction bands with increasing energy.

At room temperature, electrons scatter in the lattice by electron-phonon interactions and the carrier velocity saturates in high electric fields. At very low temperatures (4.2 K), this effect is weakened as hot electron thermalization in the lattice becomes inefficient. The observation of negative differential conductance at $V_A \sim -1.5$ V i.e. the brim of the conduction band valley at the **L** point in the Brillouin zone supports the model of plasma charging described above. Hot electrons thermalize into the conduction band near the zone edge **Γ→X**, and the mobility decreases due to increase in the effective mass of electrons. Further increasing reverse voltage results in nearly ballistic transport.

The hybrid contact structure investigated in this chapter is experimental proof of concept for high speed applications in Ge based devices. New device geometries could lead to applications that would allow the use of hot electron emitter contacts. Hybrid contacts offer a means to overcome high contact resistance, frequently encountered in nanoscale devices[129]. Ge forms a good interface with Si[130][131] and GaAs[132][133][134]. Hence, there is an

opportunity to integrate the hybrid contact structure into existing technology. However, in order to implement these methods in ultra-small devices (sub-10 nm), the process needs to be optimized to control the size of the Ge nanocrystals in the film. Controlling the size of the Ge nanocrystals will allow exploration of other non-equilibrium phenomenon (e.g. microwave generation, light emission). Sharp triple interfaces formed in the hybrid material improve performance, but polycrystalline semiconductor nanocrystals should also be investigated. The test structures used in this chapter are built on thick substrates (0.5 mm) using a back contacted configuration. A greater part of the substrate volume only adds to current spreading and series resistance in the measurement but is not pertinent to operation. Reducing the substrate volume by growing the substrate as required will considerably improve performance by reducing these parasitic elements in small hybrid contacts.

The layout of the hybrid geometry has parallels with the embedded metal nanoparticles approach described in Chapter 1. Both methods use nanostructures and rely on high electric fields arising from triple junctions to form Ohmic contacts to *n* and *p* semiconductors. However, it must be emphasized that the hybrid film geometry is a complementary system that proves to be superior when performance on low doped substrates is considered. Here, the triple point field enhancement creates surface plasmas in semiconductor nanostructures and conductivity is improved from the resulting charge transfer. Whereas for embedded metal nanoparticles, carriers are field emitted close to the Fermi level. This limits the use of the approach to heavy doped substrates. These contacts will lose their Ohmic property at cryogenic temperatures due to this condition.

The hybrid contact's active interfaces are vertical, giving it an effectively one-dimensional current cross section. A similar effect has previously been demonstrated in vertical diamond cathodes, where surface state channels are used to provide field driven hot electrons, emitted along the edge of the cathode[135]. The lateral junctions produced in the film are of crucial importance to the formation of well defined, triple interfaces. Controlling the eutectic reaction would make it possible to grow very small Ge nanocrystals where electron heating effects will be more pronounced. The results discussed in this chapter have a general applicability to many materials. It may even be possible to move away from the bottom-up approach used in this study and towards sophisticated top-down methods to realize similar hybrid structures. Achieving lateral epitaxy using top-down approaches is quite challenging. However, annealing near eutectic temperatures may resolve these issues by thermally healing defects and misaligned interfaces.

5.6. Conclusions

A new method to achieve low resistance metal/Ge junctions has been discovered. Voltage controlled hot electron emitter structures are demonstrated using self-assembled nanomaterials. Two major drawbacks caused by severe FLP, namely doping insensitivity and asymmetric conductivity on *n* and *p* substrates, have been bypassed simply by modifying the contact geometry. Ohmic contact is achieved using low doped Ge substrates by employing hot electrons that circumvent the Schottky barrier. This is a significant advance, considering the problem of doping uncertainty in ultra-small geometries (e.g. 2D materials). It is anticipated that hot carrier sources using similar hybrid geometries will advance the state of the art and aid in development of prototypes for future generations of microelectronic and nanoelectronic devices.

"Everything is energy, and that is all there is to it. Match the frequency of the reality you want, and you cannot help but get that reality. It can be no other way. This is not philosophy. This is physics."

-Albert Einstein

Chapter 6:

Island metal films – hot carrier emitters

Abstract

This chapter explores a dispersed nanostructure contact formed by rapid annealing thin Au/Cr films. A network of large (~1 µm) and small (nm scale) metal islands is formed, interconnected with metal Au(Cr) nanowires on Ge due to annealing. Small metal nanoparticles are susceptible to non-equilibrium electron heating from incident tunnelling electrons. Hot carriers are emitted from these island metal films (IMFs) under nominal applied bias. Hot carrier surface plasmas improve conductivity of the contact, allowing ohmic behaviour at room temperature, down to 4.2 K, where nearly ballistic hot electron and hot hole currents are observed for low doped n-Ge. The electron temperature is estimated to be ~10^3 K from emission spectra collected from the IMF in high vacuum. These results will have a wider applicability to many material systems.

6.1. Introduction

In the previous chapter, Ge nanocrystals within the contact were shown to be susceptible to dielectric breakdown at small applied voltages, owing to geometric field enhancements occurring at triple interfaces in the contact. The effect has been confirmed to be non-destructive and presented no hysteresis over multiple measurements performed. Carrier pairs are generated in semiconductor nanocrystals with energy ~ E_g, just sufficient to circumvent the Ge Schottky barrier. Nearly ballistic hot electron tunnelling current was observed in n-type Ge at 4.2 K but no hole current was observed in the forward bias.

In a sustained plasma under DC bias conditions (steady state, see Chapter 2), hot electrons at the periphery are screened by double layer/ Debye sheath formation ($\lambda_D \propto \frac{1}{\sqrt{n}}$). This is a positive space charge layer which screens the free electrons at the plasma boundary. As carrier concentration n varies with temperature, its value at 4.2 K is much smaller than the room temperature value ($n \ll 10^{13}$ cm^{-3}), screening of field excited carriers may occur within the nanocrystal over length scales comparable to the size of the nanocrystal itself (>> 10 nm). This creates a wide barrier and hole tunnelling is forbidden. On the other hand, there is evidence of 1D current scaling over a wide range of temperatures, which is consistent with hot electron

tunnelling from the nanocrystal surfaces within the contact. In this chapter, metal nanostructures are shown to achieve a superior effect. Both hot electron and hot hole currents are observed from IMF contacts on Ge. The screening length in metals is < 1 Å owing to their high free carrier density ($n \sim 10^{22}$ cm^{-3}). Direct evidence of non-equilibrium carrier transport phenomena is presented in the electrical results section. Ohmic behaviour is observed at room temperature down to 4.2 K in low doped n^- and p-Ge.

Lattice spacing in a crystal directly influences hot carrier mean free path[136] and non-close packed nanocrystal formations e.g. (110)Au have highest inter-planar spacings in the growth direction along the reference normal to the substrate. Hot carrier mean-free path in metals is usually < 20 nm in close packed crystallization and smaller nanostructures express non-equilibrium phenomena upon electrical and/or optical excitation. The theoretical calculations in ref.[136] suggest (110) crystals will offer the largest mean-free path (20-40 nm) for hot carriers with energy close to the Fermi level (± 2 eV), particularly while dealing with intra-band electron-electron interactions (not optical).

Island metal films (IMFs) have previously been investigated mainly on dielectric substrates like SiO_2. This approach exploits the *unwettability* of dielectric surfaces by metals to assist island formation. A detailed description of IMFs and their exceptional properties can be found in ref.[137] and papers cited therein. Only a few reports have been made for IMFs on semiconductors, and they have somehow not been introduced in mainstream microelectronic technology. This is probably because the conventional method used in preparing IMFs by electroforming is not scalable. However, IMFs seem to have several engineering applications in areas of sensing, catalysis, switching, and energy conversion. IMFs are typically reported from electroforming thin metal films (< 10 nm thick). Usually Au or Ag is evaporated onto a small gap (≤ 10 μm) between two thick contact electrodes (~100's nm), shown schematically in Fig. 6.1-a. A high voltage (20-30 V) is applied between the contacts for 2-5 minutes. Current initially flows in the thin metal with high resistance, prior to island formation (destructive step). Current density of the order of 10^6 A/cm^2 causes electro-migration in the thin metal layer, accompanied with Joule heating. There is also thermal migration of atoms. Nanoscale percolation channels

are formed, composed of sub-10 nm metal islands. The inter-island separation is on the order of nm and tunnelling processes between islands dominate conduction beyond this stage. The thin film is irreversibly transformed into a dispersed material that demonstrates a switching behaviour like semiconductors (low and high resistance states). Once electroforming is complete, the low resistance state is onset at much smaller voltages (5-10 V) than that needed

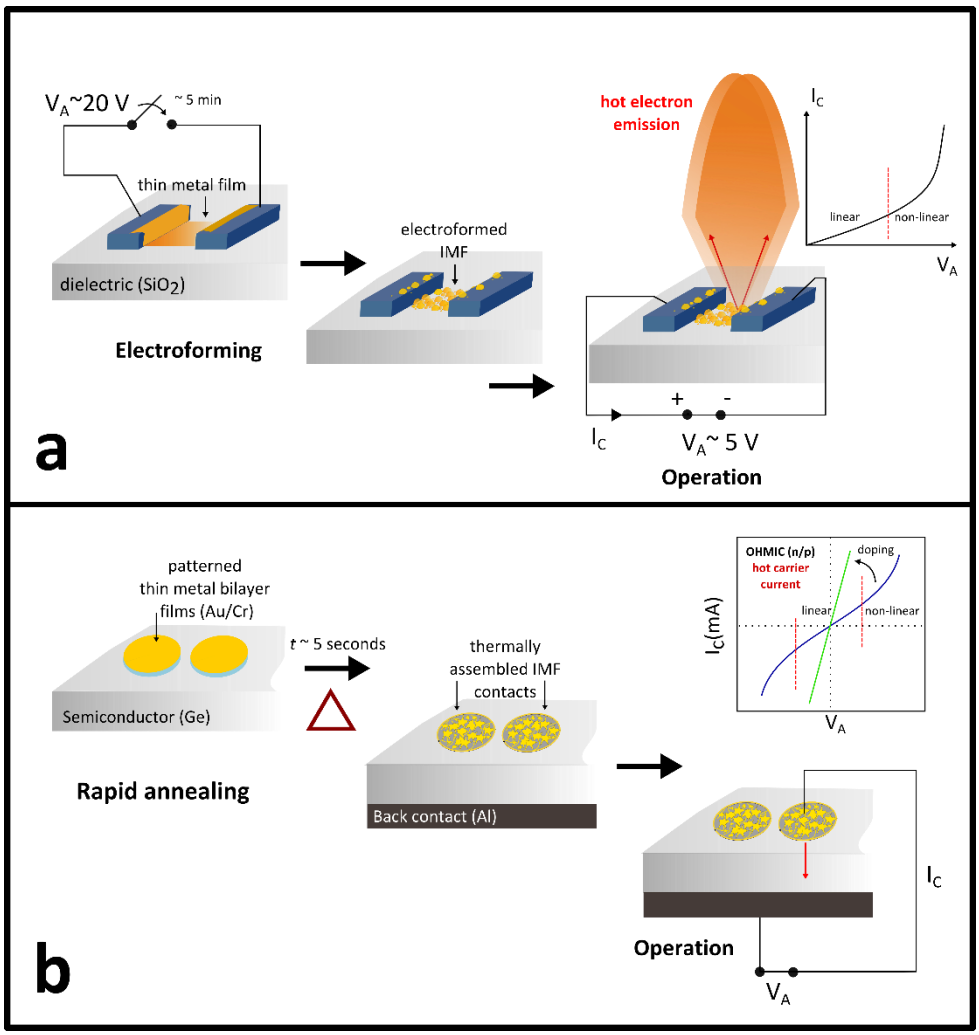

Figure 6.1:a. Traditional IMF prepared by electroforming. After IMF is formed, feeding power into the system results in hot electron emission. **b.** Thermally assembled IMF (this work) formed by rapid annealing thin Au/Cr bilayers.**c.** Electrically biasing the IMF relative to the substrate (large area back contact) results in hot carrier injection, circumventing the Schottky barrier.

for the electroforming step (20-30 V). Typical I-V characteristics of the IMF are shown schematically in Fig. 6.1-a. Non-linear I-V characteristics are observed when the IMF is electrically biased between contacts. Borzjak *et al.*(1965) first discovered that the non-linear tunnel current in IMFs is accompanied with electroluminescence and electron emission phenomena[138]. Several decades of work and numerous experiments led to the development of various models to explain these observations, advocating either field emission[139] or non-equilibrium electron heating in islands[140]. The field emission model[141] was found to be inconsistent with some experimental findings - There is poor correlation between conduction current across the island film and emission current into vacuum and this contradicts the main premise of the field emission model, where the emission current is treated as a part of the

conduction current that was diverted towards the collecting anode[142]. The collecting anode voltage does not alter the emission peak energy significantly. Moreover, the electron emission into vacuum was not observed using externally applied electric fields alone (without current excitation). The second model of non-equilibrium electron heating describes the observed phenomena quite convincingly. Power is fed into small metal nanostructures, either electrically or optically, which increases the electron temperature (T_e) in the metal. This is accompanied with an increase in conductivity in the IMF, as well as electron emission into vacuum. Hot electron emission originates at IMF surfaces, with energies comparable to the workfunction (Φ_M) of the active nano-islands. The steps leading up to this process are described in terms of ballistic electrons in metal nanostructures exchanging heat with incident tunnelling electrons. A similar mechanism will also improve conductivity in semiconductors because IMFs emit hot carriers that can easily overcome the Schottky barrier in semiconductor/ metal junctions. The yield of hot carriers depends on the power fed into the IMF. This chapter documents new evidence of IMFs formed by rapid annealing thin Au/Cr bilayers on Ge. In Chapter 5, a 3 nm Cr adhesive layer was used. Here the Cr layer used is 5 nm thick. A thicker Cr layer is used to exploit stresses (N/m^2) arising from surface energy mismatch at the bilayer interface. If a thin Au layer (~ 100 nm or less) is evaporated over 5 nm Cr the annealing process yields a network of IMFs on Ge, shown schematically in Fig. 6.1-b. Increasing Au thickness for the same process eventually presents a coalesced continuous metal film (CMF) albeit with significant eutectic events occurring during the annealing schedule. The first results section presents a few material studies describing IMF and CMF systems on Ge. HRSEM surveys, Energy filtered transmission electron microscopy (EFTEM), Electron backscatter diffraction (EBSD) and Scanning Transmission electron microscopy (STEM) experiments (in High angle annular dark/bright field modes/ HAADF[BF]) were done by Dr. Karl Dawson at Liverpool University. Phi-scan X-Ray diffraction experiments were done by Dr. Mikko Heikkilä and Dr. Peter King at the University of Finland, to complement EBSD studies. These data help understand the complex material structure of the thermally assembled IMF on Ge.

6.2. Results I: Material characterization

6.2.1. Annealing results in encapsulated Au/Cr nanostructures

According to Fick's law of diffusion, the time to diffuse through a material over a small distance is inversely proportional to the diffusivity of the migrating species. Cr atoms typically have diffusivities of the order of 10^{-12} m^2/s and diffuse into Au quite readily[143], covering a distance of 1 µm in only ~ 0.5 s. At finite temperatures, Cr will almost certainly diffuse into the

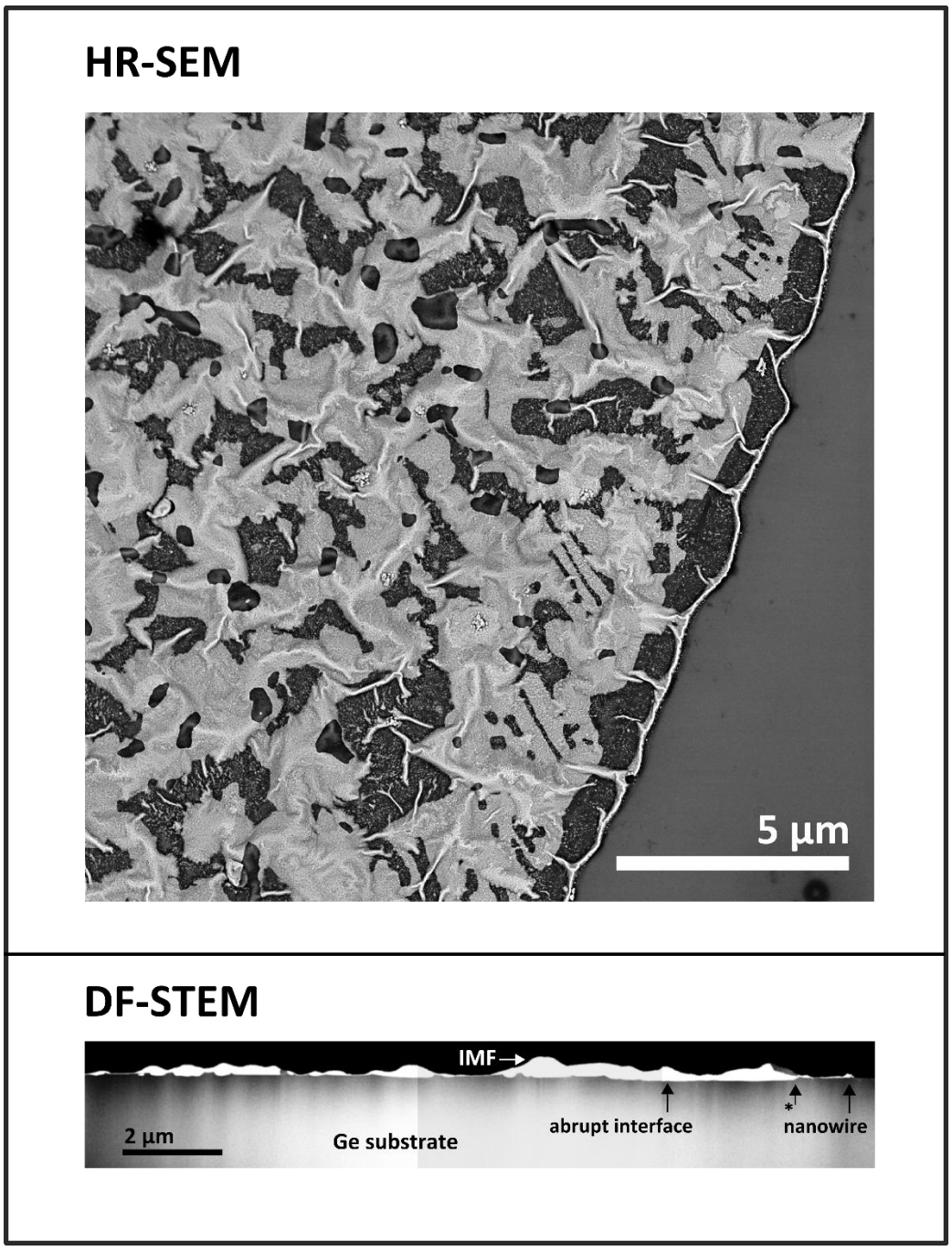

Figure 6.2: **Top panel:** HRSEM of a patterned Au/Cr contact containing IMFs prepared by rapid annealing. Buckled Au clusters and nanowires form within the pattern. Dark regions are Ge. **Bottom panel:** Abrupt interface is observed in cross section HAADF-STEM. Film folding and retraction processes result in a nonuniform topography.

Au lattice and this process cannot be stopped unless barrier layers are used. This process is further accelerated during annealing, as diffusion processes are highly temperature sensitive. Cr diffusion into Au thin films usually improves adhesion but rapid annealing very thin Au layers also causes film delamination and folded edge formations[144]. Although annealing the

Au/Cr/Ge material system favours (110)Au crystallization, increasing the Cr layer thickness beyond its coalescence limit results in higher internal stresses at the final Au/Cr interface[145]. The intrinsic stress arising from surface energy mismatch is expected to be lower for 3 nm Cr interlayer used in the previous chapter compared to a fully formed 5nm Cr film. Surface energy and surface stress are closely related quantities[146]. At 0 K, DFT computations show that (100)Cr has much higher surface energy (3.9 J-m^{-2}) than (110)Au (1.7 J-m^{-2}) while experimental measurements performed at the melting temperature of these metals find that the surface energy of Cr and Au are 2.3 J-m^{-2} and 1.5 J-m^{-2} respectively[147]. The surface energy mismatch causes delamination in thin Au/Cr films under thermal stress. Experiments show evidence of folded Au clusters surrounded by nanostructures that qualify as IMFs in the traditional sense (after Borzjak *et al*) because these are dispersed media and exhibit non-equilibrium electronic properties. A key difference in this method and traditional IMFs described previously, is the wettability of the substrate. In this study, the as-deposited Cr layer is sufficiently thick (5 nm) to ensure the evaporated film would have coalesced more uniformly-*enabling* Au/ Cr wetting on Ge.

Au was deposited by e-beam evaporation over a 5 nm Cr adhesion layer on patterned Ge substrates, using the standard method described in Chapter 3. Contacts were formed, followed by rapid annealing for 5-10 s at 400-450 °C. Fig. 6.2 shows the process outcome for 100/5 nm Au/Cr close to a circular patterned edge. The initially planar film has retracted during annealing, along with regions where the Ge is segregated in Au (dark regions within wrinkled clusters). The initially continuous film develops holes, exposing the substrate underneath (darker patches). A web of raised Au formations is observed among holes and buckled Au nanowires. The Au film develops conical projections in the substrate normal direction, forming a heap due to expanding holes. The contact surface is not flat and this is observed in the HAADF STEM image shown in the bottom panel. Liquid transport during annealing results in an abrupt sunken interface.

Film folding, bending and retraction are energy minimizing processes, known to occur in several material systems and lead to intricate features arising from self-replicating processes[144][148]. Fig. 6.3(a) illustrates a step (dashed line) undergoing retraction. (image source: ref. [148]). Dewetting occurs at triple interfaces (where the film and ambient meet the substrate), providing a net material flux (*J*) to minimize the step curvature and forms a mound. (b) Because the curvature of this region is higher than the flatter region ahead, (c) mass transport continues, (d) to eventually form a hole. This rolling process (a-d) repeats at the newly formed

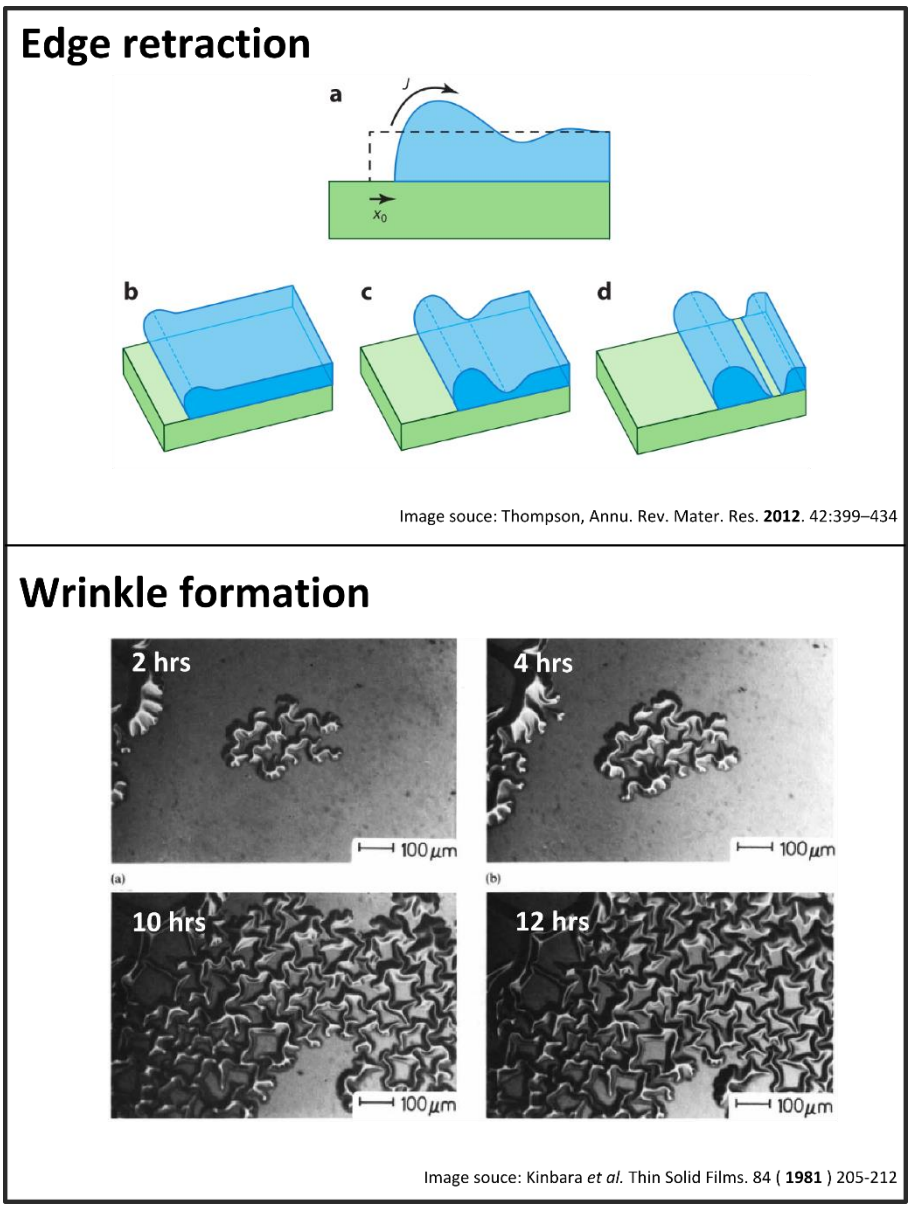

Figure 6.3: Top panel: Schematics (**a-d**) illustrating film retraction at sharp edges (e.g. step - dashed line), proceeding into wire formation- reproduced from ref.[148]. **Bottom panel:** photographs reproduced from ref. [149] showing wrinkle formation on an 80 nm thick carbon coating on glass at room temperature in atmosphere. Wrinkles emerge from a single nucleation site and sweep the entire film over time.

edges, to form increasingly intricate structures. Meanwhile, differences in thermal expansion of materials creates stress and causes wrinkle formation. This process occurs in several materials, an example is shown from ref.[149] where thin carbon films (80 nm) on glass were shown to develop wrinkles at room temperature due to internal stresses. The effect of rapid annealing is to accelerate all the above processes- Cr diffusion into Au, edge retraction and wrinkle formation, in addition to selective uptake of liquid Ge from cracks/ defects in the delaminated Cr film. This causes the film to break apart and create a web pattern.

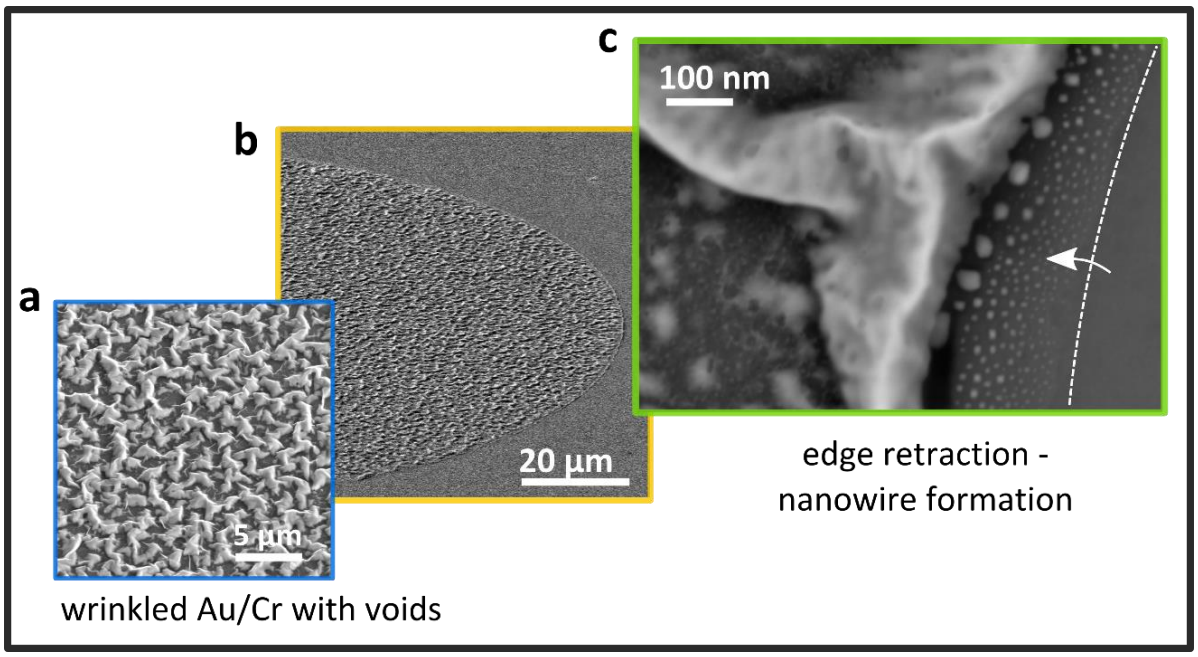

Figure 6.4: Detailed views of the thermally prepared Au/Cr IMF on Ge- a. web of wrinkled Au clusters separated by holes in the patterned film (**b.**). **c.** Edge retraction forms nanowires at patterned edges (dashed line) and retracted cluster boundaries within the film. A distribution of closely spaced self-similar Au nano-islands is observed at edges and within expanded holes.

Large clusters serve as nodes and typically have prong like protrusions, interconnecting other clusters and nanowires, notably following the lithographically patterned step at the boundary, where the process begins. Hot Au/Cr edges under retraction produce a carpet of nanosized clusters with a self-similar fractal appearance. Detailed views of the thermally assembled IMF are shown in Fig. 6.4. The retracted edges and wrinkled clusters form a semi-continuous metallic entity, while the nano-islands decorate its periphery. When the annealing process stops and cooling begins, the molten crystals reorganize to produce highly (110) oriented Au island metal films (IMFs) on Ge. The final moments of this complex material rearrangement are preserved in the crystallized solid phase, observed in TEM (Fig. 6.5).

HAADF/BF modes in STEM allow observation of z-contrast, which helps identify material interfaces in the specimen. High resolution HAADF measurements of a Au cluster are shown in Fig. 6.5-a, next to an incompletely formed Au nanowire (in the green box). Liquid Ge spills over the Au cluster when the original Cr interface cracks under compressive stress. The mass exchange causes the Au/Cr clusters to sink into the liquid Ge interface. An outline of the original Cr interface (~ 5 nm), before displacement is marked in the image (dashed line).

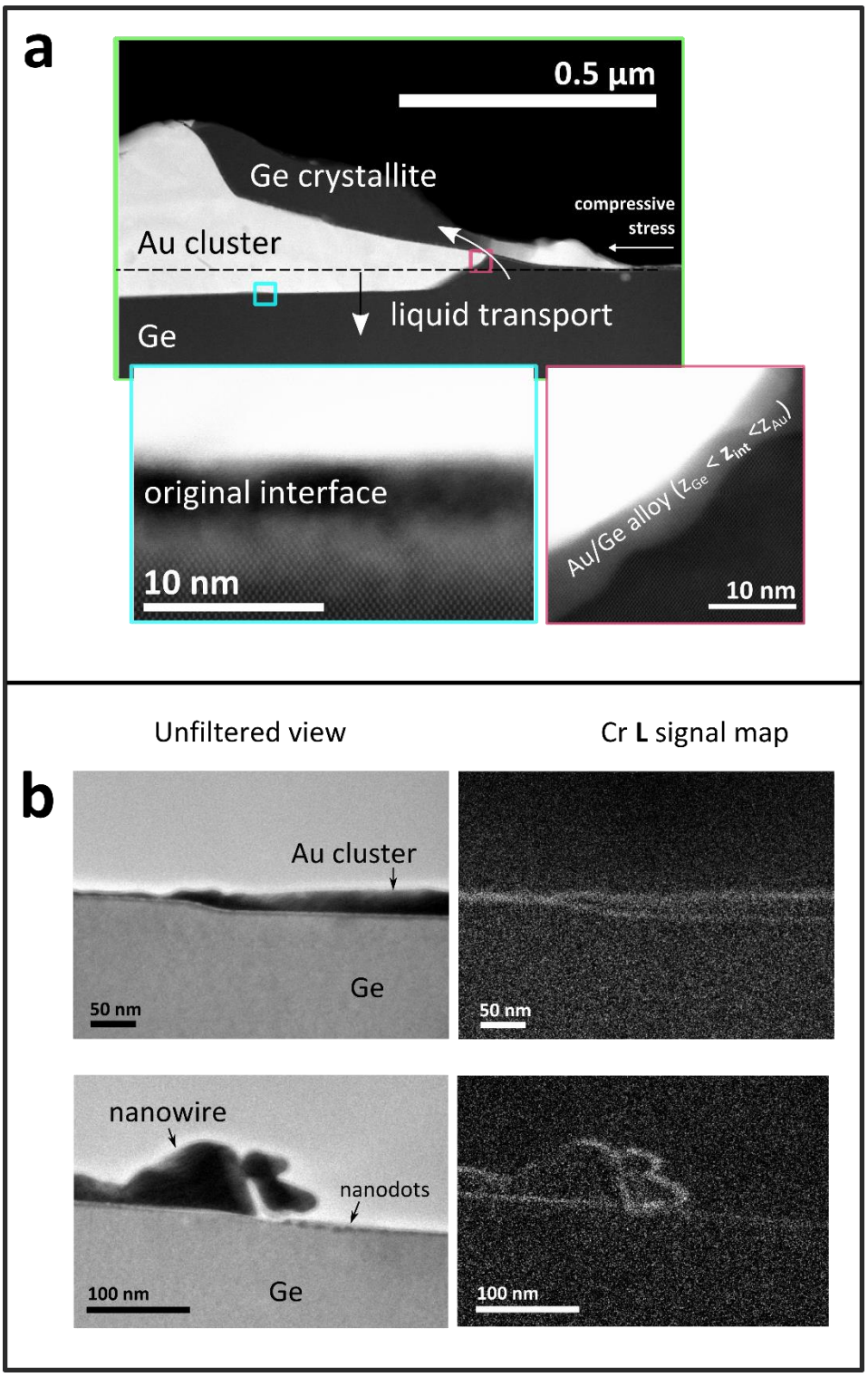

Figure 6.5: a. High resolution HAADF-STEM cross-section of a Au cluster captures the details of material formation. The Au clusters sink into the Ge substrate (~100 nm) displacing liquid Ge out of cracks formed in the original Cr interface. **b.** Cr encapsulation of Au geometries confirmed in energy filtered TEM (EFTEM), by reconstructing images using only electrons corresponding to the Cr **L** signal. Cr encapsulation occurs on all Au geometries. The migrated Cr causes further deformation in hot nanowire structures and the folding process is seen to progress to form smaller cantilevered nanowires. These observations indicate Cr diffusion in Au is faster than the film retraction process.

If the annealing proceeds above the Au/Ge eutectic temperature ($T_{Au/Ge}$) over an extended period, liquid Ge completely encapsulates Au/Cr clusters[94][150] and imbed the folded clusters (not shown) into the Ge substrate. Hot Ge/Au clusters formed by annealing thin Au/Ge bilayers have previously been shown to form an amorphous Ge shell layer over imbedded Au[94]. Because the Cr layer is subject to cracking (red box), hot Au comes into direct contact with Ge rushing out. An intermixed light interface ($z_{Ge}<z_{int}<z_{Au}$) is marked in the HAADF TEM image. This is not observed in other regions (blue box) where the original Cr interface acts like a barrier. The Au clusters sink into the substrate along with the original interface. It is inferred that all Au clusters with dark Ge spots in Fig. 6.2 have cracked the surrounding Cr layer during formation.

Cr encapsulates all Au structures due to thermally accelerated diffusion. The Cr covered surfaces would have oxidized upon exposure to atmosphere. Energy filtered transmission electron microscopy (EFTEM) results for the cross-section are shown in Fig. 6.5-b. The column on the left shows the unfiltered view and the right column shows the reconstructed image using Cr **L** intensities only. Two regions (i) Au cluster (prong) from the interior region of the contact pattern and (ii) the nanowire formed at its retracted pattern edge (see Fig. 6.4 for plan view). The Cr signal map clearly shows complete encapsulation of the Au nanostructures.

Interestingly, additional reshaping is apparent within the nanowire itself. Cr diffuses very quickly in Au and reaches the periphery of the clusters, while the film is still undergoing retraction. The thermal stress in these diffused Au/Cr interfaces continues to fold the structure at least until annealing is complete. A rigid cantilever formation is seen above a trail of nanodots (~ 2-10 nm). Closely spaced nanodots decorating clusters/wire formations serve as the active elements in the IMF and their importance will be discussed later in the second results section.

The entire IMF is sinking into the substrate as the annealing proceeds to exchange Ge to the surface. The nano-islands surrounding the cluster and wire boundaries are vital to hot carrier effects but these may be lost under the Ge surface if the rolling process continues (>10 s) at peak temperatures > $T_{Au/Ge}$. Purified Ge crimp layers encapsulate the sinking Au clusters[95]. Ge crimp layers outlining the light Au structures appear in all the HRSEM images shown in this work as darker regions, compared to the Ge substrate outside the contact pattern (see Fig. 6.2).

Inferences:

IMF fabrication by rapid annealing is a highly temperature sensitive process and needs to be carefully controlled to prevent nanostructures from completely sinking into the substrate[150].

When this happens, the hot carrier effects are not observed electrically. This level of sophisticated control is not easy to achieve using standard annealing equipment as the annealing trials were already kept short < 10 s at peak temperature. Several trials were necessary to obtain usable IMFs repeatedly. Only electrically active IMF specimens were selected for investigations carried out externally (at Liverpool, R.H.U.L.) and for supporting crystallography experiments at Helsinki University.

6.2.2. Texture and crystallinity of thermally assembled IMFs

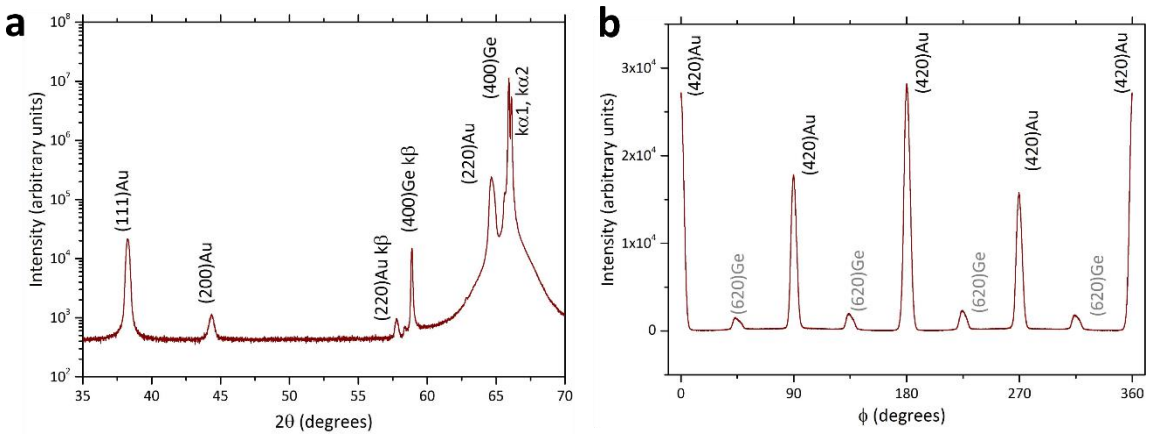

Figure 6.6: a. XRD diffractogram of an IMF contact. The intense peak at 2θ = 65° indicates predominantly (220)Au crystallization. Other identified phases have also been annotated **b.** XRD phi (ϕ) scan of the (420)Au plane demonstrating the registration of the IMF to the Ge substrate. (620)Ge plane substrate peaks appear offset 45° to the Au signal, confirming the orientation relationship (100)Au//(110)Ge.

The theta-2theta (θ/2θ) X-ray diffractogram of the Au IMF contact is shown in Fig.6.6-a. The (220)Au is the most intense reflection indicating a preferred orientation with (110)Au planes arranged parallel to the (100)Ge substrate. Further analysis with an XRD phi-scan measuring the (420)Au plane (Fig.6.6-b) shows clear epitaxial arrangement with peaks occurring every 90° of rotation around the surface normal. (620)Ge substrate contributions to the scan are also seen, offset by 45°. Corroborating field emission gun scanning electron microscopy/ Electron backscattered diffraction (FEG-SEM) / EBSD analysis done at Liverpool (not shown) indicated two strong orientation relationships in the IMF film: [110]Au//[001]Ge and (100)Au//(110)Ge. (EBSD) texture scans confirmed that (110)Au crystals were the dominant orientation over entire patterned areas with some dispersed (111) regions. Despite the distributed nature of the IMFs, heteroepitaxy is observed similar to hybrid films in Chapter 5.

6.2.3. Transition to continuous metal films (CMF)

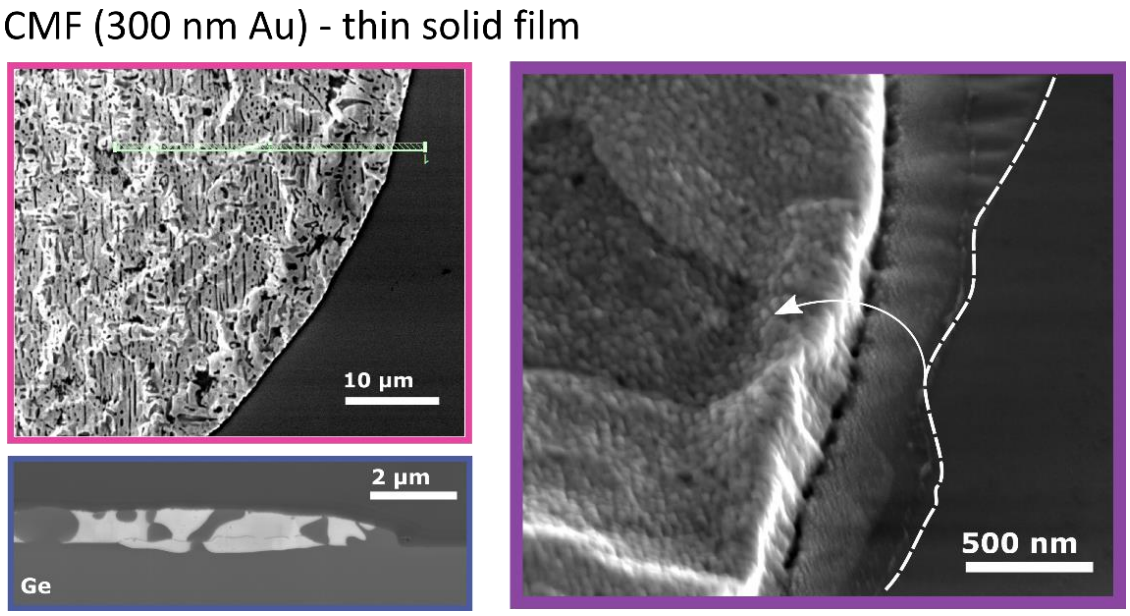

Figure 6.7: Detailed views of thick (300/5 nm) Au/Cr using an identical rapid annealing process used for the IMF produces a eutectic mixed thin solid film.

The (110)Au crystallinity will enhance hot carrier lifetime. But the formation of nanostructures is necessary for observation of hot carrier effects by current excitation. Thicker Au films may or may not crystallize into predominantly (110) form. The rapid annealing process is quite unpredictable for thicker Au films. On separate occasions, different annealed 300/5 nm Au/Cr specimens on Ge presented distinct results – one specimen had predominantly (110) Au and the other showed no preferred texture (see Fig. S3-a in ref. [43]). There is a considerable internal delamination of Cr and the Ge segregations appear chaotic. However, neither specimen showed hole formations within patterned areas. Nano-island and nanowire formations were not observed within or surrounding the patterned areas. Edge retraction is observed at the pattern boundary, leaving behind a trail of nanodots beyond the new boundary (outside the CMF contact). The process outcome is a eutectic mixed thin solid film that has electrical properties like planar metal film contacts on Ge (shown in electrical results). Fig. 6.7 shows detailed views of the annealed Au/Cr CMF on Ge in HRSEM and cross-section HAADF/TEM. There is evidence of film retraction (dashed line) and liquid transport. Metal nanostructures are absent and hole formations are not observed. Wrinkle formation is observed and the film is raised in places. These regions appear brighter in SEM. The dark boundary and ripples around the contact suggests evidence of the CMF also undergoing a considerable displacement into the substrate, pushing out purified Ge crimp layers.

6.3. Summary I

Material characterization using TEM, XRD and EBSD provides a physical description of the thermally assembled IMF and CMF. Internal stresses at Au/Cr interfaces, in addition to film retraction processes reshape the initially planar metal film. Cracks in the Cr layer allow liquid Ge transport/ spillage over the original interface. Even in the annealed CMF case (300/5 nm Au/Cr), there is a significant eutectic mixing as seen in HRSEM and in cross section studies using TEM. A larger part of the contact interface to the Ge substrate appears abrupt, due to liquid transport dominating over diffusion across the Cr barrier layer. Au sinks into the substrate over the course of annealing because of outward Ge transport (above the original Cr interface).

Only thin Au films form IMFs that provide enhanced conductivity. The annealing process needs to be kept short in order not to lose the Au nanostructures beneath the surface. If the annealing process (> $T_{Au/Ge}$) continues >> 10s, the IMFs are lost beneath the surface, along with their associated hot carrier effects. The exact reaction kinetics occurring over the annealing schedule were not studied and this requires further investigation. Extensive simulation work may serve as a guide to improved annealing recipes. Sensitive temperature control may prevent cracking in the Cr layer and therefore, prevent the contact from sinking into the substrate. The nanostructures would presumably still form by retraction and would be saved using such a methodology. The Cr layer would still assist predominant (110) Au crystallization. Moving on to alternative annealing techniques such as pulsed laser annealing will improve results significantly. Further studies are required to controllably reproduce thermally assembled IMFs. The next results section documents novel electrical behaviour provided by successfully prepared IMFs on Ge.

6.4. Results II: Electrical characterization

6.4.1. Hot carrier current – size effects of metal nanostructures

For short annealing routines, the final material depends on the initial metal film thickness. Very thin metal films (<10 nm) on dielectrics are known to form isolated islands (Volmer Weber growth), even during deposition[151]. This occurs alongside delamination and de-wetting processes described in the previous results section. As the film thickness increases, larger clusters form and eventually coalesce into a continuous film. Au thickness plays a crucial role

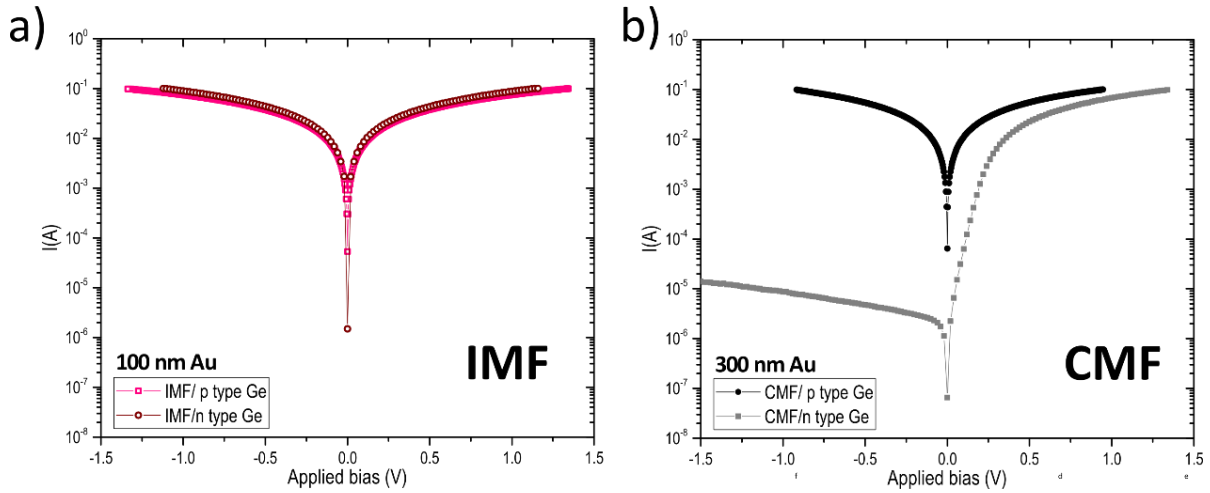

Figure 6.8: a. Room temperature I-V characteristics of island metal film (IMF) contacts to moderately doped n-Ge (N_D~ 1 × 10^{17} cm^{-3}) and low doped p-Ge (N_A~ 5.6 × 10^{14} cm^{-3}). Ohmic contact is achieved using the same contact material on both substrates. **b**. Room temperature I-V characteristics of continuous metal film (CMF) contacts using thick Au/Cr annealed contacts to n- and p-Ge. Ohmic characteristics are observed for p-Ge but the contact to n-Ge is rectifying, consistent with FLP in Ge.

in the size distribution of Au islands for annealed Au/Cr bilayers and this directly affects the observed electrical properties of these contacts.

Au/Cr IMF and CMF contacts were fabricated on both n^-, n- and p type Ge specimens in each experimental trial to ensure the same conditions were applied to both substrates. Concurrent ohmic contacts are shown in Fig. 6.8-a using patterned structures (d ~ 300 µm) containing IMFs on moderately doped n-Ge (N_D ~1 × 10^{17} cm^{-3}) and low doped p-Ge (N_A ~5.6 × 10^{14} cm^{-3}). The IMFs formed within the patterns were electrically excited/ biased by direct probe contact, additional patterned top contacts, as well as wire bonded top contacts (shown later). The probes used to perform electrical measurements on the IMFs come into direct contact with the network of larger Au clusters. Like results shown in chapter 5, the contacts on p-Ge remain Ohmic after processing while the n-Ge conductivity is modulated exclusively. This again suggests that improved conductivity on n-type Ge cannot be attributed to Fermi level depinning. Instead it is attributed to hot carriers circumventing the Schottky barrier. On the other hand, CMF contacts (Fig. 6.8-b) present characteristics of FLP, with rectifying n-Ge

contacts and Ohmic p-Ge contacts. The influence of increasing Au thickness on electrical properties was investigated. The results are shown for three Au thicknesses in Fig. 6.9. Only the n-Ge series shows a change in conductivity, as expected. The p-Ge contacts remain Ohmic regardless of Au thickness and processing conditions, because the FLP condition is unchanged. This suggests the hot carrier production increases for thinner Au layers. The size of the average

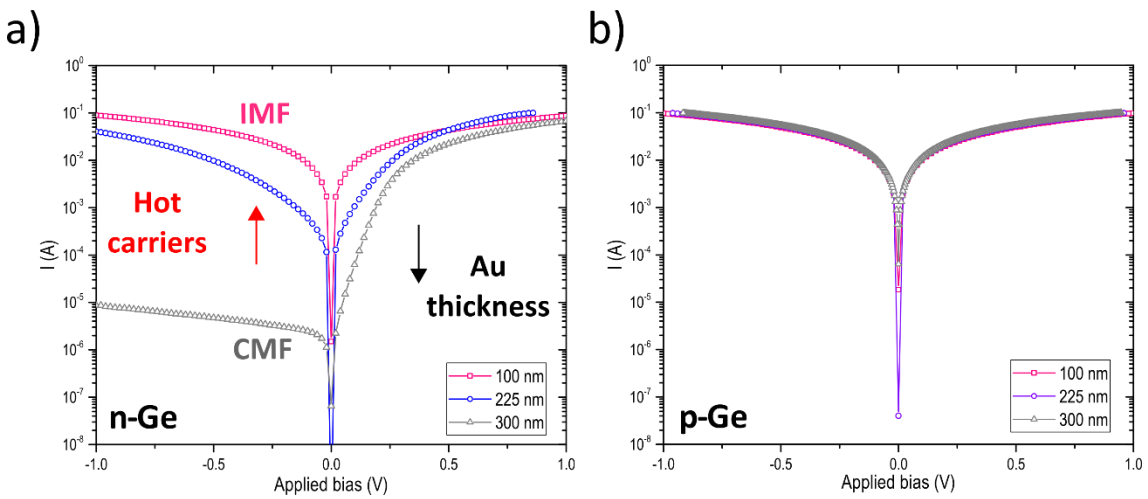

Figure 6.9: a. Hot carrier emission over the n-Ge barrier increases for decreasing as deposited Au thicknesses, corresponding to a smaller average island size formed after annealing. CMF contacts are rectifying, as expected. **b.** Contact to p-Ge is independent of island size and film thickness.

de-wetted clusters must be comparable to the initial film thickness. As the film thickness is increased, larger clusters grow at the expense of smaller ones (Ostwald ripening). Hence, the density of smaller nanostructures required for observable hot carrier effects must decrease. Hence, the reverse current follows a trend against Au thickness (almost linear, not shown), indicated using arrows in Fig. 6.9-a. The transition from IMF to CMF behaviour exclusively on n-Ge confirms that the nanostructures play a crucial role in improving conductivity. However, simply evaporating thin Au films on Ge does not produce Ohmic contacts, or at least there is no report on this in the literature, indicating that the Cr layer also plays a role. As stated in the previous chapter, the Au/Cr interface sustains a permanent dipole owing to differences in metal workfunction, causing electron accumulation on the Au side of the interface. This is likely to be an active element in the functioning of IMFs. Further experiments on metal bilayers using tilted target sputtering may shed light on this topic. The outcome of the rapid annealing process in this work can be visualized schematically according to Fig. 6.10-a. As the initial Au thickness is increased, the final product changes from isolated islands to IMFs and then finally CMFs. As shown in Fig. 6.9-a, only the IMFs exhibit hot carrier effects. This can be understood in terms of the way heat is exchanged in small metal nanostructures.

Normally, the electron and lattice subsystems are in equilibrium. Electron and lattice temperatures reach equilibrium via electron-phonon interactions. For nanoscale metal islands, electron-phonon interactions become limited by the cut-off Debye frequency ($\omega_{D\infty}$) in the phonon spectrum of the metal. Electron motion becomes ballistic in nanostructures having

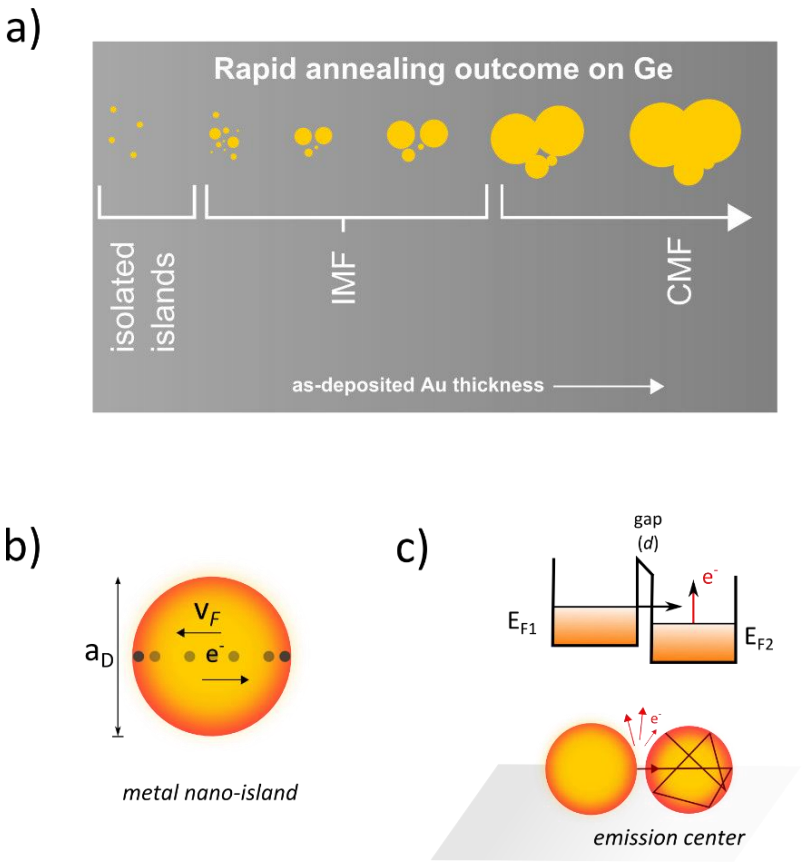

Figure 6.10: a. Schematic showing the outcome of rapid annealing on the recrystallized material as the initial Au thickness varies. **b.** Ballistic electrons undergo specular/ elastic reflections in a metal nano-island of critical dimensions (a_D) corresponding to the cutoff Debye frequency of the metal. **c.** Schematic showing how tunnelling current in IMFs causes non-equilibrium electron heating, resulting in hot electron emission

critical dimensions below the electron mean free path. The size limit (a_D) corresponding to $\omega_{D\infty}$ is sketched schematically for the case of a metal nano-island in Fig. 6.10-b. A simple calculation using the cut-off Debye frequency of Au ($\omega_{D\infty}$) ~ 10^{13} Hz and Fermi velocity (v_F ~ 10^6 m/s) shows that $a_D = \frac{v_F}{\omega_{D\infty}}$ ~ 100 nm. Consequently, nanostructures smaller than this size would be susceptible to non-equilibrium electron heating effects. Rapid annealing of e-beam evaporated Au thin films (< 100 nm thick) without Cr on Ge produces small Au clusters but they are separated by gaps too large for tunnelling to be an efficient current mechanism. Introducing a thin Cr layer dramatically alters the outcome of annealing. Ensembles of closely spaced nano-islands and nanowires develop within patterned regions on Ge around the edges of holes, wherein hot carrier effects are expressed.

A network of such closely spaced metal islands separated by gaps $d < 5$ nm constitutes an island metal film (IMF). A simple case is shown schematically in Fig. 6.10-c for two metal nano-islands. Under bias, tunnelling electrons arriving at the right-hand metal nano-island undergo

electron–electron interactions with ballistic electrons. The power fed into the receiving island gives rise to hot electrons and holes, broadening the Fermi distribution. Groups of such closely spaced metal islands behave as hot electron *emission centers*[137]. Therefore, when a sufficient potential difference is applied to the IMF, hot electrons are emitted from the metal surface into the lowest available energy states in the semiconductor, or into vacuum. This scenario contrasts the typical case of bulk metal contacts, where the electron and phonon sub-systems remain in equilibrium and the Fermi distribution depends mainly on the ambient temperature, provided the substrate has good thermal conductivity. Fig. 6.10-c shows a special case of equally sized nano-islands capable of exhibiting non-equilibrium electron heating. However, the principle of non-equilibrium electron heating applies to small nanostructures and is equally valid for unequally sized nano-islands of critical dimensions[152].

Inferences:

The size range for IMF hot carrier production has been identified. Nanostructures are capable of non-equilibrium electron heating effects. Closely spaced metal nanostructures/ IMFs below a critical size behave as emission centres. The IMF contact does not change the condition of FLP in Ge and improvements in conductivity are completely attributed to size effects and electron heating in nanostructures. CMFs do not possess the nanostructured arrangements required for evoking hot carriers and retain characteristics of FLP, like conventional planar contacts.

6.4.2. Voltage controlled hot electron emission in IMFs

Particularly on Ge, since FLP is severe, the distributed nanostructures, as well as the web of clusters will have the Fermi level pinned close to the Ge valence band. Hence, contacts to p-Ge are Ohmic while on the other hand, there is a profound size effect for contacts on n-Ge. The negative surface charge on n-Ge will create a distribution of built in potentials between nanostructures due to screening effects. Consequently, the vacuum level will adjust spatially over the contact, creating electrostatic barriers between neighbouring nano-islands. This is not easy to measure, although techniques like high resolution kelvin probe force microscopy (KPFM)[153] may provide an answer.

Hot electron emission into vacuum is typically observed in IMFs[137] using a lateral biasing setup, shown schematically in Fig.6.11-a. for a single chain of equally spaced nano-islands. The gap between electrodes is typically ~10 µm and the gap between islands is small (≤ 5 nm).

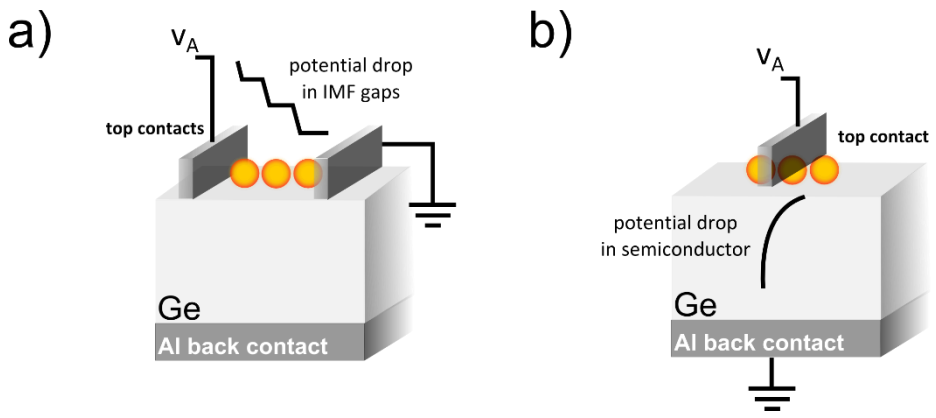

Figure 6.11: a. Schematic illustrating potential drop in the IMF for lateral biasing. **b.** Schematic illustrating potential drop in the semiconductor for vertical biasing (IMF/ semiconductor), with only mV potential drop needed vertically for hot electron emission into the semiconductor.

For typical bias voltage (1-10 V) the applied electric field is on the order of 10^3 -10^4 V/cm. This field by itself is insufficient to provoke field emission into vacuum. Higher *local* electric fields may exist between the IMF gaps, thereby allowing tunnel current to flow through the chain. As described previously, electron-electron interactions result in a broadening of the Fermi distribution in the islands. The electron temperature can reach thousands of Kelvin by this mechanism. However, the lattice remains stable (does not evaporate), owing to high thermal conductivity of the substrate and the relatively large surface area/ volume ratio of nano-islands. Electron emission into vacuum is a relaxation mechanism and is sustained in the steady state.

It is recalled that the thermally assembled IMF in this work is composed of a web of larger Au clusters, surrounded by smaller nano-islands in hole formations within patterned areas. In the electrical data for IMFs shown in Fig. 6.8-6.9, the larger cluster network is biased relative to the Ge substrate. This picture is simplified in the schematic shown in Fig.6.11-b, where an equally sized island chain is excited vertically, using only one probing contact. The second probe is connected to the Al back contact. In contrast to the lateral biasing case (Fig.6.11-a), here the potential is mainly dropped in the semiconductor. However, the electron heating effect will occur in smaller nanostructures near the cluster boundary, providing the observed hot carrier currents. To test this hypothesis, the IMFs were tested for hot electron emission into vacuum.

Additional Ti/Al (80:20) top contacts shown in Fig. 6.11-a. were patterned over the IMF and CMF contacts on low doped n^- Ge to perform control measurements. The gap between the back-to-back top contacts is ~10 µm. This allows lateral biasing of the metal contacts, like the schematic shown in Fig. 6.10-a. The specimens were loaded in our (Thermo Fisher Scientific)

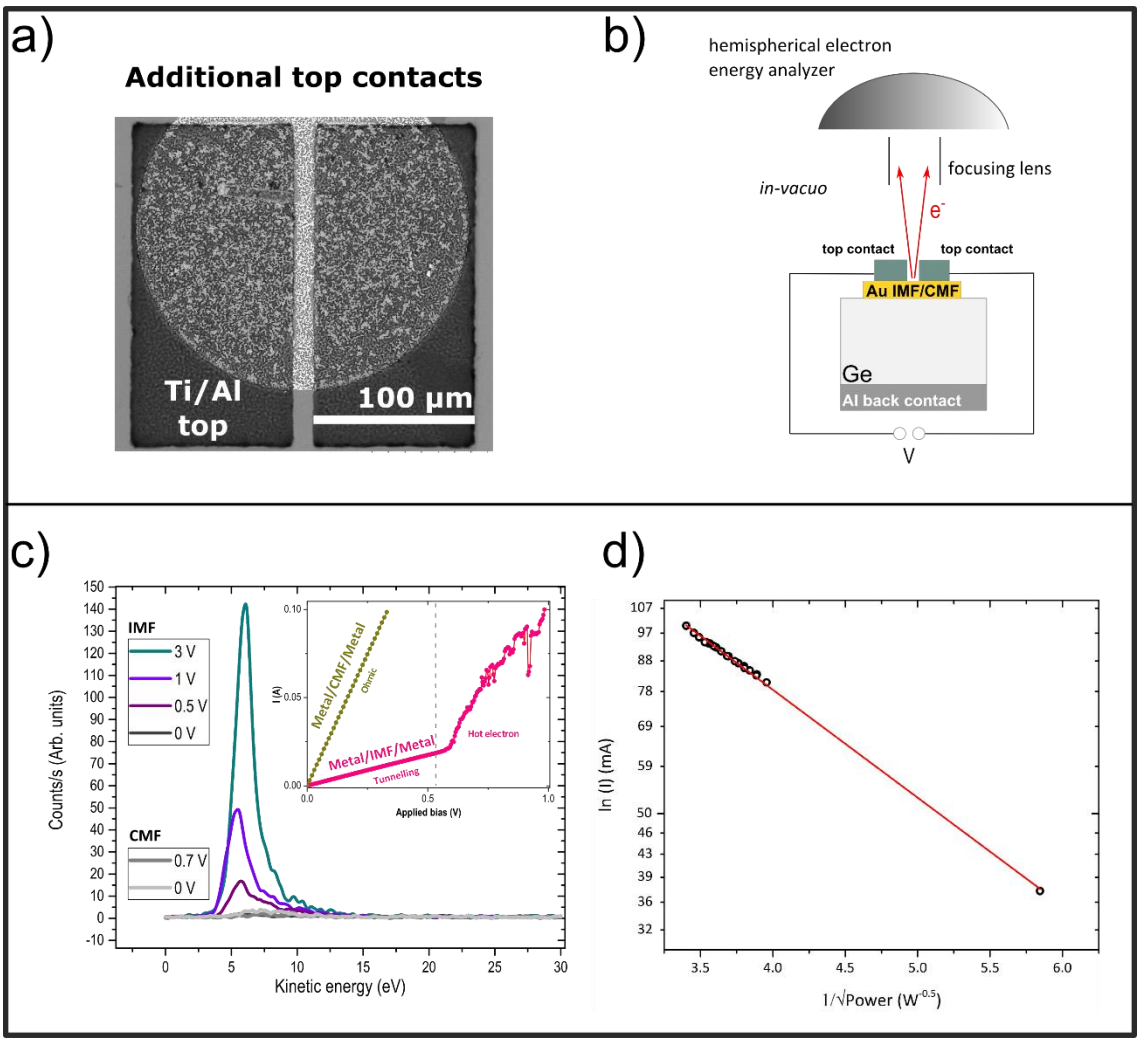

Figure 6.11: a. SEM showing additionally patterned Ti/Al top contacts on the IMF. The gap between top contacts is ~10 µm. **b.** Schematic of the experimental setup used to detect hot electron emission into vacuum by laterally biasing a 10 µm region containing IMF or CMF on Ge. **c.** Electron emission spectra from IMF and CMF at various applied bias, showing that there is only hot electron emission from the IMF. Inset shows I-V characteristics of the IMF and CMF showing their respective conduction modes. Higher resistance in the IMF case at low voltage is due to tunnelling conduction across islands, prior to the onset of hot electron emission. **d.** Semi-ln plot of hot electron current in the gap against the reciprocal square root of power (V.I) fed into the film. A linear relationship is observed, consistent with the theory of carrier heating in IMFs.

theta probe X-ray photoelectron spectrometer, fitted with electrical feed-throughs for *in vacuo* electrical measurements. Electrical excitation was supplied by a Keithley (2600) Source Measure Unit (SMU). Measurements were performed (with Dr. Billy Murdoch at SEAL, Newcastle University) at ambient temperature with a background pressure < 1 x 10^{-7} mbar. The X-ray and flood gun (charge compensation) sources were disabled during acquisition. The measurement setup is shown schematically in Fig. 6.11-b. Electron emission spectra were collected under electrical excitation of the IMF gap, shown in Fig. 6.11-c. at ambient

temperature *in vacuo* for IMFs and CMFs using a hemispherical electron energy analyzer at various applied biases. Hot electron emission spectra were only observed from the IMF and not from the CMF. The corresponding I-V characteristics for this measurement configuration are shown in Fig. 6.11-c as an inset. The CMF shows low resistance Ohmic I-V characteristics like a bulk metal. On the other hand, the IMF exhibits a relatively high resistance (~33 ohms) linear region for $V_A < 0.5$ V, attributed to tunnelling conduction[154] between metal islands in the gap. Conductivity increases for higher applied voltage, as the electric field within the nanostructured film becomes sufficiently large for hot electron

transport to be the dominant current mechanism. Hot electrons are emitted in this non-linear regime, at rates increasing with laterally applied bias. Hot electron emissions are not detected from the CMF (or from the IMF for $V_A < 0.5$ V). The emission spectra peak near the Au workfunction (~ 5.5 eV) using only small applied biases. These data cannot be attributed to field emission (peak energy > $q.V_A$) but are consistent with the notion of hot electrons emitted from metal nano-islands. The emission distribution appears Maxwellian with effective electron temperature T_e estimated from the variance ($\sigma = kT_e$) in the energy distribution is in the 10^3 K range. This is typical of previous observations in metal-IMF-metal arrays[137] and comparable with recently reported electron temperatures obtained from electron fed Au/Cr gap junctions[155].

The electric field corresponding to the onset of hot electron emission into vacuum is approximated by considering Fig. 6.10-a for the IMF region (~ 10 µm) between the two electrodes. The potential remains constant across metal islands and is assumed to drop lineally between metal islands. The minimum voltage for the onset of hot electron emission into vacuum is 0.5 V in this case. Then the electric field (V_A/10 µm) for the onset of hot electron emission is ~ 10^4 V/cm. A comparable electric field is needed vertically through the IMF for the contact, as illustrated in Fig. 6.10-b. By considering the simple depletion approximation, it is inferred that this minimum electric field is already present at the contact interface even for n^- Ge ($N_D \sim 6.4 \times 10^{14}$ cm^{-3}). Additionally, due to the FLP position, an inversion layer is formed under the surface, which serves as a two dimensional conduction channel over short distances[21][110]. The contact potential is mainly across to this p-type layer, which is expected to be < 10 nm wide. Hence, the vertical biasing configuration evokes the electron heating mechanism for V_A < mV, resulting in Ohmic/ symmetric conduction by hot carrier emission mainly *over the barrier*. This is verified on low doped n^- Ge, shown next.

Inferences:

Hot electrons are emitted from the IMF into vacuum when sufficient power is fed into the film. The emission yield (counts per second/ cps) increases at higher bias. The emission energy is maximum near the Au workfunction, which indicates that the emission occurs from the metal nanostructured surfaces in the IMF. The mechanism of emission is akin to thermionic emission, not field emission. The electron temperature in metal nanostructures is elevated to ~ 10^3 K range.

6.4.3. Hot carrier transport

Fig. 6.12-a. compares I-V characteristics of IMF and CMF contacts on low doped n^- Ge. The CMF contact is rectifying, as expected. Using the IMF contact, a high conductivity regime is observed (0.008 ohm.cm^2), like that seen at higher doping levels (Fig.6.8-a). An inflection in the I-V curve is seen around −0.6 V, corresponding to a lower conductivity mode (0.03 ohm.cm^2). This larger resistance may be due to the wider space charge region in low doped n^- Ge, which has increased from ~100 nm (N_D ~1×10^{17} cm^{-3}) to ~ 0.7 µm (N_D ~ 6.4×10^{14} cm^{-3}). Increased hot electron emission at higher bias overcomes this obstacle by a kind of *electrical doping*[156][157]. The depletion region is effectively charge neutralized by injected electrons and so conductivity increases. Thus, it can be inferred that hot carrier transport observed here is ballistic in nature, shown schematically in Fig. 6.12-b using energy band diagrams. In contrast, the geometry induced electric field enhancement is minimal in a CMF contact. The absence of Au islands eliminates an important pathway for non-equilibrium carrier heating in the metal and hence, hot carrier transport and hot electron emission into vacuum are not observed.

To further confirm the role of hot carriers in enhancing the conductivity of IMF/semiconductor contacts, cryogenic measurements (in liquid helium, 4.2 K) were taken on IMF and CMF contacts to n^- and p-Ge (performed by Dr. John Quilter, RHUL). In Fig. 6.12-c, the I-V characteristics using a CMF contact shows negligible current because of carrier freeze out in Ge at 4.2 K. In contrast, by using an IMF contact there is a significant current, which can only be attributed to hot carrier emission from the IMF, as cooling to this temperature is detrimental to Fermi level de-pinning schemes, resulting in rectifying behavior below 111 K[158]. Symmetric I-V characteristics are observed in forward and reverse bias, as was the case at room temperature. The current is small for $-0.1 < V_A < 0.1$, where fewer carriers from the IMF have sufficient energy to inject into the semiconductor. Inversion layer limited current (ILLC) is

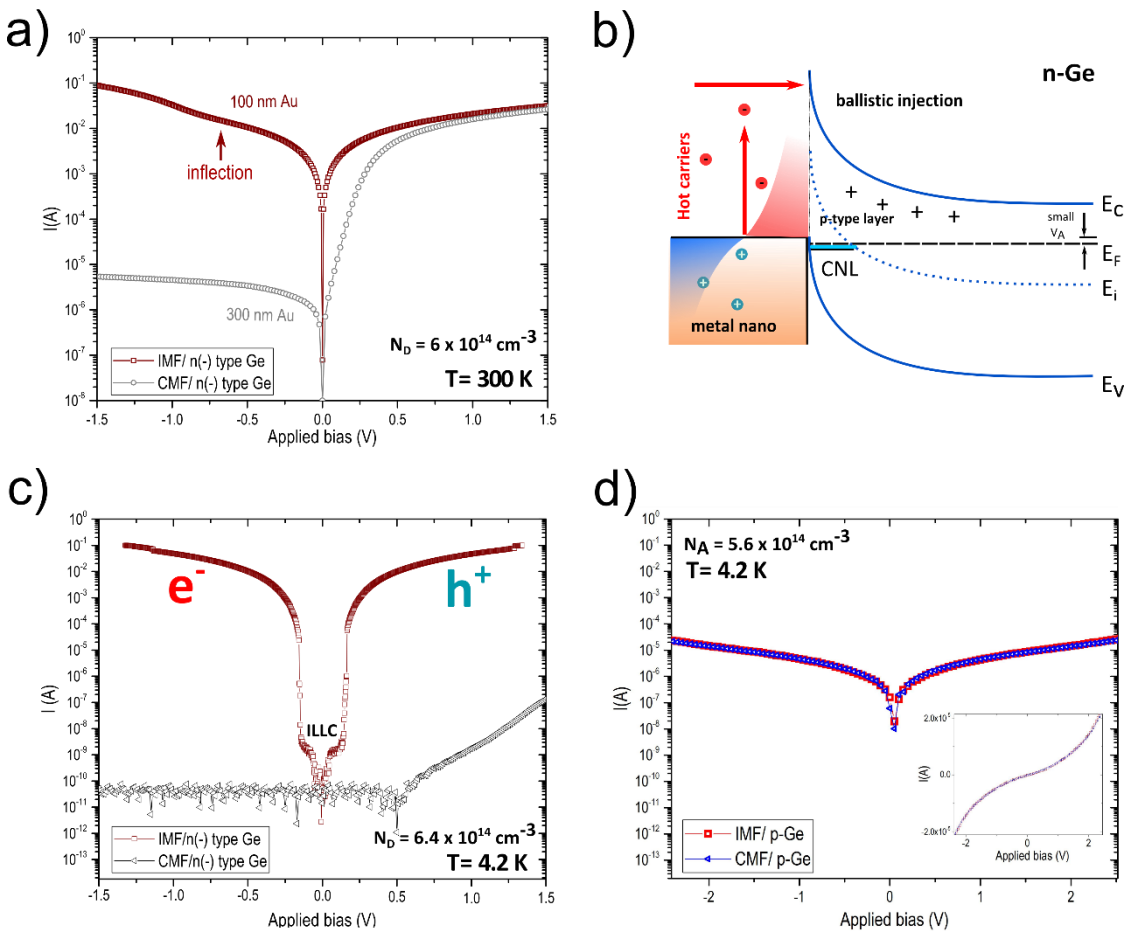

Figure 6.12: a. Room temperature I-V characteristics of IMF and CMF contacts to low doped n^- Ge (N_D~6.4 × 10^{14} cm^{-3}). IMF contact shows high conductivity modes in forward and reverse bias, while the CMF contact retains rectifying characteristics. **b.** Energy band diagram of IMF/ n^- Ge for a small applied reverse bias, resulting in ballistic hot electron injection. **c.** Cryogenic (Liquid helium, 4.2 K) I-V characteristics of IMF and CMF contacts to low doped n^- Ge. IMF shows symmetric, inversion layer limited current (ILLC) confirming non-equilibrium carrier transport, while CMF contact shows very low current due to the presence of a Schottky barrier and carrier freeze-out. **d.** Cryogenic (Liquid helium, 4.2 K) I-V characteristics of IMF and CMF contacts to low doped p Ge (N_A~5.6 × 10^{14} cm^{-3}). IMF and CMF contact both show identical I-V characteristics. A small Schottky barrier for holes allows tunnelling near the metal Fermi level, resulting in double exponent I-V characteristics.

observed, which the hot carriers easily overcome for $|V_A| > 0.1$ V. The resistance of the depletion region can be neglected at 4.2 K, which explains why the current magnitude (and conductance) at higher voltages is greater than that seen at room temperature. The current sharply increases initially at a rate of 10 mV/ decade. This data can be fitted to a voltage power law (order 2-2.5), which is in qualitative agreement with ballistic electron emission transport across the interface being the main conduction mechanism[159].

The IMF allows voltage controlled hot carrier emission into n^- Ge resulting in Ohmic characteristics. Under reverse bias, this corresponds with hot electron emission from the IMF

into the semiconductor, with sufficient energy to overcome the Schottky barrier in n-Ge. Under forward bias there is a current of similar magnitude to that seen in reverse bias. This must result from hot hole emission from the IMF into the semiconductor. An applied bias across the IMF gives rise to both hot electron and hot hole distributions that rapidly establish an equilibrium[160]. I-V characteristics for the corresponding IMF and CMF contacts to p-Ge taken at 4.2 K are identical, as shown in Fig. 5.d. Tunnelling current is observed, as expected from the condition of FLP. These curves fit the functional form: $y = \alpha \sinh(\beta x)$, which is often characteristic of tunnelling. Here, α and β are fitting parameters.

6.5. Summary II

Voltage controlled non-equilibrium current transport has been experimentally demonstrated on a strongly pinned semiconductor (Ge) using thermally assembled IMFs. The IMF contact to n-Ge is improved by hot carrier emission, without degrading the already Ohmic p-Ge. Evidence for both hot electron and hot hole transport is obtained using cryogenic measurements on low doped n^- Ge. Symmetric high conductivity is observed well below the carrier freeze-out temperature (< 20 K), despite the condition of FLP in Ge because hot carriers can easily circumvent the Schottky barrier. These results will have applicability to a wider range of materials.

6.6. Discussion

IMFs are nano-dispersed solid-state media which possess unique electronic properties. Although the level of control in the fabrication process shown here is far from satisfactory, the performance of IMFs surpasses traditional contact engineering strategies that rely on heavy doping or Fermi level depinning. The main issue encountered here is reproducibility, which may be improved using a more suitable annealing technique like pulsed laser annealing[161]. By adjusting the pulse width and intensity, it would be possible to achieve fine control over the size and distribution of previously templated patterns. In principle, only two closely spaced nano-islands are required for the electron heating effect (with electrical excitation). Tunnelling current from one island to the next will provide the required energy to elevate the electron temperature as required. Such dimer structures could be encapsulated with ultra-thin oxides, polymers etc. to ensure that even nano-islands in contact with one another would be susceptible to electron heating. A thin barrier will be semi-transparent to the incoming tunnelling flux. Nanoimprinting such structures is quite challenging[162], although recent advances in EUV

immersion interference lithography have enabled mass patterning of sub 10 nm structures[163].

Electron-electron interactions (this work) as well as photon-electron[164][165] interactions can be used to create energetic charge carriers that may be harvested over the Schottky barrier and by tunnelling through the Schottky barrier[166]. There is a tremendous opportunity to apply these nanoscale phenomena in catalysis[167] and energy harvesting[168][169]. Bypassing the FLP problem and the need for heavy doping is especially attractive in microelectronics. Once fabrication challenges are overcome, novel designs may allow the realization of ultra-high-speed hot carrier transistors as well.

Carrier scattering is considerably minimized at low temperatures. Very high conductance was observed on low doped n^- Ge once the inversion layer is overcome by ballistic carriers, with a subthreshold slope S = 10 mV/decade. This result has direct applications in the areas of sensing in harsh environments e.g. outer space. The electron heating effect occurs over fs timescales, whereas electron-phonon relaxation i.e. thermalization occurs on ps timescales[136]. Hence, hot carrier switching at optical frequencies is possible.

Scaling down to the sub-nm regime for single electron transistors (SET) is accompanied by a variety of problems[170] and reliability issues. CMOS compatible SET operating at room temperature have been shown previously[171]. The choice of using colloidal Au nanoparticles in a CMOS foundry is debatable due to contamination rising from suspended media and the reliability of tethering nanostructures reproducibly. Furthermore, the overall device footprint is well above the current technology node (7 nm due in 2018). SET are a long way from becoming the commercial standard in consumer electronics and these works are mainly driven by scientific interest to push technological boundaries eventually.

The IMF contacts show impressive results notwithstanding enormous scope for improvements in processing methods and design. Similar effects could also be produced in other common plasmonic metals like Al[172], which has a similar lattice constant to Au (a_{Al} = 4.046 Å, a_{Au} = 4.065 Å), in conjunction with other wrinkled 2D electronic surfaces[173] or using combinations of different metals by co-sputtering tilted targets in a slowly oxidizing environment. *In situ* formations of encapsulated metal nanoparticles approaching 2D character may allow the fabrication of interesting IMFs or individual emission centres. Particularly in Si, anisotropic chemical etching could be exploited to “preassemble” sharp grooves in the substrate, enabling chain structure formations within patterned areas, prior to annealing.

6.7. Conclusions

Thermally assembled IMF contacts are realized on Ge, which allow Ohmic conduction at room temperature and nearly ballistic hot carrier emission at cryogenic temperatures. The fabrication process is highly sensitive to the annealing conditions and needs to be carefully controlled in order not to lose the nanostructures essential to the observed effects. IMFs composed of small metallic nanoparticles are susceptible to electron heating effects. A proof of concept is shown i.e. Electrically generated hot carriers readily overcome electrostatic barriers over a wide range of temperatures and this will have a wide applicability to several material systems. Novel hot carrier transport phenomena have been discovered using IMF contacts, applicable to semiconductors and 2D electronic surfaces. Optimizing this new paradigm for metal-semiconductor contacts offers the prospect of improved nano-electronic systems and the study of voltage controlled hot holes and electrons.

"In Physics, what counts, I found, is not what you cover, but what you uncover."

- Walter Lewin

Chapter 7:

Outlook and future work

7.1. Outlook – new device elements

This thesis explored metal-semiconductor contact engineering solutions to overcome limitations set by FLP in semiconductors. Ohmic contacts are essential elements in microelectronic device technology and FLP is a dominant effect that governs interface properties. Metal contact properties were studied on Si and Ge, the most important elemental semiconductors in microelectronic device technology. Metal contacts to pure and low doped Si, Ge exhibit non-ideal behaviour i.e. they do not obey the Schottky-Mott theory of barrier height formation, which predicts the height of the Schottky barrier formed at the contact interface is equal to the workfunction difference between the metal and semiconductor. Instead, the Fermi level appears to be pinned at some energy within the band gap of the semiconductor, known as the charge neutral level (CNL) and this condition presents serious challenges in meeting required device specifications, particularly overcoming high contact resistance. The CNL is located ~ 0.6 eV in Si (mid-gap) and ~ 0.1 eV above the valence band in Ge. It is the crossover point between donor and acceptor type interface state density distributions lying within the band gap of the semiconductor[108].

Fermi level depinning provides a means to change the CNL by introducing external surface dipoles and by the passivating action of certain interlayer materials. If the new CNL at equilibrium is close to either conduction or valence band of the semiconductor, the Schottky barrier height formed at the contact interface is reduced for electrons or holes respectively. Ideally, if the Schottky barrier height becomes zero it would result in perfect Ohmic contact to either n- or p-semiconductor while forming an ideal Schottky (rectifying) contact to p- or n-semiconductor respectively. This is rarely ever seen in experiment. The new CNL usually still lies somewhere within the semiconductor bandgap and so the Schottky barrier height cannot become zero.

Conductivity can be improved by heavy doping of the semiconductor or interlayer material (e.g. tuning density of Oxygen vacancies using variable doping[35]) by narrowing the effective

tunnel barrier. Tunnelling near the metal Fermi level becomes favourable when a small Schottky barrier is made nearly transparent to charge carriers in the metal and semiconductor. At these heavy doping levels, carrier transport occurs via tunnelling and this mechanism has so far provided the best Ohmic contacts in the literature. However, when heavy doping is not used the Schottky barrier affects carrier transport across the contact interface, resulting in saturating or non-linear I-V characteristics.

An external electric field can modify the effective Schottky barrier height for an engineered contact interface, allowing tunnel current to improve conductivity on both n- and p-type semiconductors. The action of screening the electric field increases band bending, which narrows the tunnel barrier at the contact interface, allowing multi-step tunnelling processes across interfacial layers. The source of the external field could be engineered in a variety of ways, shown for example using charged interfaces (ALD AlO_x/ SiO_2) in Chapter 4, and at sharp triple junctions within hybrid contacts in Chapter 5. These engineering methods could be used to form Ohmic contact in several planar device technologies using low doped Si and Ge, among other potential material combinations.

Emergent non-equilibrium phenomena within nanostructured materials enable voltage controlled hot carrier transport across interfaces. Chapter 5 documented new findings of a thermally self-assembled hybrid thin film material. A generic method for realizing Ohmic contact has been discovered, without disturbing the CNL of chemically cleaned surfaces i.e. conductivity is enhanced for n-Ge without affecting the properties of p-Ge. Semiconductor nanocrystalline regions embedded in the hybrid contact are susceptible to dielectric breakdown caused by large local electric field enhancements at triple points in the contact layer. Hot electrons overcome the Schottky barrier and Ohmic conduction characteristics are observed using low/ moderately doped substrates. Cryogenic I-V measurements revealed the mechanism of carrier transport and provided an interesting demonstration of voltage controlled electron valley transfer, resulting from hot electron tunnelling into the Ge substrate. This is a new nanoscale device element which may be operated over a range of temperatures including cryogenic environments (tested down to 4.2 K). A device symbol for the hot electron reverse diode (hybrid contact) is proposed in Fig. 7.1.

The conventional diode symbol has been modified for hybrid contacts to include the main aspects of its unique material geometry, particularly its triple interface and one dimensional current cross-section, as well as its operating principle. Three lines intersect at the cathode, encircled to illustrate the triple point between metals and vertical edges of semiconductor

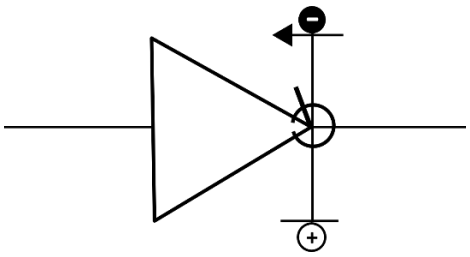

Fig. 7.1- Proposed device symbol for hybrid contacts- A triangle points in the forward direction. The small arrow is reversed to indicate backward diodes formed at triple interfaces, drawn as an open circle around the cathode intersection. The horizontal bars represent the band gap of the embedded semiconductor nanocrystals within the metal/cathode. Hot carrier pairs generated at the hybrid contact interface are emitted towards the anode.

nanocrystals. Geometrically enhanced electric field at triple points causes dielectric breakdown in embedded nanocrystals. This creates carrier pairs (solid and hollow circles) with energy comparable to the semiconductor band gap (from broken bonds). Good thermal contact with metals protects the embedded semiconductor nanostructures during operation, preventing disintegration of the lattice. A plasma of excited carriers and ions is sustained in the hybrid contact under bias. When the embedded semiconductor nanocrystals are the same material as the substrate (e.g. Ge-nanocrystals/ Ge substrate shown in Chapter 5) their respective energy bands are closely matched, allowing efficient hot electron tunnelling into the substrate plane.

The physical dimensions and bandgap of semiconductor nanocrystals in the hybrid film could be engineered using state of the art fabrication tools because the bandgap of semiconductors is largely an intrinsic property. Potentially, hybrid heterostructure contacts could also be used. Rather than changing the CNL of crystal surfaces, which results in asymmetric contacts (Ohmic/ rectifying) on n- or p- semiconductors, this thesis concludes that it may be more convenient to engineer and modify the contact geometry instead. This way Ohmic contacts to semiconductors can be realized regardless of their bulk doping species or concentration. The hot carrier current density depends on the density of vertical edges in the contact layer, which has to be maximized to improve conductivity further. Contact resistance could potentially be improved in a scalable manner without using heavy doping.

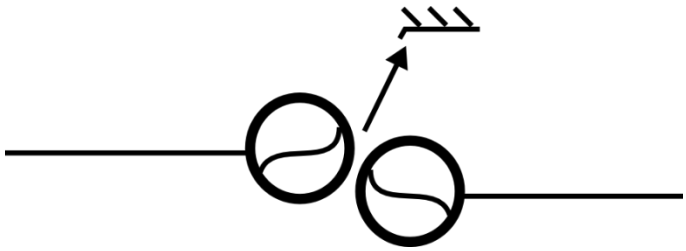

Fig. 7.2- Proposed device symbol for IMF contacts- Two representative metal nano-islands are shown as circles, separated by a small gap which allows tunnelling current to flow between islands when applied voltage offsets the electric potential between the islands. The Fermi distributions of the islands are broadened by non-equilibrium electron heating due to tunnelling electrons, resulting in hot carrier emission (arrow) into the available continuum of states (shown as hatched lines).

Distributed nanoscale contact geometries could be used as active elements that potentially outperform planar metallization at the nanoscale in terms of conductivity ($\sigma_{plasma} > \sigma_{metal}$). Chapter 6 investigated thermally self-assembled Au island metal films (IMFs) on Ge. Voltage controlled hot carrier emission from IMFs gives rise to Ohmic behaviour at room temperature and hot electron/ hole emission at 4.2 K, without changing the CNL. Closely spaced metal nano-islands (IMF) having critical dimensions operate as voltage controlled hot carrier emitters.

Below critical nanoscale dimensions, lattice vibrations become ineffective at dissipating energy. Electrons with their small heat capacity exchange heat quickly (on fs timescales), which raise their average temperature, thus broadening the Fermi energy distribution significantly[137]. The effective electron temperature can reach ~10^3 K. The excited metal clusters are stabilized by the emission of hot carriers into the available continuum of energy states[174]. The applied voltage between the IMF and substrate sets up additional drift field to extract hot carriers. Chapter 6 results demonstrated these phenomena using only electrical excitation i.e. applying bias to thermally assembled IMF contacts on low and moderately doped Ge. The general operating principle of IMFs is captured by the symbol proposed in Fig. 7.2.

The findings in this thesis show the impact of material geometry and material selection on electrical properties of contacts. Engineering nanostructured material geometries offer a means to overcome key limitations imposed by FLP. While these methods offer a means to improving conductivity, their usefulness in current device designs might concern the development of high electric fields near dielectrics as this can compromise gate oxide integrity due to hot electron injection effects. So appropriate isolation technology is required to protect the gate oxides from hot carrier contacts during their operation. Fortunately, metal layers can serve this purpose and it is built into the architecture of hybrid contacts but not the IMFs. As metal films can screen

electric field below the plasmon frequency, a thin continuous metal layer can protect the dielectric gate oxide from hot carriers emitted from sharp corners within the hybrid contact geometry. Further research and development in this field could lead to new designs for nanoscale devices.

7.2. Future work – bottom up and top down methods

One of the main challenges faced in the works of Chapters 5 and 6 was poor process control. The interplay between short annealing times and peak temperature is quite complex and it is difficult to predict how a given set of annealing parameters would affect the process outcome, without a set of very detailed, careful experiments to study the various processes at play in the creation of hybrid films as well as IMFs. Process variability in experimental trials needs to be minimized to improve fabrication protocols. Some of these drawbacks could be addressed by using spatially resolved infra-red pyrometry, in conjunction with pulsed laser annealing as described in Experiment - A. Alternatively, top down methods could be used to write nanostructures as required, described later in Experiment - B.

7.2.1. Experiment - A: Fine-tuned self-assembly, in-situ crystallization

Annealing thin Au/Cr films (e.g. 100/3 nm) on Ge results in the emergence of Ge nanocrystal/ bimetallic hybrid structures by lateral eutectic segregation, forming abruptly contained geometries with sharp triple interfaces, covered in Chapter 5. With the right combination of starting materials, techniques and previous insight gained from this thesis, it may be possible to develop a well-controlled method for synthesis of nanoscale hybrid junctions. A series of pilot experiments would eventually lead to Experiment – A using state of the art pulse/ probe laser annealing technology, in conjunction with spatially resolved pyrometry. The instrument modules operate on the material specimen shown schematically in Fig. 7.3.

The pyrometer monitors the substrate temperature in real time. The energy input required for the eutectic rearrangement of materials is regulated using a closed loop control system. Pulsed laser intensity/ annealing duty cycle (ON: OFF time) is modulated using the pyrometer feedback loop, maintaining optimal annealing conditions during processing. Under the right experimental conditions, the size and density of the Ge nanocrystals could be controlled

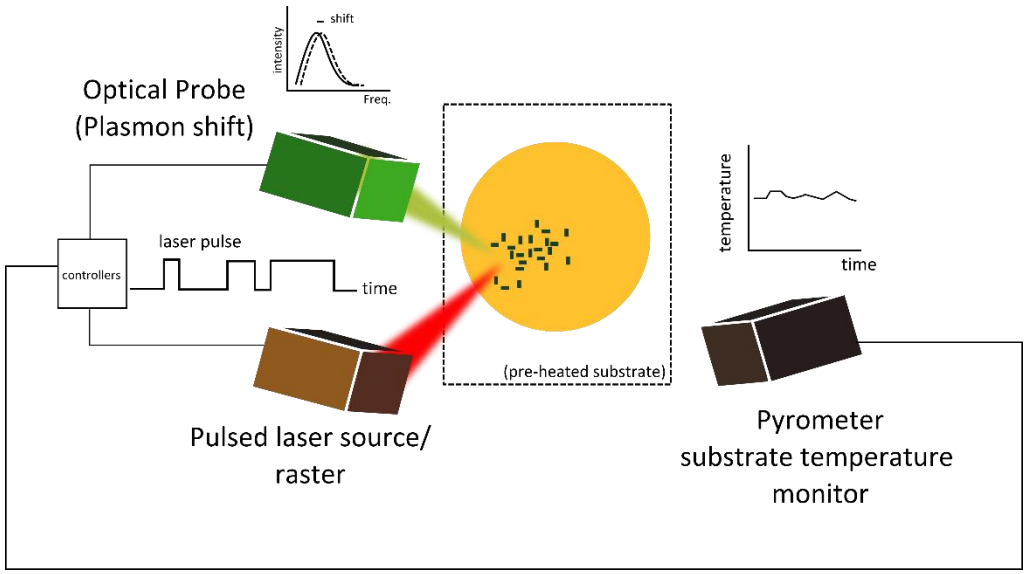

Fig. 7.3- Proposed Experiment – A – Laser pulse/ probe apparatus for controlled synthesis of hybrid materials. An elaborate closed loop system monitors various physical quantities. A pyrometer reads the actual substrate temperature and actively returns data to the controller, modulating the pulsed laser source - raster scanned over thin Au/Cr films on Ge, resulting in epitaxial embedded nanocrystals, as covered in Chapter 5. An optical probe monitors the plasmon shift of the Au thin film, arising from emerging nanocrystalline geometries within patterned areas. This data are collected for post analysis, correlating nanoparticle size/ density and the annealing parameters to establish a standardized protocol for synthesis.

precisely. An optical probe (yellow – UV laser) setup records the bulk and surface energy loss function of thin Au films, similar to the setup shown in ref.[175]. The emergence of Ge nanocrystals would result in a shift in the plasmon response from the hybrid film. This acquired data (intensity, spectral variations over time) would inform the study of reaction kinetics describing the eutectic rearrangement of materials.

The controller code will be iteratively improved with updated look-up tables that translate the substrate temperature (input variable) into signals controlling the power supplied by the laser pulse/probe setup, modulating the annealing duty cycle (output variable). The aim of these experiments is to achieve ultimate process control over the size, edge density of the emerging Ge nanocrystals in the Au/Cr film. The substrates could be preheated prior to laser annealing, maintaining a base setpoint temperature to fine-tune the throughput. The incoming laser pulse train will swing the material interfaces in and out of the liquid phase, thereby allowing sensitive control in the synthesis of self-assembled vertical interfaces (and triple points). Crystallization will occur in-situ, during laser annealing and result in extended heteroepitaxy in lateral and vertical directions (in and out of substrate plane). Either the specimen, or focused pulsed laser

beam head could be raster scanned over device regions requiring Ohmic contact. Variants using different material combinations will also be studied to obtain a wide range of new contact materials. Similar processing could be used for fabrication of various IMFs as well. As such, this experiment will result in the development of an important fabrication tool that is built for purpose.

7.2.2. Experiment – B: Top down fabrication, ex-situ crystallization

Recent advances in nanoscale lithography have made top down fabrication of sub-10 nm features possible, shown for example shown in refs. [176],[177] among other works in literature. A recent report demonstrated "… a straightforward and cost-effective method for fabricating sub-10 nm slit arrays formed in Cr thin film on transparent substrate using photolithography, ALD, and chemical etching."[178] Large scale patterning of nanoscale structures using photolithography, coupled with other advanced techniques may enable integration of hybrid contacts into state of the art device technology and potentially in mainstream technology.

Semiconductor or metal fillings into e.g. split ring patterns could be superimposed onto a contact test structure. Subsequent low temperature annealing treatment could be used to repair misaligned interfaces, finally producing the required contact geometry. In contrast to Experiment -A, crystallization will occur ex-situ. An idealized example of spiralling ~10 nm split ring patterns within the contact layer is shown schematically in Fig. 7.3. A via is suggested, leading to potential interconnects/ hard contacts used to initiate voltage controlled hot carrier effects in the hybrid contact. This work needs to be verified experimentally to discover potential process issues that may arise in developing the technology. The sequence of materials, and their dimensions need to be carefully selected to achieve highest possible hot carrier throughput i.e. lowest contact resistance.

Likewise, IMFs could be fabricated by exploiting film/ wire retraction as described in Chapter 6, but using ~ 10 nm slit ring metal wires as the starting material template. By using similar laser annealing setup shown in Experiment -A the size and gaps of IMFs could be controlled to deliver nm scale templated IMFs for voltage controlled hot carrier applications, among others.

It is necessary to achieve precise control over whichever fabrication route A, or B is chosen in order to compete towards achieving ITRS requirements, that demand contact resistivity better than 10^{-9} ohm.cm^2.

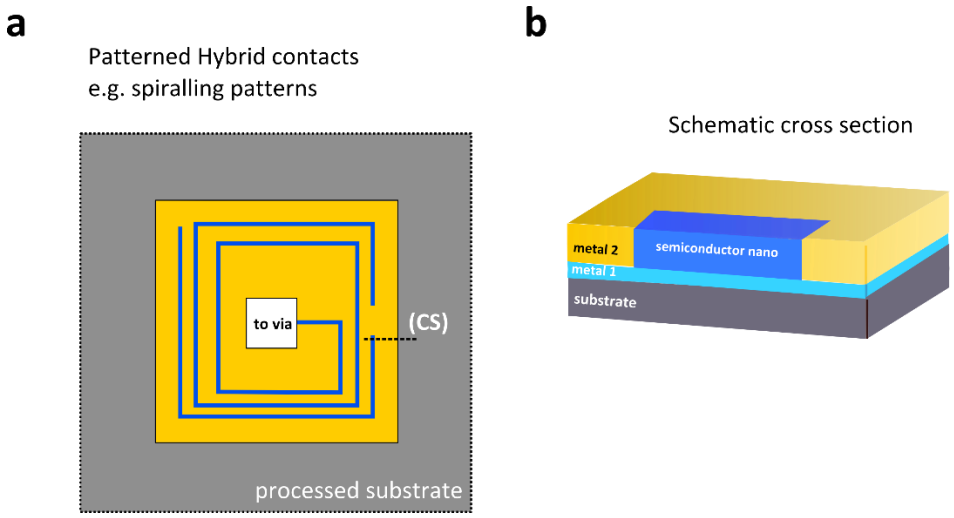

Fig. 7.3- Proposed Experiment – B – Top down fabrication of hybrid contacts for integration into modern process technology. **a.** Schematic showing a spiralling pattern of semiconductor nano-split rings (blue) embedded in the contact metal (yellow) on the fully processed wafer (gray). Its representative cross section (CS) is shown schematically in **b.** Triple points form between $metal_1$/$metal_2$/semiconductor nanostructures and are isolated from the substrate by $metal_1$, thereby improving conductivity extrinsically.

7.3. Concluding remarks

Hot carrier technology is an emergent and thriving field in applied science. The research chapters of this thesis present a timely contribution to the field, with demonstration of new contact materials employing non-equilibrium phenomena, distinguished by their unique physical geometries. Experimental demonstration of non-equilibrium electronic phenomena using small voltages, over a wide range of temperatures has many technologically significant implications. New applications and designs are anticipated to emerge from these studies and future works, applicable in the fields of high speed telecommunication, nano-electronics, energy harvesting, active catalysis and sensing. It is highly likely that further research will lead to even more exciting discoveries and the development of other new technologies.

Several experimental leads remain to be investigated e.g extending the present technique to other semiconductors, using smaller contact geometries to verify that the scaling trends continue as per design. A major challenge to this research that remains unsolved, is to realize a precise method of determining contact resistance, as traditional techniques like (C)TLM require that the transfer length is sufficiently small ($L_T \ll d$) to obtain a linear relationship between

measured total resistance and the gap separation (d_{gap}). This is of course not applicable to distributed nanostructures, and a considerable spreading resistance is encountered, making the calculation of specific contact resistivity difficult. The value of specific contact resistivity obtained by simply scaling with area is an underestimate.

Using nanoprobe I-V measurements for top down fabricated IMF contacts may provide an answer to this problem by directly probing small gaps between nano-islands in the IMF. Likewise, in hybrid contacts, as the current scales one dimensionally, it is the edge density of embedded semiconductor nanostructures in the contact that determines the contact resistance, and this needs to be included in the electronic model of the contact to determine the true contact resistance. New theoretical formulations are necessary to obtain analytical expressions for contact resistance in terms of island size, island density and spacings, are reserved for future work.

Appendix – Fabrication Procedures

- Wear appropriate PPE while handling dangerous chemicals.
- Ensure that the following chemicals are ready; Isopropyl alcohol (IPA), N-Methyl-2 Pyrrolidone (NMP), Hydrogen Peroxide, 96% Sulphuric Acid, 37% Hydrochloric Acid, 28-30 % Ammonia solution and 7:1 BOE (HF : NH_4F = 12.5 : 87.5%). Check that the UltraPure water source (deionized water – 15 -20 mega ohm) is available for use. This is a key process liquid and will be frequently needed in various cleaning steps.
- Set Ultrasonic Bath to 85° C; obtain petri dishes and tweezers – rinse petri dishes with IPA then blow dry with N_2. Pour 50ml IPA into beaker (100ml), insert tweezers into IPA solution and place beaker in ultrasonic bath for 5min to clean tweezers, then blow tweezers dry with N_2.
- Handle specimens and glassware with care. They can shatter if dropped. Careful about scratch marks from tweezers on the polished face of the substrates, and chipping around points of contact with tweezers. The substrates need to be picked and placed in several steps throughout processing by hand, so it is useful to practice holding dummy substrates to learn gripping with the correct tweezers (plastic/ ceramic for acids/ alkalis, metal for other).

Silicon Cleaning Recipe

Initial Organic Clean

1. Pour 50ml of NMP into beaker (100ml). Add samples to NMP, don't touch any part of samples other than the edges. Put beaker of samples into ultrasonic bath on max power for 10min.
2. After ten minutes, remove the beaker out of the ultrasound bath and pour NMP into solvent waste (leaving samples in bottom of beaker covered with small amount of NMP). Rinse samples and beaker with IPA (maybe 50ml total), then pour IPA into solvent waste (leaving samples in bottom of beaker covered with small amount of IPA). Rinse with IPA twice before filling with IPA to 50ml and putting samples beaker into ultrasound bath for 5min.

3. Rinse a large beaker (500ml) with UltraPure water, then fill it with UltraPure water. Put wipe/ plug over the sink to prevent specimens from flushing away during pouring steps.

4. Pour IPA into 'solvent waste' container (leaving samples in bottom of beaker covered with small amount of IPA). Then rinse 500ml of UltraPure water over samples in the samples beaker (leaving samples in bottom of beaker covered with small amount of UltraPure water).

Fill 500ml beaker with UltraPure for future use.

Piranha Clean

5. Pour 25ml of Sulphuric Acid into samples beaker (using measuring cylinder) and put into ultrasonic bath at 85º C and at max. power as before, leave for 5min.

6. Pour 8ml Hydrogen Peroxide into same measuring cylinder as used in (5), then add this to samples/sulphuric acid solution beaker in the ultrasonic bath (this will bubble, free/ nascent O_2), leave this for 10min (grow sacrificial oxide).

Clean the measuring cylinder used with 500ml UltraPure water, **prior** to RCA procedure (below) whilst waiting the 10min. If this is not done, there could be risk of a violent acid/base reaction while preparing SC1/ SC2.

RCA procedure

Use the rinsed measuring cylinder to prepare SC1, SC2.

7. SC1: Add 40ml of Ammonia solution to the beaker (labelled SC1), then add 30ml of Hydrogen Peroxide to this solution – SC1 now prepared.

8. SC2: Add 20ml of UltraPure water to beaker (labelled SC2), then add 15ml Hydrogen Peroxide, then 15ml of Hydrochloric Acid.

9. Pour 50ml BOE/ BHF into labelled plastic beaker (100ml).

Now there are 3 solutions prepared whilst the samples have been in ultrasonic bath for 10min in Hydrogen Peroxide/Sulphuric Acid solution; these are SC1 / SC2 / BOE. The solutions SC1 and SC2 decompose very quickly, so do not waste time when using them.

Fill 500ml plastic beaker with UltraPure water again in preparation for usage.

10. First pour the previous samples solution (Hydrogen Peroxide/Sulphuric Acid) into the Acid Waste container, rinse samples with the prepared UltraPure water until the 500ml is spent (leaving samples in bottom of beaker covered with small amount of UltraPure water). Keep the 'Acid Waste' bottle open as bottle will expand!!

11. Pour half of the SC1 solution into the samples beaker and place in ultrasonic bath for 10 min.

Whilst waiting the 10min refill (500ml) beaker with UltraPure water again.

12. Next pour SC1 solution down the sink (leaving samples in bottom of beaker covered with small amount of SC1), then rinse with the prepared UltraPure water until the 500ml is spent (leaving samples in bottom of beaker covered with small amount of UltraPure water).

Fill a 2nd glass beaker (100ml) with about 40ml of UltraPure water..

13. So now you have 3 beakers, 1- the samples solution, 2- BOE solution and 3- UltraPure water. Remove samples one by one from sample beaker to the BOE solution (5sec dip in BOE), then transfer straight to the UltraPure water.

14. Pour UltraPure water out from sample beaker (leaving samples in bottom of beaker covered with small amount of UltraPure), then pour half of previously made-up SC2 onto samples – put this beaker into ultrasonic bath again for 5-10min.

Whilst waiting the 10 minutes refill big (500ml) beaker with UltraPure water again.

15. Remove samples beaker from ultrasonic bath and pour the SC2 into the Acid Waste (open top), then rinse with the prepared UltraPure water until the 500ml is spent (leaving samples in bottom of beaker covered with small amount of UltraPure water).

16. Repeat procedures (11-15), using the second halves of both the SC1 and SC2 solutions. Leave samples at end of the procedure in UltraPure water for a few minutes.

17. Remove samples from UltraPure water, place substrate down on dry wipe, blow dry with N_2 gun and place samples into clean sample container.

18. Tidy work area etc.

Germanium Cleaning Recipe

- Handle Ge samples and glassware with care. They can shatter if dropped. Careful about scratch marks from tweezers on the polished face of the substrates, and chipping around points of contact with tweezers. The substrates need to be picked and placed in several steps throughout processing by hand, so practice holding dummy substrates to learn gripping with the correct tweezers (plastic/ ceramic for acids/ alkalis, metal for other).
- Ensure that the following chemicals are ready; acetone, Isopropyl alcohol (IPA), Buffered oxide etch/ Buffered hydrofluoric acid (BOE/ BHF). Do not use ultrasound bath for Ge samples. They are more brittle than silicon and are prone to shatter even using 50 % power (MIN).
- Set Ultrasonic Bath to 85º C; obtain petri dishes and tweezers – rinse petri dishes with IPA then blow dry with N_2. Fill a large beaker with 500ml UltraPure water. Pour 50ml IPA into a small beaker, insert tweezers into IPA and place beaker in ultrasonic bath for 5min at MAX power to clean tweezers. Remove the beaker and dispose IPA in the 'solvent waste' bottle. Switch off the ultrasound bath. Rinse the beaker and tweezers with 500ml UltraPure water. Then blow dry tweezers with N_2.
- Set the hot plate to 70º C. Fill 500ml UltraPure water.

<u>Organic clean</u>

1. Pour 50 ml acetone in a clean beaker. Add Ge samples into this beaker. Place beaker on hot plate. Wait 10min. Pour acetone into the 'solvent waste' bottle. (Leave small amount of acetone at the bottom of the beaker). Careful not to spill any chemicals on the hot plate.

2. Place the hot beaker on a dry surface. Add 20 ml IPA to the beaker and rinse away acetone residues on the samples. Dispose the IPA in solvent waste container. (Leave small amount of IPA at the bottom of the beaker).

3. Add 50 ml IPA to the beaker and place it on the hot plate. Leave for 10min.

4. Dispose IPA into solvent waste container. Leave small amount of IPA covering the samples.

5. Rinse, flush samples with 500 ml UltraPure water.

6. Remove samples from UltraPure water, place substrate down on dry wipe, blow dry with N_2 gun and place samples into clean sample container

BHF/ UltraPure water - Etch

7. Prepare a plastic beaker and ceramic/ plastic tweezers for BOE etch.

8. Keep two containers filled with UltraPure water ready. Pick and place the samples into the BOE for 90s. Pick sample and quench in UltraPure water, without dropping it. Transfer to the second container. Repeat this for each sample.

9. Dispose UltraPure water from first container. Fill it with 500ml UltraPure water.

10. Dispose Ultrapure water from second container, leaving small amount at the bottom. Flush and rinse using the 500ml of UltraPure water from the first container.

11. Repeat step (8-9). Ultrapure water dissolves native Ge oxides, creating microroughened surfaces. Remove samples from UltraPure water, place substrate down on dry wipe, blow dry with N_2 gun and place samples into clean sample container.

Solvent lift-off

1) Metal coated PR patterned samples are removed from the sample holder by unscrewing the clips in reverse. Place samples in a clean petri dish. Pour ~20ml NMP and warm to 60º C on a hot plate. Wait ~ 10- 15min. The additional PR underneath the film is dissolved in NMP, lifting away metal regions, everywhere but the developed contact windows.

2) Use a fine haired art-brush to gently clear metal debris from the samples in NMP.

3) Transfer samples carefully into another petri dish containing IPA to dissolve NMP residues.

4) Gently brush away remaining metal debris. Dispose remaining IPA and NMP in the 'solvent waste' bottle.

5) Rinse samples in 500 ml UltraPure water.

6) Repeat steps (3-5) if necessary. Check under optical microscope for PR residues.

7) Dry samples in N_2 jet on a clean dry wipe. Store processed samples in a clean sample container.

8) Fully processed samples may be cleaved into smaller sections using the technique described in Fig. 3.1, e.g. processed Ge samples used in Chapter 5 are shown in Fig. 3.4-d. cleaved < 4 mm^2. Smaller cuts should be performed using laser cutting/ dicing if required.

Contact lithography workflow

All photolithography work is done in a dark room e.g. Fig. (3.2-left). Set the fan oven temperature to 120º C. Place chemically cleaned, blow dried samples into a cleaned petri dish, using clean tweezers. Place the petri dish into a fan oven, preheated at 120º C. Wait 30min. During this time, ensure that a plastic pipette filled with enough AZ 5214-E (Microchemicals Ltd.) photoresist, at ambient temperature is available at the spinning station. Heating samples in the oven for 30min will evaporate solvent and UltraPure water residues from the previous cleaning steps. Remove petri dish containing samples from oven and place on Aluminium desk. Set fan oven temperature to 90º C. Allow dried samples to cool for 15min before spinning photoresist (PR) for patterning. Use the correct chuck holder for the spinning step, appropriate for the size of the samples. This needs to be done to ensure no PR gets stuck on the sample underside and only the top is covered. Follow steps below to begin,

1) Place ~2-3 drops of PR (without air bubbles) in the centre of the mounted sample, aligned to the spinning chuck axis. Use the spinner to spin-coat photoresist on samples at ~ 4000-5000 RPM for 60s. Place the PR coated samples in a clean petri dish. Careful not to scratch curing PR while picking up samples.

2) Place the petri dish in the fan oven, preheated to 90º C to soft-bake the PR for 15min.

3) Remove the petri dish from the oven and allow samples to cool for 15min.

4) Use the Karl-Suss MJB-3 mask aligner (Fig. 3.3-top) to expose the soft baked, PR coated samples to UV light shone through the photomask with the desired pattern. During exposure, the samples (PR) must be in hard contact (Fig. 3.3-middle) with the mask to ensure sharp features are retained in the PR. Exposure time in this step is usually 6-8sec. Cover PR coated samples (prepare to sort exposed and pending samples in advance) in an opaque container between exposures.

5) If using a negative mask, the exposed specimens are then hard-baked in the oven at 110º C for 10min. If using a positive mask this step is skipped. To reverse a negative pattern, expose the hard-baked samples to UV light once more for 16-18sec (without using the contact mask). Use 'Soft contact' mode (Fig. 3.3-middle) for this step.

6) Keep 2 containers filled with UltraPure water ready, with clean room wipes and plastic pipettes at hand. Develop the imprinted patterns in the PR using AZ 326 MIF developer (Microchemicals Ltd.) in a clean petri dish (usually ~ 1 min). Use a pipette to flow developer over the samples. Observe patterns develop using a magnifying glass. Dispose excess developer in the 'developer waste bottle.' Rinse the petri dish with samples in it in some UltraPure water. Rinse the samples one by one by dipping in UltraPure water in container 1 and store in the second container, by immersing in UltraPure water.

7) Flush away the UltraPure water in container 2. Remove samples from the container with tweezers and place on a clean dry clean room wipe, samples facing up. Dry samples in N_2 jet one by one. Check samples under optical microscope to ensure PR residues within developed patterns are removed (appears clear, not rainbow-like).

8) Include steps (1-7) for additional patterned layers, edge bead removal step if needed (first pattern). This completes the patterning workflow, illustrated in schematic Fig. 3.3-bottom. Tidy work area and switch off equipment. Samples are ready for further processing, deposition etc.

Bibliography

[1] F. Pivec, *Measuring the information society*, vol. 8, no. 3. 2003.

[2] C. A. MacK, "Fifty years of Moore's law," in *IEEE Transactions on Semiconductor Manufacturing*, 2011, vol. 24, no. 2, pp. 202–207.

[3] R. P. Feynman, "There's plenty of room at the bottom: An invitation to enter a new field of physics," *Eng. Sci.*, vol. 23, pp. 22–35, 1960.

[4] R. P. Feynman, "There's plenty of room at the bottom [data storage]," *J. Microelectromechanical Syst.*, vol. 1, no. 1, pp. 60–66, 1992.

[5] K. Sawano *et al.*, "Ultrashallow Ohmic contacts for n-type Ge by Sb ?? -doping," *Appl. Phys. Lett.*, vol. 97, no. 16, p. 162108, Oct. 2010.

[6] F. Chiodi, A. D. Chepelianskii, C. Gardès, G. Hallais, D. Bouchier, and D. Débarre, "Laser doping for ohmic contacts in n-type Ge," *Appl. Phys. Lett.*, vol. 105, no. 24, p. 242101, Dec. 2014.

[7] J. Bardeen, "Surface states and rectification at a metal semi-conductor contact," *Phys. Rev.*, vol. 71, no. 10, pp. 717–727, May 1947.

[8] W. Mönch, "Barrier heights of real Schottky contacts explained by metal-induced gap states and lateral inhomogeneities," *J. Vac. Sci. Technol. B Microelectron. Nanom. Struct.*, vol. 17, no. 4, p. 1867, 1999.

[9] W. E. Spicer, "Unified defect model and beyond," *J. Vac. Sci. Technol.*, vol. 17, no. 5, p. 1019, Sep. 1980.

[10] H. Hasegawa, "Unified disorder induced gap state model for insulator–semiconductor and metal–semiconductor interfaces," *J. Vac. Sci. Technol. B Microelectron. Nanom. Struct.*, vol. 4, no. 4, p. 1130, Jul. 1986.

[11] W. Mönch, "Interface-induced gap states and band-structure lineup at TiO_2 heterostructures and Schottky contacts," *J. Appl. Phys.*, vol. 107, no. 1, p. 13706, Jan. 2010.

[12] W. Mönch, "Adsorbate-induced surface states and Fermi-level pinning at semiconductor surfaces," *J. Vac. Sci. Technol. B Microelectron. Nanom. Struct.*, vol. 7, no. 5, p. 1216, Sep. 1989.

[13] E. H. Rhoderick and R. H. Williams, "Metal-semiconductor contacts," *Phys. Technol.*, vol. 5, no. 4, pp. 223–223, 1988.

[14] R. T. Tung, "Schottky-Barrier formation at single-crystal metal-semiconductor interfaces," *Phys. Rev. Lett.*, vol. 52, no. 6, pp. 461–464, Feb. 1984.

[15] R. T. Tung, "Electron transport at metal-semiconductor interfaces: General theory," *Phys. Rev. B*, vol. 45, no. 23, pp. 13509–13523, Jun. 1992.

[16] J. L. Freeouf, "Are interface states consistent with Schottky barrier measurements," *Appl. Phys. Lett.*, vol. 41, no. 3, pp. 285–287, Aug. 1982.

[17] R. T. Tung, "Chemical bonding and fermi level pinning at metal-semiconductor interfaces.," *Phys. Rev. Lett.*, vol. 84, no. 26 Pt 1, pp. 6078–6081, 2000.

[18] A. B. Fowler, "Contact Potential Measurements on Cleaned Germanium Surfaces," *J. Appl. Phys.*, vol. 30, no. 4, pp. 556–558, Apr. 1959.

[19] G. . Gobeli and F. . Allen, "Photoelectric properties and work function of cleaved germanium surfaces," *Surf. Sci.*, vol. 2, pp. 402–408, Jan. 1964.

[20] P. Handler and W. M. Portnoy, “Electronic Surface States and the Cleaned Germanium Surface,” *Phys. Rev.*, vol. 116, no. 3, pp. 516–526, 1959.

[21] M. Wojtaszek, J. Lis, R. Zuzak, B. Such, and M. Szymonski, “Inversion layer on the Ge(001) surface from the four-probe conductance measurements,” *Appl. Phys. Lett.*, vol. 105, no. 4, p. 42111, Jul. 2014.

[22] T. Y. Popik, V. M. Feyer, O. B. Shpenik, and Y. V. Popik, “Low-energy electron spectroscopy of Si(100) and Ge(100) surfaces,” *Radiat. Phys. Chem.*, vol. 68, no. 1–2, pp. 251–256, Sep. 2003.

[23] A. Dimoulas, P. Tsipas, A. Sotiropoulos, and E. K. Evangelou, “Fermi-level pinning and charge neutrality level in germanium,” *Appl. Phys. Lett.*, vol. 89, no. 25, 2006.

[24] R. T. Tung, “Formation of an electric dipole at metal-semiconductor interfaces,” *Phys. Rev. B*, vol. 64, no. 20, p. 205310, 2001.

[25] F. J. Giessibl, “Atomic Resolution of the Silicon (111)-(7x7) Surface by Atomic Force Microscopy,” *Science (80-.).*, vol. 267, no. 5194, pp. 68–71, 1995.

[26] W. Mönch, “Chemisorption-induced defects at interfaces on compound semiconductors,” *Surf. Sci.*, vol. 132, no. 1–3, pp. 92–121, Sep. 1983.

[27] P. Krüger and J. Pollmann, “Dimer Reconstruction of Diamond, Si, and Ge (001) Surfaces,” *Phys. Rev. Lett.*, vol. 74, no. 7, pp. 1155–1158, Feb. 1995.

[28] E. Kamiyama and K. Sueoka, “First principles analysis on interaction between vacancy near surface and dimer structure of silicon crystal,” *J. Appl. Phys.*, vol. 111, no. 1, p. 13521, Jan. 2012.

[29] E. Kamiyama, K. Sueoka, and J. Vanhellemont, “Surface-induced charge at a Ge (100) dimer surface and its interaction with vacancies and self-interstitials,” *J. Appl. Phys.*, vol. 113, no. 9, 2013.

[30] T. Hanrath and B. A. Korgel, “Influence of surface states on electron transport through intrinsic Ge nanowires,” *J. Phys. Chem. B*, vol. 109, no. 12, pp. 5518–5524, Mar. 2005.

[31] P. Paramahans Manik *et al.*, “Fermi-level unpinning and low resistivity in contacts to n-type Ge with a thin ZnO interfacial layer,” *Appl. Phys. Lett.*, vol. 101, no. 18, p. 182105, Oct. 2012.

[32] D. R. Gajula, P. Baine, M. Modreanu, P. K. Hurley, B. M. Armstrong, and D. W. McNeill, “Fermi level de-pinning of aluminium contacts to n-type germanium using thin atomic layer deposited layers,” *Appl. Phys. Lett.*, vol. 104, no. 1, p. 12102, Jan. 2014.

[33] J. Robertson and L. Lin, “Fermi level pinning in Si, Ge and GaAs systems - MIGS or defects?,” in *Technical Digest - International Electron Devices Meeting, IEDM*, 2009, pp. 1–4.

[34] G.-S. Kim *et al.*, “Effective Schottky Barrier Height Lowering of Metal/n-Ge with a TiO_2 /GeO_2 Interlayer Stack,” *ACS Appl. Mater. Interfaces*, vol. 8, no. 51, pp. 35419–35425, Dec. 2016.

[35] P. P. Manik and S. Lodha, “Contacts on n-type germanium using variably doped zinc oxide and highly doped indium tin oxide interfacial layers,” *Appl. Phys. Express*, vol. 8, no. 5, p. 51302, May 2015.

[36] A. Agrawal *et al.*, “Fermi level depinning and contact resistivity reduction using a reduced titania interlayer in n-silicon metal-insulator-semiconductor ohmic contacts,” *Appl. Phys. Lett.*, vol. 104, no. 11, p. 112101, Mar. 2014.

[37] M. Iyota, K. Yamamoto, D. Wang, H. Yang, and H. Nakashima, “Ohmic contact formation on n-type Ge by direct deposition of TiN,” *Appl. Phys. Lett.*, vol. 98, no. 19, p. 192108, May 2011.

[38] V. Pavan Kishore, P. Paramahans, S. Sadana, U. Ganguly, and S. Lodha, “Nanocrystal-based

Ohmic contacts on n and p-type germanium," *Appl. Phys. Lett.*, vol. 100, no. 14, p. 142107, Apr. 2012.

[39] H. Yu *et al.*, "Contact resistivities of metal-insulator-semiconductor contacts and metal-semiconductor contacts," *Appl. Phys. Lett.*, vol. 108, no. 17, pp. 1–5, 2016.

[40] P. Skeath, C. Y. Su, I. Hino, I. Lindau, and W. E. Spicer, "New Fermi energy pinning behavior of Au on GaAs (110) suggesting increased Schottky-barrier heights on n-type GaAs," *Appl. Phys. Lett.*, vol. 39, no. 4, pp. 349–351, Aug. 1981.

[41] S. Bhargava, H.-R. Blank, V. Narayanamurti, and H. Kroemer, "Fermi-level pinning position at the Au–InAs interface determined using ballistic electron emission microscopy," *Appl. Phys. Lett.*, vol. 70, no. 6, pp. 759–761, Feb. 1997.

[42] P. J. King, E. Arac, S. Ganti, K. S. K. Kwa, N. Ponon, and A. G. O'Neill, "Improving metal/semiconductor conductivity using AlO_x interlayers on n-type and p-type Si," *Appl. Phys. Lett.*, vol. 105, no. 5, 2014.

[43] S. Ganti *et al.*, "Voltage Controlled Hot Carrier Injection Enables Ohmic Contacts Using Au Island Metal Films on Ge," *ACS Appl. Mater. Interfaces*, vol. 9, no. 33, pp. 27357–27364, Aug. 2017.

[44] F. F. Chen, *Introduction to Plasma Physics*, vol. 1. Boston, MA: Springer US, 1995.

[45] S. M. Sze, "Physics of semiconductor devices 3rd edition," *Phys. Semicond. Devices, 3rd Ed. John Wiley Sons, Inc.; NJ*, pp. 227–229, 2007.

[46] S. Richard, F. Aniel, and G. Fishman, "Energy-band structure of Si, Ge and GaAs over the whole brillouin zone via the k.p method," in *AIP Conference Proceedings*, 2005, vol. 772, pp. 1123–1124.

[47] C. R. Crowell, "The Richardson constant for thermionic emission in Schottky barrier diodes," *Solid. State. Electron.*, vol. 8, no. 4, pp. 395–399, Apr. 1965.

[48] H. C. Card and E. H. Rhoderick, "Studies of tunnel MOS diodes I. Interface effects in silicon Schottky diodes," *J. Phys. D. Appl. Phys.*, vol. 4, no. 10, p. 319, Oct. 1971.

[49] H. C. Card and E. H. Rhoderick, "Studies of tunnel MOS diodes II. Thermal equilibrium considerations," *J. Phys. D. Appl. Phys.*, vol. 4, no. 10, p. 320, Oct. 1971.

[50] H. Dreicer, "Electron and ion runaway in a fully ionized gas. I," *Phys. Rev.*, vol. 115, no. 2, pp. 238–249, 1959.

[51] H. Dreicer, "Electron and Ion Runaway in a Fully Ionized Gas. II," *Phys. Rev.*, vol. 117, no. 2, pp. 329–342, Jan. 1960.

[52] C. W. Malley, Chris, Sam McKagan, Kathy Perkins, "Quantum Tunneling and Wave Packets," *PhET Interactive Simulations, University of Colorado, Boulder*. [Online]. Available: https://phet.colorado.edu/en/simulation/quantum-tunneling.

[53] A. W. Ott, J. W. Klaus, J. M. Johnson, and S. M. George, "Al_2O_3 thin film growth on Si(100) using binary reaction sequence chemistry," *Thin Solid Films*, vol. 292, no. 1–2, pp. 135–144, Jan. 1997.

[54] A. C. Dillon, A. W. Ott, J. D. Way, and S. M. George, "Surface chemistry of Al_2O_3 deposition using $Al(CH3)_3$ and H_2O in a binary reaction sequence," *Surf. Sci.*, vol. 322, no. 1–3, pp. 230–242, 1995.

[55] Nicolas Schoeni and Gervais Chapuis, "DiffractOgram," *École Polytechnique Fédérale de Lausanne, Switzerland*. [Online]. Available: http://escher.epfl.ch/new_website/.

[56] AMMRF, "MyScope - training for advanced research." [Online]. Available: http://www.ammrf.org.au/myscope/sem/practice.

[57] XDB, "X-Ray Properties of the Elements," *Center for X-Ray optics and Advanced Light source, Lawrence Berkeley National Laboratory*. [Online]. Available: http://xdb.lbl.gov/Section1/Periodic_Table/X-ray_Elements.html.

[58] F. Krumeich, "SEM: Imaging with Secondary Electrons," *ETH Zürich*. [Online]. Available: http://www.microscopy.ethz.ch/se.htm.

[59] T. C. Sam Subramanian, Gary Clark, Kheim Ly, "Energy-Filtered Transmission Electron Microscopy (EFTEM) of Semiconductor Devices," in *Electron Device Failure Analysis*, vol. 13, no. 1, ASM International, 2011, pp. 20–28.

[60] P. J. Thomas and P. a. Midgley, "An Introduction to Energy-Filtered Transmission Electron Microscopy," *Top. Catal.*, vol. 21, no. 4, pp. 109–138, 2002.

[61] D. K. Schroder, *Semiconductor Material and Device Characterization: Third Edition*. 2005.

[62] G. P. Carver, J. J. Kopanski, D. B. Novotny, and R. A. Forman, "Specific contact resistivity of metal-semiconductor contacts-a new, accurate method linked to spreading resistance," *IEEE Transactions on Electron Devices*, vol. 35, no. 4. pp. 489–497, 1988.

[63] A. Shepela, "The specific contact resistance of Pd_2Si contacts on n- and p-Si," *Solid. State. Electron.*, vol. 16, no. 4, pp. 477–481, 1973.

[64] J. M. Andrews and M. P. Lepselter, "Reverse current-voltage characteristics of metal-silicide Schottky diodes," *Solid State Electron.*, vol. 13, no. 7, pp. 1011–1023, 1970.

[65] A. Agrawal *et al.*, "Fermi level depinning and contact resistivity reduction using a reduced titania interlayer in n-silicon metal-insulator-semiconductor ohmic contacts," *Appl. Phys. Lett.*, vol. 104, no. 11, p. 112101, Mar. 2014.

[66] H. Bender, "Hydrogen Passivation of HF-Last Cleaned (100) Silicon Surfaces Investigated by Multiple Internal Reflection Infrared Spectroscopy," *J. Electrochem. Soc.*, vol. 141, no. 11, p. 3128, 1994.

[67] A. J. Chiquito, C. a Amorim, O. M. Berengue, L. S. Araujo, E. P. Bernardo, and E. R. Leite, "Back-to-back Schottky diodes: the generalization of the diode theory in analysis and extraction of electrical parameters of nanodevices," *J. Phys. Condens. Matter*, vol. 24, p. 225303, 2012.

[68] J. H. Werner, "Schottky barrier and pn-junction I/V plots - Small signal evaluation," *Appl. Phys. A Solids Surfaces*, vol. 47, no. 3, pp. 291–300, 1988.

[69] S. K. Cheung and N. W. Cheung, "Extraction of Schottky diode parameters from forward current-voltage characteristics," *Appl. Phys. Lett.*, vol. 49, no. 2, pp. 85–87, Jul. 1986.

[70] W. S. Wang, C. Ho, and T. M. Chuang, "Investigation of PtSi/p-Si Schottky barrier height using I-V-T technique," *Mater. Chem. Phys.*, vol. 51, no. 1, pp. 88–91, 1997.

[71] A. Lauwers *et al.*, "Materials aspects, electrical performance, and scalability of Ni silicide towards sub-0.13 μm technologies," *J. Vac. Sci. Technol. B Microelectron. Nanom. Struct.*, vol. 19, no. 6, p. 2026, 2001.

[72] S. Zhu, R. L. Van Meirhaeghe, S. Forment, G. Ru, and B. Li, "Effects of the annealing temperature on Ni silicide/n-Si(100) Schottky contacts," *Solid. State. Electron.*, vol. 48, no. 1, pp. 29–35, Jan. 2004.

[73] K.-W. Ang *et al.*, "Effective Schottky Barrier Height modulation using dielectric dipoles for source/drain specific contact resistivity improvement," in *2012 International Electron Devices Meeting*, 2012, p. 18.6.1-18.6.4.

[74] V. Naumann, M. Otto, R. B. Wehrspohn, and C. Hagendorf, "Chemical and structural study of electrically passivating Al_2O_3/Si interfaces prepared by atomic layer deposition," *J. Vac. Sci. Technol. A Vacuum, Surfaces, Film.*, vol. 30, no. 4, p. 04D106, 2012.

[75] G. Agostinelli *et al.*, "Very low surface recombination velocities on p-type silicon wafers passivated with a dielectric with fixed negative charge," *Sol. Energy Mater. Sol. Cells*, vol. 90, no. 18–19, pp. 3438–3443, Nov. 2006.

[76] R. S. Johnson, G. Lucovsky, and I. Baumvol, "Physical and electrical properties of noncrystalline Al_2O_3 prepared by remote plasma enhanced chemical vapor deposition," *J. Vac. Sci. Technol. A Vacuum, Surfaces, Film.*, vol. 19, no. 4, pp. 1353–1360, Jul. 2001.

[77] B. Hoex, S. B. S. Heil, E. Langereis, M. C. M. van de Sanden, and W. M. M. Kessels, "Ultralow surface recombination of c-Si substrates passivated by plasma-assisted atomic layer deposited Al_2O_3," *Appl. Phys. Lett.*, vol. 89, no. 4, p. 42112, Jul. 2006.

[78] Y.-C. Yeo, T.-J. King, and C. Hu, "Metal-dielectric band alignment and its implications for metal gate complementary metal-oxide-semiconductor technology," *J. Appl. Phys.*, vol. 92, no. 12, pp. 7266–7271, Dec. 2002.

[79] E. Bersch, S. Rangan, R. A. Bartynski, E. Garfunkel, and E. Vescovo, "Band offsets of ultrathin high-k oxide films with Si," *Phys. Rev. B*, vol. 78, no. 8, p. 85114, Aug. 2008.

[80] C.-N. Ni *et al.*, "Ultra-low contact resistivity with highly doped Si:P contact for nMOSFET," in *2015 Symposium on VLSI Technology (VLSI Technology)*, 2015, pp. T118–T119.

[81] R. V. Ghita, C. Logofatu, C. Negrila, A. S. Manea, M. Cernea, and M. F. Lazarescu, "Studies of ohmic contact and schottky barriers on Au-Ge/GaAs and Au-Ti/GaAs," *J. Optoelectron. Adv. Mater.*, vol. 7, no. 6, pp. 3033–3037, 2005.

[82] C. . Card, "Aluminum-Silicon Schottky barriers and ohmic contacts in integrated circuits," *Electron Devices, IEEE Trans.*, vol. 23, no. 6, pp. 538–544, 1976.

[83] S. U. Yang, W. S. Jung, I. Y. Lee, H. W. Jung, G. H. Kim, and J. H. Park, "Ohmic contact formation process on low n-type gallium arsenide (GaAs) using indium gallium zinc oxide (IGZO)," *Mater. Res. Bull.*, vol. 50, pp. 409–412, Feb. 2014.

[84] S. Kim *et al.*, "Non-Alloyed Ohmic Contacts on GaAs Using Metal-Interlayer-Semiconductor Structure With SF 6 Plasma Treatment," *IEEE Electron Device Lett.*, vol. 37, no. 4, pp. 373–376, Apr. 2016.

[85] A. . Baca, F. Ren, J. . Zolper, R. . Briggs, and S. . Pearton, "A survey of ohmic contacts to III-V compound semiconductors," *Thin Solid Films*, vol. 308, pp. 599–606, Oct. 1997.

[86] F. D. Heinz *et al.*, "Microscopic origin of the aluminium assisted spiking effects in n-type silicon solar cells," *Sol. Energy Mater. Sol. Cells*, vol. 131, pp. 105–109, 2014.

[87] J. R. Black, "Electromigration failure modes in aluminum metallization for semiconductor devices," *Proc. IEEE*, vol. 57, no. 9, pp. 1587–1594, 1969.

[88] Y. Wang, D. Liu, G. Feng, Z. Ye, Z. Gao, and X. Wang, "Effect of Pt diffusion barrier layer in Ni/AuGe/Pt/Au on ohmic contact to n-GaAs," *J. Semicond.*, vol. 36, no. 3, p. 36002, Mar. 2015.

[89] K. Yamamoto *et al.*, "Role of an interlayer at a TiN/Ge contact to alleviate the intrinsic Fermi-level pinning position toward the conduction band edge," *Appl. Phys. Lett.*, vol. 104, no. 13, p. 132109, Mar. 2014.

[90] W. M. Bullis, "Properties of gold in silicon," *Solid State Electron.*, vol. 9, pp. 143–168, 1966.

[91] Y. Eichhammer, M. Heyns, and N. Moelans, "Calculation of phase equilibria for an alloy nanoparticle in contact with a solid nanowire," *Calphad Comput. Coupling Phase Diagrams Thermochem.*, vol. 35, no. 2, pp. 173–182, 2011.

[92] C. Ratsch and J. a. Venables, "Nucleation theory and the early stages of thin film growth," *J. Vac. Sci. Technol. A Vacuum, Surfaces, Film.*, vol. 21, no. 5, p. S96, Sep. 2003.

[93] T. Karakouz, A. B. Tesler, T. Sannomiya, Y. Feldman, A. Vaskevich, and I. Rubinstein, "Mechanism of morphology transformation during annealing of nanostructured gold films on glass.," *Phys. Chem. Chem. Phys.*, vol. 15, no. 13, pp. 4656–65, Mar. 2013.

[94] S. J. Jung, T. Lutz, M. Boese, J. D. Holmes, and J. J. Boland, "Surface energy driven agglomeration and growth of single crystal metal wires," *Nano Lett.*, vol. 11, no. 3, pp. 1294–1299, Mar. 2011.

[95] F. Krok *et al.*, "Controlled growth of hexagonal gold nanostructures during self-assembling on Ge(001) surface," *Sci. Rep.*, vol. submitted, no. 1, pp. 1–8, Feb. 2016.

[96] J. W. Mayer, "Gold contacts to semiconductor devices," *Gold Bull.*, vol. 17, no. 1, pp. 18–26, Mar. 1984.

[97] H. Hieber, "Aging properties of gold layers with different adhesion layers," *Thin Solid Films*, vol. 37, no. 3, pp. 335–343, Sep. 1976.

[98] M. C. Hanf, C. Pirri, J. C. Peruchetti, D. Bolmont, and G. Gewinner, "Persistence of the Au(100)-(1 X 1) M3 surface state at the Cr/Au(100) interface: Epitaxial growth of a gold-chromium alloy," *Phys. Rev. B*, vol. 39, no. 15, 1989.

[99] R. Soulairol, C. C. Fu, and C. Barreteau, "Magnetic and energetic properties of low-index Cr surfaces and Fe/Cr interfaces: A first-principles study," *Phys. Rev. B - Condens. Matter Mater. Phys.*, vol. 84, no. 15, p. 155402, Oct. 2011.

[100] J. Vancea, G. Reiss, F. Schneider, K. Bauer, and H. Hoffmann, "Substrate effects on the surface topography of evaporated gold films-A scanning tunnelling microscopy investigation," *Surf. Sci.*, vol. 218, no. 1, pp. 108–126, Aug. 1989.

[101] Y. Tolstova, S. T. Omelchenko, A. M. Shing, and H. A. Atwater, "Heteroepitaxial growth of Pt and Au thin films on MgO single crystals by bias-assisted sputtering," *Sci. Rep.*, vol. 6, no. 1, p. 23232, Mar. 2016.

[102] M. Nikiel, B. R. Jany, D. Wrana, K. Szajna, and F. Krok, "SEM studies of vacuum condition influence on thermally induced Au self-organization on Ge(001) surface," *Surf. Coatings Technol.*, vol. 277, pp. 165–169, Sep. 2015.

[103] S. Jung Jung, T. Lutz, and J. J. Boland, "Anisotropic etching induced by surface energy driven agglomeration," *J. Vac. Sci. Technol. A Vacuum, Surfaces, Film.*, vol. 29, no. 5, p. 51403, Sep. 2011.

[104] C. V. Thompson, "Solid-State Dewetting of Thin Films," *Annu. Rev. Mater. Res.*, vol. 42, no. 1, pp. 399–434, 2012.

[105] J. Trice, D. Thomas, C. Favazza, R. Sureshkumar, and R. Kalyanaraman, "Pulsed-laser-induced dewetting in nanoscopic metal films: Theory and experiments," *Phys. Rev. B - Condens. Matter Mater. Phys.*, vol. 75, no. 23, 2007.

[106] A. N. Banerjee, S. Qian, and S. W. Joo, "Large field enhancement at electrochemically grown quasi-1D Ni nanostructures with low-threshold cold-field electron emission.," *Nanotechnology*, vol. 22, no. 3, p. 35702, Jan. 2011.

[107] N. D. Lang and W. Kohn, "Theory of metal surfaces: Induced surface charge and image potential," *Phys. Rev. B*, vol. 7, no. 8, pp. 3541–3550, 1973.

[108] M. Kuzmin *et al.*, "Origin of Fermi-level pinning and its control on the n -type Ge(100) surface," *Phys. Rev. B*, vol. 94, no. 3, p. 35421, Jul. 2016.

[109] K. Yamane *et al.*, "Effect of atomically controlled interfaces on Fermi-level pinning at metal/Ge interfaces," *Appl. Phys. Lett.*, vol. 96, no. 16, p. 162104, Apr. 2010.

[110] S. Just, H. Soltner, S. Korte, V. Cherepanov, and B. Voigtländer, "Surface conductivity of Si(100) and Ge(100) surfaces determined from four-point transport measurements using an

analytical N -layer conductance model," *Phys. Rev. B*, vol. 95, no. 7, p. 75310, Feb. 2017.

[111] R. G. Chambers, "Anomalous Skin Effect in Metals," *Nature*, vol. 165, no. 4189, pp. 239–240, 1950.

[112] D. Kuzum, K. Martens, T. Krishnamohan, and K. C. Saraswat, "Characteristics of surface states and charge neutrality level in Ge," *Appl. Phys. Lett.*, vol. 95, no. 25, p. 252101, Dec. 2009.

[113] N. Chandra, C. J. Tracy, J. H. Cho, S. T. Picraux, R. Hathwar, and S. M. Goodnick, "Vertically grown Ge nanowire Schottky diodes on Si and Ge substrates," *J. Appl. Phys.*, vol. 118, no. 2, p. 24301, Jul. 2015.

[114] Y. Ando *et al.*, "Electrical injection and detection of spin-polarized electrons in silicon through an Fe_3Si/Si Schottky tunnel barrier," *Appl. Phys. Lett.*, vol. 94, no. 18, p. 182105, May 2009.

[115] L. Esaki, "What did I explore in half a century of research?: What discovery, what invention, where, when?," *Jpn. J. Appl. Phys.*, vol. 54, no. 4, p. 40101, Apr. 2015.

[116] K. Kobayashi and E. Ishikawa, "Surface-state conduction through dangling-bond states," *Surf. Sci.*, vol. 540, no. 2–3, pp. 431–440, Aug. 2003.

[117] P. Tsipas and A. Dimoulas, "Modeling of negatively charged states at the Ge surface and interfaces," *Appl. Phys. Lett.*, vol. 94, no. 1, p. 12114, Jan. 2009.

[118] R. Feenstra, G. Meyer, F. Moresco, and K. Rieder, "Buckling and band gap of the Ge(111)2×1 surface studied by low-temperature scanning tunneling microscopy," *Phys. Rev. B*, vol. 64, no. 8, pp. 2–5, Aug. 2001.

[119] W. Fawcett and E. G. S. Paige, "Negative differential mobility of electrons in germanium: A Monte Carlo calculation of the distribution function, drift velocity and carrier population in the (111) and (100) minima," *J. Phys. C Solid St. Phys.*, vol. 4, no. 13, pp. 1801–1821, Sep. 1971.

[120] D. M. Chang and J. G. Ruch, "Measurement of the velocity field characteristic of electrons in germanium," *Appl. Phys. Lett.*, vol. 12, no. 3, pp. 111–112, Feb. 1968.

[121] M. K. Husain, X. V. Li, and C. H. De Groot, "Observation of Negative Differential Conductance in a Reverse-Biased Ni/Ge Schottky Diode," *IEEE Electron Device Lett.*, vol. 30, no. 9, pp. 966–968, Sep. 2009.

[122] L. D. Bell and W. J. Kaiser, "Observation of interface band structure by Ballistic-Electron-Emission-Microscopy," *Phys. Rev. Lett.*, vol. 61, no. 20, p. 2368, 1988.

[123] A. Javey, J. Guo, Q. Wang, M. Lundstrom, and H. Dai, "Ballistic carbon nanotube field-effect transistors," *Nature*, vol. 424, no. 6949, pp. 654–657, 2003.

[124] M. Zapata Herrera, J. Aizpurua, A. K. Kazansky, and A. G. Borisov, "Plasmon Response and Electron Dynamics in Charged Metallic Nanoparticles," *Langmuir*, vol. 32, no. 11, pp. 2829–2840, Mar. 2016.

[125] J. S. Johannessen, W. E. Spicer, and Y. E. Strausser, "*LVV* Spectra of Si, SiO_2 and Si_3N_4," *Physica Scripta*, vol. 19, no. 4. pp. 355–359, 1979.

[126] H. Bialas, "Acoustic amplification in Ge at 9.3GHz," *Phys. Stat. Sol.*, vol. 9, p. 191, 1972.

[127] W.-S. Chang *et al.*, "Tuning the acoustic frequency of a gold nanodisk through its adhesion layer," *Nat. Commun.*, vol. 6, p. 7022, 2015.

[128] D. Schriver, M. Ashour-Abdalla, and R. L. Richard, "On the origin of the ion-electron temperature difference in the plasma sheet," *J. Geophys. Res. Sp. Phys.*, vol. 103, no. A7, pp. 14879–14895, Jul. 1998.

[129] F. Léonard and A. A. Talin, "Electrical contacts to one- and two-dimensional nanomaterials," *Nat. Nanotechnol.*, vol. 6, no. 12, pp. 773–783, Nov. 2011.

[130] D. . Paul, “Silicon germanium heterostructures in electronics: the present and the future,” *Thin Solid Films*, vol. 321, pp. 172–180, 1998.

[131] D. W. Greve, “Growth of epitaxial germanium-silicon heterostructures by chemical vapour deposition,” *Mater. Sci. Eng. B*, vol. 18, no. 1, pp. 22–51, 1993.

[132] M. S. Song *et al.*, “Vertically standing Ge nanowires on GaAs(110) substrates.,” *Nanotechnology*, vol. 19, no. 12, p. 125602, 2008.

[133] G. Brammertz *et al.*, “GaAs on Ge for CMOS,” *Thin Solid Films*, vol. 517, no. 1, pp. 148–151, 2008.

[134] R. L. Anderson, “Experiments on Ge-GaAs heterojunctions,” *Solid State Electron.*, vol. 5, no. 6, pp. 341–351, 1962.

[135] M. W. Geis *et al.*, “A new surface electron-emission mechanism in diamond cathodes,” *Nature*, vol. 393, no. 6684, pp. 431–435, Jun. 1998.

[136] M. Bernardi, J. Mustafa, J. B. Neaton, and S. G. Louie, “Theory and computation of hot carriers generated by surface plasmon polaritons in noble metals,” *Nat. Commun.*, vol. 6, p. 7044, 2015.

[137] R. D. Fedorovich, A. G. Naumovets, and P. M. Tomchuk, “Electron and light emission from island metal films and generation of hot electrons in nanoparticles,” *Phys. Rep.*, vol. 328, no. 2–3, pp. 73–179, Apr. 2000.

[138] P. G. Borzjak, O. G. Sarbej, and R. . Fedorowitsch, “Neue Erscheinungen in sehr dünnen Metallschichten (in German),” *Phys. Stat. Sol.*, vol. 8, p. 55, 1965.

[139] G. Dittmer, “Electrical conduction and electron emission of discontinuous thin films,” *Thin Solid Films*, vol. 9, no. 3, pp. 317–328, 1972.

[140] E. D. Belotskii and P. M. Tomchuk, “Electron-phonon interaction and hot electrons in small metal islands,” *Surf. Sci.*, vol. 239, p. 143, 1990.

[141] H. Araki and T. Hanawa, “The temperature dependence of electron emission from a discontinuous carbon film device between silver film electrodes,” *Thin Solid Films*, vol. 158, no. 2, pp. 207–216, Apr. 1988.

[142] S. A. Gorban, S. A. Nepijko, and P. M. Tomchuk, “Electron-phonon interaction in small metal islands deposited on an insulating substrate,” *Int. J. Electron.*, vol. 70, no. April 2013, pp. 37–41, Mar. 2007.

[143] R. E. Thomas and G. A. Haas, “Diffusion measurements in thin films utilizing work function changes: Cr into Au,” *J. Appl. Phys.*, vol. 43, no. 12, pp. 4900–4907, Dec. 1972.

[144] G. Gioia and M. Ortiz, “Delamination of compressed thin films,” *Adv. Appl. Mech.*, vol. 33, no. 8, pp. 119–192, 1997.

[145] R. C. Cammarata, “Surface and interface stress effects in thin films,” *Prog. Surf. Sci.*, vol. 46, no. 1, pp. 1–38, 1994.

[146] P. Müller, A. Saúl, and F. Leroy, “Simple views on surface stress and surface energy concepts,” *Adv. Nat. Sci. Nanosci. Nanotechnol.*, vol. 5, no. 1, p. 13002, 2013.

[147] L. Vitos, A. V. Ruban, H. L. Skriver, and J. Kollár, “The surface energy of metals,” *Surf. Sci.*, vol. 411, pp. 186–202, 1998.

[148] C. V Thompson, “Solid-State Dewetting of Thin Films,” *Annu. Rev. Mater. Res*, vol. 42, pp. 399–434, 2012.

[149] A. Kinbara, S. Baba, N. Matuda, and K. Takamisawa, “Mechanical properties of and cracks and wrinkles in vacuum-deposited MgF_2, carbon and baron coatings,” *Thin Solid Films*, vol. 84, no. 2, pp. 205–212, Oct. 1981.

[150] M. K. Khristosov, L. Bloch, M. Burghammer, Y. Kauffmann, A. Katsman, and B. Pokroy, "Sponge-like nanoporous single crystals of gold," *Nat. Commun.*, vol. 6, no. May, p. 8841, Nov. 2015.

[151] G. Seguini, J. L. Curi, S. Spiga, G. Tallarida, C. Wiemer, and M. Perego, "Solid-state dewetting of ultra-thin Au films on SiO_2 and HfO_2.," *Nanotechnology*, vol. 25, no. 49, p. 495603, Dec. 2014.

[152] C. Voisin *et al.*, "Size-dependent electron-electron interactions in metal nanoparticles," *Phys. Rev. Lett.*, vol. 85, no. 10, pp. 2200–2203, 2000.

[153] K. Hiehata, A. Sasahara, and H. Onishi, "Local work function analysis of Pt/TiO_2 photocatalyst by a Kelvin probe force microscope," *Nanotechnology*, vol. 18, no. 8, p. 84007, Feb. 2007.

[154] B. Abeles, P. Sheng, M. D. Coutts, and Y. Arie, "Structural and electrical properties of granular metal films," *Adv. Phys.*, vol. 24, no. 3, pp. 407–461, 1975.

[155] M. Buret *et al.*, "Spontaneous Hot-Electron Light Emission from Electron-Fed Optical Antennas," *Nano Lett.*, vol. 15, no. 9, pp. 5811–5818, 2015.

[156] Z. Fang *et al.*, "Plasmon-induced doping of graphene," *ACS Nano*, vol. 6, no. 11, pp. 10222–10228, 2012.

[157] M. L. Brongersma, N. J. Halas, and P. Nordlander, "Plasmon-induced hot carrier science and technology," *Nat. Nanotechnol.*, vol. 10, no. 1, pp. 25–34, 2015.

[158] M. Iyota, K. Yamamoto, D. Wang, H. Yang, and H. Nakashima, "Ohmic contact formation on n-type Ge by direct deposition of TiN," *Appl. Phys. Lett.*, vol. 98, no. 19, p. 192108, 2011.

[159] L. D. Bell and W. J. Kaiser, "Observation of interface band structure by ballistic-electron-emission microscopy," *Phys. Rev. Lett.*, vol. 61, no. 20, pp. 2368–2371, 1988.

[160] H. Inouye, K. Tanaka, I. Tanahashi, and K. Hirao, "Ultrafast dynamics of nonequilibrium electrons in a gold nanoparticle system," *Phys. Rev. B*, vol. 57, no. 18, pp. 11334–11340, 1998.

[161] W. J. Baumgardner *et al.*, "Pulsed laser annealing of thin films of self-assembled nanocrystals," *ACS Nano*, vol. 5, no. 9, pp. 7010–7019, 2011.

[162] S. Y. Chou, P. R. Krauss, W. Zhang, L. Guo, and L. Zhuang, "Sub-10 nm imprint lithography and applications," *J. Vac. Sci. Technol.*, vol. 15, no. 6, pp. 2897–2904, 1997.

[163] B. Päivänranta, A. Langner, E. Kirk, C. David, and Y. Ekinci, "Sub-10 nm patterning using EUV interference lithography.," *Nanotechnology*, vol. 22, no. 37, p. 375302, 2011.

[164] Y. K. Lee, C. H. Jung, J. Park, H. Seo, G. A. Somorjai, and J. Y. Park, "Surface plasmon-driven hot electron flow probed with metal-semiconductor nanodiodes," *Nano Lett.*, vol. 11, no. 10, pp. 4251–4255, 2011.

[165] M. W. Knight *et al.*, "Embedding plasmonic nanostructure diodes enhances hot electron emission," *Nano Lett.*, vol. 13, no. 4, pp. 1687–1692, 2013.

[166] P. J. Schuck, "Nanoimaging: Hot electrons go through the barrier.," *Nat. Nanotechnol.*, vol. 8, no. 11, pp. 799–800, 2013.

[167] S. Mukherjee *et al.*, "Hot electrons do the impossible: Plasmon-induced dissociation of H_2 on Au," *Nano Lett.*, vol. 13, no. 1, pp. 240–247, 2013.

[168] H. Chalabi and M. L. Brongersma, "Plasmonics: Harvest season for hot electrons.," *Nat. Nanotech.*, vol. 8, no. 4, pp. 229–30, 2013.

[169] P. V Kamat, "Photovoltaics: capturing hot electrons.," *Nat. Chem.*, vol. 2, no. 10, pp. 809–810, 2010.

[170] K. K. Likharev, "Single-electron devices and their applications," *Proc. IEEE*, vol. 87, no. 4, pp.

606–632, 1999.

[171] V. Ray, R. Subramanian, P. Bhadrachalam, L. Ma, C. Kim, and S. J. I. N. Koh, “CMOS-compatible fabrication of room- temperature single-electron devices,” *Nat. Nanotechnol.*, vol. 3, no. 10, pp. 603–8, 2008.

[172] M. W. Knight *et al.*, “Aluminum plasmonic nanoantennas,” *Nano Lett.*, vol. 12, no. 11, pp. 6000–6004, 2012.

[173] X. Chen, B. Jia, Y. Zhang, and M. Gu, “Exceeding the limit of plasmonic light trapping in textured screen-printed solar cells using Al nanoparticles and wrinkle-like graphene sheets,” *Light Sci. Appl.*, vol. 2, no. 8, p. e92, 2013.

[174] M. Zapata Herrera, J. Aizpurua, A. K. Kazansky, and A. G. Borisov, “Plasmon Response and Electron Dynamics in Charged Metallic Nanoparticles.,” *Langmuir*, vol. 32, no. 11, pp. 2829–40, Mar. 2016.

[175] J. Gong, R. Dai, Z. Wang, and Z. Zhang, “Thickness Dispersion of Surface Plasmon of Ag Nano-thin Films: Determination by Ellipsometry Iterated with Transmittance Method,” *Sci. Rep.*, vol. 5, no. 1, p. 9279, 2015.

[176] B. Päivänranta, A. Langner, E. Kirk, C. David, and Y. Ekinci, “Sub-10 nm patterning using EUV interference lithography,” *Nanotechnology*, vol. 22, no. 37, p. 375302, 2011.

[177] S. Y. Chou and P. R. Krauss, “Imprint lithography with sub-10 nm feature size and high throughput,” *Microelectron. Eng.*, vol. 35, no. 1–4, pp. 237–240, 1997.

[178] W. Park, J. Rhie, N. Y. Kim, S. Hong, and D.-S. Kim, “Sub-10 nm feature chromium photomasks for contact lithography patterning of square metal ring arrays,” *Sci. Rep.*, vol. 6, no. 1, p. 23823, Jul. 2016.